Measurement of the Exclusive (ν_μ p $\rightarrow$ μ^- p π^+) and Inclusive (ν_μ N $\rightarrow$ μ^- N' π^+) Single Pion ν Interaction Cross Section in a Carbon Target Using the SciBar Detector at the K2K Experiment

Ana Yaiza Rodríguez Marrero

Ph.D. Dissertation

supervised by

Federico Sánchez Nieto

Univeristat Autònoma de Barcelona
Departament de Física
Edifici Cn, E-08193 Bellaterra, Barcelona

March 2007

Resumen

El descubirmiento del fenómeno de las oscilaciones de neutrinos es uno de los desarrollos más excitantes hechos en los últimos años en el campo de la física de partículas. El anuncio de este resultado revivió el interés en la física de neutrinos, y estimuló la preparación de actuales y futuros experimentos con el ánimo de hacer medidas precisas de los parámetros que controlan las oscilaciones de neutrinos. Las medidas que se presentan en este trabajo usan datos tomados por el experimento de neutrinos K2K. K2K usa un beam de neutrinos producido artificialmente para medir oscilación de neutrinos muónicos. La energía media de esos neutrinos es 1.3 GeV. Los neutrinos se detectan en un sistema de detectores cercanos (en el laboratorio KEK), y en un detector lejano (Super-Kamiokande). Las capacidades de los detectores permiten medir las razones de interacción de neutrinos y sus energías, de donde se puede obtener una clara indicación sobre la oscilación de los neutrinos.

Mejorar el entendimiento de las secciones eficaces en las interacciones neutrino-núcleo es crucial para estudiar con precisión las oscilaciones de neutrinos. Las interacciones alrededor de 1 GeV son particularmente importantes porque esta es la región donde se espera la señal de oscilación en muchos experimentos, pero las secciones eficaces en esta región no se conocen muy bien. Esta región de energía es complicada debido a las contribuciones solapadas de scattering quasi-elástico, producción resonante de piones individuales, y scattering profundamente inelástico. Todas estas interacciones se miden conjuntamente para estudiar el déficit en el número esperado de eventos de neutrinos, y las interacciones quasi-elásticas se estudian a parte para medir el déficit como una función de la energía. Este trabajo describe una medida integrada en energía y otra dependiente de la energía del neutrino de la sección eficaz para producción resonante de piones cargados individuales frente a un blanco de carbono. Las medidas se dan tomando como referencia la sección eficaz de scattering quasi-elástico en corrientes cargadas. Medimos el canal de interacción exclusivo, $\nu_\mu p \rightarrow \mu p \pi^+$, y el inclusivo, $\nu_\mu N \rightarrow \mu N' \pi^+$. Los datos se recogieron con un detector de centelleador totalmente activo, SciBar, en el detector cercano de K2K. Los resultados que se presentan son consistentes con experimentos anteriores y un modelo teórico aceptado ampliamente.

Abstract

The discovery of neutrino oscillations phenomena is one of the most exciting developments made in the recent years in the particles physics field. The announcement of this result revived the interest in the neutrino physics, and estimulated the preparation of current and future neutrino experiments with the aim of making precise measurments of the parameters controlling the neutrino oscillations. The measurements presented in this dissertation use data collected by the K2K long-baseline neutrino experiment. It uses an artificially-produced neutrino beam to measure muon neutrino oscillations. The mean energy of those muon neutrinos is 1.3 GeV. The neutrinos are detected in a near detector system (at the KEK laboratory), and in a far detector (Super-Kamiokande). The detectors capabilities allow the measurement of the neutrino interaction rates and their energy, from which a clear indication of oscillations is obtained.

Improving our understanding of neutrino-nucleus cross section is crucial to these precision studies of neutrino oscillations. Interactions in the neutrino energy around 1 GeV are particularly important because this is the region of the expected oscillation signal in many experiments, but the cross sections in this region are not very well-known. This energy region is complicated due to overlapping contributions from quasi-elastic scattering, resonant single pion production, and deep inelastic scattering. All these interactions are measured together to study the deficit in the expected number of neutrino events, and the quasi-elastic interactions apart to give this deficit as a function of the neutrino energy. We describe in this dissertation an integrated and energy neutrino dependent measurement of the cross section for resonant single charged pion production in charged-current muon neutrino interactions with a carbon target. The measurements are given taking as reference the cross section for charged-current quasi-elastic scattering. We measure the exclusive interaction channel, $\nu_\mu p \rightarrow \mu p \pi^+$, and the inclusive interaction channel, $\nu_\mu N \rightarrow \mu N' \pi^+$. The data are collected with a fully active scintillator detector, SciBar, at the K2K near detector system. The results are consistent with previous experiments, and predictions based on a widely-accepted model.

Contents

List of Figures **v**

List of Tables **xi**

1 Overview **1**

2 Introduction to neutrinos and neutrino oscillation **3**

2.1 Introduction . . . 3

2.2 Neutrino and neutrino mass . . . 5

2.3 Neutrino oscillations theory . . . 6

2.3.1 Neutrino oscillations in vacuum . . . 6

2.3.2 Neutrino oscillations in matter . . . 9

2.4 Neutrino oscillation experiments and results . . . 10

2.4.1 Atmospheric neutrinos . . . 10

2.4.2 Solar neutrinos . . . 13

2.4.3 Neutrinos from reactors and accelerators . . . 14

3 K2K experiment **17**

3.1 Introduction . . . 17

3.2 K2K experimental technique . . . 18

3.2.1 Signatures . . . 19

3.2.2 Measurements in the K2K Experiment . . . 20

3.2.3 Expected Sensitivity of the K2K Experiment . . . 23

3.3 K2K experimental setup . . . 25

3.3.1 Neutrino beam and beam monitor . . . 25

3.3.2 Near Detector . . . 30
3.3.3 Far Detector: Super-Kamiokande (SK) . . . 35
3.4 Monte Carlo Simulation . . . 37
3.4.1 Neutrino Beam Simulation (Beam-MC) . . . 37
3.4.2 Neutrino interaction (NEUT) . . . 39
3.4.3 Detector Simulation . . . 40
3.4.4 SciBar MC . . . 40
3.5 Recent Results and History of the K2K Experiment . . . 41

4 SciBar detector **45**
4.1 Design concept . . . 45
4.2 Detector components . . . 48
4.2.1 Extruded scintillator . . . 48
4.2.2 Wave-length shifting fiber . . . 50
4.2.3 64-channel multi-anode PMT . . . 51
4.2.4 Gain monitoring . . . 52
4.2.5 Electro-magnetic calorimeter . . . 52
4.2.6 Readout system . . . 53
4.2.7 Data acquisition . . . 54
4.3 Basic performance . . . 54
4.3.1 Energy scale calibration . . . 55
4.3.2 Timing calibration . . . 56
4.3.3 Calibration using test beam . . . 58
4.3.4 Alignment of the detector . . . 59

5 Theory of Neutrino Nucleus Interaction around 1 GeV **61**
5.1 Introduction to the Single Pion Production . . . 61
5.2 Neutrino production of isolated resonances . . . 62
5.3 Interfering resonances . . . 65
5.4 Computing of the Production and Decay Amplitudes . . . 69
5.5 Summary on Single Pion Production Theory . . . 72
5.6 Elastic and Quasi-Elastic Scattering . . . 73
5.7 Nuclear effects . . . 76

5.7.1 Fermi Gas Model and Pauli Blocking . . . 76
5.7.2 Absorption and Rescattering Processes . . . 79

6 Data and Event Selection **81**
6.1 Muon track reconstruction . . . 81
6.1.1 Muon track selection . . . 81
6.1.2 Muon energy reconstruction . . . 85
6.1.3 Muon angle . . . 86
6.2 Track counting . . . 88
6.3 Event selection and classification . . . 90
6.3.1 Exclusive and inclusive single pion selection . . . 91
6.3.2 CCQE selection . . . 99
6.4 Basic distributions . . . 99
6.5 Selection summary . . . 103

7 Measurement of the Single Pion Cross Section **107**
7.1 Method to determine the Single Pion Cross Section Ratio . . . 107
7.2 Reconstruction of the neutrino energy . . . 111
7.3 Corrections factors from MC for the energy dependet measurement . . . 115
7.4 Behaviour of the migration matrix . . . 117
7.5 Measurement of the Cross Section Ratio . . . 119

8 Systematic effects **121**
8.1 MC statistics . . . 121
8.2 Interaction model . . . 122
8.3 Nuclear effects . . . 123
8.4 Detector effects . . . 123
8.5 Reconstruction effects . . . 125
8.6 Systematic effect in the cut distributions . . . 128
8.7 Systematic uncertainties on the measurement of the cross section of the single $p\pi^+$ interaction normalized to CCQE . . . 133
8.8 Systematic uncertainties on the measurement of the cross section of the single $1\pi^+$ interaction normalized to CCQE . . . 133
8.9 Statistical MC uncertainties on the measurement of the cross section ratio . . . 133

9 Results and Discussion **145**
9.1 Measurement of the cross section of the single $p\pi^+$ interaction normalized to CCQE interaction . . . 145
9.2 Measurement of the cross section of the single $1\pi^+$ interaction normalized to CCQE interaction . . . 148
9.3 Previous experiments and their results . . . 151
9.4 Comparison with the previous experiments . . . 154
9.4.1 Scaling the result . . . 154
9.4.2 Comparison . . . 156
9.5 Measurement of the cross section of the single $n\pi^+$ interaction normalized to CCQE . . . 161
9.6 Cross checks . . . 162

10 Conclusions **167**

Bibliography **169**

A Tracking and Matching definition in SciBar **179**
A.1 Tracking . . . 179
A.2 Matching . . . 180

B SciBar Calculations **183**
B.1 Coordinate Systems . . . 183
B.2 Calculation of Angles . . . 184
B.3 Calculation of Momentum Elements . . . 187
B.4 Calculation of Neutrino Energy . . . 188
B.5 Calculation of $\Delta\theta_p$ . . . 189
B.6 Calculation of momentum transfer, q^2 . . . 192

C Systematic error on the measurement of the cross section of the single $p\pi^+$ interaction **193**
C.1 Using only the 2 track sample . . . 193
C.2 Using only the 3 track sample . . . 200

List of Figures

2.1 Forward elastic scattering of a neutrino from a particle of matter 9
2.2 Atmospheric neutrinos from pion decay 11
2.3 Confidence intervals for Δm^2 and $\sin^2 2\theta$ for $\nu_\mu \leftrightarrow \nu_\tau$ two-neutrino oscillations from Super-Kamiokande 12
2.4 Possible solutions before and after Super-Kamiokande and SNO results 14

3.1 Schematic view of K2K experiment placement 18
3.2 Neutrino energy spectrum distorted by oscillation compared with null case 20
3.3 Flow of number of events analysis in K2K 21
3.4 Flow of spectrum shape analysis in K2K 22
3.5 Correlation between true and reconstructed neutrino energy in Monte Carlo . . . 23
3.6 Sensitivity to the $\nu_\mu \rightarrow \nu_x$ oscillation in K2K. 24
3.7 Schematic view of the K2K setup 25
3.8 Schematic view of the KEK-PS and neutrino beam line 26
3.9 Number of protons delivered to the production target 27
3.10 Schematic view of the two horn magnets 29
3.11 Schematic view of the neutrino Near Detector 31
3.12 Schematic view of the 1 kiloton water Čerenkov detector 32
3.13 Photograph of the inner detector of the 1KT from the bottom 33
3.14 Schematic view of the SciFi detector 34
3.15 Schematic view of the Super-Kamiokande detector 36
3.16 The energy spectrum for each neutrino type at Near Detector and Far Detector estimated by the beam MC simulation 38
3.17 Neutrino cross section divided by E_ν as a function of E_ν with CH target 40
3.18 Reconstructed neutrino energy for the single-ring muon-like sample 43

3.19 Allowed regions of oscillation parameters for K2K. 44

4.1 Schematic view of SciBar detector 46
4.2 Conceptual scheme of the WLS fiber readout of the scintillation fiber 47
4.3 Conceptual design of the SciBar readout system 47
4.4 Definition of the SciBar local coordinate system 48
4.5 The emission light spectrum of the scintillator 49
4.6 The absorption and emission spectrum of the WLS fiber 49
4.7 Drawing of a scintillator strip 50
4.8 The wavelength-shifting fiber Kuraray Y11 (200) MS 50
4.9 Schematic view of the gain monitoring system 53
4.10 Picture of the data acquisition board 54
4.11 Timing diagram of the data acquisition 55
4.12 Light yield distribution of a typical scintillator strip for cosmic-ray muons 55
4.13 Energy calibration constant of all strips 56
4.14 Sensibility of the energy scale calibration constant for a typical strip in SciBar . . 57
4.15 Timing difference between adjacent TA channels along a muon track 57
4.16 Ratio of the observed dE/dx to the expected one as a function of the expected . . 58
4.17 Plane position correction using the transverse deviation, Δt_0, and the z deviation, Δz 60

5.1 Production of the Δ^{++} resonance in a charged-current neutrino interaction 66
5.2 Cross section for the different single pion production modes for previous measurements and NEUT simulation 73
5.3 Cross section of charged current quasi-elastic channels in NEUT 76
5.4 Effect of the Pauli Blocking in the cross section as a function of the $Q^2 = -q^2$ . . 78
5.5 Effect of the Fermi motion in the $\Delta\theta_p$ distribution 79

6.1 Event display of SciBar with a track matched to a MRD track and to MRD hits . 82
6.2 The vertex distribution of SciBar-MRD matching events and fiducial volume definition 83
6.3 Beam timing distribution 84
6.4 Definition of the upstream edge of the MRD matched track as the interaction vertex 84
6.5 Vertex resolution estimated from MC simulation 85

6.6 Muon detection efficiency as a function of the true muon energy, and as a function of the true muon angle . . . 86
6.7 Energy and energy resolution of the muon reconstructed track in SciBar . . . 87
6.8 Angle respect to the beam direction and angular resolution of the muon reconstructed track in SciBar . . . 87
6.9 Distance between the reconstructed event interaction vertex and the initial or final point of the other tracks in fiducial volume and on time with muon tracks . . . 88
6.10 Distribution of the number of tracks in the fiducial volume, time window and from the interaction vertex . . . 89
6.11 Opening angle between the expected track (assuming CCQE) and the observed track which is measured . . . 92
6.12 Distribution of the angle, $\Delta\theta_p$, between the expected track (assuming CCQE) and the observed track . . . 93
6.13 The purity square times efficiency of selecting CC1π^+ events in the two track sample as a function of the $\Delta\theta_p$ angle . . . 94
6.14 dE/dx distribution of the muon and proton track . . . 95
6.15 Comparison between the dE/dx distribution of the muon and proton track in MC and in data . . . 95
6.16 Muon confidence level (MuCL) in the three track sample . . . 96
6.17 Purity square times efficiency of selecting CCpπ^+ events in the three track sample as a function of muon confidence level value . . . 97
6.18 Muon confidence level (MuCL) in the two non-QE track sample . . . 98
6.19 Distribution of the number of hits of the muon track and vertex tracks in the single pπ^+ selection . . . 100
6.20 Distribution of the number of hits of the muon track and vertex tracks in the single 1π^+ selection . . . 100
6.21 Distribution of the number of hits of the muon track and vertex tracks in the CCQE selection . . . 101
6.22 Muon track momentum and angle distribution for single pπ^+ . . . 101
6.23 Muon track momentum and angle distribution for single 1π^+ . . . 102
6.24 Muon track momentum and angle distribution for CCQE . . . 102
6.25 Event display of a two track selected single pπ^+ and 1π^+ event . . . 104
6.26 Event display of a three track selected single pπ^+ event . . . 105

7.1 Scheme of the migration matrix application . . . 111
7.2 Hadron mass distribution for the exclusive and inclusive single pion channel . . . 112
7.3 Reconstructed neutrino energy for single pπ^+ . . . 113
7.4 Reconstructed neutrino energy for single 1π^+ . . . 113
7.5 Reconstructed neutrino energy for CCQE . . . 114
7.6 Reconstructed neutrino energy for single pπ^+, single 1π^+, and CCQE in the 4 energy bins . . . 114
7.7 Q^2 distribution in the three different selections considered in the analysis . . . 115

8.1 Crosstalk model . . . 124
8.2 Distribution of the dE/dx per plane of the muon track . . . 124
8.3 Number of photo-electron distribution for all hits survived after the crosstalk correction . . . 125
8.4 Photo-electron distribution for the muon tracks . . . 126
8.5 Tangent resolution in data and in MC (σ_{tan}) . . . 127
8.6 Dependency of the tangent resolution in data and in MC with the muon energy . . . 127
8.7 Dependency of tangent resolution in data and in MC with the muon tangent . . . 128
8.8 Distance to the reconstructed vertex interaction point with MC variation bands . . . 129
8.9 Number of tracks at vertex distribution with MC variation band . . . 130
8.10 $\Delta\theta_p$ distribution with MC variation band . . . 131
8.11 MuCL distribution with MC variation band . . . 132

9.1 Comparison between the total exclusive measurement normalized to CCQE and MC prediction . . . 146
9.2 Comparison between the energy dependent exclusive measurement normalized to CCQE and MC prediction as a function of the neutrino energy . . . 147
9.3 Comparison between the total inclusive measurement normalized to CCQE and MC prediction . . . 149
9.4 Comparison between the energy dependent inclusive measurement normalized to CCQE and MC prediction . . . 150
9.5 Comparison between the overall exclusive measurement normalized to CCQE, and ANL, BNL, and GGM previous experimental results . . . 157
9.6 Comparison between the energy dependent exclusive measurement normalized to CCQE, and ANL, BNL, and GGM previous experimental results . . . 158

9.7 Comparison between the overall inclusive measurement normalized to CCQE, and ANL and MiniBooNE previous experimental results 159
9.8 Comparison between the energy dependent inclusive measurement normalized to CCQE, and ANL and MiniBooNE previous experimental results 160
9.9 Comparison between the CCnπ^+ measurement normalized to CCQE and MC prediction 161
9.10 Comparison between the energy dependent CCnπ^+ measurement normalized to CCQE and MC prediction 162
9.11 Comparison between the total measurement normalized to CCQE for the three ways of selecting CCpπ^+ : two and the track sample, two track ample, three track sample 163
9.12 Comparison between the energy dependent measurement normalized to CCQE for the three ways of selecting CCpπ^+ : two and the track sample, two track ample, three track sample 164
9.13 Comparison among nominal single pπ^+ measurement and those ones obtained with different final hadron mass values 165
9.14 Comparison among nominal single 1π^+ measurement and those ones obtained with different final hadron mass values 166

A.1 Extrapolation of a track leaving the detector from the side in one view. Cells in orange represent veto cells which are not read 181
A.2 Example of matching tracks accepted by each class 182

B.1 xyz coordinate system vs. beam (x'y'z') coordinate system 184
B.2 The muon track is labeled μ, the expected proton track is labeled **p**, and tracks **1** and **2** are examples of candidate proton tracks. Track **1** is forward and track **2** is backward 190
B.3 Momentum vectors of the tracks shown in Figure B.2 191
B.4 Correct momentum vectors of the tracks shown in Figure B.2 191

List of Tables

3.1 Specification summary of KEK-PS for K2K experiment 28
3.2 Neutrino flux weighting factors 41
3.3 Summary of the K2K history 44

4.1 Specifications of multi-anode photo-multiplier tube 51

5.1 Nucleon resonances below 2 GeV/c^2 67

6.1 Number of events for different track samples 90
6.2 Data and MC compatibility for different track samples within only statistical error 90
6.3 Breakdown of MC track samples by interaction type 90
6.4 Purity and efficiency in the two track CC$p\pi^+$ selection based on the nominal MC 93
6.5 Purity and efficiency in the two track CC$1\pi^+$ selection based on the nominal MC 94
6.6 Purity and efficiency in the three track CC$p\pi^+$ selection based on the nominal MC 96
6.7 Purity and efficiency in the two and three track CC$p\pi^+$ selection based on the nominal MC 97
6.8 Purity and efficiency in the one and two track CCQE selection based on the nominal MC 99
6.9 Purity, efficiency and number of selected events in the CC$p\pi^+$ selection, CC$1\pi^+$ selection, and CCQE selection. 103

7.1 Index notation for energy-dependent cross section ratio measurement 109
7.2 Energy dependent purity in the two and three track CC$p\pi^+$ selection based on the nominal MC 116
7.3 Energy dependent purity in the two track CC$1\pi^+$ selection based on the nominal MC 116

7.4 Energy dependent efficiency in the two and three track CC$p\pi^+$ selection based on the nominal MC . . . 117
7.5 Energy dependent efficiency in the two track CC$1\pi^+$ selection based on the nominal MC . . . 117
7.6 Energy dependent efficiency in the one and two track CCQE selection based on the nominal MC . . . 117
7.7 Number of events in the three selections for the different energy bins . . . 118
7.8 Measurment of the CC$p\pi^+$ to CCQE cross section ratio . . . 119
7.9 Measurment of the energy dependent CC$p\pi^+$ to CCQE cross section ratio . . . 119
7.10 Measurment of the CC$1\pi^+$ to CCQE cross section ratio . . . 120
7.11 Measurment of the energy dependent CC$1\pi^+$ to CCQE cross section ratio . . . 120

8.1 Systematic errors for the overall CC$p\pi^+$ to CCQE cross section ratio . . . 134
8.2 Systematic errors for the CC$p\pi^+$ to CCQE cross section ratio in the first energy bin 135
8.3 Systematic errors for the CC$p\pi^+$ to CCQE cross section ratio in the second energy bin . . . 136
8.4 Systematic errors for the CC$p\pi^+$ to CCQE cross section ratio in the third energy bin . . . 137
8.5 Systematic errors for the CC$p\pi^+$ to CCQE cross section ratio in the fourth energy bin . . . 138
8.6 Systematic errors for the overall CC$1\pi^+$ to CCQE cross section ratio . . . 139
8.7 Systematic errors for the CC$1\pi^+$ to CCQE cross section ratio in the first energy bin 140
8.8 Systematic errors for the CC$1\pi^+$ to CCQE cross section ratio in the second energy bin . . . 141
8.9 Systematic errors for the CC$1\pi^+$ to CCQE cross section ratio in the third energy bin . . . 142
8.10 Systematic errors for the CC$1\pi^+$ to CCQE cross section ratio in the fourth energy bin . . . 143
8.11 Statistical errors for the overall CC$p\pi^+$ to CCQE cross section ratio for the different MC samples . . . 144
8.12 Statistical errors for the overall CC$1\pi^+$ to CCQE cross section ratio for the different MC samples . . . 144

9.1 Measurment of the CC$p\pi^+$ to CCQE cross section ratio . . . 146
9.2 Measurment of the energy dependent CC$p\pi^+$ to CCQE cross section ratio . . . 147

9.3 Measurment of the CC1π^+ to CCQE cross section ratio 148
9.4 Measurment of the energy dependent CC1π^+ to CCQE cross section ratio 148
9.5 ANL experiment: Radecky et al 1982 single pπ^+ measurement 152
9.6 ANL experiment: Barish et al 1977 CCQE measurement 152
9.7 GGM experiment: Lerche et al 1978 single pπ^+ measurement 152
9.8 GGM experiment: Pohl et al 1979 CCQE measurement 153
9.9 $R = \frac{\sigma(\nu_\mu p \to \mu^- p \pi^+)}{\sigma(\nu_\mu n \to \mu^- p)}$ 154
9.10 $R = \frac{\sigma(\nu_\mu N \to \mu^- N' \pi^+)}{\sigma(\nu_\mu n \to \mu^- p)}$ 154

10.1 Measurment of the CCpπ^+ to CCQE cross section ratio 167
10.2 Measurment of the energy dependent CCpπ^+ to CCQE cross section ratio 168
10.3 Measurment of the CC1π^+ to CCQE cross section ratio 168
10.4 Measurment of the energy dependent CC1π^+ to CCQE cross section ratio 168

C.1 Measurment of the CCpπ^+ to CCQE cross section ratio 193
C.2 Measurment of the energy dependent CCpπ^+ to CCQE cross section ratio 194
C.3 Systematic errors for the overall CCpπ^+ to CCQE cross section ratio 195
C.4 Systematic errors for the CCpπ^+ to CCQE cross section ratio in the first energy bin 196
C.5 Systematic errors for the CCpπ^+ to CCQE cross section ratio in the second energy bin 197
C.6 Systematic errors for the CCpπ^+ to CCQE cross section ratio in the third energy bin 198
C.7 Systematic errors for the CCpπ^+ to CCQE cross section ratio in the fourth energy bin 199
C.8 Measurment of the CCpπ^+ to CCQE cross section ratio 200
C.9 Measurment of the energy dependent CCpπ^+ to CCQE cross section ratio 200
C.10 Systematic errors for the overall CCpπ^+ to CCQE cross section ratio 201
C.11 Systematic errors for the CCpπ^+ to CCQE cross section ratio in the first energy bin 202
C.12 Systematic errors for the CCpπ^+ to CCQE cross section ratio in the second energy bin 203
C.13 Systematic errors for the CCpπ^+ to CCQE cross section ratio in the third enerrgy bin 204
C.14 Systematic errors for the CCpπ^+ to CCQE cross section ratio in fourth energy bin 205

Chapter 1

Overview

In 1998 the Super-Kamiokande collaboration announced the discovery of neutrino oscillations in atmospheric neutrinos. The same collaboration confirmed the deficit in the observation of solar neutrinos reported by many previous experiments. Its data, combined with that obtained by the SNO collaboration proves without doubt the oscillation of the neutrinos originating in the Sun. These results imply that the neutrinos have mass, even though a very small one. The announcements revived the interest in neutrino physics, and have stimulated the preparation of many experiments with the aim of elucidating the oscillation phenomenon.

The Super-Kamiokande collaboration also proposed another parallel experiment: the KEK to Kamioka (K2K) experiment. The main goals of K2K are to confirm the oscillation of muon neutrinos in a controlled experiment and to measure the oscillation parameters in a way independent of SK did. It is a neutrino experiment located in Japan, in which a muon neutrino beam is sent from the High Energy Accelerator Research Organization (KEK) Laboratory to the Super-Kamiokande detector (SK), located at a distance of 250 km. At the near site there is placed a Near Detector (ND) located 300 m downstream of the production point in KEK. The Near Detector consists of several detectors. The beam is produced in a 12 GeV proton synchrotron accelerator at KEK Laboratory. These neutrinos have an average energy of 1.3 GeV, with a spectrum which was chosen to be close to that of atmospheric neutrinos. This long baseline technique is necessary for the study of neutrino oscillations as this phenomenon only takes place over long distances for this energy range. K2K is the first neutrino oscillation experiment with artificially produced and controlled beam using this technique.

A deficit in the measured muon neutrino flux is expected at Super-Kamiokande. This measurement is based on a comparison of muon neutrino fluxes observed in the near detector and in the far detector. The neutrino energy spectrum is also measured and compared. This neutrino energy spectrum is measured from charged current quasi-elastic (CCQE) interactions: $\nu_\mu n \rightarrow \mu p$. Therefore, the neutrino detection efficiency in each detector and the fraction of the non charged current quasi-elastic (non-QE) events in the sample are crucial information.

The ND was constructed to better understand neutrino interactions. Specially, one of the sub-detectors, SciBar, was designed to detect low momentum particles such as the proton from the CCQE interactions but also from the other neutrino interactions, giving us the capability of distinguishing CCQE events and non-QE, and providing the framework to study each one of the neutrino interactions.

The CCQE interaction is the dominant reaction at these energies being the main source of background to this signal the single pion production, which is the second dominant interaction. The study of the single pion production process is the main goal of this thesis. The measurement of the cross section of the single pion interaction is carried out.

In Chapter **2** a brief historical introduction is followed by the description of some aspects about neutrino oscillations and by a summary of experiments and data in this topic. The experimental technique and setup of K2K experiment are described in Chapter **3**, together with a short description of the Monte Carlo simulation. The Chapter **4** describes the design and performance of the SciBar detector. Following, Chapter **5** presents the theoretical model employed in the K2K experiment to simulate the single pion and the CCQE neutrino interactions. After introducing the experiment, focusing in the detector from where the data is taken, and the theoretical model, we describe the data treatment and selection in Chapter **6**. The method use to measure the single pion cross section is explained in Chapter **7**. After that, the study of the systematic sources affecting the measurement is discussed in Chapter **8**. In Chapter **9** the results are presented in detail and contrasted with the K2K Monte Carlo prediction and previous experiments; also some cross checks are brought in. Finally, the Chapter **10** remarks the main points of this work.

Chapter 2

Introduction to neutrinos and neutrino oscillation

In this Chapter, first a brief historical introduction about neutrinos is given. Afterwards, neutrino mass is considered. Some aspects of the neutrino oscillation theory are explained later. Finally, neutrino oscillation experiments and their results are described.

2.1 Introduction

In the 1930's, scientists exploring the nascent field of nuclear physics were confronted with a troubling mystery: one of their most important laws appeared to be no longer valid. Physicists asked themselves if energy was really conserved: a situation where energy appeared not to be conserved, a reaction called β *decay*, was discovered.

The nucleus of some atoms is unstable and spontaneously emits an electron (β particle) and in the process changes into a stable nucleus of a different element. When the masses and energies of the visible particles before and after the β decay were measured, neither energy nor momentum seemed to be conserved. The nucleus seemed to break into two pieces but the pieces didn't fit together.

As a solution, Pauli postulated in 1930 that a third particle was emitted in β decay. He called neutron to this third particle and said about it,

> "the continuous β spectrum would then become understandable by the assumption that in β decay a neutron is emitted in addition to the electron such that the sum of the energies of the neutron and the electron is constant [...] the mass of the neutron should be of the same order as the electron mass and, in any case, not larger than 0.01 proton mass"

It was presented in the Pauli's letter of the 4^{th} of December 1930 to the Tübingen congress [1]. The neutron was renamed to neutrino ν by Fermi in 1934.

The neutrino was directly detected in 1956 by F. Reines, C. Cowan and collaborators in an experiment at the Savannah River nuclear reactor (intensive $\overline{\nu}$ sources) in South Carolina [2, 3]. The detector contained 200 liters of water in two tanks with up to 40 kg of dissolved $CdCl_2$.

The detection method was based on the so called *inverse β decay*. In this reaction an antineutrino $\overline{\nu}$ interacts with a proton *p*, and a neutron *n* and a positron e^+ are obtained as products, $\overline{\nu} + p \rightarrow n + e^+$. The positron e^+ was detected by its slowing down and annihilating with an electron. The neutron was also slowed down by the water and captured by the cadmium microseconds after the positron capture.

This test confirmed that the signal was indeed due to reactor antineutrinos being captured by proton in the water tanks of the detector and inducing inverse β decay.

One year later, the theory of the massless neutrino with two chiralities (left and right) to explain parity violation in β decays was proposed by Landau [4], Salam [5] and Lee and Yang [6]. The neutrinos were thought to be massless particles.

A second type of neutrino was discovered in 1962 at the Brookhaven experiment [7]. This was the first experiment done with neutrinos from an accelerator. Neutrinos were produced in the decays of pions produced in proton interactions with a target. The charged particles were absorbed in iron shield. After the shield was installed a neutrino detector. Processes of interaction of neutrinos with nucleons $\nu + N \rightarrow \mu^- + X$, $\nu + N \rightarrow e^- + X$ were expected to be observed.

Pions π^+ can decay to a muon μ^+ plus a muon neutrino ν_μ or in a positron e^+ plus a electron neutrino $\nu_{\rm e}$, but the ratio of the probabilities of the two modes is approximately the ratio of the muon and electron mass and that is 10^4, thus in decays of pions predominantly muon neutrinos are produced. Then, if ν_μ and $\nu_{\rm e}$ were thought to be the same particles muons and electrons should have appeared in the detector, since they would interact in the same way. In the Brookhaven experiment 29 muons and only 6 electrons were detected. All electron events

could be explained as background events. It was proved that the process $\nu_\mu + N \to e^- + X$ is forbidden and that muon and electron neutrinos are different particles.

The next studies related to neutrinos showed up when it was proposed that the sun emits enormous numbers of neutrinos. These studies were done by placing detectors in underground mines, such as the Homestake gold mine in South Dakota [8]. The detector was built in 1967 at Brookhaven laboratory, it contains about 615 tons of tetrachloroethylene. Under neutrino interaction, the Chlorine becomes Argon, which is radiative with a half-life of 35 days. By measuring the amount of radiative Argon, the number of neutrinos from the sun can be inferred. A deficit in the number of neutrinos that the Sun was expected to emit was found. This problem was called "the Solar neutrino problem": the particle physics theory, the model of the Solar interior and the experiments were questioned.

One solution to the solar neutrino problem would be that neutrinos could oscillate during their travels through space. Therefore, an electron neutrino could spontaneously change into a muon (or any kind of) neutrino. The neutrino oscillation probability depends on the mass difference of the neutrinos involved in the oscillation. If this mass difference is zero the oscillation probability is also zero. So, the neutrino oscillations existence required neutrinos with finite mass.

In 2000, the first direct observation of a third flavor of neutrino, the tau neutrino, took place [9]. It was expected to exist in the framework of the Standard Model since a quite massive cousin of the electron and the muon, the tau lepton, was discovered in 1975.

2.2 Neutrino and neutrino mass

Three neutrino flavors: electron neutrino ν_{e}, muon neutrino ν_μ and tau neutrino ν_τ, exist in nature with mass $m < M_Z/2.0$ where M_Z is the Z boson mass. The number of neutrino flavors $n_\nu = 2.984 \pm 0.008$ was obtained by the LEP experiments [10] from the measurement of the width of the decay $Z \to \nu + \overline{\nu}$. The possibility of the fourth light neutrino $m_\nu < M_Z/2.0$ is excluded from the measurement.

Neutrino mass is searched for in the following three types of experiments: (1) direct kinematic measurement, (2) search for neutrinoless double β-decay and (3) neutrino oscillation experiments. In addition, another limit on neutrino masses measurements comes from cosmology.

The direct mass measurements are performed by measuring the kinematics of a particle decay. The most sensitive measurement of $\nu_{\rm e}$ mass is performed by using the Tritium β decay, which gives an upper limit of 2.3 eV for the $\nu_{\rm e}$ mass (95% C.L.) [11]. The mass limit of $\nu_{\rm e}$ is also obtained from the spread of the arrival time of neutrinos from Supernova-1987A to be 5.7 eV [12]. The best limit of the ν_μ mass of 170 keV (90% C.L.) has been obtained from the two-body pion decay at rest, $\pi^+ \rightarrow \mu^+ + \nu_\mu$, by the PSI group [13]. For ν_τ, the current mass limit was given by the ALEPH collaboration. Results from two kinds of tau decays, $\tau \rightarrow 3\pi\nu_\tau$ and $\tau \rightarrow 5\pi(\pi^0)\nu_\tau$, were combined to set the limit at 18.2 MeV at 95% C.L. [14].

The neutrinoless double β decay ($0\nu\beta\beta$) occurs only if the neutrino is massive and a Majorana particle [15]. Majorana particles are formed by making the neutrino its own particle. The $0\nu\beta\beta$-decay rate is proportional to the square of the effective Majorana neutrino masses, $\langle m_\nu \rangle$. Confident evidence of $0\nu\beta\beta$-decay is not obtained although Heidelberg-Moscow group reported a positive signal in 2001 [16]. The upper limit of the mass is set at $\langle m_\nu \rangle < 0.2$ eV [17].

The Wilkinson Microwave Anisotropy Probe (WMAP), together with the Sloan Digital Sky Survey (SDSS), the Lyman-α forest, and other observations, lead to strong constraints on $\Sigma m_\nu \leq 1$ eV for the three degenerate neutrino species [18], in which the most stringent limit is reported as 0.42 eV [19]. However, the upper bound depends strongly on other cosmological parameters, such as the matter density and the Hubble constant.

No evidence for finite neutrino masses is obtained from any of these measurements until now. The smallness of neutrino masses, if they exist, is not explained in the standard model of the particle physics (SM) while the interaction of neutrinos with other particles through electroweak interactions is explained [20]. However, some extensions of those models, a theory know as "see-saw" mechanism [21] explains tiny neutrino mass most naturally. In this theory, the smallness of neutrino masses appears in the new physics of the higher energy scale, beyond SM.

2.3 Neutrino oscillations theory

2.3.1 Neutrino oscillations in vacuum

Neutrino oscillations are considered in the framework of three-neutrino mixing. The hypothesis of neutrino mixing is based on the assumption that the total Lagrangian contains a *neutrino mass*

term, which does not conserve flavor lepton numbers: if neutrinos have small mass and are mixed particles, neutrino oscillations take place [22].

The state of a neutrino $|\nu_\alpha\rangle$ (α = e, μ, τ) produced in a weak process (for example, the neutrino that is produced together with μ^+ in the decay $\pi^+ \to \mu^+\nu_\mu$ is the muon neutrino ν_μ; the electron antineutrino $\overline{\nu}_\mathrm{e}$ produces e^+ in the process $\overline{\nu}_\mathrm{e} + p \to e^+ + n$) is a coherent superposition of the states of neutrinos with definite mass,

$$|\nu_\alpha\rangle = \sum_{i=1}^{3} U^*_{\alpha i} |\nu_\mathrm{i}\rangle \tag{2.1}$$

where $|\nu_\mathrm{i}\rangle$ is the state of a neutrino with momentum p, mass m_i, and energy

$$E_i = \sqrt{p^2 + m_i^2} \simeq p + \frac{m_i^2}{2p} \tag{2.2}$$

At the time t after the production process the neutrino state will be

$$|\nu_\alpha\rangle_t = \sum_{i=1}^{3} U^*_{\alpha i} e^{-iE_i t} |\nu_\mathrm{i}\rangle \tag{2.3}$$

Neutrinos can be only detected via weak interaction processes. Decomposing the state $|\nu_\alpha\rangle_\mathrm{t}$ in terms of weak eigenstates $|\nu_\beta\rangle$, we have

$$|\nu_\alpha\rangle_t = \sum_{\beta=e,\mu,\tau} |\nu_\beta\rangle A(\nu_\alpha \to \nu_\beta) \tag{2.4}$$

where

$$A(\nu_\alpha \to \nu_\beta) = \sum_{i=1}^{3} U_{\beta i} e^{-iE_i t} U^*_{\alpha i} \tag{2.5}$$

is the amplitude of the transition $\nu_\alpha \to \nu_\beta$ at the time t. Taking into account the unitary of the mixing matrix, from Equation 2.5 the following expression for the probability of transition $\nu_\alpha \to \nu_\beta$ can be obtained (labeling neutrino masses in such a way that $m_1 < m_2 < m_3$):

$$P(\nu_\alpha \to \nu_\beta) = \left| \delta_{\alpha\beta} + \sum_{i \geq 2} U_{\beta i} \left(e^{-i\Delta m^2_{i1} \frac{L}{2E}} - 1 \right) U^*_{\alpha i} \right|^2 \tag{2.6}$$

where $L \simeq t$ is the distance between a neutrino source and a neutrino detector, E is the neutrino energy and $\Delta m^2_{i1} = m^2_i - m^2_1$. It is clear that if the following condition is satisfied

$$\Delta m^2_{i1} \frac{L}{2E} \ll 1, \forall i \neq 1 \tag{2.7}$$

the Equation 2.6 becomes $P(\nu_\alpha \to \nu_\beta) \simeq \delta_{\alpha\beta}$. Then, in order to observe neutrino oscillations, it is necessary that $1 \lesssim \Delta m^2_{i1} \frac{L}{2E}$.

For simplicity in the discussion the oscillation between two neutrino species is considered. The mixing matrix of Equation 2.1 is then real

$$U = \begin{pmatrix} \cos\theta & \sin\theta \\ -\sin\theta & \cos\theta \end{pmatrix} \tag{2.8}$$

so that the transition probabilities are given by $(\nu_\alpha \neq \nu_\beta)$

$$P(\nu_\alpha \to \nu_\beta) = \sin^2 2\theta \sin^2 \left(\frac{\Delta m^2 L}{4E} \right) \tag{2.9}$$

$$P(\nu_\alpha \to \nu_\alpha) = 1 - P(\nu_\alpha \to \nu_\beta) \tag{2.10}$$

where $\Delta m^2 = m_2^2 - m_1^2$. An oscillation length can be defined in the form

$$L_0 = 4\pi \frac{E}{\Delta m^2} \tag{2.11}$$

with E in MeV (GeV), Δm^2 in eV^2 and L in m (km)

$$L_0 \simeq 2.48 \frac{E}{\Delta m^2} \tag{2.12}$$

Finally, the transition probability can be written as

$$P(\nu_\alpha \to \nu_\beta) = \sin^2 2\theta \sin \left(\pi \frac{L}{L_0} \right) = \sin^2 2\theta \sin \left(\frac{1.27 \Delta m^2 (eV^2) L(km)}{E(GeV)} \right) \tag{2.13}$$

giving the dependence with L_0 or with E in MeV (GeV), Δm^2 in eV^2 and L in m (km).

Therefore, if the neutrino mass states mix with different masses, neutrinos change flavor during flight. This phenomenon is the called "neutrino oscillation". The existence of neutrino oscillation is evidence of the finite neutrino mass. The amplitude of the oscillation is determined by the mixing angle θ. The L/E dependence of the oscillation probability is characterized by Δm^2. In the case of three-neutrino mixing, there are two independent mass splittings Δm^2_{12}, Δm^2_{23}, three mixing angles θ_{12}, θ_{13}, θ_{23}, and one Dirac phase δ.

2.3.2 Neutrino oscillations in matter

If the neutrinos pass through the Sun, the Earth, etc., matter can significantly alter the neutrino mixing and the probabilities of the transitions between different types of neutrinos. An effective Hamiltonian has to be taken into account to get the new neutrino oscillation pattern. Detailed discussion of neutrino oscillations in matter can be found in [23, 24].

For instance, solar neutrinos coming from nuclear reactions in the core of the Sun traverse significant amount of solar material on their way out of the Sun. Also, atmospheric neutrinos cross large amount of material, they can be produced in the atmosphere on one side of the Earth, and then travel through the whole Earth before being detected in a detector in the other side.

The interaction between neutrinos and matter is extremely weak. Nevertheless, if they cross dense material, such as, the Sun or the Earth, the matter effects become important. Forward elastic scatterings of neutrinos from particles of matter (electrons and nucleons) can appear as it is showed in Figure 2.1. Since one of these reactions is only possible for ν_{e}, the term to be added to the vacuum Hamiltonian depends on which neutrinos are crossing the matter: if electron neutrinos are considered, an additional term must be added. This asymmetry causes changes in the oscillation pattern. Some oscillations parameters can be modified and others, not considered in oscillations in vacuum, can be determined. The matter effects in terrestrial very long baseline neutrino oscillation experiments and how they change oscillation pattern are discussed in Reference [25].

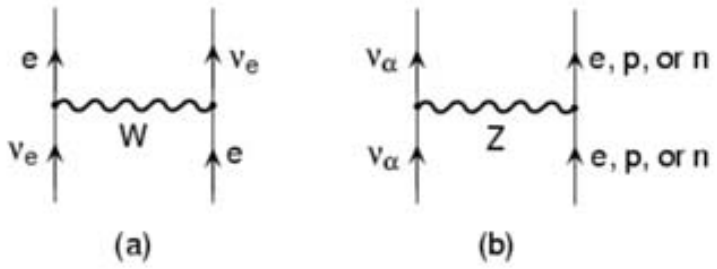

Figure 2.1: Forward elastic scattering of a neutrino from a particle of matter. (a) W-exchange-induced scattering from an electron, which is possible only for ν_{e}. (b) Z-exchange-induced scattering from an electron, proton or neutron. This is possible for ν_{e}, ν_{μ} or ν_{τ}.

2.4 Neutrino oscillation experiments and results

The neutrino oscillation experiments can be classified in different ways. It is possible to classify them taking into account the manifestation of the oscillation or the origin of neutrinos which will be detected.

Attending to the manifestation of the oscillation:

- Appearance experiments. Neutrinos of a certain flavor are produced and then neutrinos of a different flavor are searched after certain distance.
- Disappearance experiments. Neutrinos of a certain flavor are produced, and after some distance, neutrinos of the same flavor are accounted for.

Attending to the origin of neutrinos there are neutrinos coming from natural sources and neutrinos coming from artificial ones:

- Atmospheric neutrinos
- Solar neutrinos
- Neutrinos from reactors and accelerators

2.4.1 Atmospheric neutrinos

Atmospheric neutrinos are produced in the collision of primary cosmic rays (typically protons) with nuclei in the upper atmosphere. This interaction creates a shower of hadrons, mostly pions. Most of these hadrons decay to several particles including neutrinos.

In the case of pions, the decay products are mostly a muon and a muon neutrino. The muon decays to an electron, another muon neutrino, and an electron neutrino as shown in Figure 2.2. Based on this chain, the flux ratio of muon neutrinos to electron neutrinos should be 2-to-1. Small contribution from kaons produced in the hadronic shower, and the fact that at high energy some muons live long enough to be stopped in the Earth before decaying in flight to high energy neutrinos, change this ratio by a factor of 5%.

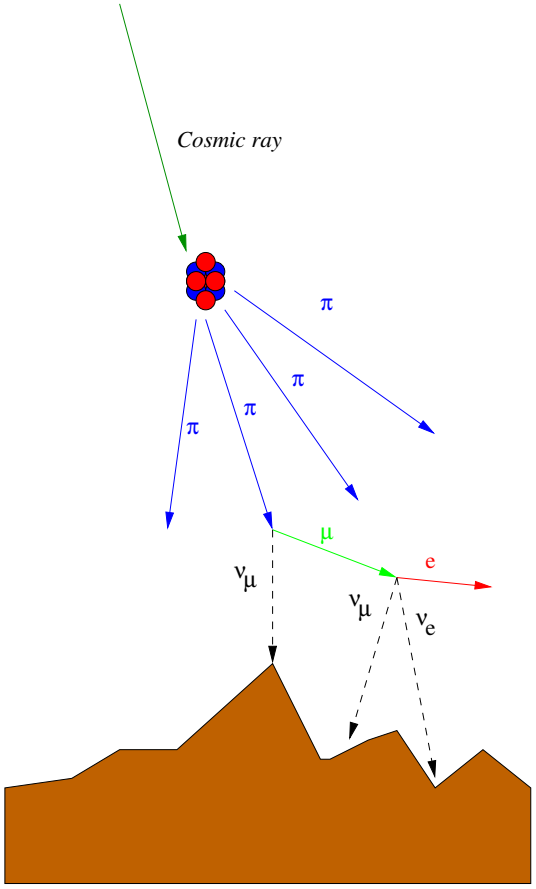

Figure 2.2: Atmospheric neutrinos from pion decay.

Evidence for oscillation of atmospheric neutrinos was found at Super-Kamiokande [26, 27]. An anomalous number of muon neutrino events compared to electron neutrino events was observed. The double ratio of the number of muon neutrino events compared to electron neutrino events measured and predicted should be about 1 (assuming that the flux ratio mentioned above is reasonably well predicted). The ratio obtained was $0.63 \pm 0.03(statistical) \pm 0.05(systematic)$ for sub-GeV ($E_{vis} \leq 1.33$ GeV) and $0.65 \pm 0.05(statistical) \pm 0.08(systematic)$ for multi-GeV ($E_{vis} > 1.33$ GeV). E_{vis} is defined to be the energy of an electron that would produce the observed amount of Čerenkov light. E_{vis}=1330 MeV corresponds to $p_\mu \sim 1400$ MeV/c. In addition a significant up-down asymmetry of high energy muon neutrino events was measured in Super-Kamiokande. The amount of muon neutrinos reaching the detector through the Earth (down) was smaller than the amount of those reaching the detector for the top side (up).

The data presented by the Super-Kamiokande Collaboration and the data of other atmospheric neutrino experiments, SOUDAN 2 [28] and MACRO [29, 30], are in good agreement with the assumption of a two-flavor $\nu_\mu \leftrightarrow \nu_\tau$ oscillation. From the Super-Kamiokande analysis the neutrino oscillations parameters for atmospheric neutrino are in the range $1.6 \text{ x } 10^{-3} < \Delta m^2 < 3.9 \text{ x } 10^{-3}$ eV^2 and $\sin^2 2\theta > 0.92$ at 90% confidence level [31]. This region is shown in Figure 2.3.

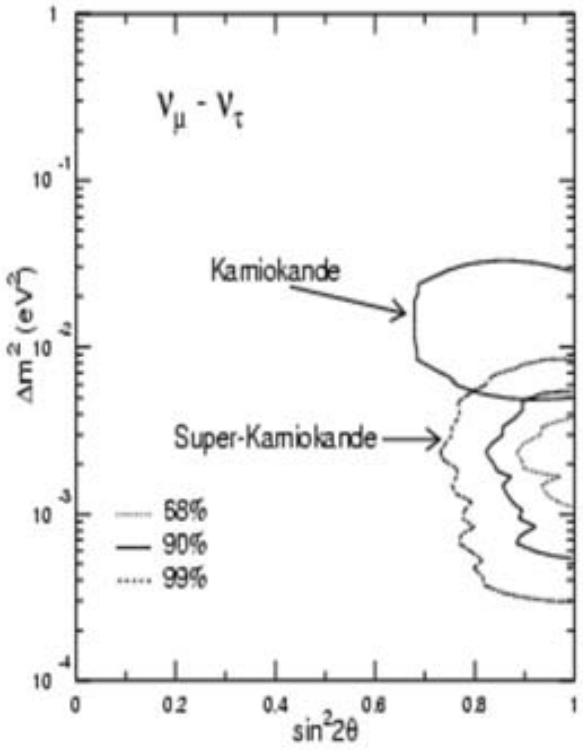

Figure 2.3: The 68%, 90% and 99% confidential intervals are shown for Δm^2 and $\sin^2 2\theta$ for $\nu_\mu \leftrightarrow \nu_\tau$ two-neutrino oscillations from Super-Kamiokande. The 90% confidence interval obtained by the Kamiokande experiment is also shown [32].

2.4.2 Solar neutrinos

Solar neutrinos are produced in nuclear reactions inside the Sun and only consist of electron neutrinos. The reactions are the proton-proton chain and the CNO cycle [33]. The theoretical solar neutrino flux at the Earth can be predicted as a function of the luminosity.

However, in all the solar neutrino experiments (Homestake [8], Kamiokande [34], GALLEX [35], GNO [36], SAGE [37], Super-Kamiokande [38, 39], SNO [40, 41, 42]) the observed event rates are significantly smaller than the expected ones.

In the Homestake experiment solar neutrinos are detected through the observation of the reaction $\nu_{\mathrm{e}} + {}^{37}Cl \rightarrow e^{-} + {}^{37}Ar$, in the GALLEX, GNO and SAGE experiments through the reaction $\nu_{\mathrm{e}} + {}^{71}Ga \rightarrow e^{-} + {}^{71}Ge$ and in the Kamiokande and Super-Kamiokande experiments solar neutrino are detected via the observation of the process $\nu + e^{-} \rightarrow \nu + e^{-}$. The ratio R of the observed and the predicted event rates was given by:

1. $R = 0.34 \pm 0.03$ (Homestake [8])
2. $R = 0.58 \pm 0.05$ (GALLEX [35], GNO [36])
3. $R = 0.60 \pm 0.05$ (SAGE [37])
4. $R = 0.465 \pm 0.018$ (Super-Kamiokande [38, 39])

The possible oscillations of solar neutrinos into another type of neutrino can not be detected in Homestake, GALLEX, GNO and SAGE experiments, because there is not sufficient energy to produced the associated charge lepton. In Super-Kamiokande mainly ν_{e} are detected through electrons. Even though the reaction considered is sensitive to all neutrino species, the sensitivity of the experiment to ν_{μ} and ν_{τ} is about six times smaller than the sensitivity to ν_{e}. Hence, in these experiments only the disappearance of solar ν_{e} was observed.

The evidence of the transitions of solar ν_{e} into ν_{μ} or ν_{τ} was found in SNO experiment. The SNO experiment is a heavy water Čerenkov detector (1 kton of D_2O). In it, neutrinos from the Sun are detected via the observations of the following three reactions:

1. $\nu_{\mathrm{e}} + d \rightarrow e^{-} + p + p$, sensitive to electron neutrino
2. $\nu + d \rightarrow \nu + n + p$, sensitive to all neutrino species

3. $\nu + e^- \rightarrow \nu + e^-$, sensitive to all neutrino species

SNO is sensitive to the three ν species inclusively and to the ν_e exclusively. The absolute neutrino flux can be measured and the oscillation parameters can be studied at the same time. Prior to the measurement of the absolute neutrino flux by SNO and the recoil electron scattering by Super-Kamiokande, several allowed solutions for the solar neutrino oscillation parameters were obtained from the other experiments [43]: Large Mixing Angle (LMA), Small Mixing Angle (SMA), Low mass (LOW), Vacuum Oscillation (VO) and other regions. These regions are shown in Figure 2.4 (a). The best-fit values of the solar neutrinos oscillations parameters were found for the LMA and LOW solutions [42] in Figure 2.4 (b).

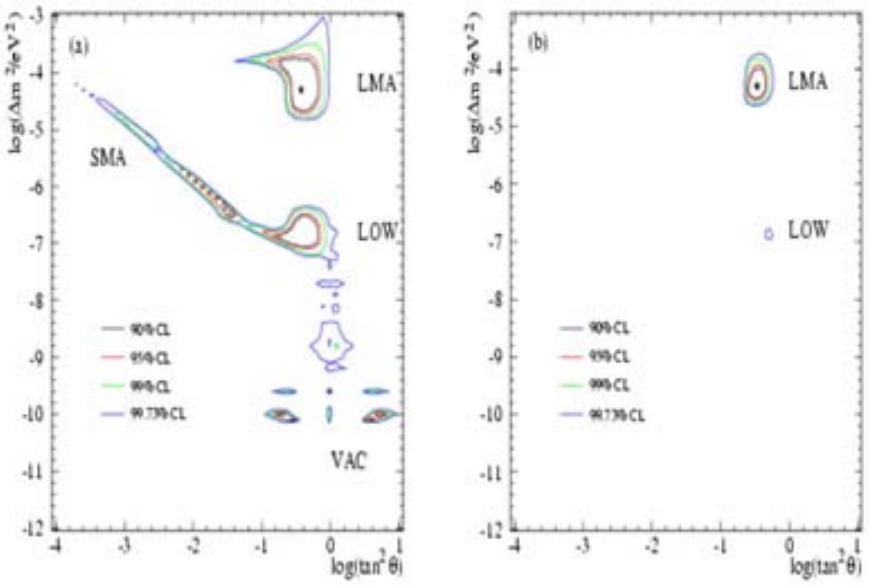

Figure 2.4: (a) Possible solutions before Super-Kamiokande and SNO results. (b) Solutions after Super-Kamiokande and SNO results.

2.4.3 Neutrinos from reactors and accelerators

Neutrinos from reactors. $\overline{\nu}_{\mathrm{e}}$ are produced in conventional nuclear reactors. Several experiments try to profit from these sources of $\overline{\nu}$. The flux of $\overline{\nu}$ can be estimated from power production of the reactors allowing experiments of $\overline{\nu}$ disappearance.

$\overline{\nu}_{\rm e}$ are produced in reactors from Japan and Korea and then are detected via the observation of the process $\overline{\nu}_{\rm e} + p \rightarrow e^+ + n$ in the KamLAND experiment (at an average distance $\sim$ 180 km). The KamLAND results [44, 45] showed that the number of $\overline{\nu}_{\rm e}$ candidate events with energies above 3.4 MeV was 258 compare to 365.2$\pm$ 23.7 events expected in the absence of neutrino oscillations. Accounting for 17.8 $\pm$ 7.3 expected background events, the statistical significance for $\overline{\nu}_{\rm e}$ disappearance is 99.998%. The energy spectrum distorsion was also observed. A two-neutrino oscillation analysis of the KamLAND data gives $\Delta m^2 = 7.9$ x 10^{-5} eV^2 and $\tan^2\theta = 0.46$. A global analysis of data from KamLAND and solar neutrino experiments yields $\Delta m^2 = 7.9$ x $10^{-5} eV^2$ and $\tan^2\theta = 0.40$. These values are compatible with the values of the oscillations parameters in the solar neutrino LMA and allow to exclude the LOW, SMA, VO regions of the neutrino oscillation parameters.

Other experiments with reactor antineutrinos as CHOOZ [46] and Palo Verde [47, 48] did not observe indications in favor of neutrino oscillation. In these experiments the ratio of the number of observed events to the expected number of events without disappearance was close to 1. These experiments detected $\overline{\nu}_{\rm e}$ at smaller distances to the reactor than those of KamLAND, and so they were sensitive to oscillations in different regions of the oscillations parameters.

Neutrinos from accelerators. Neutrinos from accelerator are also produced to study neutrino oscillations. The K2K collaboration has already reported evidences for muon neutrino oscillation and neutrino spectral distortion. The details about the oscillation studies, experimental setup and results of K2K are explained in next chapter.

Furthermore, the Main Injector Neutrino Oscillation Search (MINOS) has been designed to study the flavor composition of a beam of muon neutrinos as it travels between the near detector (ND) at a distance of 1 km from the target at Fermilab and the far detector in the Soudan mine at 735 km. Results based on its initial exposure to neutrinos has recently been presented [49]. The rate and energy spectra of charged current muon neutrino interactions are compared in the two detectors: 215 events with energies below 30 GeV are observed at the far detector, compared to an expectation of 336 $\pm$ 14.4 events. The data are consistent with muon neutrino disappearance via oscillation with $|\Delta m^2| = 2.74^{+0.44}_{-0.26} \cdot 10^{-3}$ eV^2 and $\sin^2(2\theta) > 0.87$ (at 60% C.L.).

Both, K2K and MINOS reported the results in the same region as atmospheric neutrino experiments do.

Indications in favor of another type of oscillations of neutrinos produced in a accelerator were obtained in the LSND (Liquid Scintillator Neutrino Detector) experiment [50]. The

LSND data can be explained by neutrino oscillations through the transition $\overline{\nu}_\mu \rightarrow \overline{\nu}_\mathrm{e}$ (muon antineutrinos $\overline{\nu}_\mu$ are obtained from μ^+ decay at rest). It was observed an excess of events consistent with $\overline{\nu}_\mathrm{e} + p \rightarrow e^+ + n$ scattering above the expected background. LSND obtained $2 \text{ x } 10^{-1} \lesssim \Delta m^2 \lesssim 1eV^2$ and $3 \text{ x } 10^{-3} \lesssim \sin^2 2\theta \lesssim 4 \text{ x } 10^{-2}$ as ranges for the values of the oscillation parameters. If this result is correct a 3 neutrino model can not explain the neutrino oscillations, and it would have to be changed to a 4 neutrino model. It is necessary to consider another neutrino with larger mass in order to explain in the same model the atmospheric, solar and LSND signatures for neutrino oscillations. A *sterile* neutrino (ν_s) [51] which does not interact through electroweak interactions (it was not measured by LEP) should be added to the three *active* neutrino ν_e, ν_μ, ν_τ (measured by LEP). The LSND signal needs verification and should be confirmed or refuted by the MiniBooNE experiment at Fermilab [52]. The experiment started the data collection in late August 2002.

Chapter 3

K2K experiment

In this Chapter an introduction to K2K experiment is given. After that, the physics experimental technique is explained followed by the experimental setup. A brief summary of the Monte Carlo simulation is also presented. Finally, the history of the K2K experiment is summarized and the results achieved by the experiment are presented.

3.1 Introduction

The K2K (KEK to Kamioka) experiment [53, 54, 55, 56] was proposed by the Super-Kamiokande Collaboration. Its main goal is to confirm the oscillation of ν_μ in a well controlled experiment and to measure the oscillation parameters in an independent way. To achieve this goal a ν_μ beam is produced in the 12 GeV Proton Synchrotron at the High Energy Accelerator Research Organization (KEK), in Tsukuba city in Ibaraki Prefecture, and is sent down into the earth 250 km, across Japan, to the Super-Kamiokande detector, in Kamioka town in Gifu Prefecture. A schematic view of K2K is shown in Figure 3.1. The K2K experiment belongs to the so-called "long baseline" category. This technique is needed since the neutrino oscillations only takes place over long distances at these energies. K2K is the first neutrino oscillation experiment using this technique.

Protons accelerated at the Proton Synchrotron hits an aluminum target producing a variety of particles (mainly pions). The positive charged pions are focused using magnetic horns to a decay pipe. The pions decay mainly through the channel $\pi^+ \rightarrow \mu^+\nu_\mu$. The beam is mainly composed

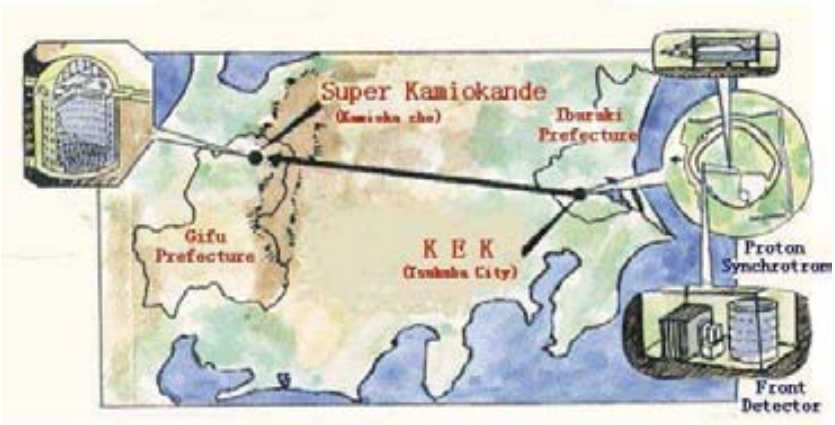

Figure 3.1: Schematic view of K2K experiment placement. Neutrino beam is produced at KEK site and sent to Super-Kamiokande. Neutrinos are detected 250 km from the production point.

for ν_μ (98%) with an average energy of 1.3 GeV. The spectrum of these neutrinos was chosen to be close to that of atmospheric neutrinos to probe the same Δm^2.

In order to control the beam a set of detectors is placed at the near site, Near Detector (ND), it is located 300 m downstream from the production point in KEK. The neutrino flux, neutrino energy spectrum and the purity of the ν_μ beam are measured in the ND. The far detector, Super-Kamiokande (SK) is placed at the detection point located 250 km far away. Any possible effects due to neutrino oscillations are searched for by comparing the Super-Kamiokande measurement with the Near Detector measurement and its extrapolation.

We will describe more detailed the K2K physics experimental technique in next section. After that, the experimental setup of the experiment is described.

3.2 K2K experimental technique

We describe the experimental techniques to search for neutrino oscillation and to measure the oscillations parameters in the K2K experiment.

3.2.1 Signatures

For neutrinos of a few GeV and being detected at 250 km, the dominant oscillation is between ν_μ and ν_τ flavor states and two-flavor oscillations suffice to describe and analyze the data. In the two-flavor neutrino oscillation framework the probability that a neutrino of energy E_ν with a flavor state ν_μ will later be observed in the ν_τ flavor state, after travelling a distance L_ν in vacuum, is:

$$P(\nu_\mu \to \nu_\tau) = \sin^2 2\theta \sin\left(\frac{1.27\Delta m^2(eV^2)L_\nu(km)}{E(GeV)}\right) \tag{3.1}$$

where θ is the mixing angle between the mass eigenstates and the flavor eigenstates and Δm^2 is the difference of the squares of the masses of mass eigenstates.

Neutrino oscillation causes both a suppression in the total number of ν_μ events observed at SK and a distortion of the measured energy spectrum compared to that measured at the production point. All of the beam-induced neutrino events observed within the fiducial volume of SK are used to measure the overall suppression of the flux. In addition, in order to study the spectral distortion, the subset of these events for which the incoming neutrino energy can be reconstructed are separately studied.

The deficit of events is observed because the K2K neutrino energy is below the threshold of ν_τ charged-current interactions, the oscillated neutrino do not interact through charged-current interactions, only the ν_μ charged-current interactions are detected.

The flight length of ν_μ is fixed to 250 km, so the oscillation probability only has a dependence with the neutrino energy. The neutrino energy spectrum is distorted according to Equation 3.1 as shown in Figure 3.2, where we assume the oscillation parameters of $(\sin^2 2\theta, \Delta m^2) = (1.00, 0.0030\text{eV}^2)$. The depth of the first dip corresponds to $\sin^2 2\theta$ and the energy at the dip position corresponds to Δm^2.

Furthermore, the oscillation channel $\nu_\mu \to \nu_\text{e}$ is also searched at K2K experiment, as a signature of the nonzero value of the unknown neutrino mixing parameter θ_{13}. Because this expected signal is so small, precise understanding of background and its reduction is very important. One of the background source is the ν_e component of the beam, less than 2 %. Hence, if the background is well controlled, electron signal observed in the far detector is the consequence of the oscillation $\nu_\mu \to \nu_\text{e}$.

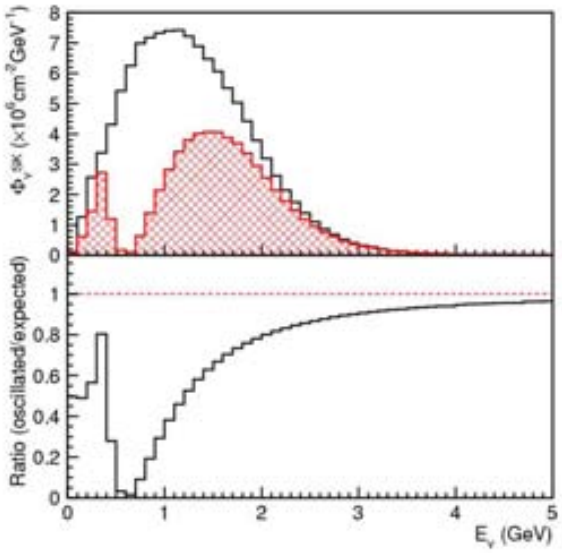

Figure 3.2: Neutrino energy spectrum distorted by oscillation (hatched histogram) compared with that for null oscillation case (open histogram). Assuming oscillations parameters to be $(\sin^2 2\theta, \Delta m^2) = (1.00, 0.0030\text{eV}^2)$. The ratio between both spectra is show in the bottom figure.

3.2.2 Measurements in the K2K Experiment

The effects of $\nu_\mu \rightarrow \nu_\tau$ neutrino oscillation appear as a reduction in the number of neutrino events and as a distortion of the neutrino energy spectrum in SK. The observation for these quantities are compared to their expectations in SK to study neutrino oscillation. The ND measures the neutrino flux and spectrum before neutrinos oscillate. Those measurements are then extrapolated by the expected ratio of muon neutrino fluxes at the far and near detector locations, the far-to-near (F/N) flux ratio, to predict the number of neutrino events and energy spectrum in SK.

3.2.2.1 Comparison of the number of events between ND and SK

First, the number of neutrino events at the near site, N_{ND}^{Obs}, is counted to derive the neutrino flux before oscillation ϕ_{ND}. The neutrino interaction cross section, σ_{ND}, and neutrino detection efficiency, ϵ_{ND}, are evaluated with neutrino-nucleus interaction models and a detector simulation. The measurement is performed with a similar detector to SK, a one-kiloton water Čerenkov

detector (1KT) in the ND, in order to cancel out a large part of the uncertainties on the cross section and the detection efficiency.

Then, the neutrino flux at SK, ϕ_{SK}, is extrapolated from that at the near site by multiplying the flux ratio of the far site to the near site, $R_{F/N}(E_\nu)$. The number of events in SK, N_{SK}^{Exp}, is estimated by using the extrapolated flux, selection efficiency, ϵ_{SK}, and the neutrino interaction cross section, σ_{SK}. When the number of observed events, N_{SK}^{Obs}, is smaller than the prediction, this means ν_μ disappearance. In addition, the oscillations parameters are determined so that the expectations of oscillations matches with the observation.

Figure 3.3 shows a simple sketch of the number of events analysis.

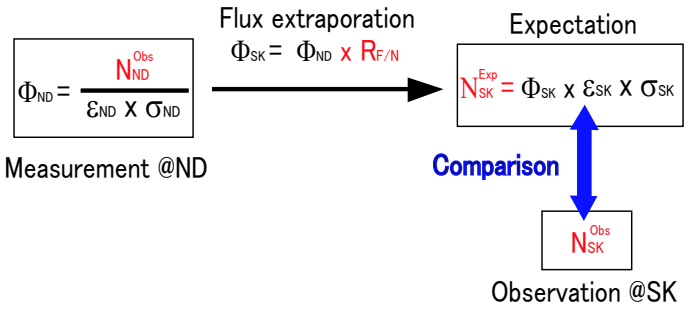

Figure 3.3: Flow of number of events analysis in K2K.

3.2.2.2 Comparison of the energy spectra between ND and SK

The neutrino energy spectrum is reconstructed from the muon kinematics parameters, muon momentum (p_μ) and angle respect to the beam direction (θ_μ), assuming charged current quasi-elastic (CCQE) interactions $\nu_\mu + n \rightarrow \mu + p$. CCQE is the dominant process in our neutrino energy region. The Equation 3.2 is used to get the reconstructed neutrino energy:

$$E_\nu^{rec} = \frac{(m_n - V)E_\mu + \frac{m_p^2 - (m_n - V)^2 - m_\mu^2}{2}}{(m_n - V) - E_\mu + p_\mu \cos\theta_\mu} \tag{3.2}$$

where m_p, m_n, m_μ, E_μ, V are the proton mass, the neutron mass, the muon mass, the muon energy, and nuclear potential set at 27 MeV, respectively. In order to derive the true neutrino energy from E_ν^{rec}, the understanding of the neutrino nucleus interaction is important. The neutrino energy spectrum at the near site, $\phi_{ND}(E_\nu)$, is derived from the (p_μ,θ_μ) two-dimensional

distribution by using the neutrino-nucleus cross section and a detector simulation. The neutrino flux is extrapolated from the measurements at the ND.

In SK, the CCQE events are detected as an event with only one muon-like Čerenkov ring ($1R_\mu$) because the proton is typically below Čerenkov threshold. The E_ν^{rec} distribution is measured using the CCQE candidate ($1R_\mu$) sample. The observed E_ν^{rec} is compared with the expectation, (E_ν^{exp}). The disagreement of E_ν^{rec} observed and extrapolated is evidence of neutrino oscillation. In addition, the oscillation parameters are determined to match the expectation with the observation.

Figure 3.4 shows a simple sketch of the spectrum shape analysis.

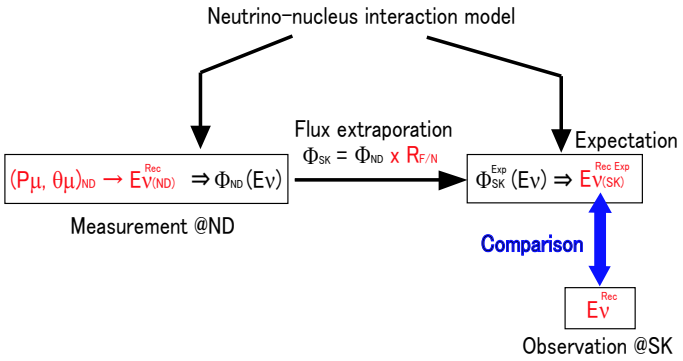

Figure 3.4: Flow of spectrum shape analysis in K2K.

3.2.2.3 Neutrino-nucleus interaction study

As mentioned above, in the oscillation analysis, the neutrino energy spectrum is measured from charged-current quasi-elastic (QE) interactions. Therefore, the neutrino detection efficiency in each detector and the fraction of the non quasi-elastic (non-QE) events in the sample are crucial information.

In the K2K experiment, the fine-grained detector (FGD) system in the near site was constructed to better understand neutrino interactions. Specially, one of the sub-detectors, SciBar, was designed to detect low momentum particles such as the proton from the CCQE interactions but also from the other neutrino interactions, giving us the capability of distinguishing CCQE events and non-QE, and providing the framework to study each one of the neutrino interactions.

In the spectrum analysis, the neutrino energy should be reconstructed correctly. However, the E_ν^{rec} of the non-QE events is lower than true energy because of the missing particles in the reconstruction as shown in Figure 3.5. The fraction of the non-QE components in the QE candidate sample should be correctively evaluated since the E_ν^{rec} is affected by the non-QE fraction. The main source of background to those CCQE events are the single pion

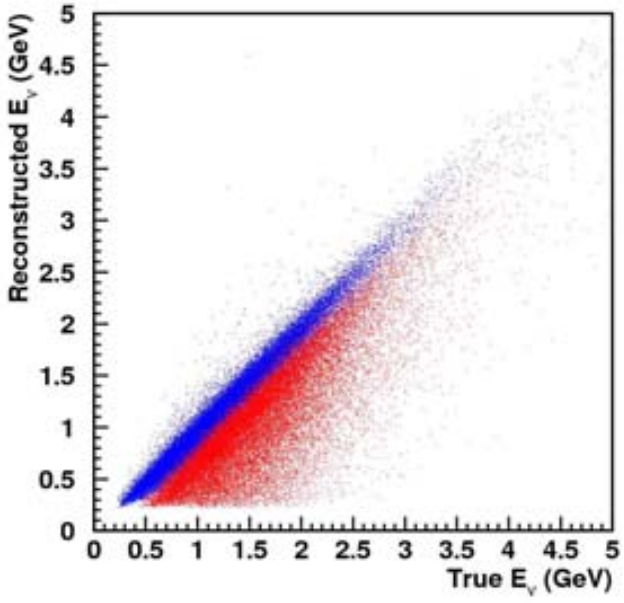

Figure 3.5: Correlation between true and reconstructed neutrino energy in Monte Carlo simulation. Blue dots represented charged-current quasi-elastic events (CCQE) and red dots charged-current non-quasi-elastic events (non-QE). Energy of neutrino can be better reconstructed in CCQE events.

production events. The single pion production process is the consequence of a resonance process $\nu + N \rightarrow l + N^*$ where ν denotes the interacting neutrino, N the nucleon target, l the lepton, either charged or neutral, and N^* the nucleon resonance. The study of the single pion production process is the main goal of this thesis.

3.2.3 Expected Sensitivity of the K2K Experiment

The K2K experiment is designed to be sensitive to the parameter region constrained by the atmospheric observations. Figure 3.6 shows the region of sensitivity to the $\nu_\mu \rightarrow \nu_x$ oscillation in K2K experiment, together with the results from several experiments. As shown in this figure,

K2K has the sensitivity to the region of $\Delta m^2 \geq 10^{-3}$ eV^2 on the axis of $\sin^2 2\theta = 1.0$. The Monte

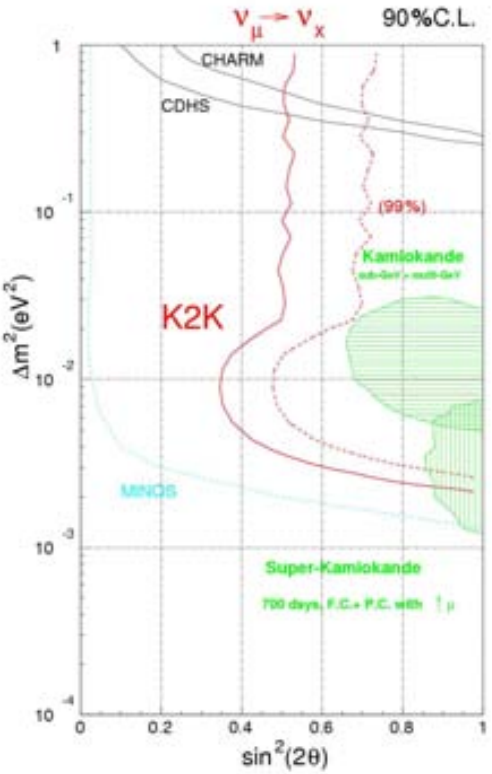

Figure 3.6: Sensitivity to the $\nu_\mu \rightarrow \nu_x$ oscillation in K2K. The vertical and the horizontal axis are Δm^2 (eV^2) and $\sin^2\theta$, respectively. The red lines show the sensitivity contours of K2K experiment with the confidence levels of 90% (solid line) and 99% (dotted lines). The results of Kamiokande ([34]), Super-Kamiokande ([38, 39]), CHARM ([57, 58]) and CDHS ([59]) are also shown in this figure. The hatched results showed the allowed regions. These contours are of the confidence level of 90%. In addition the sensitivity region of the long baseline neutrino experiment MINOS ([49]) is also drawn with light blue line.

Carlo simulation is used to check the rejection power of null oscillation if neutrino oscillations exists. Assuming oscillations parameters within the expected sensitivity and neutrinos data corresponding to the total number of protons on target, it is possible to reject the null oscillation hypothesis at 99.994% C.L.(4.02σ) level.

3.3 K2K experimental setup

The K2K experimental facility consists of the neutrino beam line, the near detector system (ND), and the far detector, Super-Kamiokande (SK). Figure 3.7 shows the schematic view of the K2K setup.

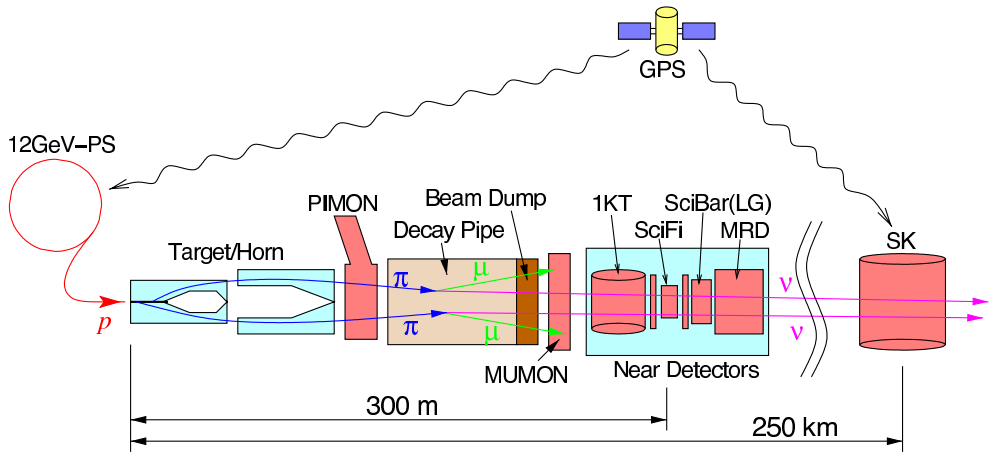

Figure 3.7: Schematic view of the K2K setup.

3.3.1 Neutrino beam and beam monitor

The accelerator and the neutrino beam line for K2K consist of a 12 GeV Proton Synchrotron (KEK-PS) at the High Energy Accelerator Research Organization (KEK), a primary proton transportation line, a hadron production target, a set of focusing horn magnets for secondary particles, a decay volume, and a beam dump. A schematic view of the KEK-PS and neutrino beam line is shown in Figure 3.8. In this section we describe each beam line component from upstream to downstream.

3.3.1.1 Primary proton beam

Protons are accelerated by the KEK-PS to a kinetic energy of 12 GeV. After acceleration, all protons are extracted in a single turn to the neutrino beam line. The duration of an extraction,

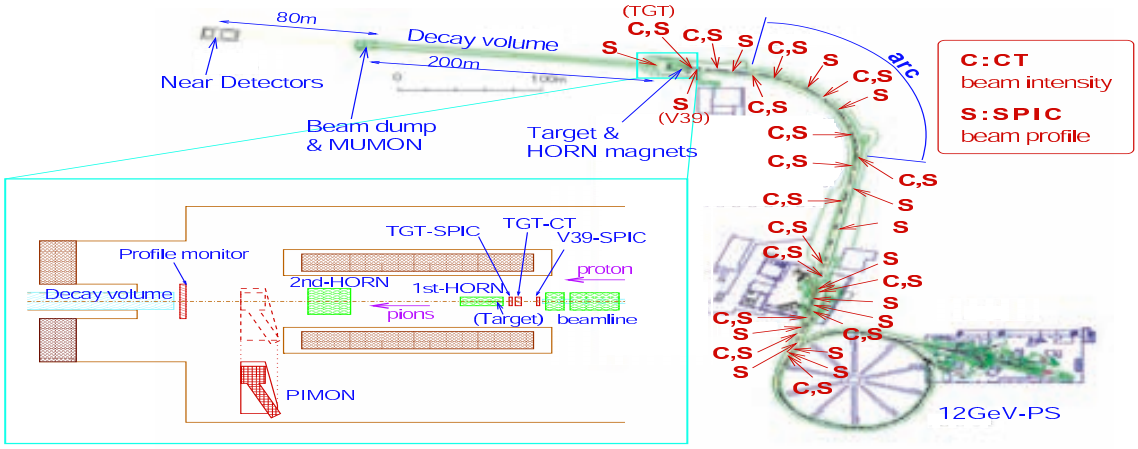

Figure 3.8: Schematic view of KEK-PS experiment and neutrino beam line and the location of the beam line components. The EP1 neutrino beam line leads proton through a distance of 400 m from the EP1-A extraction point to the target station via the straight and arc sections. The characters *C* and *S* show the locations of the CT and SPIC installations, respectively. The lower-left inset is a magnified view of the target station. The production target and a set of horn magnets are located in the target station. A pion monitor was installed on two occasions downstream the horn magnets.

called spill, is 1.1 μs, which contains 9 bunches of protons with a 125 ns time interval between them. The cycle is repeated each 2.2 s. As shown in Figure 3.8, the beam is extracted toward the north, bent 90° toward the direction of SK, and transported to the target station. There is a final steering magnet just before the target which directs the beam to SK at an angle of about 1° downward from horizontal.

The beam intensity is monitored by 13 current transformers (CTs) installed along the neutrino beam line (Figure 3.8). The CTs are used to monitor the beam transportation efficiency. The overall transportation efficiency along the beam line is about 85%. A CT placed just in front of the production target is used to estimate the total number of protons delivered to the target. A typical beam intensity just before the target is about 5 x 10^{12} in a spill. Figure 3.9 shows the accumulated number of protons on the target (POT) monitored by CT from June 1999 to November 2004. In total, 104.9 x 10^{18} protons are delivered on the target to generate the neutrino beam.

In order to measure the profile and the position of the beam, 28 segmented plate ionization chambers (SPICs) are also installed (Figure 3.8). They are used to steer and monitor the beam,

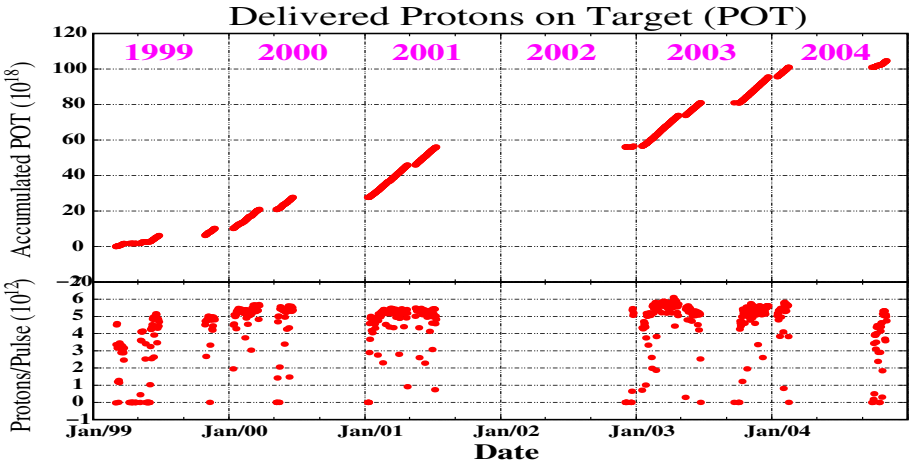

Figure 3.9: Number of protons delivered to the production target in the period from March 1999 to November 2004. The horizontal axis corresponds to the date. The upper plot shows the total number of protons on target (POT) accumulated since March 1999, and the lower plot shows the POT per spill averaged in a day. In total, 104.9 x 10^{18} protons were delivered during the entire period including beam commissioning and tunning periods.

while the last two SPICs in front of the target are used to estimate the beam size and divergence, which is used as an input to our beam MC simulation.

Table 3.1 summarizes the KEK-PS specifications.

3.3.1.2 Hadron production target and horn magnet system

A hadron production target and a set of horn magnets are placed in the target station. Protons hit the target and after that, secondary particles are generated at the production target. Two toroidal magnetic horns are employed to focus positively charged particles, mainly $\pi^+ s$, in the forward direction by the magnetic field. The momentum of focused pions is around $2-3$ GeV/c, which corresponds to about $1.0-1.5$ GeV for those neutrinos decaying in the forward direction. According to the MC simulation, the flux of neutrinos above 0.5 GeV is 22 times greater with horn magnets with 250 kA current than without the horn magnet.

A schematic view of the horn magnets is shown in Figure 3.10. The dimensions of the first horn are 0.70 m in diameter and 2.37 m in length, while those of the second horn are 1.65 m in diameter and 2.76 in length. Both horns are cylindrically symmetric in shape. The production

Accelerator components	Pre-injector (750 keV, Cockroft-Walton acc.) LINAC (40 MeV) BOOSTER (500 MeV) Main ring (12 GeV in kinetic energy)
Operation mode for K2K	fast extraction (single turn) to EP1-A
Typical intensity in main ring	7 x 10^{12} protons per spill
Typical intensity after extraction	6 x 10^{12} protons per spill
Typical intensity at the target	5 x 10^{12} protons per spill
Number of bunches	9
Bunch spacing	125 ns
Total spill length	1.1 μs
Repetition cycle	2.2 sec

Table 3.1: Specification summary of KEK-PS for K2K experiment.

target, a rod of aluminum of a length of 66 cm and diameter of 3 cm, is embedded inside the first horn. The target diameter was 2 cm in June 1999 and was changed to 3 cm in November 1999 for improved mechanical strength. The target also plays the role of inner conductor of the first horn, making a strong magnetic field inside the horn to achieve high focusing efficiency. The second horn is located 10.5 m downstream from the first horn, playing the role of a reflector, which re-focuses over-bent low energy pions, and, in addition, further focuses under-bent high energy pions.

Pulse current with a duration of 2 msec and an amplitude of 250 kA (200 kA in June 1999) is supplied by four current feeders to each horn. The peaking time of the current is adjusted to match the beam timing. The maximum magnetic field in the horn is 33 kG at the surface of the target rod with 3 cm diameter target and 250 kA horn current.

The values of the current supplied to the horn magnet are read out by CTs put in between current feeders and recorded by a flash-ADC on a spill-by-spill basis. Overall current and current balance between feeders are monitored to select good beam spills. The magnetic field inside the prototype of the first horn was measured using pickup coils; results showed that the radial distribution of the field was in agreement with the design distribution and the azimuthal symmetry was confirmed within a measurement error of 15%.

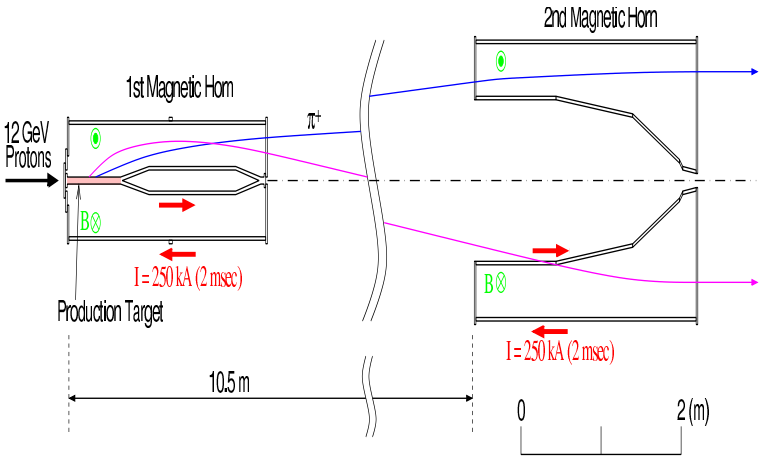

Figure 3.10: Schematic view of the two horn magnets. An electrical current of 250 kA is supplied to both horns, creating a toroidal magnetic field inside the horns. The production target, an aluminum rod of 66 cm in length and 3 cm in diameter, is embedded inside the first horn magnet, which also plays the role of inner conductor of the horn. The second horn is located 10.5m downstream of the first horn.

3.3.1.3 Decay volume, beam dump and secondary beam monitors

The positive pions focused by the horn magnets go into a 200 m long decay volume which starts 19 m downstream of the production target, where the π^+ decay to $\mu^+\nu_\mu$. The decay volume is cylindrical in shape and is separated into three sections with different dimensions. The diameters of the pipe are 1.5 cm the first 10 m, 2 m the following 90 m, and 3 m the remaining 100 m. The decay volume is filled with helium gas of 1 atm to reduce the loss of pions by absorption and to avoid uncontrollable pion production in the gas. The beam dump is located at the end of the decay volume to absorb all the particles except the neutrinos. It consists of 3.5 m thick iron, 2 m thick concrete, and a region of soil about 60 m long.

Energy spectrum, direction and yield of neutrino beam is monitored using a pion monitor (PIMON) and a muon monitor (MUMON) by measuring the pions, and the muons from the pion decay. The PIMON was installed on two occasions just downstream the horn magnets to measure the pion momentum (p_π) and the pion angle with respect to the beam direction (θ_π) of pions entering in the decay volume. The neutrino energy spectrum at any location can be obtained from the (p_π, θ_π) distribution since the decay kinematics of the two-body pion decay is perfectly known. Thus, the ratio of neutrino spectrum between KEK and SK called “far/near ratio“ can be estimated based on the PIMON data. The PIMON measurements were done once

in June 1999 for the configuration of 200 kA horn current with 2 cm target diameter and the other was done in November 1999 for the configuration of 250 kA horn current with 3 cm target diameter.

The PIMON is a gas Čerenkov imaging detector which consists of a gas vessel, a spherical mirror, and an array of 20 photomultiplier tubes (PMT). The Čerenkov photons emitted by the pions passing through the gas vessel are reflected toward and focused onto the PMT array by the spherical mirror. Then, the PMT array on the focal plane detects the Čerenkov image. Due to the characteristics of the spherical mirror, photons propagating in the same direction are focused to the same position on the focal plane, giving us information on the direction of the pions. The pion momentum is also obtained from the size of the Čerenkov ring. Therefore, the direction and momentum of pions can be measured separately by looking at the Čerenkov light distribution on the focal plane.

There is a pit called pit-muon just downstream of the iron and concrete shields. Muons with momentum greater than 5.5 GeV/c can reach the muon-pit. The flux at the pit is roughly 10^4 muons/cm^2/spill. The parent particles of both muons and neutrinos are pions, so the profile center of muons corresponds to that of neutrinos. A change in the beam direction of 3 mrad corresponds to a change in the neutrino flux and spectrum at SK of about 1%, and hence it must be controlled and monitored to be within 3 mrad to keep the maximun change of 1%. Two detectors (MUONs) are installed in the pit: one is an ionization chamber (ICH) and the other an array of silicon pad detectors (SPD) array. The purpose of these detectors is to measure the profile and intensity of muons penetrating the shields on a spill-by-spill basis.

3.3.2 Near Detector

A near neutrino detector system (ND) is located 300 m downstream from the proton target in the underground hall of 24 m in diameter and 16 m in depth. The main purpose of ND is to measure the direction, flux and energy spectrum of neutrinos at KEK before they oscillate. ND also provides the measurements of neutrino-nucleus interactions, which are necessary inputs for the neutrino oscillation study. The schematic view of the ND is shown Figure 3.11.

The ND is comprised of two detector systems; a one kiloton water Čerenkov detector (1KT) and a fine-grained detector (FGD) system. The FGD consists of a scintillating-fiber/water target tracker (SciFi), a Lead-Glass calorimeter in the first period K2K-I, a totally active fine-segmented

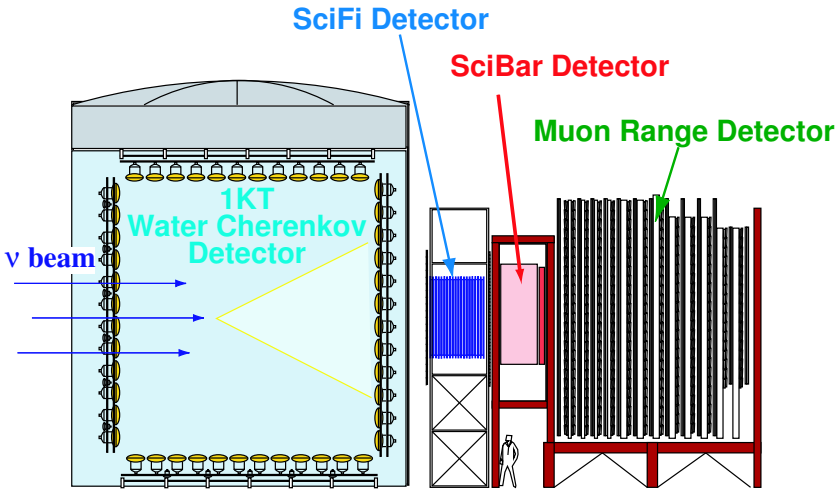

Figure 3.11: Schematic view of the neutrino Near Detector. The ND is comprised of two detector systems; a one kiloton water Čerenkov detector (1KT) and a fine-grained detector (FGD) system. The FGD consists of a scintillating-fiber/water target tracker (SciFi), a totally active fine-segmented scintillator-bar tracker (SciBar), and a muon range detector (MRD).

scintillator-bar tracker (SciBar) in the last period K2K-IIb and K2K-IIc, and a muon range detector (MRD).

3.3.2.1 1 kiloton water Čerenkov detector (1KT)

A one kiloton water Čerenkov detector (1KT) is located in the experimental hall at KEK as the upstream detector. The 1KT detector is a miniature version of the far detector Super-Kamiokande (SK), and uses the same neutrino interaction target and instrumentation. The primary role of the 1KT is to measure the ν_μ interaction rate and the ν_μ energy spectrum. The 1KT also provides a high statistics measurement of neutrino-water interactions. Details about the performance and physics studies of the 1KT can be found in [60].

A schematic drawing of 1KT is shown in Figure 3.12. The cylindrical tank of 10.8 m diameter and 10.8 m height, holds approximately 1000 tons of pure water. The center of the tank is 294 m downstream of the pion production target.

The water tank is optically separated into two regions, the inner detector (ID) and the outer detector (OD), by opaque black sheets and Tyvek (a material manufactured by DuPont) sheets.

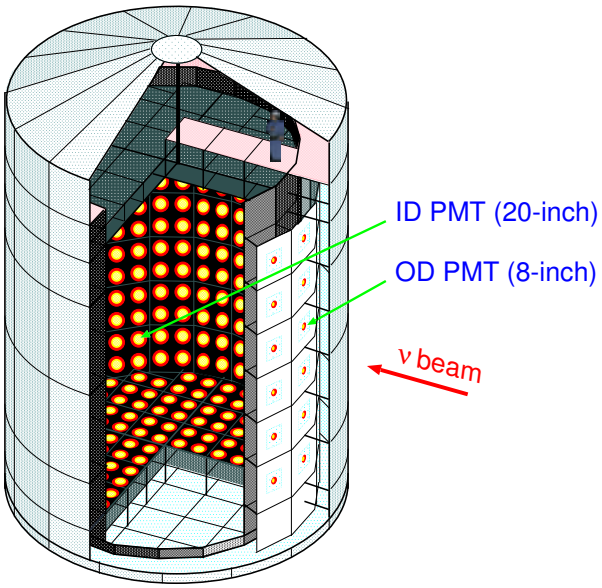

Figure 3.12: Schematic view of the 1 kiloton water Čerenkov detector.

The ID volume is a cylinder of 8.6 m in diameter and 8.6 m in height. This volume is viewed by 680 photomultiplier tubes (PMTs) of 50 cm diameter facing inward to detect Čerenkov light from neutrino events. The PMTs and their arrangement are identical to those of SK; 70 cm spacing between PMTs gives a 40% photocathode coverage. The OD covers the upstream third of the barrel wall and the whole of the bottom wall. The OD volume is viewed by 68 PMTs of 20 cm diameter facing outward to veto the incoming particles. The OD is also used to trigger through-going/stopping cosmic ray muon events for detector calibrations. Figure 3.13 shows a photograph of ID.

The physical parameters of an event in the 1KT detector such as the vertex position, the number of Čerenkov rings, particle types and momenta are determined using the same algorithms as in SK. First, the vertex position of an event is obtained from the PMT timing information. With knowledge of the vertex position, the number of Čerenkov rings and their directions are determined by a maximum-likelihood procedure. Each ring is then classified as e-like, representing a showering particle ($e^{\pm}, \gamma$), or μ-like, representing a non-showering particle ($\mu^{\pm}, \pi^{\pm}$), using its ring pattern and Čerenkov opening angle. On the basis of this particle type information, the vertex position of a single-ring event is further refined. The momentum corresponding to each ring is determined from the Čerenkov light intensity. Fully contained (FC) neutrino events, which deposit all of their Čerenkov light inside the inner detector, are

Figure 3.13: Photograph of the inner detector of the 1KT from the bottom.

selected by requiring the maximum number of photoelectrons on a single PMT to be less than 200. The events with the maximum number of photoelectrons greater than 200 are identified as a partially contained (PC) event. This criterion is used because a muon passing through the wall produces a considerable amount of light in the nearest PMTs. According to the Monte Carlo (MC) simulation, 0.3% of muon neutrino charged-current quasi-elastic events with single-ring are mis-identified as e-like events while 3.3% of electron neutrino charged-current quasi-elastic events with a single ring are mis-identified as μ-like. The resolution of muon momentum (p_μ) is estimated to be $2.0 - 2.5\%$ in the whole momentum range of the 1KT. The energy scale is stable within about 1% from 2000 to 2004.

3.3.2.2 Scintillating fiber tracker (SciFi)

The scintillating fiber tracker (SciFi) detector is a 6 ton tracking detector with integral water target layers as shown in Figure 3.14. Details of the design and performance of the detector are described in Reference [61]. The SciFi detector is used to measure the neutrino spectrum, and to reconstruct with high resolution the charged particles tracks produced in neutrino interactions. It can estimate the rates for quasi-elastic and inelastic interactions and is sensitive to higher energy events, and hence has complementary capabilities to the 1KT detector. The SciFi detector consists of 20 layers of 2.6 m x 2.6 m tracking modules, placed 9 cm apart. Each layer contains a double layer of sheets of scintillating fiber arranged, one each, in the horizontal and vertical directions; each sheet is itself two fibers thick. The length of each fiber is 3.7 m and the diameter 0.692 mm. In between the fiber modules, there are 19 layers of water target contained in extruded aluminum tanks. The fiber sheets are coupled to an image intensifier tube (IIT) with a CCD readout system.

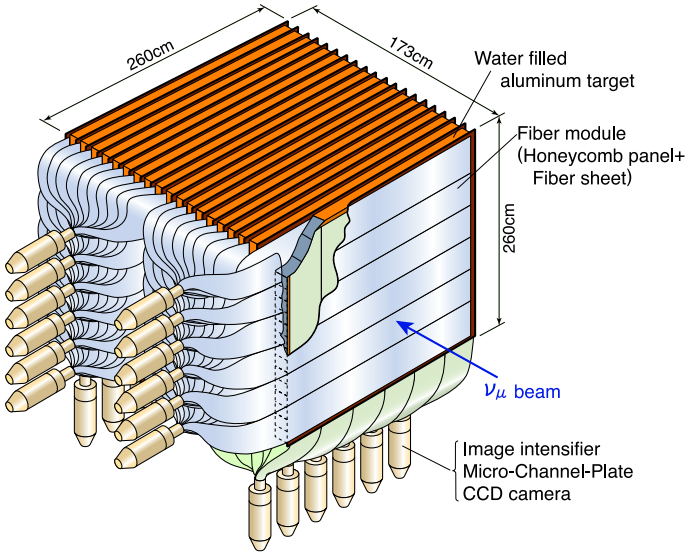

Figure 3.14: Schematic view of the SciFi detector.

Hit fibers are extracted using the CCD images. The raw data consists of hit CCD pixels and their digitized brightness. Neighboring hit pixels are grouped to make a pixel cluster. Those clusters are then combined and matched to the location of specific scintillating fibers. The efficiency to identify a fiber through which a charged particle passed is estimated using cosmic rays muons to be about 95%, but closer to 90% at angles within 30° of the beam. After hit fibers are reconstructed, tracks with three or more hit layers are reconstructed using conventional fitting techniques. The efficiency to find a track is also estimated using cosmic ray muons, and is about to 70% for tracks with length of three layers, and about to 87% for four layers, and approaches 100% for longer tracks.

3.3.2.3 Scintillator-bar tracker (SciBar)

A fully-active scintillator-bar detector (SciBar) was installed in summer 2003 in the place of Lead-Glass calorimeter ([62]) to study neutrino interaction with the better sensitivity. The details about the performance and neutrino studies using the SciBar detector are described in the next chapter.

3.3.2.4 Muon range detector (MRD)

The muon range detector (MRD) has two purposes. One is to monitor the stability of the neutrino beam direction, profile and spectrum by measuring the energy, angle and production point of muons produced by charged-current (CC) neutrino interaction by using its huge mass of iron as the target. The other is to identify the muons produced in the upstream detectors and to measure their energy and angle in combination with other fine grain detectors. This enables us to measure the energy of the incident neutrino for those charge-current quasi-elastic events.

The MRD is located at the most downstream of the near detector system. It consists of 12 layers of iron absorber sandwiched in between 13 sets of vertical and horizontal drift-tube layers. The size of the layer is approximately 7.6 m x 7.6 m. In order to have a good muon energy resolution for the whole energy region, the four iron plates in the upstream side are 10 cm thick, while the other eight planes are 20 cm thick. The total iron thickness is 2.0 m covering the muon energy up to 2.8 GeV/c which corresponds to 95% of all the muons in neutrino interaction. The mass of iron is 864 tons and the mass of drift tubes is 51 tons.

A conventional track finding algorithm is employed to reconstruct tracks from hits. The track finding efficiency is 66%, 95%, and 97.5% for tracks with one, two and three traversed iron plate(s), respectively, and it goes to 99% for longer tracks. The range of tracks is estimated using the path length of the reconstructed path in iron. The error on the muon range is quoted to be at maximum 1.7% difference among various calculations.

The construction and performance of the near muon range detector for the K2K experiment is detailed described in [63].

3.3.3 Far Detector: Super-Kamiokande (SK)

The far detector of the K2K experiment is Super-Kamiokande (SK), which is located in the Mozumi mine of Kamioka Mining and Smelting Company, in the Kamioka Observatory, operated by the Institute for Cosmic Ray Research, University of Tokyo. It is 250 km away from KEK site and $1,000$ m ($2,700$ m water equivalent) below the peak of Mt. Ikenoyama in Gifu prefecture.

The SK detector is a cylindrically shape water Čerenkov detector which is 41 m height, 39 m in diameter and has a total mass of 50 kilotons of pure water. A schematic drawing of SK detector is shown in Figure 3.15. The water tank is optically separated into two parts, the inner detector (ID)

and the outer detector (OD), by the stainless steel structure covered by opaque black sheets and Tyvek sheets. The size of ID is 36.2 m in height and 33.8 m in diameter, which contains 32 ktons of water. The ID is viewed by 11,146 20-inch PMTs facing inward covering 40% from June 1999 to June 2001 (period called SK-I and K2K-I), while it is viewed by 5182 PMTs enclosed in a fiber reinforced plastic and sealers with acrylic covers on their front surface, covering 19% of the ID surface from December 2002 (SK-II and K2K-II). The transparency and the reflection of these covers in water is 97% and 1%, respectively. In the OD region, outward-facing, 1,885 8-inch PMTs are attached to the outer side of the supporting structure. The fiducial volume is defined to be a cylinder whose surface is 2 m away from the ID wall providing a fiducial mass of 22.5 kilotons.

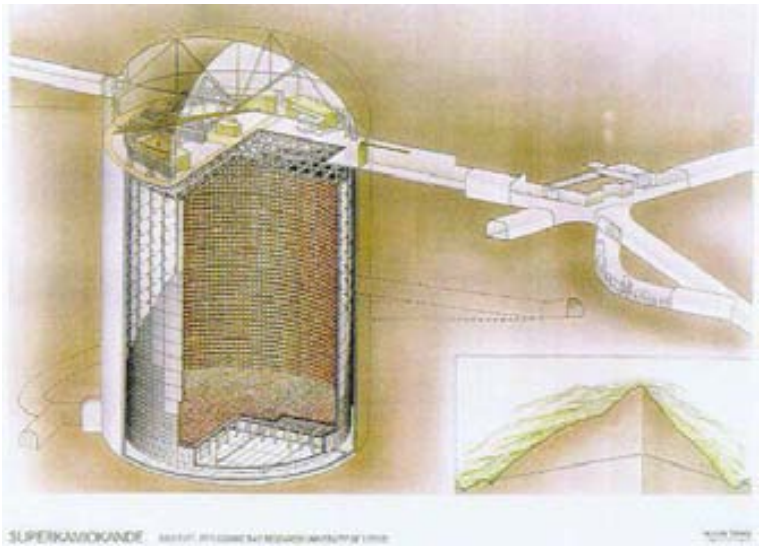

Figure 3.15: Schematic view of the Super-Kamiokande detector.

The physical parameters of an event in SK such as the vertex position, the number of Čerenkov rings, particle types and momenta are reconstructed as it is done for the 1KT detector. First, the vertex position of an event is reconstructed from the PMT timing information. Then, the number of Čerenkov rings and their directions are reconstructed based on the vertex position by a maximum-likelihood procedure. Events with only one ring are called single-ring events, and those with greater than one ring are called multi-ring events. Each ring is then classified as e-like or μ-like by using its ring pattern. The vertex position of a single-ring event is refined based on the particle type. The momentum of each ring is reconstructed from the Čerenkov light intensity.

The vertex resolution of muons and electrons is evaluated to be better than 30 cm for momentum region above 300 MeV/c with the MC simulation. For the particle identification, the expected probability of identifying μ-like as e-like and an e-like as μ-like is about few $\%$. The resolution of momentum and angle for muons are estimated to be $2-3\%$ and 2°, respectively. The momentum scale uncertainty is evaluated to be 2.0% (2.1%) for SK-I (SK-II) from the various calibration sources. All the reconstruction performances of SK-I and SK-II are comparable ([64]).

In this long baseline experiment, timing information is used to distinguish beam neutrino events and cosmic ray induced background events in the SK detector. The global positioning system (GPS) is used to synchronize the timing of the beam spill between KEK and SK [65]. At both sites there are a running local time counter connected to a GPS receiver and an event trigger (at SK) or the beam spill trigger (at KEK). This counter is synchronized using the one pulse-per-second signal from the GPS. In this way, events can be synchronized within 50 ns, after compensation for oscillation drift. This accuracy is sufficient to observe the bunch structure of the neutrino beam in the SK neutrino data.

3.4 Monte Carlo Simulation

Monte Carlo (MC) simulations for the K2K experiment consist of three parts:

- A simulation for the neutrino beam. It gives the neutrino flux of each type as a function of the neutrino energy.
- A simulation for the neutrino interaction. It provides final state particles from a neutrino-nucleus scattering, according to models of neutrino cross-section and interaction.
- A simulation for detectors. It simulates the passage of particles in a material and the response from detector components.

3.4.1 Neutrino Beam Simulation (Beam-MC)

Beam-MC simulates the process of neutrino beam generation to provide neutrino flux and energy spectrum shape at the near and far site. The beam line geometry is implemented in GEANT3 and particles are tracked in materials. The far to near flux ratio is estimated by this beam MC simulation. In this simulation, while the Cho-CERN model [66] compilation is used as a

reference model, the HARP experiment [67] result is employed as an input for he simulation of pion production. The pion production measurement done by HARP is of direct relevance for K2K, since it uses the same beam proton momentum and the same production target, and it covers a large fraction of the phase space contributing to the K2K neutrino flux. In particular, the measured momentum region by the HARP experiment reaches below 2 GeV/c down 0.75 GeV/c where the PIMON is insensitive. The PIMON measurement is performed for a confirmation of the validity of the beam MC simulation. All three predictions of the far to near ratio are consistent with each other within their measurement uncertainties. The HARP measurement also gives the most accurate measurements on hadron production.

The result of neutrino flux at the near (ND) and far site (SK) with the 250 kA horn current and the target of 3 cm in diameter are shown in Figure 3.16. The neutrino beam is 97.3% (97.9%) pure muon neutrino with contamination of ν_e/ν_μ estimated to be 0.013 (0.009), $\overline{\nu}_\mu/\nu_\mu \sim 0.015$ (0.012), and $\overline{\nu}_e/\nu_\mu \sim 1.8 \times 10^{-4}(2.2 \times 10^{-4})$ at ND (SK).

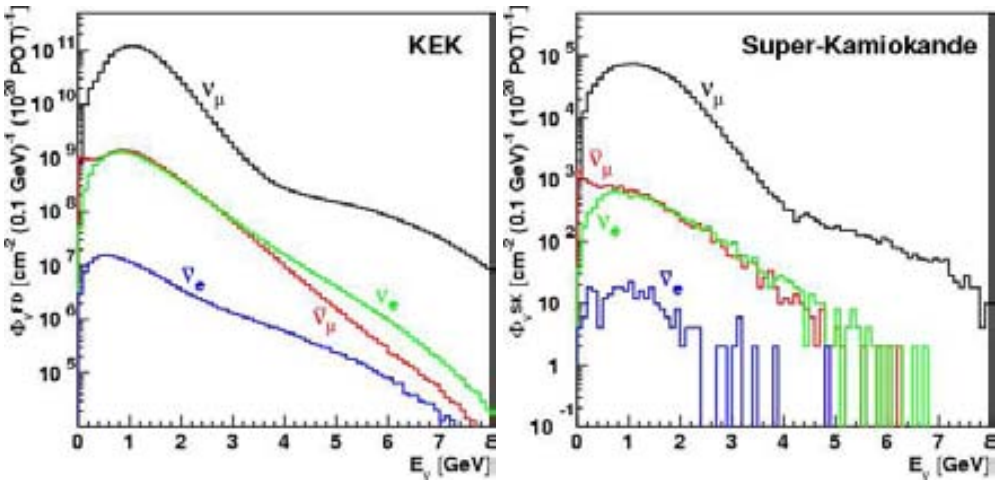

Figure 3.16: The energy spectrum for each neutrino type at ND at KEK (left) and SK (right) estimated by the beam MC simulation. The neutrino beam is 97.3% (97.9%) pure muon neutrino with contamination of $\nu_e/\nu_\mu \sim 0.013$ (0.009), $\overline{\nu}_\mu/\nu_\mu \sim 0.015$ (0.012), and $\overline{\nu}_e/\nu_\mu \sim 1.8 \times 10^{-4}(2.2 \times 10^{-4})$ at ND (SK).

3.4.2 Neutrino interaction (NEUT)

The NEUT program library [68] is used to simulate neutrino interactions with the nucleus. The library was first developed by the atmospheric neutrino experiment in SK. The target materials are H_2O for water Čerenkov detectors and SciFi, and $(CH)_n$ for SciBar.

Neutrino interactions channels around 1 GeV region can be studied for both, ν_μ and ν_e, depending on the final statistics at the end of taking data. These interactions are summarized as follows:

- Charge Current (CC) interactions ($\nu N \to lX$):

  - CC quasi-elastic interaction ($\nu N \to lN'$)
  - CC single/multi pion production ($\nu N \to lN' + n\pi, n > 0$)
  - CC coherent pion production ($\nu N \to l\pi N'$)
  - CC deep-inelastic scattering ($\nu q \to lq'$)

- Neutral Current (NC) interactions ($\nu N \to \nu X$)

  - NC elastic interaction ($\nu N \to \nu N'$)
  - NC single/multi pion production ($\nu N \to \nu N' + n\pi, n > 0$)
  - NC coherent pion production ($\nu N \to \nu\pi N'$)
  - NC deep-inelastic scattering ($\nu q \to \nu q'$)

where *N, X, N'* are nucleons, *l* is a charged lepton, and *n* an integer number.

The simulation of elastic and quasi-elastic interactions is based on Llewellyn Smith's formula [69]. For the single pion production the Rein and Sehgal model is employed [70, 71]. This model will be explained in Chapter 5. The axial vector mass in the dipole formula of the nucleon form factor is set at 1.1 GeV/c^2 for both elastic, quasic-elastic and single pion production. For coherent pion production, we neglect the interactions on the analysis according to previous K2K results given in Reference [72]. For deep inelastic scattering and multi-π, the GRV94 nucleon structure functions [73] with a cross section correction by Bodek and Yang [74] is used. The kinematics of the hadronic system is simulated using two methods according to the invariant mass, W. For W > 2.0 GeV/c^2, PYTHIA/JetSet package is used [75]. For the W < 2.0 GeV/c^2 region a custom library [76] based on experiments data is used. The multiplicity of pions is required to be larger than one for W < 2.0 GeV/c^2, because single pion production in this region is already taken into account.

Figure 3.17 shows the result of the cross section divided by E_ν of each neutrino interaction mode with CH target as a function of E_ν. NEUT also simulates kinematic information of produced particles.

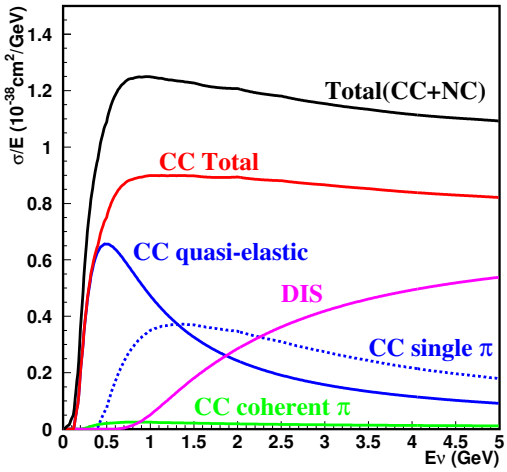

Figure 3.17: Neutrino cross section divided by E_ν of each interaction mode with CH target as a function of E_ν.

3.4.3 Detector Simulation

Once a neutrino event is generated, the detector response to the particles is simulated as the next step. The response of each detector is correctly digitized so that analysis code would work for both the real data and MC data in the same way. In K2K, GEANT-3.21 package [77] is utilized. It takes the simulated data from NEUT and traces each particle in the detector and simulates the detector response.

3.4.4 SciBar MC

In addition to the previous simulation we weight the SciBar MC to account for several things listed below:

E_ν (GeV)	Weighting factor
0.00-0.50	1.657
0.50-0.75	1.107
0.75-1.00	1.154
1.00-1.50	$\equiv 1$
1.50-2.00	0.911
2.00-2.50	1.069
2.50-3.00	1.152
> 3.00	1.260

Table 3.2: Neutrino flux weighting factors from Reference [56]

- Each MC event is weighted according to the true neutrino energy. The weighting factors were determined by a spectrum fit described in [56]. Table 3.2 gives the weighting factors.
- Charged current coherent pion interactions are given a weight of 0 to be consistent with the SciBar measurement described in [72].
- Multi-pion and DIS events are weighted by a function of the true lepton momentum transfer, $Q^2 = -(p_l - p_{l'})^2$. This correction is described by Bodek and Yang in [74].

$$weight = \frac{Q^2}{Q^2 + 0.188}$$

- Neutral current coherent pion interactions are weighted by a function of the true neutrino energy. This correction is based on the Marteau model [78].

$$weight = -0.00483E_\nu^4 + 0.08058E_\nu^3 - 0.4838E_\nu^2 + 1.247E_\nu - 0.2149$$

3.5 Recent Results and History of the K2K Experiment

Results. For K2K-I+II a total of 112 beam-originated neutrino events were observed in the 22.5 kiloton fiducial volume of Super-Kamiokande that are fully contained, have no energy seen in the outer veto detector and have at least 30 MeV deposited in the inner detector; with an expectation of $158.1^{+9.2}_{-8.6}$ events without oscillation. The spectrum distortion is also seen in 58 single-ring muon-like events. Details can be found in [56].

To estimate the total number of events expected, the 1KT data are used, because the same water target and the same detection technique as SK allows cancellation of most of the systematic uncertainties. To estimate the expected E_ν spectrum the 1KT 1-ring μ-like subsample is used together with data of the others near detectors.

The reconstruction of the proton in SciFi and SciBar allows to select events in which one or two tracks are seen. For the latter a QE enriched sub-sample is selected requiring the direction of the second track to lie within 25° from the predicted recoil proton direction assuming a QE interaction. A non-QE enriched sub-sample is selected when this difference is larger than 25° (30° for SciFi). The E_ν spectrum at the ND is measured by simultaneously fitting the p_μ and θ_μ two-dimensional distributions for the seven data samples (1KT 1-ring μ-like; SciFi and SciBar single track, two tracks QE and two tracks non-QE). For this fit we use templates of a baseline MC with our best knowledge of neutrino interaction cross-sections.

All basic ND distributions agree well with the fit results and the χ^2 value is 688.2 for 588 degrees of freedom. From the fit we obtain the cross section ratio of non-QE to QE interactions relative to our MC simulation, $R_{nqe} = 0.96$. We assign to it a ± 0.20 systematic uncertainty to account for its variation while repeating the fit on different sub-detector samples.

The spectrum distortion is shown in Figure 3.18. These events are selected as charged-current quasi-elastic and their energy is reconstructed according to 3.2.

A two-flavor ν_μ disappearance neutrino oscillation analysis is performed using a maximum likelihood fit to the total number of fully contained events and the energy shape of the 1-ring μ-like events. The likelihood is the product of three different terms $\mathcal{L}_{norm}\mathcal{L}_{shape}\mathcal{L}_{syst}$, the first describing the Poisson probability of the expected number of events and the second term the expected E_ν^{rec} shape at SK. The likelihood depends on the two oscillation parameters, $sin^2(2\theta)$ and Δm^2, and 32 additional parameters describing the systematic sources. These parameters, constrained by $\mathcal{L}_{syst}$, take into account the E_ν spectrum measured at the ND, the F/N ratio, the SK efficiency and energy scale, the ratio of neutral current to CCQE cross section, R_{nqe} and the overall normalization.

Figure 3.19 shows, in a two flavor oscillation scenario, the allowed oscillation parameters. Δm^2 region at $\sin^2 2\theta = 1.$ is between 1.9 and $3.5 \times 10^{-3} eV^2$ at the 90 % C.L. with a best-fit value of $2.8 \times 10^{-3} eV^2$. At this point, the expected number of events is 107.2, which agrees well with the 112 observed within the statistical uncertainty. The probability that the observations are explained by a statistical fluctuation with no neutrino oscillation is 0.0015% (4.3σ).

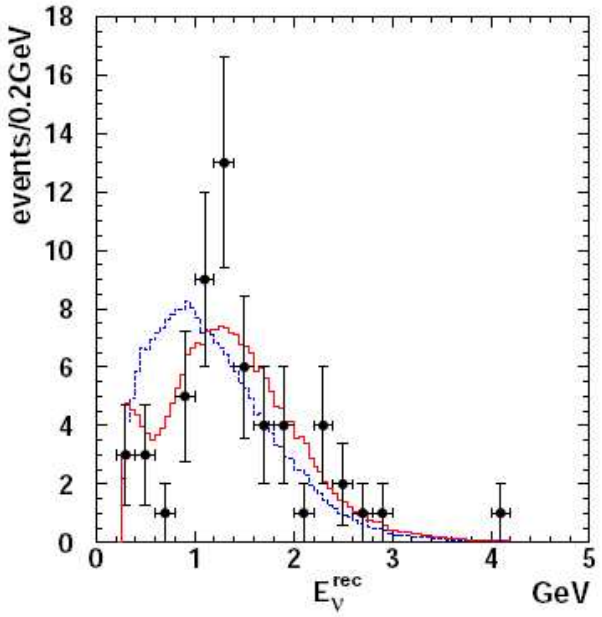

Figure 3.18: Reconstructed neutrino energy distribution for the single-ring muon-like sample [56]. Points with error bars are data. The solid line is the best fit spectrum with neutrino oscillation and the dashed line is the expectation without oscillation. These histograms are normalized by the number of observed events (58).

History. We summarize the history of the K2K experiment in Table 3.3. The K2K experiment was proposed in 1995 to confirm atmospheric neutrino oscillations. The civil construction of the beam line and detectors started in 1996. The construction was completed in 1998. The test operations of the beam and horn system were done in early 1999. From June 1999, physics data-taking started with the horn current of 200kA. This period is refereed to as K2K-Ia. The first K2K neutrino events was observed at SK on June 19th, 1999. From November 1999 to July 2001, the horn was operated with 250kA. This period is called K2K-Ib. In November 2001, a severe accident happened in SK and more than half of PMTs were broken. To resume K2K, SK detector was re-built quickly with half of PMTs. We restarted the data-taking from January 2003 (K2K-IIa). Before this period, the Lead Glass calorimeter was removed. After the K2K-IIa run, in the summer 2003, a new near detector (SciBar) was installed. From October 2003, data taking was started together with SciBar, and continued until November 2004. The period until February in 2004 is refereed as K2K-IIb, and the rest of period as K2K-IIc respectively. In

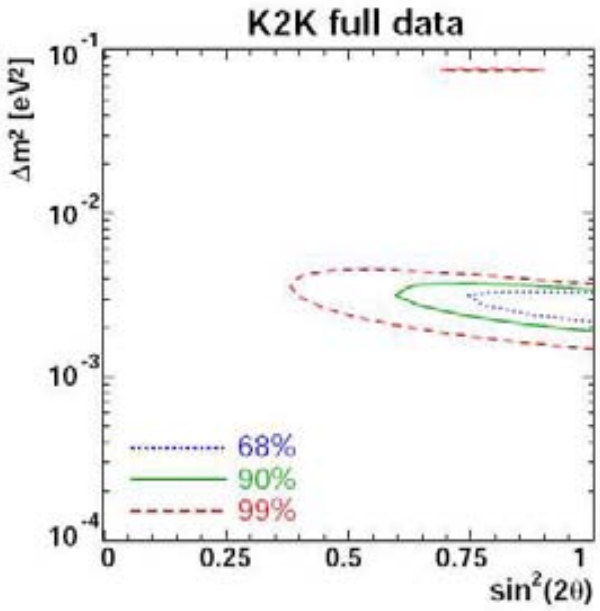

Figure 3.19: Allowed regions of oscillation parameters for K2K [56]. Three contours correspond to the 68% (dotted line), 90 % (solid line) and 99% (dashed line) C.L. allowed regions, respectively.

1995	Proposal was approved at KEK
1996	Civil construction started
1999 Jun.	Data taking with the horn current of 200 kA (K2K-Ia)
1999 Nov. to 2001 Jul.	Data taking with the horn current of 250 kA (K2K-Ib)
2001 Nov.	SK accident. Removal of LG.
2003 Jan. to 2003 Jun.	Data taking with a half PMT density of SK (K2K-IIa)
2003 Jul. to 2003 Sep.	Construction of SciBar
2003 Oct. to 2004 Nov.	Data taking with SciBar (K2K-IIb K2K-IIc)
2004 Nov.	1st magnetic horn was broken and K2K finished

Table 3.3: Summary of the K2K history.

November 2004, the first magnetic horn was broken and the K2K experiment was finished with accumulation of almost all the planned neutrino data, 10^{20} protons on target. Data taken by the K2K experiment between June 1999 and November 2004 is used to observe and measure the parameters of neutrino oscillation.

Chapter 4

SciBar detector

The SciBar detector [79, 80] is a fully-active tracking detector made of scintillator bars. SciBar was newly constructed at the near site in summer 2003. In this Chapter, the design concept, the different components, and the basic performance of SciBar are explained.

4.1 Design concept

The main purposes of SciBar are to improve the measurement of neutrino energy spectrum at the near site and to study the neutrino-nucleus interaction with high detection efficiency for low momentum particles. SciBar is designed to detect charged-current quasi-elastic (CCQE) events more efficiently than the other detectors with less contamination of non-quasi-elastic (non-QE) events. The signal of CCQE is that a muon and a proton appear from a common vertex and that no other particles are produced. In addition, because of the two-body process, there is a relationship between the kinematics of the muon and the proton, such as co-planarity. Other neutrino-nucleus interaction as the charged-current single pion production (CC$p\pi^+$) have a muon, a proton and a pion in the final state, which can be observed. In the cases when the pion is not detected both CCQE and CC$p\pi^+$ events can be mis-selected. Therefore, it is important detect both two particles, muon and proton, and to distinguish between CCQE interaction and non-QE interactions when these events are presented with the same signatures in the final state.

An electro-magnetic calorimeter (EC) is installed downstream of SciBar. The purpose of EC is to measure the ν_e contamination in the beam and the π^0 production from neutrino interaction.

Muons are observed easily because the range of a muon above 0.3 GeV/c is long enough to be reconstructed as a track. The proton range is shorter for higher momentum. In order to achieve these particle detection, SciBar detector is totally active and finely segmented, increasing the probability of having neutrino interaction, since the neutrino interaction cross section is very small. The scintillator also acts as the neutrino interaction target. The minimum reconstructible track length is 8 cm, which corresponds to 450 MeV/c for a proton and 100 MeV/c for a muon, respectively.

To reconstruct neutrino events, hit scintillator strips in SciBar with at least two photo-electrons are selected. Charged particles are reconstructed by looking for track projections in each of two dimensional view (x-z and y-z), using a cellular automaton algorithm [81]. Then, the track candidates in two views are combined based on matching of the edges in z direction and timing information. Reconstructed tracks are required to have hits at least in three consecutive layers. The reconstruction efficiency for an isolated track longer than 10 cm is 99%. Further information on the SciBar tracking and matching is presented in Appendix A.

Figure 4.1 shows a schematic view of SciBar. The main part of SciBar consists of 14,848 extruded plastic scintillator strips arranged in 64 layers of alternating vertical and horizontal planes. The dimension of each strip is 1.3 cm thick, 2.5 cm wide, and 300 cm long. As a whole, the detector size is $3. \times 3. \times 1.7\text{m}^3$, providing the total weight of about 15 ton.

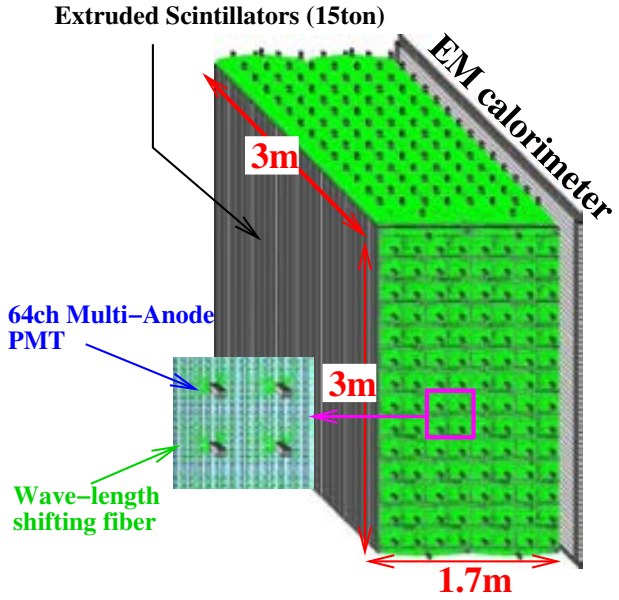

Figure 4.1: Schematic view of SciBar detector.

The scintillation light is guided to multi-anode photomultiplier tubes (MAPMT) by wavelength-shifting (WLS) fibers inserted into the holes of scintillator strips as shown in Figure 4.2. The MAPMT signals are processed with a custom-made electronics. Readout electronics record charge information of each strip and timing information on logical OR of 32 channels. The conceptual view of the readout system is show in Figure 4.3.

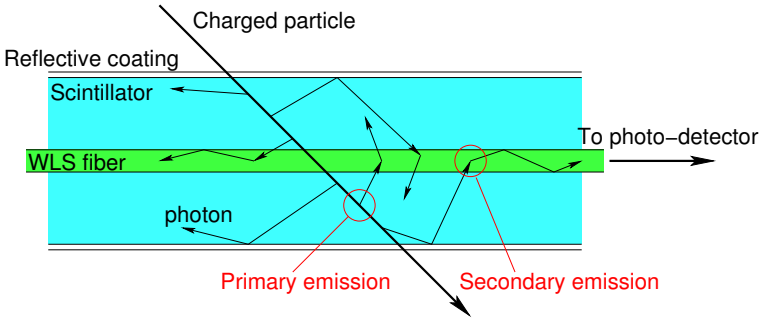

Figure 4.2: Conceptual scheme of the WLS fiber readout of the scintillation fiber.

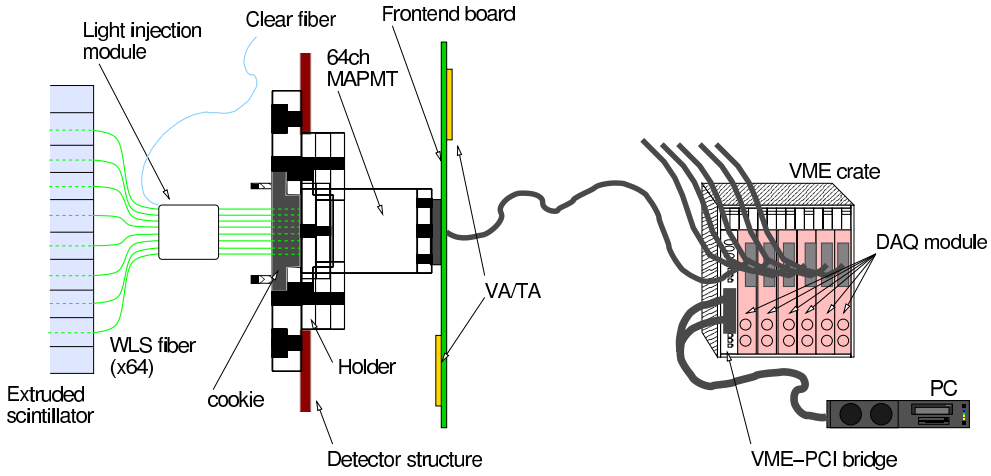

Figure 4.3: Conceptual design of the SciBar readout system.

We define the SciBar local coordinate system, which is commonly used in this thesis, as in Figure 4.4. In the Cartesian coordinate system, the z-axis is the beam direction, the y-axis the vertical upward direction, and the x-axis is obtained as $x = y \times z$.

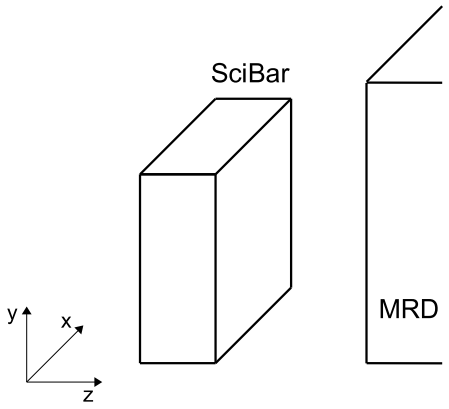

Figure 4.4: Definition of the SciBar local coordinate system.

4.2 Detector components

4.2.1 Extruded scintillator

The extruded scintillator used in SciBar is made of polystyrene, infused with the fluors PPO (1% by weight) and POPOP (0.03% by weight). The composition is the same as the scintillator for the MINOS experiment [82]. The wavelength at the emission peak is 420 nm (blue) which matches with the absorption spectrum of the WLS fiber as shown in Figures 4.5, and 4.6.

The profile of the SciBar scintillator strip is show in Figure 4.7. It has a rectangular cross section of 2.5 cm wide and 1.3 cm thick. There is a 1.8 mm diameter hole in the center for the 1.5 mm diameter WLS fiber. A 0.25 mm thick white reflective coating, composed of TiO_2 infused in polystyrene (15% by weight), surrounds the scintillator bar. The coating improves light collection efficiency, and it acts an optical isolator. The scintillator, hole, and reflective coating are extracted together. The extruded scintillator is developed and produced by Fermilab [83].

In SciBar, $14,848$ strips are used in total. The scintillator strips are arranged in 64 layers. Each layer consists of two planes, with 116 strips to give horizontal and vertical position. The whole size of SciBar is $3 \times 3 \times 1.7\text{m}^3$, and the weight is $\sim$ 15 tons.

In order to build a large scintillator structure, vertical and horizontal planes were glued together using epoxy resin, Cemedine PM-200, with aluminum frames surrounding it. The module was

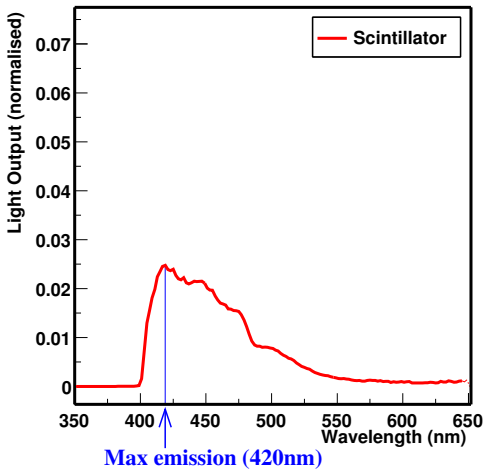

Figure 4.5: The emission light spectrum of the scintillator.

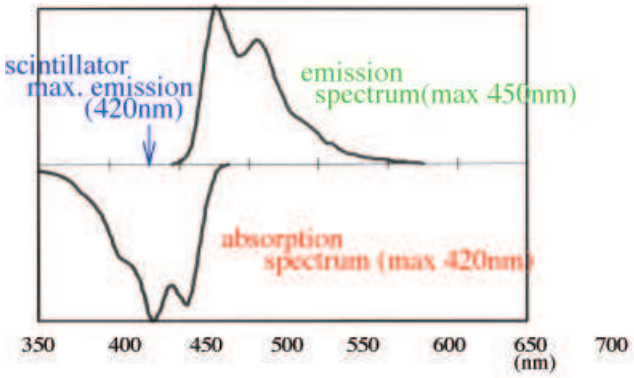

Figure 4.6: The absorption and emission spectrum of the WLS fiber.

installed using a crane. During the installation, 10% of all the strips were sampled and the dimensions and weight were measured.

Since the pixels of the 64-pixel MAPMT are arranged in 8×8, there are 8×14 MAPMTs to cover 64×112 strips in each projection plane. The remaining two strips at the edges of each plane are called "outer detector" (OD). OD is read by a single-anode PMT, which is connected to 64 fibers from 2×32 strips.

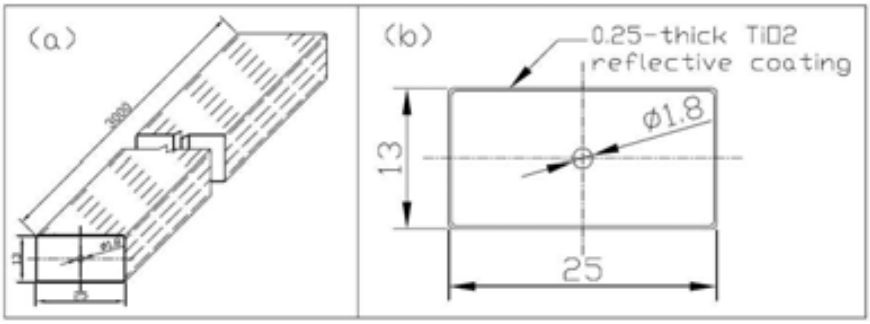

Figure 4.7: Drawing of a scintillator strip. Units are in mm. The left figure shows a 3 dimensional view and the right figure shows a detailed description of the cross-section.

4.2.2 Wave-length shifting fiber

The green wavelength-shifting (WLS) fiber (1.5mm in diameter), Kuraray Y11 (200) MS type, is used to collect the scintillation light. Blue photons produced in the scintillation process suffer many reflections by the reflective coating of the scintillator strip as shown in Figure 4.2. The blue photons eventually hit a fiber where they are absorbed and re-emitted as green photons. As shown in Figure 4.6, the absorption spectrum, centered at the wavelength of 420 nm (blue), has only a little overlap with the emission spectrum, centered at 476 nm (green), so that self-absorption in the fiber is small. The fibers then act as light guides to transport the green light to a photo-detector. The WLS fiber provides a very efficient light concentration in a very small area.

The fibers are double-clad type to give a maximum trapping fraction for the green light, as show in Figure 4.8. The WLS fiber has a polystyrene inner core containing the WLS flour (200 ppm),

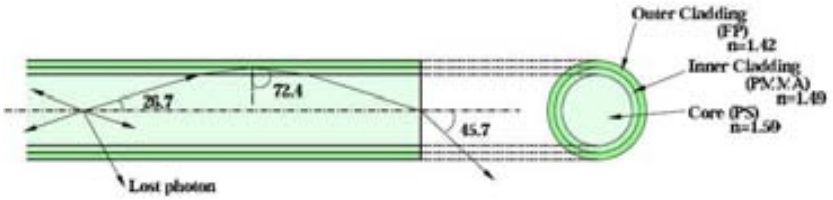

Figure 4.8: The wavelength-shifting fiber Kuraray Y11 (200) MS.

an acrylic thin intermediate layer and a thin polyfluor outer clad. They have refraction indices of 1.59, 1.49 and 1.42, respectively. The green light whose angle with respect to the fiber axis is

Photo-cathode	Bialkali
Quantum efficiency	12% for 500 nm photons
Number of pixels	64
Pixel size	2×2 mm^2
Typical gain	6×10^5 at $\sim$ 800 V
Response linearity	200 photo-electron at gain 6×10^5
Cross talk	4% (adjacent pixel)
Number of MAPMTs	224

Table 4.1: Specifications of multi-anode photo-multiplier tube

less than 26.7 degree is trapped and transported along the fiber, satisfying the relation:

$$\cos\theta \geq \frac{1.42}{1.59} \Longrightarrow \theta < 26.7^\circ \tag{4.1}$$

The light intensity attenuates exponentially as a function of propagation length. Before the installation, the attenuation length of all WLS fibers was measured by using blue LED light. As a result, the attenuation length was distributed around 350 cm. In addition, the attenuation length was checked by cosmic rays after the installation.

Sixty-four wavelength-shifting fibers are bundled together and glued to an attachment to be precisely coupled between fibers and the photo-cathode of the multi-anode PMT. Each bundle is connected to the photo-detector. All fibers are aligned to pixels of MAPMT within 0.2 mm precision.

4.2.3 64-channel multi-anode PMT

A 64-channel multi-anode PMT (MAPMT), manufactured by Hamamtsu Photonics, is used for a photo-sensor of SciBar. The MAPMT is placed at the edges of the detector. Table 4.1 summarizes its specifications.

The MAPMT behaves like 64 miniature single-channel PMTs. The pixel size is 2×2 mm^2, and they are arranged in an 8x8 array. The photocathode area is made of a bialkali material. The quantum efficiency is about 12% at the wavelength of 500 nm. Only a few additional and potentially adverse features, like cross-talk and non-uniformity of pixel response, are introduced by the dense packaging. The cross-talk effect, which is mainly caused by the incident light

spreading at the face-window, is measured to be 4% for adjacent pixels and 1% for orthogonally opposite pixels with 1.5 mm diameter WLS fiber[1]. The pixel-to-pixel gain uniformity is measured to be 21% in RMS.

The ratio of the maximum to minimum gain is less than two for typical tubes. The operation high voltage is tuned so that the averaged gain of 64 channels is 6×10^5. The temperature coefficient of the gain is measured to be 0.3%/deg. The response linearity is kept within 10% up to 200 photo-electrons (pe) with a gain of 6×10^5.

4.2.4 Gain monitoring

The MAPMTs are very sensitive to the small changes of surrounding temperature and applied high voltage. To guarantee the detector stability, the gain of all the PMT channels was monitored during the detector operation. A schematic view of the gain monitor system is shown in Figure 4.9. A blue LED is used as a light source, and pulse blue light is distributed to each fiber bundle through a clear fiber (1 mm-diameter). In order to measure the light intensity of each pulse, the LED also illuminates a pin photo-diode and a 2 inch PMT which is calibrated by an Am-NaI stable light source. A "light injection module" is assembled to a WLS fiber bundle. Blue LED light is injected into the module, and all the fibers are uniformly illuminated. By comparing the MAPMTs outputs with the pin photo-diode or the 2 inch PMT, we measure the relative gain drift with 0.1% precision.

4.2.5 Electro-magnetic calorimeter

In order to study the $\nu_\mu \to \nu_e$ oscillation channel, ν_e contamination in the beam and π^0 production from neutrino interaction are dominant backgrounds. The detection of electro-magnetic shower is required to study ν_e and π^0 events. However, the scintillator part of SciBar is only four radiation length along the beam direction, and not enough to measure energy of an electron and a photon around 1 GeV. Therefore, an electro-magnetic calorimeter (EC) is installed downstream of the scintillator part. EC is an array of "spaghetti modules" which were used at CHORUS experiment [85]. EC is comprised of 2 planes of 30 horizontal and 32 vertical modules. The module is made of lead sheets and scintillating fibers. Its dimension is $4\times8\times262$ cm^3, consisting

[1]The cross-talk measurement was done only for one MAPMT and only taken into account the first adjacent pixels. A cross-talk simulation study was done to extend this result to the behavior of all the MAPMTs. It will be explained in Chapter 8 and detailed in [84].

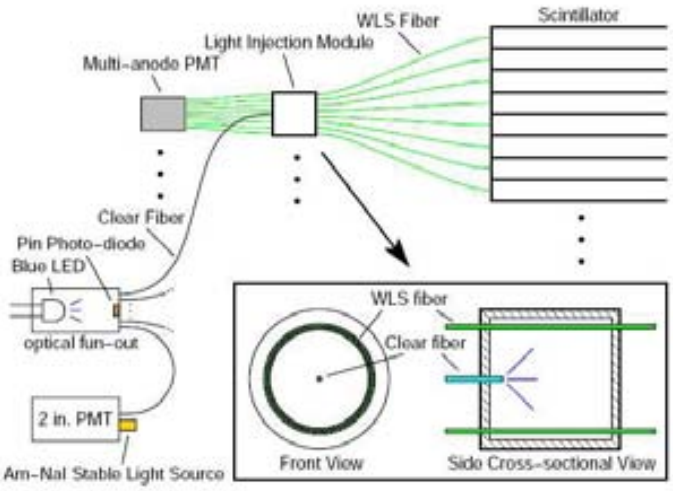

Figure 4.9: Schematic view of the gain monitoring system.

of two $4\times4\times262$ cm^3 readout cells. EC provides additional 11 radiation length along the beam direction. The response linearity is understood to be better than 10%. The energy resolution is $14\%/\sqrt{E_{GeV}}$, where E is the electron energy.

4.2.6 Readout system

The MAPMT signals are processed by custom built electronics. The electronics consists of front-end circuit boards (FEB) attached to MAPMTs and back-end VME modules (DAQ Board) to control and readout the FEBs. On FEB, a combination of ASICs-VA and TA are employed to multiplex pulse-height information and to make a fast-triggering signal. The VA has preamplifiers for 32 input channels and shapes the output with a peaking time of 1.2 μs. The 32 signals from VA shapers are captured by the sample-and-hold circuits and passed to an analog multi-plexer. The signal after preamplification in VA is sent to a fast shaper in TA, with a peak in time at 80 ns. Logical OR of distributed signal from 32 channels is sent out from a TA. The intrinsic time jitter of the discriminated output is shorter than 1 ns. Each FEB has two sets of VA and TA packages, thus processing 64 input channels in total for one MAPMT.

The DAQ Board is developed as a standard VME-9U board. A picture of the module is shown in Figure 4.10. Each of the eight channels has line drivers to control a FEB and a 12-bit flash ADC to digitize multiplexed analog signal from a FEB. Timing information is sent to a multi-hit TDC.

The timing resolution and full range are 0.78% ns and 50 μs, respectively. The resolution allows us to distinguish multiple events occurred in one spill.

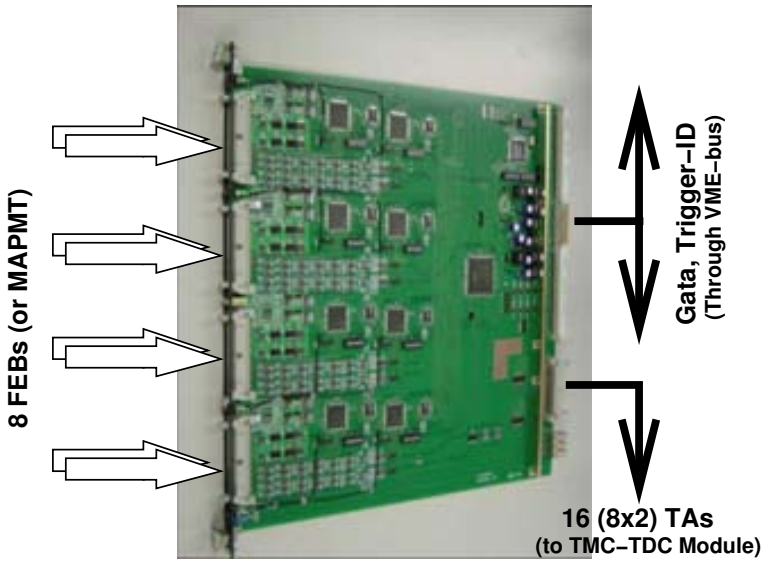

Figure 4.10: Picture of the data acquisition board.

4.2.7 Data acquisition

The timing diagram of the data acquisition is summarized in Figure 4.11. The neutrino data is taken by using the beam trigger signal from the accelerator. After the beam trigger, pedestal and LED triggers are generated. The cosmic-ray data are continuously acquired until 1.5 seconds after the beam.

4.3 Basic performance

In the rest of this Chapter, we describe basic performances of SciBar: energy scale, timing resolution, quenching effect and alignment.

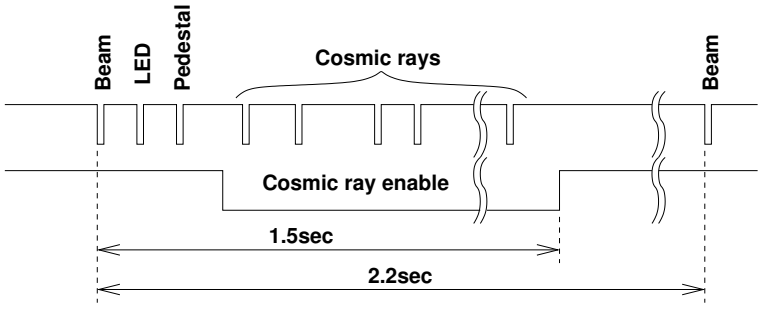

Figure 4.11: Timing diagram of the data acquisition.

4.3.1 Energy scale calibration

The energy scale of each scintillator strip is calibrated with cosmic-ray muons. Figure 4.12 shows the light yield distribution of one strip for the cosmic-ray muons. The path length inside the strip and the attenuation effect in the WLS fiber are corrected in the distribution. The mean light yield is measured to be 26 pe/1.3 cm. This value is used as the calibration constant for all the strips, Figure 4.13 shows this distribution. The mean value of 9.1 pe/MeV is consistent with the expectation of 9.3 pe/MeV from the laboratory measurements.

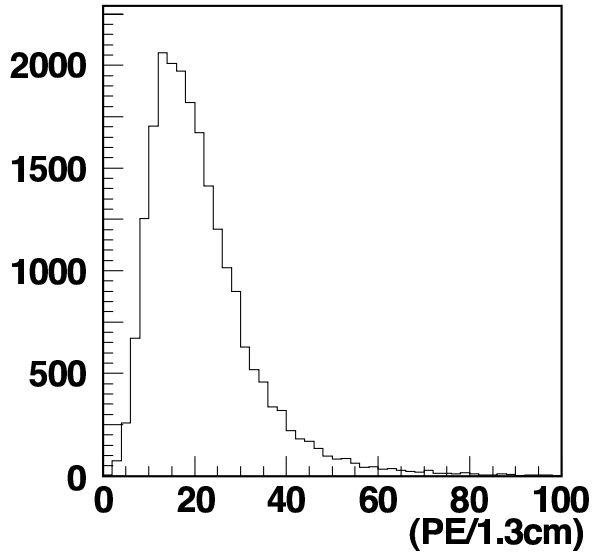

Figure 4.12: Light yield distribution of a typical scintillator strip for cosmic-ray muons.

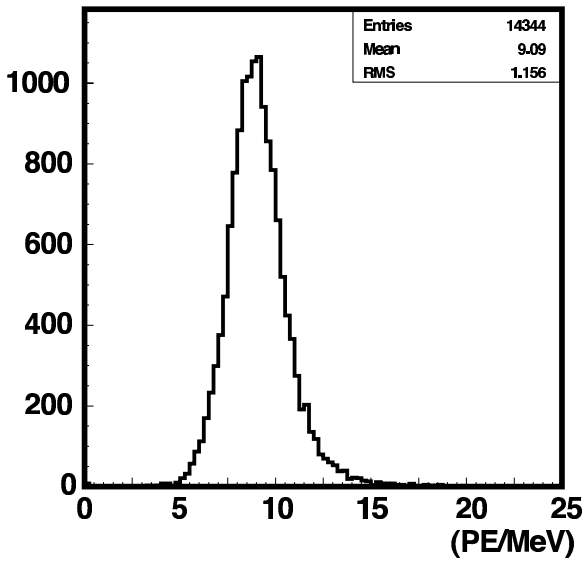

Figure 4.13: Energy calibration constant of all trips.

The stability of the calibration is also monitored with cosmic-ray muons. The upper figure in Figure 4.14 shows the time variation of the light yield of one strip. The fluctuation around 30-60 days is due to the change of the MAPMT gain. After applying the gain correction, the calibration constant is stable with 1.0% precision as shown in the lower figure of Figure 4.14.

4.3.2 Timing calibration

The timing resolution of SciBar is measured by the time difference between two adjacent TAs along a cosmic-ray muon track. After the correction for the propagation in the fiber and the correlation between timing and charge, the time difference is plotted, as shown in Figure 4.15. The standard deviation of the distribution is 1.9 ns. The timing resolution of one TA if two channels have the same resolution is evaluated to be $1.9/\sqrt{2} = 1.3$ ns. This is good enough to select the beam timing window (1.1 μs) and to distinguish the 9 bunch (125 ns spacing) in the beam spill.

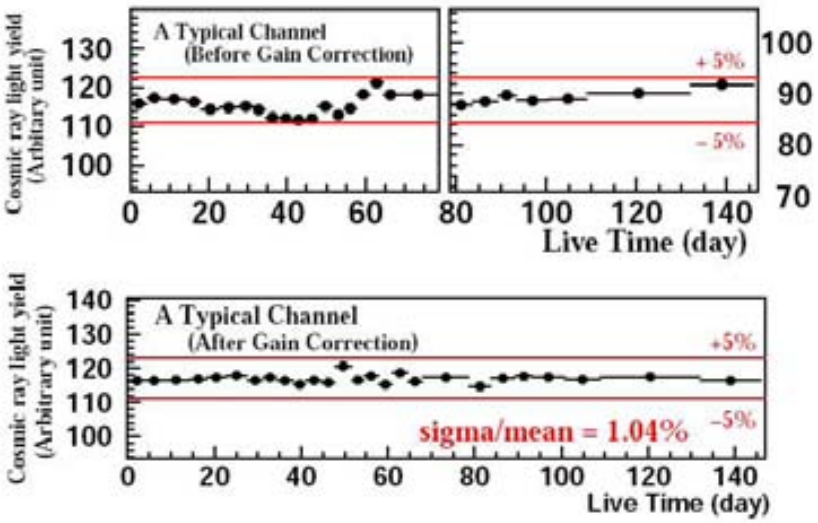

Figure 4.14: Sensibility of the energy scale calibration constant for a typical strip over the whole SciBar operation period, K2K-IIb and K2K-IIc. Before (upper) and after (lower) applying the relative gain correction of MAPMT. The light yield of cosmic-ray muons are plotted.

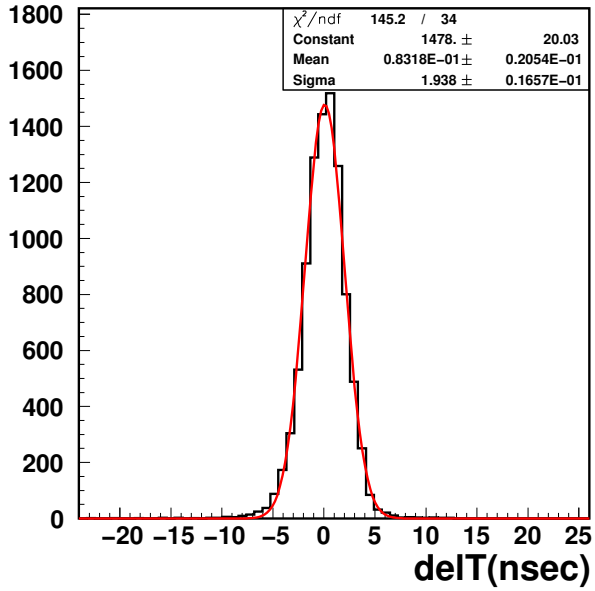

Figure 4.15: Timing difference between adjacent TA channels along a cosmic-ray muon track after applying the correction of the correlation between time and charge.

4.3.3 Calibration using test beam

A test beam experiment with a smaller proto-type detector of SciBar in the KEK T1 beam-line was performed in March 2004. This beam-line provides the pions and protons up to 2 GeV/c. The purposes of the experiment is to measure the scintillator quenching.

Scintillator light yield does not respond linearly to the energy given by ionization processes, and results in reduction of light yield. The visible energy, dE_{vis}/dx, obtained from observed light yield is not exactly equal to the deposited energy, dE/dx, especially for proton with the non-linear quenching effect. The relation is expressed as a function of the expected energy deposition per unit length, dE/dx (expected), by the Birk's formula [86], as

$$\frac{dE_{vis}/dx}{dE/dx(expected)} = \frac{c_1}{1 + c_2 \times dE/dx(expected)}, \tag{4.2}$$

where c_2 is the Birk's constant to be determined by the measurement.

Figure 4.16 shows the $(dE_{vis}/dx)/(dE/dx(expected))$ as a function of the expected dE/dx estimated by the MC simulation for various incident proton momentum. In Figure 4.16, the

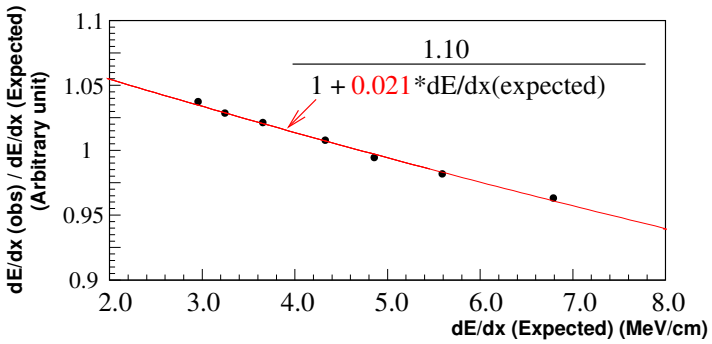

Figure 4.16: Ratio of the observed deposited energy per unit length (dE/dx) to the expected dE/dx by the MC simulation as a function of the expected dE/dx. A red line shows a Birk's relation with best fit constants.

quenching effect is clearly seen and this effect is well reproduced by Equation 4.2 with the best fit value for the Birks constant (c_2) = 0.0208 $\pm$ 0.0003 (stat.) $\pm$ 0.0023 (syst) cm/MeV; where the systematic error is evaluated by changing the fitting conditions, such as fitted region and the data set. This result is included in the MC simulation.

4.3.4 Alignment of the detector

The alignment of the SciBar detector consists of the proper placement of the different layers, each one respect to the other, and the proper placement of the all detector in the global reference system. The detector has to be aligned in order to compute the directions of the tracks correctly. A wrong direction would give a wrong track and signal from different particles could be included in the same track. The reconstruction of the track is more precise with an aligned detector and so, the selection of events is improved. All the detectors in some experiment has to be aligned. Details in SciBar alignment can be found in [87].

In order to perform the alignment cosmic ray data were considered: only one track per event and crossing all the detector . The internal alignment was done for the vertical and horizontal layers independently, considering the transverse residuals which are defined as the transverse distance from the energy weighted mean of hits position to the track position. The transverse residual, Δt, has information on the deviations of the transverse position from the nominal one of each x and y plane, the transverse deviation Δt_0, but also, on deviations in z direction, Δz. This relation is showed by a straight line dependency:

$$\Delta t = \Delta t_0 + \Delta z \tan\theta$$

Figure 4.17 shows the transverse deviation and the z deviation. For each layer the track is recomputed without taking into account the information for that layer; after that, the transverse residual is computed and the above straight line fitted. Then, the corrections are applied to get the detector aligned internally. This process was iterated several times until getting deviations negligible respect to the size of the layer. The number of recovered tracks after alignment increases 3 per thousand. In this case, the alignment was a check of how well the tracking was done.

In order to place the detector in the global reference system we perform the external alignment. Translations were studied. The method of the transverse residual was applied to that track with a SciFi and a MRD matching. A extrapolated track from SciBar was compared with the matched track in a virtual plane between the two detectors, and then the residual computed. The z deviation was found to be 5 cm, and the transverse position 1.1 in x and 0.2 in y. These corrections were added to the SciBar Data Base; and are used in the simulation and reconstruction of SciBar events.

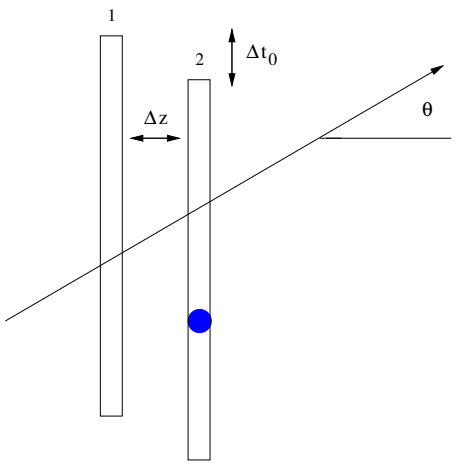

Figure 4.17: The plane in the position **2** has to be placed in the position **1**. The point is the geometrical mean of the hits position and the straight line is the track. The position is corrected using the transverse deviation, Δt_0, and z deviation, Δz. Both corrections are necessary to place the geometrical mean and the track extrapolated to the plane in the same position.

Chapter 5

Theory of Neutrino Nucleus Interaction around 1 GeV

In this Chapter we present some aspects of the theory of neutrino nucleus interaction around 1 GeV. We concentrate on the theory of single pion production and quasi-elastic scattering. At the end of the Chapter we consider the nuclear effects.

5.1 Introduction to the Single Pion Production

The single pion production process is the consequence of a resonance process

$$\begin{aligned} \nu + N &\rightarrow l + N^* \\ N^* &\rightarrow N' + \pi \end{aligned} \tag{5.1}$$

where ν denotes the interacting neutrino, N the nucleon target, l the lepton, either neutral or charged, and N^* the nucleon resonance. The nucleon resonance decays to a nucleon N' and a pion π. This is the dominant decay if the invariant mass of the hadron system N^* is less than 2 GeV/c^2.

In next sections we describe the kinematics of the neutrino production of pions according to the Rein and Sehgal model [70]. This model was employed to simulate single pion production in the K2K Monte Carlo NEUT ([68]). First, the cross section for a single isolated resonances as

the one described in Equation 5.1 is presented. Second, we consider the presence of several overlapping resonances N^*. Finally, we review the task of computing the production and decay amplitudes.

5.2 Neutrino production of isolated resonances

According to the effective current-current formulation of weak interactions the production matrix element is given by

$$T\left(\nu N \to l N^*\right) = \frac{G}{\sqrt{2}} \left[\overline{u}_l \gamma^\beta \left(1-\gamma_5\right) u_\nu\right] \left\langle N^* \mid J_\beta^+ \left(0\right) \mid N \right\rangle \tag{5.2}$$

with $G = G_F \cos\theta_c \approx G_F$ the weak coupling constant for strangeness conserving transitions. The hadronic current operator J_β^+ contains a vector and an axial vector part and may be written factoring out the resonance mass (M) as

$$J_\beta^+ = V_\beta - A_\beta = 2MF_\beta = 2M\left(F_\beta^V - F_\beta^A\right) \tag{5.3}$$

The leptonic current matrix element $\left[\overline{u}_l \gamma^\beta \left(1-\gamma_5\right) u_\nu\right]$ is interpreted as the virtual intermediate boson's polarization vector, which may be decomposed in three standard polarization vectors e_L^μ, e_R^μ, e_0^μ corresponding to left-handed, right-handed and scalar polarization. With the 3-momentum of the virtual boson q^μ along the z-axis, the usual definition is

$$\begin{aligned} q^\mu &= \left(\nu, 0, 0, Q\right), \\ e_L^\mu &= \frac{1}{\sqrt{2}}\left(0, 1, -i, 0\right), \\ e_R^\mu &= \frac{1}{\sqrt{2}}\left(0, -1, -i, 0\right), \\ e_0^\mu &= \left(1, 0, 0, 0\right), \\ e_L^\mu e_{L\mu}^+ &= e_R^\mu e_{R\mu}^+ = -e_0^\mu e_{0\mu}^+ = -1 \end{aligned} \tag{5.4}$$

ν is the modulus of the energy transfer and Q the modulus of the three momentum transfer in the Lab. This decomposition is not unique but depends on the frame of reference. The most convenient frame of reference for practical purposes is the center of mass system of the outgoing hadrons, i.e., the resonance rest frame. The resonance rest frame is reached from the nucleonic Breit frame by a Lorentz-transformation in the direction of the momentum transfer. This leaves

the transverse polarization vectors e_L^μ, e_R^μ unchanged, converting only e_0^μ to

$$e_s^\mu = \frac{1}{\sqrt{-q^2}} \left(Q^*, 0, 0, \nu^*\right) \tag{5.5}$$

where starred quantities now refer to the resonance rest frame. They are connected to the corresponding particles in the Lab frame through

$$\frac{Q^*}{Q} = \frac{m_N}{M}, \qquad q^2 = \nu^2 - Q^2 = \nu^{*2} - Q^{*2} \tag{5.6}$$

m_N being the nucleon mass. For abbreviation we define

$$u = \frac{E + E' + Q}{2E}, \qquad v = \frac{E + E' - Q}{2E} \tag{5.7}$$

where the incident and final lepton energies are denoted by E and E', respectively, finding

$$\left[\overline{u}_l \gamma^\mu \left(1 - \gamma_5\right) u_\nu\right]_{\substack{\text{resonance} \\ \text{rest frame}}} = -2\sqrt{2}E \sqrt{\frac{-q^2}{Q^2}} \left\{u \cdot e_L^\mu - v \cdot e_R^\mu + \sqrt{2uv} \cdot e_s^\mu\right\} \tag{5.8}$$

The full neutrino production matrix element reads

$$T\left(\nu N \to l N^*\right) = -4GME \left\{\sqrt{\frac{-q^2}{Q^2}} \left\langle N^* \mid uF_- - vF_+ \mid N\right\rangle + \frac{m_N}{M}\sqrt{2uv} \left\langle N^* \mid F_0 \mid N\right\rangle\right\} \tag{5.9}$$

with

$$\begin{aligned} F_+ &= e_R^\mu F_\mu = \frac{-1}{\sqrt{2}} \left(F_x + iF_y\right) \\ F_- &= e_L^\mu F_\mu = \frac{1}{\sqrt{2}} \left(F_x - iF_y\right) \\ F_0 &= \sqrt{\frac{-q^2}{Q^{*2}}} e_s^\mu F_\mu = F_t + \frac{\nu^*}{Q^*} F_z \end{aligned} \tag{5.10}$$

The production cross section of a single resonance with mass M and negligible width is quoted as follows

$$\frac{d\sigma}{dq^2 d\nu} = \frac{1}{32\pi m_N E^2} \cdot \frac{1}{2} \cdot \sum_{spins} \mid T\left(\nu N \to l N^*\right) \mid^2 \delta\left(W^2 - M^2\right) \tag{5.11}$$

The three terms of T referring to different helicities of the incident current add up incoherently (no interference) resulting in

$$\frac{d\sigma}{dq^2 d\nu} = \frac{G^2}{4\pi^2}\left(\frac{-q^2}{Q^2}\right)\kappa\left\{u^2\sigma_L + v^2\sigma_R + 2uv\sigma_s\right\} \tag{5.12}$$

Here the partial cross sections for the absorption of an intermediate vector boson of virtual "mass" q^2 and positive, negative or zero helicity are given by

$$\sigma_{\frac{L}{R}}\left(q^2, W\right) = \frac{\pi}{\kappa}\cdot\frac{M}{m_N}\cdot\frac{1}{2}\cdot\sum_{j_z} \mid \langle N, j_z \mp 1 \mid F_{\mp} \mid N^*, j_z\rangle \mid^2 \delta\left(W - M\right) \tag{5.13}$$

$$\sigma_s\left(q^2, W\right) = \frac{\pi}{\kappa}\cdot\frac{M}{m_N}\cdot\left(\frac{Q^2}{-q^2}\right)\cdot\frac{m_N^2}{M^2}\cdot\frac{1}{2}\cdot\sum_{j_z} \mid \langle N, j_z \mid F_0 \mid N^*, j_z\rangle \mid^2 \delta\left(W - M\right) \tag{5.14}$$

including a conventional kinematic factor

$$\kappa = \nu + \frac{q^2}{2m_N} = \frac{M^2 - m_N^2}{2m_N} \tag{5.15}$$

With the momentum transfer along the z-direction the matrix elements

$$f_{\pm|2j_z|} = \langle N, j_z \pm 1 \mid F_{\pm} \mid N^*, j_z\rangle \tag{5.16}$$

$$f_{0\pm} = \left\langle N, \pm\frac{1}{2} \mid F_0 \mid N^*, \pm\frac{1}{2}\right\rangle \tag{5.17}$$

are just the helicity amplitudes for the production process.

Having thus established the production cross section for a single resonance in narrow width approximation, the resonance of finite width, Γ, can be obtained replacing the δ-function in the partial cross section 5.11 by a Breit-Wigner factor

$$\delta\left(W - M\right) \longrightarrow \frac{1}{2\pi}\cdot\frac{\Gamma}{\left(W - M\right)^2 + \Gamma^2/4} \tag{5.18}$$

For a first orientation we may take the total resonance width to be energy independent. Then the total cross sections are obtained by integrating 5.12 within the bounds

$$W_{min} = m_N + m_\pi \leq W \leq W_{max} = s = 2m_N E_\nu + m_N^2 \tag{5.19}$$

$$\mid q^2 \mid_{min} = 0 \leq \mid q^2 \mid \leq \mid q^2 \mid_{max} = \frac{(s - m_N^2)(s - W^2)}{s} \tag{5.20}$$

5.3 Interfering resonances

In practice always several nearby resonances will overlap and even nonresonant background amplitudes of various quantum numbers may interfere to produce the measurable final state.

In the case of the K2K experiment, the neutrino beam is mainly composed by ν_μ. Therefore, the expected lepton is another ν_μ for those neutral current interactions or a μ^- for the charged current ones. There are altogether 14 final hadronic state, 6 of them being mediated by charged currents:

$$\begin{aligned}
&\nu_\mu p \to \mu^- \Delta^{++} && \Delta^{++} \to p\pi^+ \\
&\nu_\mu n \to \mu^- \Delta^{+} && \Delta^{+} \to p\pi^0, \Delta^{+} \to n\pi^+ \\
&\overline{\nu}_\mu p \to \mu^+ \Delta^{0} && \Delta^{0} \to n\pi^0, \Delta^{0} \to p\pi^- \\
&\overline{\nu}_\mu n \to \mu^+ \Delta^{-} && \Delta^{-} \to n\pi^-
\end{aligned}$$

while the remaining 8 reaction channels are populated by neutral current interactions:

$$\begin{aligned}
&\nu_\mu p \to \nu_\mu \Delta^{+} && \Delta^{+} \to p\pi^0, \Delta^{+} \to n\pi^+ \\
&\nu_\mu n \to \nu_\mu \Delta^{0} && \Delta^{0} \to n\pi^0, \Delta^{0} \to p\pi^- \\
&\overline{\nu}_\mu p \to \overline{\nu}_\mu \Delta^{+} && \Delta^{+} \to p\pi^0, \Delta^{0} \to n\pi^+ \\
&\overline{\nu}_\mu n \to \overline{\nu}_\mu \Delta^{0} && \Delta^{0} \to n\pi^0, \Delta^{0} \to p\pi^-
\end{aligned}$$

All these reactions amplitudes are expected to be dominant by nucleon resonance as long the nucleon-pion invariant energy does not exceed about 2 GeV. Figure 5.1 shows as an example the production of the Δ^{++} resonance.

The formalism for describing single resonance production by neutrinos must consequently be extended to include several interfering resonances N^*_γ which, by simultaneous decay, feed the same final $N\pi$ state at a fixed invariant energy. It is need to consider a sum of helicity amplitudes $f^{(\gamma)}_{\pm 1}$, $f^{(\gamma)}_{\pm 3}$, $f^{(\gamma)}_{0\pm}$ for single resonance production each of them being accompanied with the corresponding decay amplitude $\eta^{(\gamma)}$ into the $N\pi$ state under consideration.

In Table 5.1 we listed all nucleon resonances of unambiguous classification up to 2 GeV/c^2 that were considered by Rein and Sehgal [70, 71]. The central value and total width are updated from the general nucleon resonances table found in [88].

We analysis now the ν interaction amplitudes. Calling A^{CC}_3, A^{CC}_1 the reduced amplitudes for producing a $N\pi$ final state with isospin $\frac{3}{2}$ $\left(\frac{1}{2}\right)$ by a charged isovector current (CC), and A^{NC}_3,

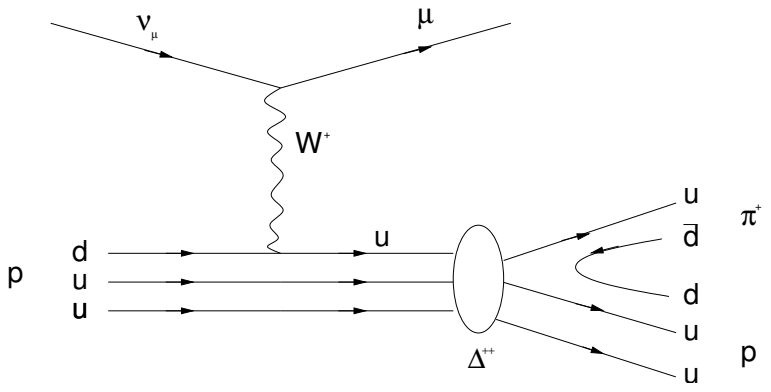

Figure 5.1: Production of the Δ^{++} resonance in a charged-current neutrino interaction.

A_1^{NC}, and S_1^{NC} the corresponding neutral current (NC) amplitudes originating from the isovector and isoscalar part, respectively, we find for isospin Glebsh-Gordan rules:

$$\begin{aligned}
A\left(\nu_\mu p \to \mu^- p\pi^+\right) &= A^{CC}\left(p\pi^+\right) = \sqrt{2}A_3^{CC} \\
A\left(\nu_\mu n \to \mu^- p\pi^0\right) &= A^{CC}\left(p\pi^0\right) = \frac{2}{3}\left(A_3^{CC} - A_1^{CC}\right) \\
A\left(\nu_\mu n \to \mu^- n\pi^+\right) &= A^{CC}\left(n\pi^+\right) = \frac{\sqrt{2}}{3}\left(A_3^{CC} + 2A_1^{CC}\right) \\
A\left(\nu_\mu p \to \nu_\mu p\pi^0\right) &= A^{NC}\left(p\pi^0\right) = \frac{2}{3}A_3^{NC} + \frac{1}{3}\left(A_1^{NC} - \sqrt{3}S_1^{NC}\right) \\
A\left(\nu_\mu p \to \nu_\mu n\pi^+\right) &= A^{NC}\left(n\pi^+\right) = \frac{\sqrt{2}}{3}A_3^{NC} - \frac{\sqrt{2}}{3}\left(A_1^{NC} - \sqrt{3}S_1^{NC}\right) \\
A\left(\nu_\mu n \to \nu_\mu n\pi^0\right) &= A^{NC}\left(n\pi^0\right) = \frac{2}{3}A_3^{NC} + \frac{1}{3}\left(A_1^{NC} + \sqrt{3}S_1^{NC}\right) \\
A\left(\nu_\mu n \to \nu_\mu p\pi^-\right) &= A^{NC}\left(p\pi^-\right) = \frac{\sqrt{2}}{3}A_3^{NC} - \frac{\sqrt{2}}{3}\left(A_1^{NC} + \sqrt{3}S_1^{NC}\right)
\end{aligned} \tag{5.21}$$

where each of these relations refers to every helicity component separately. Now A_3^{CC}, A_3^{NC} are dominated by isospin $\frac{3}{2}$ and A_1^{CC}, A_1^{NC}, and S_1^{NC} are dominated by isospin $\frac{1}{2}$ resonances. In this way we may write for charged current amplitudes

$$\begin{aligned}
\sqrt{2}A_3^{CC} &= \sqrt{3}\sum_{\substack{allI=\frac{3}{2}\\ resonances}} a^{CC}\left(N_3^{*+}\right), \\
\frac{2}{3}A_1^{CC} &= \sqrt{\frac{1}{3}}\sum_{\substack{allI=\frac{1}{2}\\ resonances}} a^{CC}\left(N_1^{*+}\right)
\end{aligned} \tag{5.22}$$

Resonance symbol	Central mass value M (MeV/c^2)	Total width Γ_0 (MeV)
$P_{33}(1232)$	1232	120
$P_{11}(1440)$	1440	350
$D_{13}(1520)$	1520	120
$S_{11}(1535)$	1535	150
$P_{33}(1600)$	1600	350
$S_{31}(1620)$	1620	150
$S_{11}(1650)$	1650	150
$D_{15}(1675)$	1675	150
$F_{15}(1680)$	1680	130
$D_{13}(1700)$	1700	100
$D_{33}(1700)$	1700	300
$P_{11}(1710)$	1710	100
$P_{13}(1720)$	1720	150
$F_{35}(1905)$	1905	140
$P_{31}(1910)$	1910	300
$P_{33}(1920)$	1920	200
$F_{37}(1950)$	1950	300
$F_{17}(1990)$	1990	535

Table 5.1: Nucleon resonances below 2 GeV/c^2 of unambiguous classification that were considered by Rein and Sehgal [70, 71]. The central value and total width are updated from the general nucleon resonances Table found in [88].

and correspondingly in neutral current case

$$\frac{2}{3}A_3^{NC} = \sqrt{\frac{2}{3}} \sum_{\substack{allI=\frac{3}{2} \\ resonances}} a^{NC}\left(N_3^{*+}\right) = \sqrt{\frac{2}{3}} \sum_{\substack{allI=\frac{3}{2} \\ resonances}} a^{NC}\left(N_3^{*0}\right),$$

$$\frac{1}{3}\left(A_1^{NC} - \sqrt{3}S_1^{NC}\right) = -\sqrt{\frac{1}{3}} \sum_{\substack{allI=\frac{1}{2} \\ resonances}} a^{NC}\left(N_1^{*+}\right), \tag{5.23}$$

$$\frac{1}{3}\left(A_1^{NC} + \sqrt{3}S_1^{NC}\right) = +\sqrt{\frac{1}{3}} \sum_{\substack{allI=\frac{1}{2} \\ resonances}} a^{NC}\left(N_1^{*0}\right)$$

where $N^{*0}_{3,1}$, $N^{*+}_{3,1}$ denote resonances of isospin $\frac{3}{2}$ or $\frac{1}{2}$ being in zero or positively charged states, respectively.

Calculating the total cross sections where the angular dependence has been already integrated out, only those resonances which have the same spin and $N\pi$ orbital angular momentum are allowed to interfere.

Any of the charged or neutral current amplitudes, $a_k(N^*_\gamma)$, referring to one single resonance in a definite state of isospin, charge and helicity ($k = 2j_z$), consists of two factors describing the production of the resonance N^*_γ and its subsequent decay into the $N\pi$ final state:

$$a_k^{CC,NC}\left(N^*_\gamma\right) = f_k^{CC,NC}\left(\nu N \to N^*_\gamma\right) \cdot \eta\left(N^*_\gamma \to N\pi\right) = f_k^{(\gamma)} \cdot \eta^{(\gamma)} \tag{5.24}$$

The resonance production amplitudes $f_k^{(\gamma)}$ ($k = 2j_z = \pm 3, \pm 1, 0\pm$) for single resonances N^*_γ have been already introduced in Equation 5.16. The corresponding decay amplitudes $\eta^{(\gamma)}$ in turn can be split into three factors.

The first factor to consider is the Breit-Wigner factor

$$\eta^{(\gamma)}_{BW}(W) = \sqrt{\frac{\Gamma_\gamma}{2\pi}} \frac{1}{W - M_\gamma + (i/2)\,\Gamma_\gamma} \cdot \frac{1}{\sqrt{N_\gamma}} \tag{5.25}$$

where the total resonance width Γ_γ has the threshold behavior

$$\Gamma_\gamma = \Gamma^0_\gamma \left(\frac{q_\pi(W)}{q_\pi(M_\gamma)}\right)^{2L+1} \tag{5.26}$$

with

$$q_\pi(W) = \mid q_\pi \mid_{N\pi \to CMS} = \left\{\left(W^2 - m_N^2 - m_\pi^2\right)^2 - 4m_N^2 m_\pi^2\right\}^{1/2} \cdot \frac{1}{2W} \tag{5.27}$$

and a correction close to one,

$$N_\gamma = \int_{W_{min}}^{\infty} dW \frac{\Gamma_\gamma}{2\pi} \frac{1}{(W - M_\gamma)^2 + \Gamma_\gamma^2/4} \tag{5.28}$$

has been applied for keeping the Breit-Wigner factor approximately normalized.

A second factor is the square root of the elasticity $x_E^{(\gamma)}$ of the resonance taking care of the branching ratio into the $N\pi$ final state.

The third factor is a pure sign. In principle, production and subsequent decay of a resonance have to be calculated in the same model in order to obtain a coherent prediction for the $N\pi$-excitation

amplitude. However, in replacing the latter by the $experimental$ Breit-Wigner factor, the sign of the amplitude is lost and has to be attached as a separate factor. For single resonance production this sign would not matter. For interfering resonances, however, it is important and must be carefully included.

The decay amplitude of a single resonance N^*_γ will be as follows:

$$\eta^{(\gamma)} = \sqrt{x_E^{(\gamma)}} \cdot \eta_{BW}^{(\gamma)}(W) \cdot \mathrm{sgn}\left(N^*_\gamma\right) \tag{5.29}$$

irrespective of its isospin, charge or helicity.

The production and decay amplitude are now attached according to Equation 5.24. Summing up all the contributing resonances then gives the full $N\pi$ amplitude to be used in the cross section of Equations 5.12.

5.4 Computing of the Production and Decay Amplitudes

In this section we take the dynamical task of computing the production, f_k (as a function of q^2, and W), and decay, $\eta(W)$, amplitudes defined in Equation 5.24. The Feynman, Kislinger, and Ravndal [89] (FKR) quark model was adopt to this end, because of its simplicity and predictive power.

Electromagnetic and weak interactions are introduced into the model by the minimal coupling scheme. Hence a vector current is given by

$$V_\mu = j^V_\mu = 3\sum_\alpha Q_\alpha \left(\not{p}_\alpha \gamma_\mu e^{iqu_\alpha} + \gamma_\mu e^{iqu_\alpha}\not{p}_\alpha\right) \tag{5.30}$$

where the sum is over the quarks in the nucleon, and the corresponding axial vector current operator is introduced by replacing γ_μ by $Z\gamma_\mu\gamma_5$. The axial vector renormalization constant Z is introduced to compensate between the predicted value for the nucleon's axial vector form factor at $q^2 = 0$ and its experimental value.

The reduction of the interaction term to a form suitable for application to resonance excitation has been carried through [89, 90]. The result is:

$$e^\mu j^{V,A}_\mu = 2W\left(e_t F_t^{V,A} + e_z F_z^{V,A} - e_+ F_-^{V,A} - e_- F_+^{V,A}\right) \tag{5.31}$$

where the charged current operators are given as follows

$$\begin{aligned} F_{\pm}^{V} &= -9\tau^{+}\left(R^{V}\sigma_{\pm} + T^{V}a_{\mp}\right)e^{-\lambda a_{z}} \\ F_{\pm}^{A} &= \pm 9\tau^{+}\left(R^{A}\sigma_{\pm} + T^{A}a_{\mp}\right)e^{-\lambda a_{z}} \\ F_{0}^{V} &= +9\tau^{+}Se^{-\lambda a_{z}} \\ F_{0}^{A} &= -9\tau^{+}\left[C\sigma_{z} + B\left(\sigma\mathbf{a}\right)\right]e^{-\lambda a_{z}} \end{aligned} \tag{5.32}$$

The neutral current operators, according to the Salam-Weinberg theory [91],[92] are obtained replaced τ^{+} by $\frac{1}{2}\tau^{3} - 2\sin^{2}\theta_{W}\cdot\tau^{em}$ for the vector current, and by $\frac{1}{2}\tau_{3}$ for the axial vector current, respectively. Charged and neutral currents contain unitary spin operators $(\tau^{+},\tau^{3},\tau^{em} = (\tau^{3}+1)/2)$ and spin operators $(1,\sigma)$ acting on the SU_{6} part of the resonance wave functions. The oscillator operators

$$a_{z}, a_{\pm} = \mp\frac{1}{\sqrt{2}}\left(a_{x} \mp ia_{y}\right) \tag{5.33}$$

act on the spatial part.

The coefficients in Equation 5.32 are the same as the given in Reference [90], [93] with the resonance mass M replaced by the $N\pi$ invariant energy W. For convenience the coefficient are quoted as follows:

$$\begin{aligned} \lambda &= \sqrt{\frac{2}{\Omega}}\frac{m_{N}}{W}Q \\ T^{V} &= \frac{1}{3W}\sqrt{\frac{\Omega}{2}}G^{V}\left(q^{2}\right) = T \\ R^{V} &= \sqrt{2}\frac{m_{N}}{W}\frac{\left(W+m_{N}\right)Q}{\left(W+m_{N}\right)^{2}-q^{2}}G^{V}\left(q^{2}\right) = R \\ S &= \left(\frac{-q^{2}}{Q^{2}}\right)\frac{3Wm_{N}+q^{2}-m_{N}^{2}}{6m_{N}^{2}}G^{V}\left(q^{2}\right) \\ T^{A} &= \frac{2}{3}Z\sqrt{\frac{\Omega}{2}}\frac{m_{N}}{W}\frac{Q}{\left(W+m_{N}\right)^{2}-q^{2}}G^{A}\left(q^{2}\right) \\ R^{A} &= \frac{Z\sqrt{2}}{6W}\left(W+m_{N}+\frac{2n\Omega W}{\left(W+m_{N}\right)^{2}-q^{2}}\right)G^{A}\left(q^{2}\right) \\ B &= \frac{Z}{3W}\sqrt{\frac{\Omega}{2}}\left(1+\frac{W^{2}-m_{N}^{2}+q^{2}}{\left(W+m_{N}\right)^{2}-q^{2}}\right)G^{A}\left(q^{2}\right) \\ C &= \frac{Z}{6m_{N}Q}\left(W^{2}-m_{N}^{2}+n\Omega\frac{W^{2}-m_{N}^{2}+q^{2}}{\left(W+m_{N}\right)^{2}-q^{2}}\right)G^{A}\left(q^{2}\right) \end{aligned} \tag{5.34}$$

The transition form factors $G^{V,A}\left(q^2\right)$ included in the coefficients 5.34 are assumed to have the form

$$G^{V,A}\left(q^2\right) = \left(1 - \frac{q^2}{4m_N^2}\right)^{\frac{1}{2}-n} \left(\frac{1}{1 - q^2/m_{V,A}^2}\right)^2 \tag{5.35}$$

The dipole form factor represents the experimentally measured elastic form factors, the parameters m_V and m_A are the vector mass and the axial vector mass respectively. The additional factor $\left(1 - \frac{q^2}{4m_N^2}\right)^{\frac{1}{2}-n}$ depends on the number n of oscillator quanta present in the final resonance.

From the vector and axial vector current (5.32) we form the relevant $(V - A)$ combinations needed for evaluating the transition matrix element between a nucleon and a nucleon resonance. For the charged current operators we then find:

$$\begin{aligned} F_{\pm}^{CC} &= F_{\pm}^{V} - F_{\pm}^{A} = 9\tau^{+} \cdot \left\{T^{\pm} a_{\mp} + R^{\pm}\sigma_{\pm}\right\} e^{-\lambda a_z} \\ F_{0}^{CC} &= F_{0}^{V} - F_{0}^{A} = 9\tau^{+} \cdot \left\{S + C\sigma_z + B\sigma\mathbf{a}\right\} e^{-\lambda a_z} \end{aligned} \tag{5.36}$$

where

$$T^{\pm} = -\left(T^{V} \pm T^{A}\right), R^{\pm} = -\left(R^{V} \pm R^{A}\right) \tag{5.37}$$

The neutral current operators are composed of isovector parts $F_{\pm}^{I_3}$, $F_0^{I_3}$ which are the same as $F_{\pm,0}^{CC}$ apart from the replacement of τ^{+} by $\frac{1}{2}\tau_3$ in Equation 5.32, and of electromagnetic pieces

$$\begin{aligned} F_{\pm}^{em} &= 9\frac{\tau_3 + 1}{2}\left(T^{V} a_{\mp} + R^{V}\sigma_{\pm}\right) e^{-\lambda a_z} \\ F_{0}^{em} &= 9\frac{\tau_3 + 1}{2} S e^{-\lambda a_z} \end{aligned} \tag{5.38}$$

Giving the neutral current operators as follows:

$$\begin{aligned} F_{\pm}^{NC} &= F_{\pm}^{I_3} - 2\sin^2\theta_w \cdot F_{\pm}^{em} \\ F_{0}^{NC} &= F_{0}^{I_3} - 2\sin^2\theta_w \cdot F_{0}^{em} \end{aligned} \tag{5.39}$$

Hence the final results on the production amplitudes

$$
\begin{aligned}
f_{-3} &= \left\langle N, \frac{1}{2} \mid F_- \mid N^*, \frac{3}{2} \right\rangle \\
f_{-1} &= \left\langle N, -\frac{1}{2} \mid F_- \mid N^*, \frac{1}{2} \right\rangle \\
f_{+1} &= \left\langle N, \frac{1}{2} \mid F_+ \mid N^*, -\frac{1}{2} \right\rangle \\
f_{+3} &= \left\langle N, -\frac{1}{2} \mid F_+ \mid N^*, -\frac{3}{2} \right\rangle \\
f_{0\pm} &= \left\langle N, \pm\frac{1}{2} \mid F_0 \mid N^*, \pm\frac{1}{2} \right\rangle
\end{aligned}
\tag{5.40}
$$

are obtained after the application of these operators to the resonance states. This proceeds along the lines indicated in the Appendix of the FKR paper [89]. A table with the explicit production amplitudes for positively charged and neutral resonances produced by electromagnetic, weak charged and neutral currents in the FKR-model is also provided in [70].

Ultimately, for the decay part of the single pion production process it is just the sign of the resonance decay amplitude which must be calculated in the quark model since the size of the decay matrix element is more accurately accounted for the Breit-Wigner factor 5.29 containing the experimental mass, width and elasticity x_E of the resonance. An overall sign is fixed requiring the $P_{33}(1232)$ to have a isospin Clebsch-Gordan coefficient for its decay into $p\pi^0$ channels. The last column of table III in [70] is used to obtain the sgn(N^*) entering in the single pion production amplitudes $a_k^{CC,NC}$ of Equation 5.24.

5.5 Summary on Single Pion Production Theory

The basic idea was to describe the amplitude for every final $N\pi$ state (14 in all for CC and NC neutrino and antineutrino reactions) as a coherent superposition of all nucleon resonances between 1 and 2 GeV contributing to the particular $N\pi$ channel under consideration. The only parameter of the model to be newly adjusted is the axial form factor mass m_A which in Reference [70] was fixed to be $m_A = 0.95$ GeV. For neutral current interactions the Salam-Weinberg theory was employed with $\sin^2\theta_W$ put at 0.22. The resonance decay part, aside from a relative sign provided by the model, has been taken as an experimental input.

As a result of calculations based on the FKR model, complemented by the Rein-Sehgal model additional assumptions, cross-sections were found nicely in agreement with experimental measurements wherever data exist at lower or at higher energies. Note that the calculation is sensitive to the choice of the axial mass parameter: a 10% variation of the value of m_A changes the cross section by about 12% in the same direction. On the other hand the cross section depends very little on the assumed shape of the resonance. The most predominant Δ^{++} resonance as studied in the $\mu^- p \pi^+$ channel is well described by the model.

In the K2K Monte Carlo Neutrino Interaction Simulation (NEUT, [68]), the $P_{33}(1232)$ and other 17 resonances with W < 2.0 GeV/c^2 are considered. In case of NEUT, $m_A = 1.1$ GeV/c^2 according to previous K2K analysis [55]. The cross-section is also consistent with past experiments.

Figure 5.2 shows the cross-section of charged current resonance production channels in NEUT, together with experimental results from the ANL experiment [94], and Gargamelle [95].

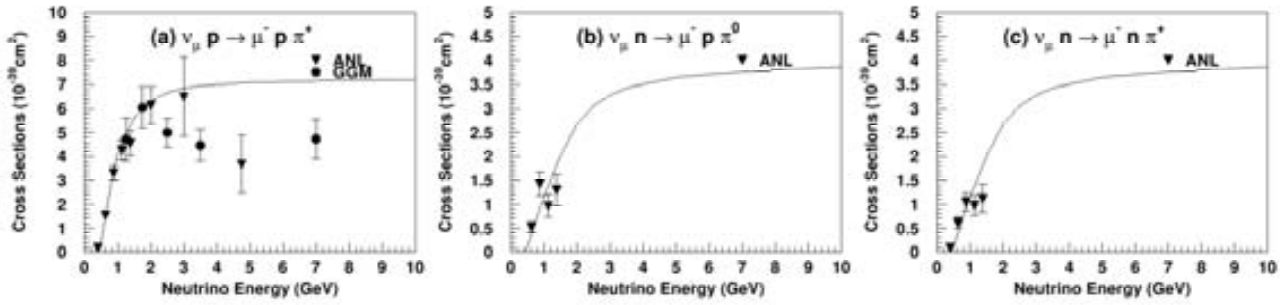

Figure 5.2: Cross section for the different single pion production modes for previous measurements [94], [95] and NEUT simulation.

5.6 Elastic and Quasi-Elastic Scattering

A brief considerations on elastic and quasi-elastic scattering theory is discussed in this section. This neutrino interaction channel is the one used to measure the neutrino energy spectrum and the oscillations parameters. Moreover, this interaction channel will be used as a reference in later chapters where the measurement of the cross section of the single pion interaction channel

is presented. The simulation of the rest neutrino interaction channels in K2K can be found in [68].

Detailed information on elastic and quasi-elastic scattering can be found in [96] and an explanation about the simulation in K2K in [68].

The elastic and quasi-elastic interaction simulation is based on LLewellyn Smith's theory [97]. The amplitude of this process is described by the product of the hadron and lepton currents

$$T\left(\nu N \rightarrow lN'\right) = \frac{G}{\sqrt{2}}\left[\overline{u}_l \gamma^\beta \left(1-\gamma_5\right) u_\nu\right] \left\langle N' \mid J_\beta^+ \left(0\right) \mid N \right\rangle \tag{5.41}$$

as was given in 5.2 for single pion production, where $G = G_F \cos\theta_c$. The hadronic current $\left\langle N' \mid J_\beta^+ \left(0\right) \mid N \right\rangle$ can be expressed as a function of the four-momentum transfer $Q^2 \equiv -q^2$

$$\left\langle N' \mid J_\beta^+ \left(0\right) \mid N \right\rangle = \overline{u}\left(N'\right)\left[\gamma_\beta F_V^1(Q^2) + \frac{i\sigma_{\beta\nu}q^\nu \xi F_V^2(Q^2)}{2m_N} + \gamma_\beta\gamma_5 F_A(Q^2)\right] u(N) \tag{5.42}$$

m_N is the nucleon mass. The vector form factors, F_V^1 and F_V^2, are represented as follows

$$\begin{aligned} F_V^1 &= \left(1+\frac{Q^2}{4m_N^2}\right)^{-1}\left[G_E^V(Q^2) + \frac{Q^2}{4m^2N}G_M^V(Q^2)\right] \\ \xi F_V^2 &= \left(1+\frac{Q^2}{4m_N^2}\right)^{-1}\left[G_M^V(Q^2) - G_E^V(Q^2)\right] \end{aligned} \tag{5.43}$$

where G_E^V and G_M^V are the Sachs electric and magnetic form factors of the nucleon respectively [98]

$$\begin{aligned} G_E^V &= \frac{1}{\left(1+\frac{Q^2}{m_V^2}\right)^2}, \\ G_M^V &= \frac{1+\xi}{\left(1+\frac{Q^2}{m_V^2}\right)^2} \end{aligned} \tag{5.44}$$

and $\xi = (\mu_p - 1) - \mu_n$ with μ_p and μ_n magnetic moments of the proton and nucleon respectively. The vector mass in the dipole parametrization m_V is set to be 0.84 GeV/c. The axial form factor, F_A, is given by

$$F_A(Q^2) = \frac{-1.23}{\left(1+\frac{Q^2}{m_A^2}\right)^2} \tag{5.45}$$

where m_A is the axial-vector mass, which is set to 1.1 GeV/c in the simulation according to previous K2K analysis [54]. Recent K2K analysis have been measured the axial-vector mass

based on the shape of the q^2 distribution. For the analysis performed using the SciFi detector ([99]), the result is m_A = 1.20 $\pm$ 0.12 GeV/c^2; and for the analysis performed using the SciBar detector ([96]), the result is m_A = 1.24 $\pm$ 0.13 GeV/c^2.

Finally, the differential cross-section [97] is expressed by

$$\frac{d\sigma}{dQ^2} = \frac{m_N^2 G^2}{8\pi E}\left[A(Q^2) \mp B(Q^2)\frac{s-u}{m_N^2} + C(Q^2)\frac{(s-u)^2)}{m_N^4}\right] \tag{5.46}$$

where E is the incident neutrino energy, $(s-u) \equiv 4m_N E - Q^2 - m_l^2$, m_l is the lepton mass, and

$$\begin{aligned}
A(Q^2) &= \frac{(m_l^2+Q^2)}{4m_N^2}\left[\left(4+\frac{Q^2}{m_N^2}\right)\mid F_A\mid^2 - \left(4-\frac{Q^2}{m_N^2}\right)\mid F_V^1\mid^2 + \frac{Q^2}{m_N^2}\mid \xi F_V^2\mid^2\left(1-\frac{Q^2}{4m_N^2}\right) + \right. \\
&\left. + \frac{4Q^2 F_V^1 \xi F_V^2}{m_N^2} - \frac{m_l^2}{m_N^2}\left(\mid F_V^1 + \xi F_V^2\mid^2 + \mid F_A\mid^2\right)\right] \\
B(Q^2) &= \pm\frac{Q^2}{m_N^2}F_A\left(F_V^1 + \xi F_V^2\right) \\
C(Q^2) &= \frac{1}{4}\left(\mid F_A\mid^2 + \mid F_V^1\mid^2 + \frac{Q^2}{m_N^2}\mid \frac{\xi F_V^2}{2}\mid^2\right)
\end{aligned} \tag{5.47}$$

The sign of $B(Q^2)$ in Equation 5.46 is minus for ν and plus for $\overline{\nu}$. The cross-section of the NC elastic scattering is derived from following relations [100]

$$\begin{aligned}
\sigma(\nu p \to \nu p) &= 0.153 \times \sigma(\nu n \to e^- p), \\
\sigma(\nu n \to \nu n) &= 1.5 \times \sigma(\nu p \to \nu p)
\end{aligned} \tag{5.48}$$

Figure 5.3 shows the cross-section of charged current quasi-elastic channels in NEUT, together with experimental results from ANL experiment [101], BNL experiment [102], Gargamelle experiment [103], and Serpukhov [104].

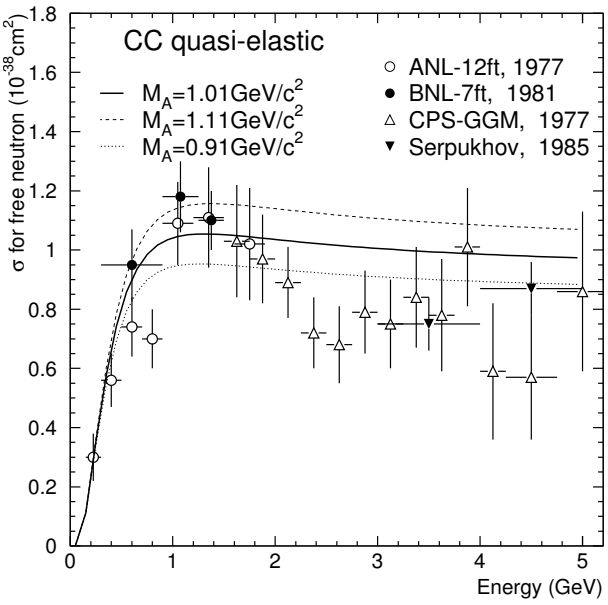

Figure 5.3: Cross section of charged current quasi-elastic channels in NEUT, together with experimental results from ANL experiment [101], BNL experiment [102], Gargamelle experiment [103], and Serpukhov [104].

5.7 Nuclear effects

The last sections described the neutrino scattering under the assumption that nucleons behaves as free particles. But, nucleons are bound to the nuclei having two important effects: Fermi Motion and Pauli Blocking. Moreover nuclear effects can also affect nucleons and other particles produced inside the nucleus by Absorption and Rescattering processes.

5.7.1 Fermi Gas Model and Pauli Blocking

The model pictures the nucleus as a zero temperature gas of neutron and another one of protons. In momentum space, this means that the gas makes a uniform density sphere of radius k_F; where the wave number is related to the momentum by the De Broglie relationship, $p = \hbar k$. For nuclei with unequal number of neutrons and protons, there are separated radii for neutrons (k_F^n) and

protons (k_F^p). Referring to a single radius for a given element gives:

$$(k_F)^3 = \frac{(k_F^p) + (k_F^n)^3}{2}$$

The volumes are normalized such that $N = 4\pi(k_F^n)^3/3$, $Z = 4\pi(k_F^p)^3/3$, and $A = N + Z = 2 * 4\pi(k_F)^3/3$. For an interaction to be allowed, the nucleon involved must receive enough momentum to position itself outside the relevant Fermi sphere. This condition is called Pauli Blocking.

For a given neutrino interaction, such as single pion interaction or quasi-elastic interaction, the fraction of available nucleons (S) for the interaction depends on the magnitude of the 3-momentum transfer (q) and the number of nucleons in the overlap region (D). Taking as example the neutrino quasi-elastic interaction; the fraction of the neutron's sphere outside of the proton sphere's is the fraction of neutrons available for the interaction. Initially, the proton and neutrons populate two concentric spheres. The factor S is the suppression factor that counts about the Pauli Blocking effect.

$$S(q) = 1 - \frac{D}{N}$$

There are three regions of momentum transfer. For very small momentum transfers, the neutron sphere is not moved enough such the entire proton sphere lies within it. In this region, the overlap volume is just the volume of protons ($D = Z$). For very large momentum transfer the two spheres are disjoint and there is no suppression ($D = 0$). Finally, there is an intermediate region where the fraction of neutrons available for the interaction must be calculated. In this calculus the Fermi momentum (k_F), maximum momentum value of the nucleons inside the nucleus, appears explicitly [1]. This value is 221 MeV/c^2 for Carbon atom ([106]). This effect is seen in the cross section as shown in Figure 5.4.

Hence, the Pauli Blocking effect, is extremely related to that of the Fermi momentum. The behavior of the cross section changes due to this effect; but it is not the only magnitude that can be affected. The Fermi motion effect is also the responsible of changing the final state of the nucleon momentum and the breaking of the planarity in the scattering process, if nucleons were at rest the interactions would lay in a plane conserving the angular momentum, but the three-momentum of target nucleons might have components perpendicular to the reaction plane, breaking the planarity of the reaction. In the particular case of the quasi-elastic scattering process, this results in a indetermination of the escaping direction of the proton and make wider the angle

[1] The explanation of the model in this way was taken from [105].

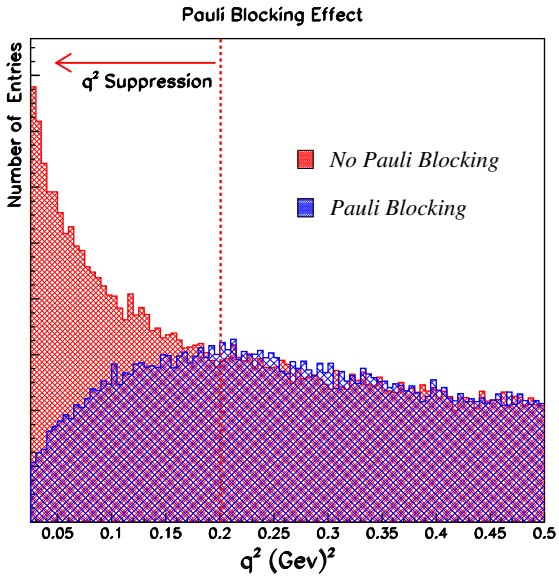

Figure 5.4: Effect of the Pauli Blocking in the cross section as a function of the $Q^2 = -q^2$

between the expected proton direction (without considering Fermi motion) and the measured proton direction. This angle is refereed as: $\Delta\theta_p$. As the momentum of the nucleon increases, the momentum transference also increase and the nucleon loose the memory of the initial collision deviating its trajectory from the expected one (Figure 5.5)

In the neutrino interaction simulation in K2K experiment [56], the momentum distribution of the target nucleon is assumed to be flat up to a fixed Fermi surface momentum of 225 MeV/c for carbon and oxygen and 250 MeV/c for iron. The same Fermi distribution is also used for all the nuclear interactions. The nuclear potential is set to 27 MeV for carbon and oxygen and 32 MeV for iron.

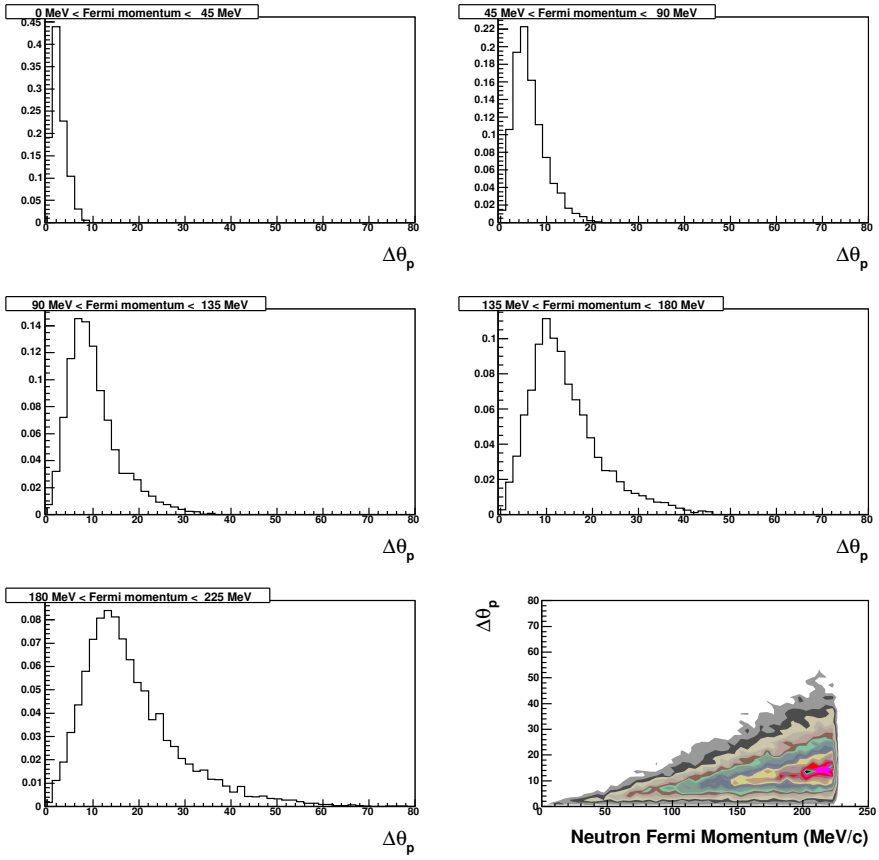

Figure 5.5: Effect of the Fermi motion in the $\Delta\theta_p$ distribution.

5.7.2 Absorption and Rescattering Processes

The intra-nuclear interaction of the mesons and nucleons produced in neutrino interactions are also important nuclear effects to be considered. Any absorption or change of kinematics of these particles can affect the event type classification to be performed in the analysis.

Among all the interactions, the interactions of pions are very important since both the interaction cross sections and also the cross section of pion production for neutrino energy above 1 GeV are large. The following pion interactions in the nucleus can occur: absorption, scattering and charge exchange.

Pion absorption interactions are those ones in which no pion is left in the final state. Elastic scattering meaning that the nucleus is left in the ground state; inelastic scattering, meaning the nucleus is left in an excited state and/or one or more nucleons are knocked out of the nucleus. Charge exchange, meaning the final state pion charge differs from the initial pion charge. A systematic studied of pion absorption and inclusive scattering reactions can be found in [107].

The re-interactions of the recoil protons and neutrons produced in the neutrino interactions are also important, because the protons tracks are used to select quasi-elastic like events. Nucleon-nucleon interactions modify the outgoing nucleon's momentum and direction, which also affects whether the nucleon will be above detection threshold ([108]). Details on the effects of proton rescattering in the SciFi detector can be found in [109].

In the neutrino interaction simulation in K2K experiment these intra-nuclear interactions of mesons and nucleons in carbon, oxygen or iron nuclei are considered. These interactions are treated using a cascade model, and each of the particles is traced until it escapes from the nucleus [68].

Chapter 6

Data and Event Selection

The data treatment and event selection for the analysis are described along this Chapter. First of all we describe how the charged current (CC) interactions are selected: a muon track identification is performed. Second, we look for other reconstructed tracks in the event that follow several requirements. Finally, we perform several event selections among the data selected sample.

6.1 Muon track reconstruction

CC events are selected asking for a muon track. We identify the muon track by requiring that a reconstructed track starting in SciBar matches with a track or hits in MRD as shown in Figure 6.1. The upstream edge of the muon track will be defined as the vertex interaction point. The muon track has to be contained in the defined fiducial volume and in coincidence with the time beam.

6.1.1 Muon track selection

The SciBar track which matches with the MRD track is defined as the SciBar-MRD 3D track. The matched MRD track is required to start from the first plane in MRD and to stop inside MRD. The SciBar track which matches with hits at the MRD first layer is defined as SciBar-MRD 1L track excluding MRD 3D tracks.

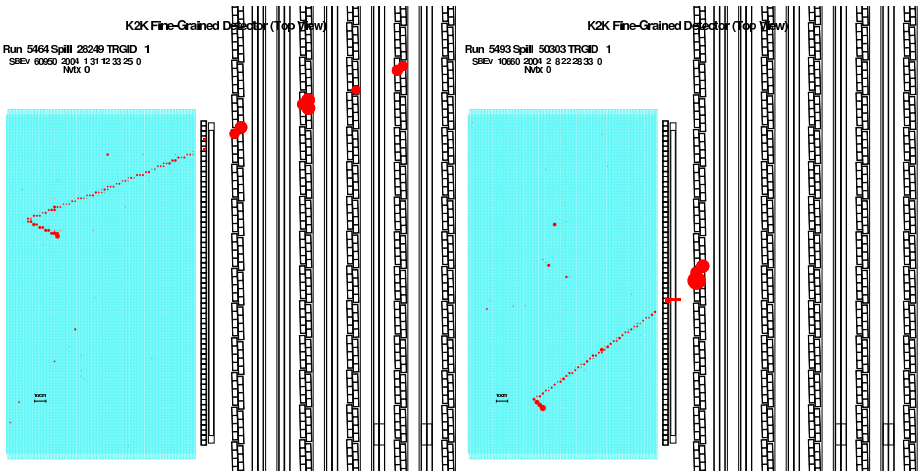

Figure 6.1: Event display of SciBar with a track matched to a MRD track (left) and to MRD hits (right).

The matching condition is that the residual distance between the extrapolation of the SciBar track and the starting point of the MRD track or first layer hits is less than 20 cm, and the angle between them is less than 0.5 radian for both X and Y projections. The candidates to be a muon track must leave the SciBar detector in any of the three directions. If more than one SciBar-MRD 3D track or SciBar-MRD 1L is found, the most energetic one is selected as the muon track.

The fiducial volume defined to select events in SciBar is a 260 cm $\times$ 260 cm $\times$ 135.2 cm volume, which corresponds to be -130 cm $<$ x $<$ 130 cm, -140 cm $<$ y $<$ 150 cm, 199.2 cm $<$ z $<$ 334.4 cm (from the 2^{nd} layer through the 53^{rd} layer) and 9.38 tons weight from a total mass of 15 tons. The reconstructed tracks are required to have the vertex track inside this volume. Figure 6.2 shows the vertex distribution in the three spatial directions for all the SciBar-MRD events (CC events) together with the MC expectation and the definition of the fiducial volume.

Figure 6.3 shows the beam timing distribution of all events with at least one reconstructed track inside SciBar, and for all the events with a SciBar-MRD track. The non neutrino-induced events of sky-shine slow neutrons, which increase with time, are seen under the beam timing structure. Those background events are removed by applying the SciBar-MRD muon track selection and they are negligible after the selection.

We define the upstream edge of the muon track as the interaction vertex as shown in Figure 6.4. Figure 6.5 shows the vertex resolution estimated with the MC simulation. For the x and y directions, the resolution is 0.8 cm and 0.8 cm, respectively, and for z, the resolution is 1.6 cm. The second peak in the z direction is caused by the cross talk effect.

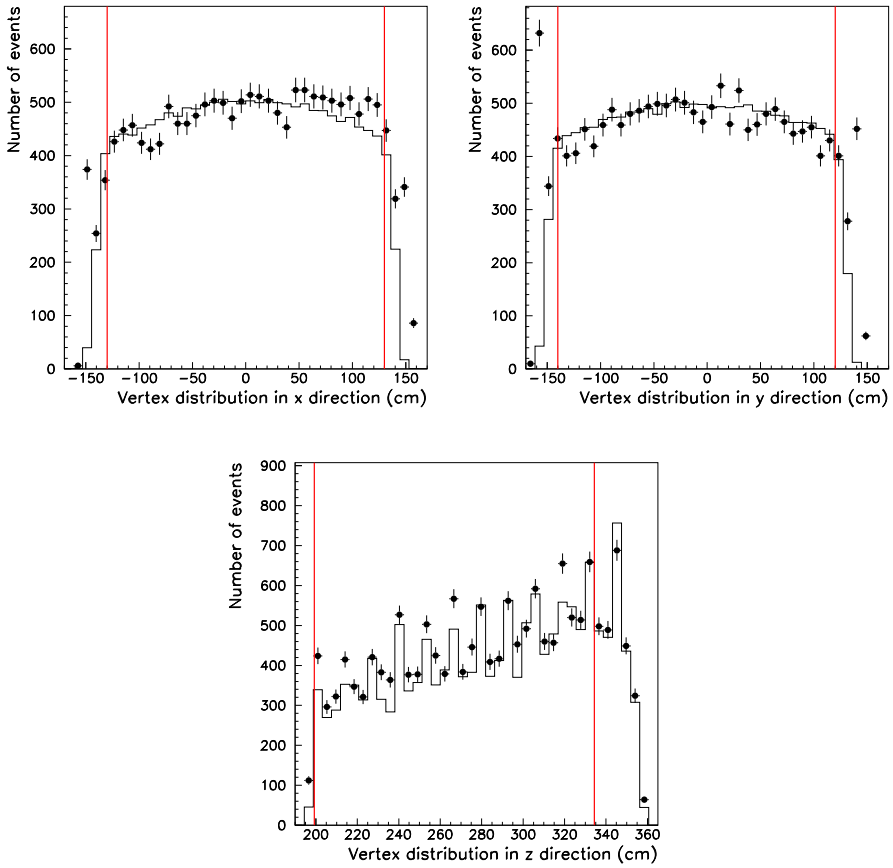

Figure 6.2: The vertex distribution of SciBar-MRD matching events in the x (top left), y (top right) and z (bottom) directions. Black points are data and open histogram MC expectation. The fiducial volume is delimited by the red lines.

The background in the muon track sample is caused when other particles leave signal in the MRD detector and the matching is wrongly considered. The selection efficiency average is 51% (41% for those SciBar-MRD 3D and 10% for the SciBar-MRD 1L) and the selection purity 96% (98% for those SciBar-MRD 3D and 89% for the SciBar-MRD 1L). The muon detection efficiency as a function of the true muon energy, and as a function of the true muon angle are shown in Figure 6.6. The efficiency increases with the muon energy and decreases with the muon angle.

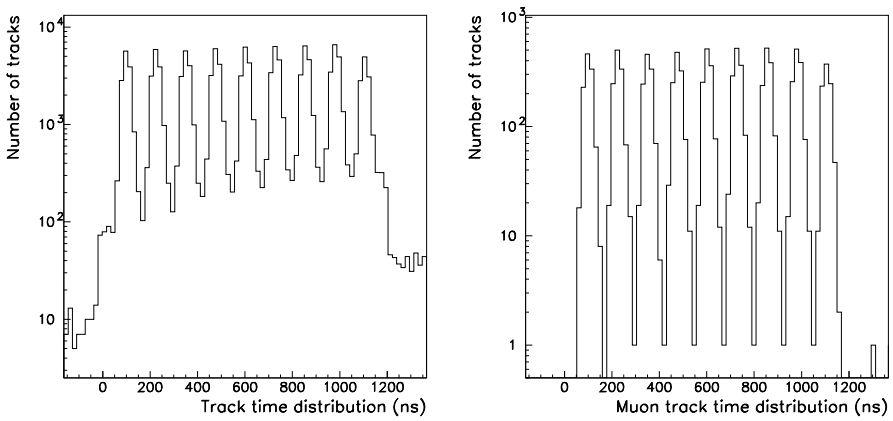

Figure 6.3: Beam timing distribution for all the SciBar events (left) and for the CC events (right). The non neutrino-induced events of sky-shine slow neutrons, which increase with time, are seen under the beam timing structure. Those background events are removed by applying the SciBar-MRD muon track selection.

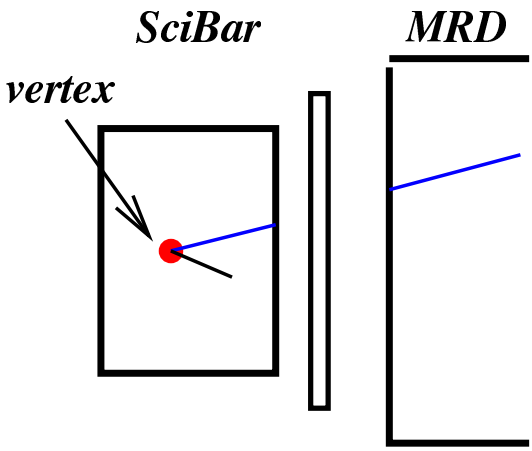

Figure 6.4: Definition of the upstream edge of the MRD matched track as the interaction vertex. The blue line represents the muon track.

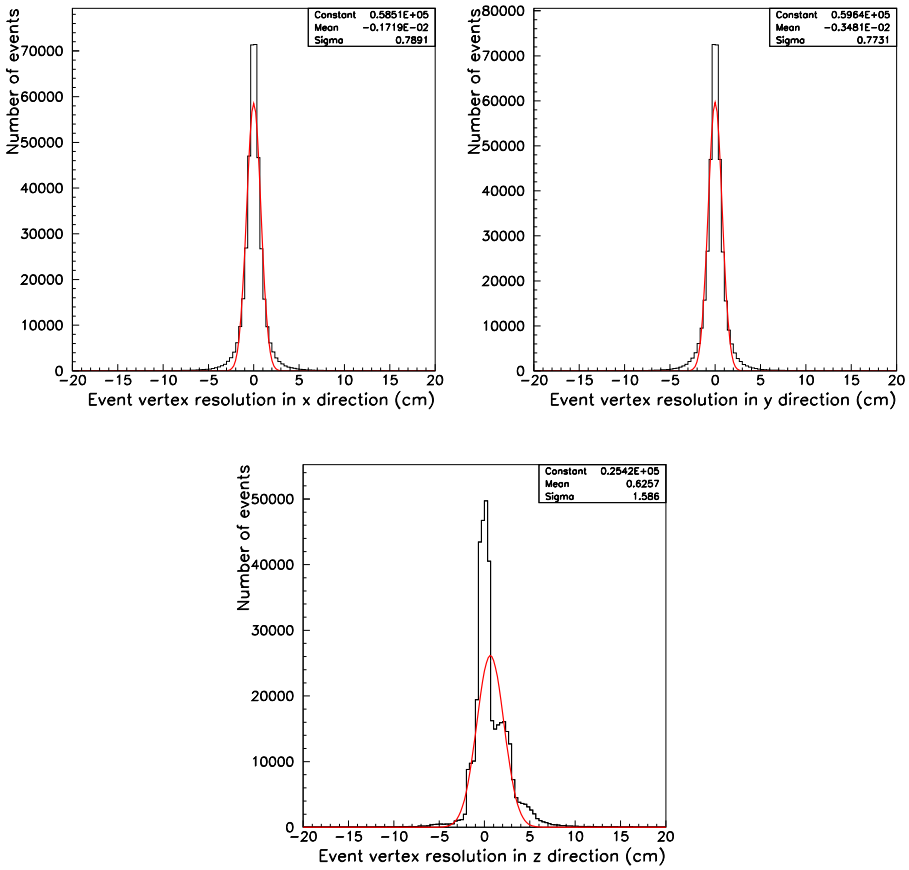

Figure 6.5: Vertex resolution (true - reconstructed) estimated from MC simulation in the x (top left), y (top right) and z (bottom) directions. The second peak in the z direction is caused by the cross talk effect.

6.1.2 Muon energy reconstruction

The energy of the selected muon is reconstructed by using the partial track length, range, through SciBar, EC, and MRD as

$$E_\mu = E_\mu^{\mathrm{SciBar}} + E_\mu^{\mathrm{EC}} + E_\mu^{\mathrm{MRD}} \tag{6.1}$$

$$E_\mu^X = \left(\frac{dE}{dx}\right)^{\mathrm{X}} \cdot L^{\mathrm{X}}, \qquad \mathrm{X} = \mathrm{SciBar,\ EC,\ MRD} \tag{6.2}$$

where E_μ^{X}, L_μ^{X} and $(dE/dx)^{\mathrm{X}}$ are the energy deposited, the track length and the energy deposited per unit length in each detector. The track length inside the EC is calculated by using the SciBar

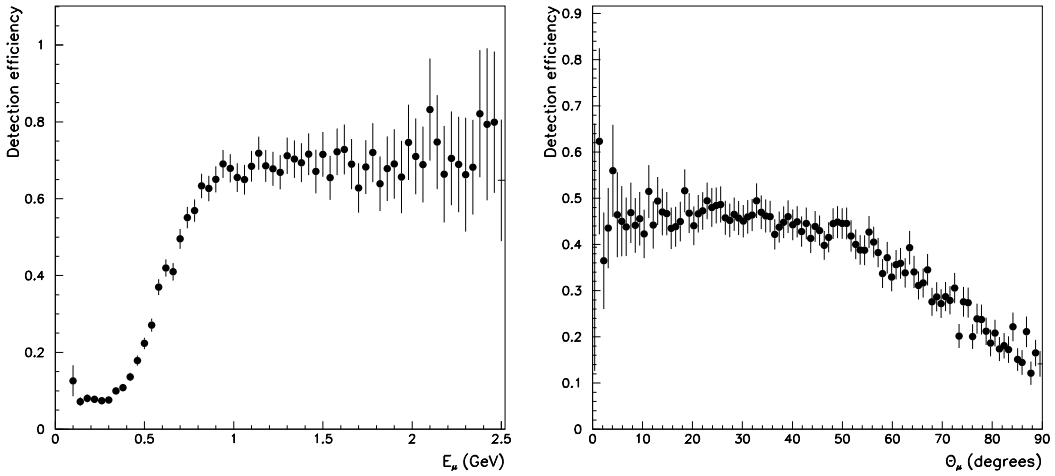

Figure 6.6: Muon detection efficiency as a function of the true muon energy (left), and as a function of the true muon angle (right). The efficiency increases with the muon energy and decreases with the muon angle.

track. The dE/dx value for SciBar is taken 2.10 MeV/cm and for EC, 11.25 MeV/cm. E_{μ}^{MRD} is calculated from the range-to-energy look-up table based on GEANT MC code [77]; where the muon mass is considered.

The muon momentum is corrected by a multiplicative factor of 0.98 in the data based on a fit of SciBar data; its systematic uncertainty is estimated to be 2.7% [56], dominated by uncertainties of muon energy reconstruction in the MRD. The muon momentum resolution is 80 MeV/c [56]. The muon energy is recalculated once the muon momentum scale factor is applied. Figure 6.7 shows the muon track energy and the energy resolution. The energy resolution is evaluated to be 100 MeV.

6.1.3 Muon angle

Figure 6.8 shows the distribution of the muon angle with respect to the beam direction of all the CC events and the angular resolution. The resolution of the 3D angle is evaluated to be 1 degree.

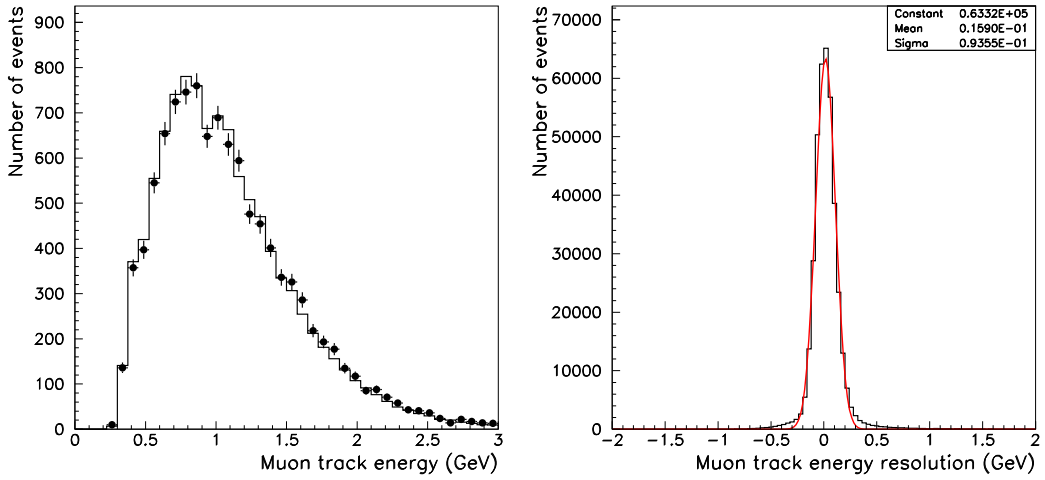

Figure 6.7: Energy (left) and energy resolution (right) of the muon reconstructed track in SciBar.

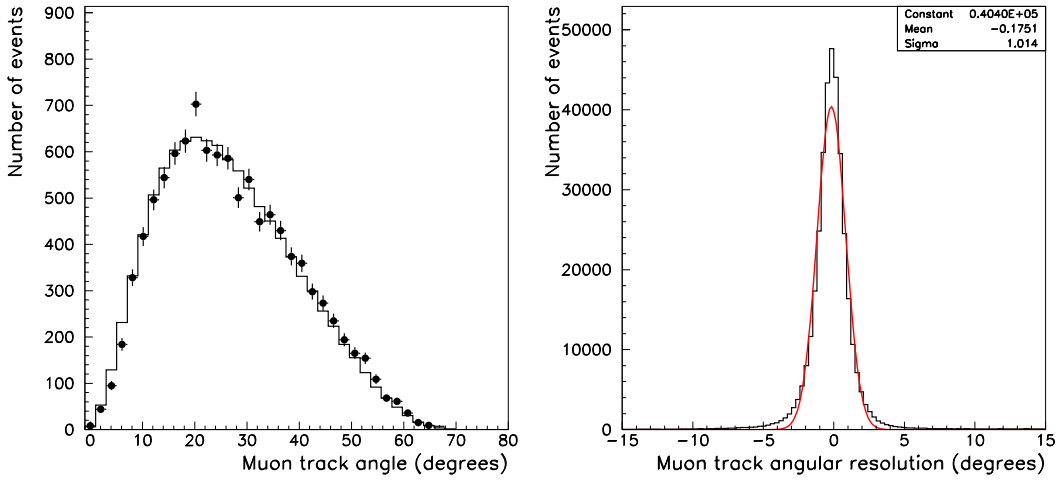

Figure 6.8: Angle (left) respect to the beam direction and angular resolution (right) of the muon reconstructed track in SciBar.

6.2 Track counting

Once the muon track and the interaction vertex are reconstructed, we search for other extra tracks. We want these tracks coming from the event interaction vertex, inside the same fiducial volume as the muon track, and in a time window of 100 ns with it. This cut in time is equal to the time width of a bunch.

To count the number of tracks at the event interaction vertex, we search for tracks in the fiducial volume that have an endpoint inside a 4.8 cm radius sphere with the reconstructed event interaction vertex as its center, and that are in coincidence with the SciBar-MRD track within 100 ns. The distance distribution to the reconstructed event interaction vertex is showed in Figure 6.9. The 4.8 cm cut corresponds to 3σ in the z direction (and more than 5σ in the x and y dimensions) for the event vertex resolution in Figure 6.5.

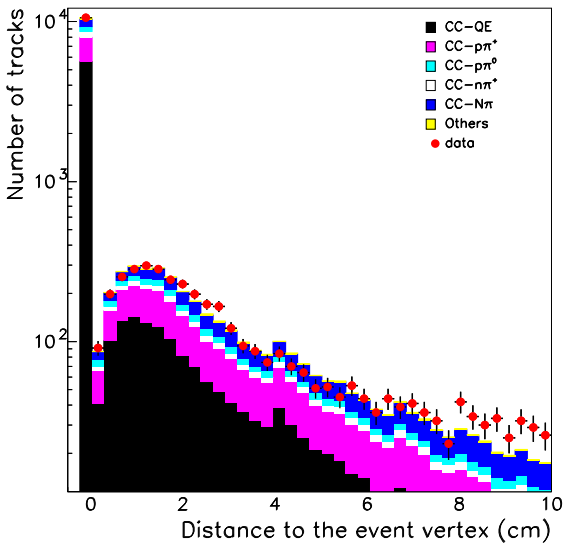

Figure 6.9: Distance between the reconstructed event interaction vertex and the initial or final point of the other tracks in fiducial volume and on time with muon tracks. The distribution is shown in log scale. The breakdown of the MC by interaction type is shown in the plot. Black color shows charged-current quasi-elastic interactions; pink, cyan, and white colors are taken for the three charged-current single pion interaction channels, $p\pi^+$, $p\pi^0$ and $n\pi^+$ in the final state, respectively; blue color represents the charged-current multi-pion and deep inelastic (DIS) interactions; others (including neutral currents) is set in yellow. Red points are data. χ^2 = 59.64, ndof = 39.

Figure 6.10 shows the distribution of the number of tracks in the fiducial volume, in a time window with the muon track and coming from the reconstructed event interaction vertex defined for the upstream edge of the muon track. Events with one track are muon single track events.

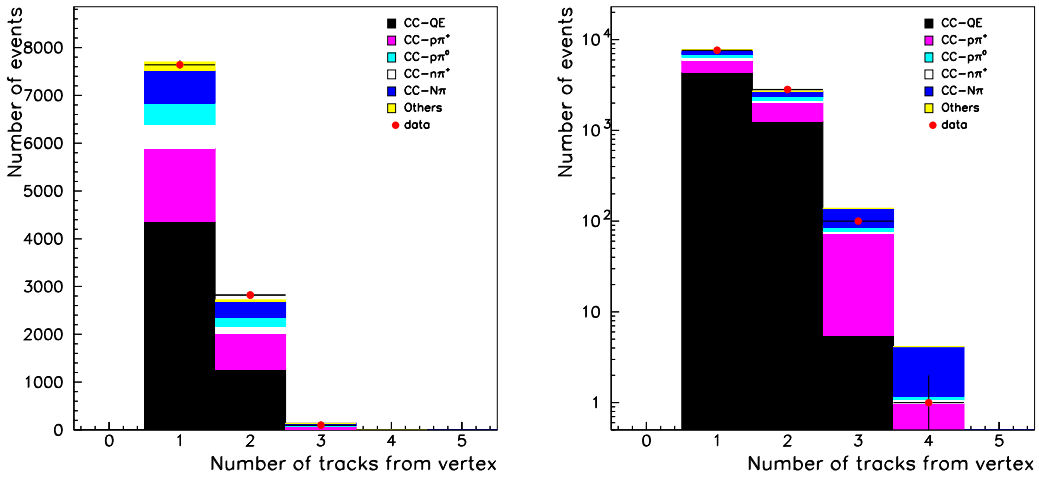

Figure 6.10: Distribution of the number of tracks in the fiducial volume, time window and from the interaction vertex. Linear scale (left), log scale (right). $\chi^2 = 27.45$, ndof = 4.

Table 6.1 shows the number of events for different number of tracks in data. The number of events for different number of tracks in MC is also presented; before and after the normalization to the number of events in data. MC statistics is approximately 40 times larger than data statistics. For the plots where data and MC are shown, we normalize the MC to 10561, the total number of events in data in the CC sample, unless other normalization is specified; the breakdown of the MC is also done as in Figure 6.9 unless other is given. The multiplicity of these events goes up to four tracks per event. Data and MC number of events for the different track samples are compatible within the values given in Table 6.2. Further discussion is found in the systematic error calculation in Chapter 8, where also the χ^2 values of the above presented distributions are considered after the systematic study.

In Table 6.3 we show the percentage of the different interactions channels according to the MC prediction for the different samples considered also in the plots.

Sample	data	MC	MC norm
CC sample	10561±103	389847±624	10561±17
1 track sample	7638±87	284163±533	7698±14
2 tracks sample	2822±53	100431±317	2721±8.6
3 tracks sample	100±10	5102±71	138±1.9
4+ tracks sample	1±1	151±12	4±0.3

Table 6.1: Number of events for different track samples in data and in MC before and after normalization.

Sample	data-MC compatible within
CC	$1.0\sigma_{data}$
1 track	$1.0\sigma_{data}$
2 tracks	$1.9\sigma_{data}$
3 tracks	$3.8\sigma_{data}$
4+ tracks	$3.0\sigma_{data}$

Table 6.2: Data and MC compatibility for different track samples within only statistical error.

Sample	CCQE (%)	CC$p\pi^+$ (%)	CC$n\pi^+$ (%)	CC$p\pi^0$ (%)	CC$N\pi$ (%)	Other (%)
CC	52	22	6.0	6.0	9.0	5.0
1 track	56	20	6.5	6.0	9.0	2.5
2 tracks	46	28	5.5	7.0	12.5	1.0
3 tracks	4	49	3.3	6.5	36.0	1.2

Table 6.3: Breakdown of MC track samples by interaction type.

6.3 Event selection and classification

We search for CC$\mu p\pi^+$, CC$\mu n\pi^+$, and CCQE interactions in this analysis. We perform three event selections: a single $p\pi^+$ selection, a single $1\pi^+$ selection (the interaction channels of CC$p\pi^+$ and CC$n\pi^+$ are labeled together as CC$1\pi^+$), and a CCQE selection. We want to measure the cross section of the exclusive single pion channel ($p\pi^+$) and the cross section of the inclusive single pion channel ($1\pi^+$); but we can not provide an absolute measurement due to the uncertainties in the neutrino flux. Therefore, we normalize the previous cross sections

to the cross section of the CCQE interaction channel: using the ratio allow us to neglect the uncertainties in the neutrino flux.

6.3.1 Exclusive and inclusive single pion selection

In the case of the exclusive single pion selection we are interested on selecting events with one or two reconstructed tracks besides the muon track, being these tracks the proton, the pion or both tracks. In the case of the inclusive single pion selection, it considers the CCpπ^+ and the CCnπ^+ channels, we could search for the events with one reconstructed track besides the muon track, being this track the pion track, which is the common particle in the final state. However, we will accept the second track being a proton track or a pion track. The reason for that is that we want to measure the cross section ratio of the single pion over CCQE interactions and not the production of π^+ itself. For the exclusive case we perform a selection in the two and three track samples; for the inclusive case, in the two track sample.

6.3.1.1 Exclusive and inclusive single pion selection in the two track sample

To reject the background in the two track sample, we apply a non-CCQE cut. For two track events in the CC sample, the kinematics of the second track can be calculated from the lepton variables, momentum, p_μ, and angle, θ_μ, assuming a CCQE interaction. This second track can be a visible proton or pion. In order to select the real proton the second track is asked to follow the CCQE expected kinematics.

We computed the opening angle, $\Delta\theta_p$, between the expected track (assuming CCQE) and the observed track which is measured (see Figure 6.11).

Thus, this angle is obtained as follows,

$$\Delta\theta_p = \text{acos}\frac{\overrightarrow{p}_{expected}\,\overrightarrow{p}_{observed}}{\mid \overrightarrow{p}_{expected} \mid\mid \overrightarrow{p}_{observed} \mid} \tag{6.3}$$

where

$$\overrightarrow{p}_{expected} = (-p_{\mu,x}, -p_{\mu,y}, E_\nu^{rec} - p_\mu cos\theta_\mu), \tag{6.4}$$

and E_ν^{rec} is the reconstructed neutrino energy taken from Equation 3.2. The $\overrightarrow{p}_{observed}$ is constructed with the directions of the second track measured in the detector. Detailed discussion about this calculation and other SciBar calculations can be found in Appendix B.

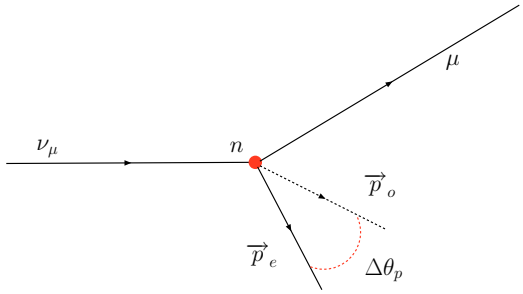

Figure 6.11: Opening angle, $\Delta\theta_p$, between the expected track (assuming CCQE) and the observed track which is measured. The momentum of the expected track is designed by $\overrightarrow{p}_e$, and the one for the observed track by $\overrightarrow{p}_o$.

Figure 6.12 shows the $\Delta\theta_p$ distribution. We want to cut in this distribution where the purity square times efficiency of selecting single $1\pi^+$ events is maximal. We want to increase the purity at a cost of losing some efficiency. Figure 6.13 shows the distribution of the purity square times efficiency. Events with $\Delta\theta_p$ equal or greater than 20 degrees are selected as single $1\pi^+$ where the second track can be the visible proton or the visible pion. We obtain the same cut to maximize purity square times efficiency of selecting single $p\pi^+$ events, it is also expected since the inclusive channel is highly dominated by the exclusive one.

Then, we quote the purity and the efficiency of selecting the signal we search for. The purity will be defined as the percentage of events selected as signal relative to the total number of events in the selected sample; and the efficiency as the percentage of events selected as signal relative to the total in the initial sample of that signal. The initial sample is defined for the events with the true vertex inside the fiducial volume. The single $p\pi^+$ purity in the selected sample is 40%, and the efficiency 12%. The purity increases 12% from the initial purity in the two track sample (see Table 6.3). The CC$n\pi^+$ interaction is a background for the exclusive signal. The single $1\pi^+$ (CC$p\pi^+$ and CC$n\pi^+$ are both signals) purity in the selected sample is 49%, and the efficiency 11% . The purity increases around 15% from the initial purity in the two track sample (see Table 6.3). Table 6.4 shows the purity and the efficiency for the exclusive signal and the background in this selection. Table 6.5 shows the purity and the efficiency for the inclusive signal and the background in this selection[1]. The number of selected events in data is 1566.

[1]The error in the purity of the signal (single pion or CCQE) is smaller than 1%, while the error in the efficiency of the signal is smaller than 0.1%. The error in the purity of the background is smaller than 1% and the error in the efficiency is smaller than 0.5%. These range of errors is valid also for following tables of purities and efficiencies.

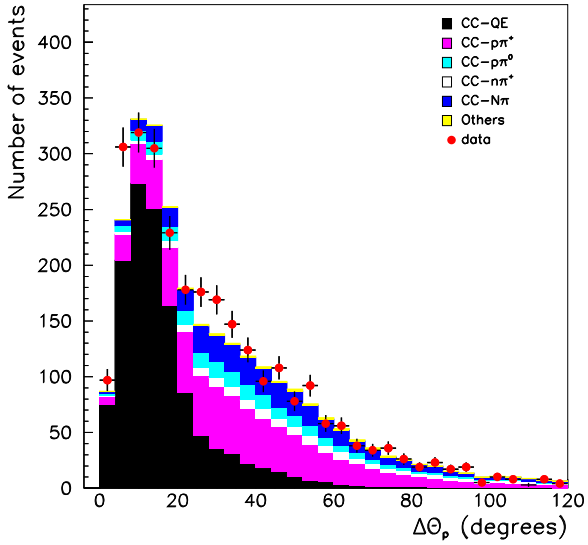

Figure 6.12: Distribution of the angle, $\Delta\theta_p$, between the expected track (assuming CCQE) and the observed track. $\chi^2 = 62.74$, ndof = 30.

CC$p\pi^+$ selection	purity (%)	efficiency (%)
CC$p\pi^+$	40.0	12.0
CCQE	19.5	3.2
CC$n\pi^+$	8.9	8.4
CC$p\pi^0$	9.8	10.0
CC$N\pi$	20.5	10.2
Others	1.7	0.6

Table 6.4: Purity and efficiency in the two track CC$p\pi^+$ selection based on the nominal MC. The purity is refered to the selected sample and the efficiency to the initial sample.

6.3.1.2 Single pπ^+ selection in the three track sample

For the three track sample we want to have the muon track plus a track selected as proton track and the other as pion track. In order to do that we need a particle identification method. Figure 6.14 shows the dE/dx distribution of the muon track and the second track of the QE sample. The proton track is clearly separated from the muon track. As shown in Figure 6.15, the MC

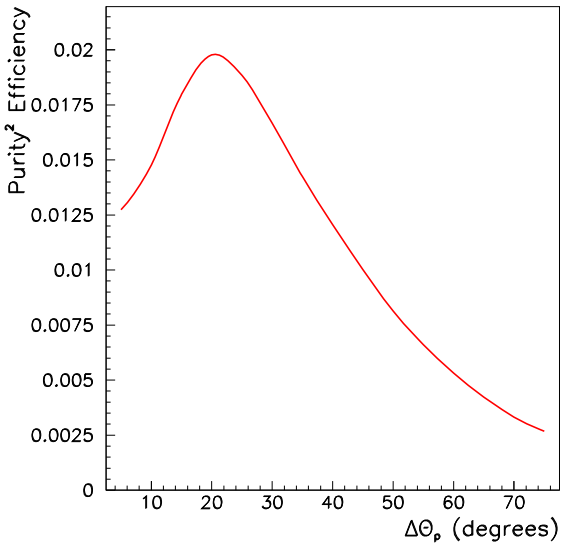

Figure 6.13: Purity square times efficiency of selecting CC1π^+ events in the two track sample as a function of the $\Delta\theta_p$ angle.

CC1π^+ selection	purity (%)	efficiency (%)
CC1π^+	48.9	11.0
CCQE	19.5	3.2
CCpπ^0	9.8	10.0
CCNπ	20.5	10.2
Others	1.7	0.6

Table 6.5: Purity and efficiency in the two track CC1π^+ selection based on the nominal MC. The purity is refered to the selected sample and the efficiency to the initial sample.

simulation reproduces well the observed dE/dx distribution of the muon track and the proton track. The separation of the proton from the pion is performed using the dE/dx information; the pion dE/dx is expected to be very close to the muon dE/dx [110]. A confidence level distribution based on the muon track dE/dx per plane was considered. It is explain in detail in [111].

Figure 6.16 shows the muon confidence level (MuCL) in the three track sample for those tracks besides the muon track. A MuCL value of 1 indicates a muon or pion, and a MuCL value of

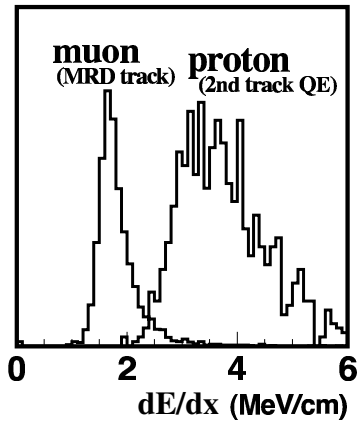

Figure 6.14: dE/dx distribution of the muon and proton track.

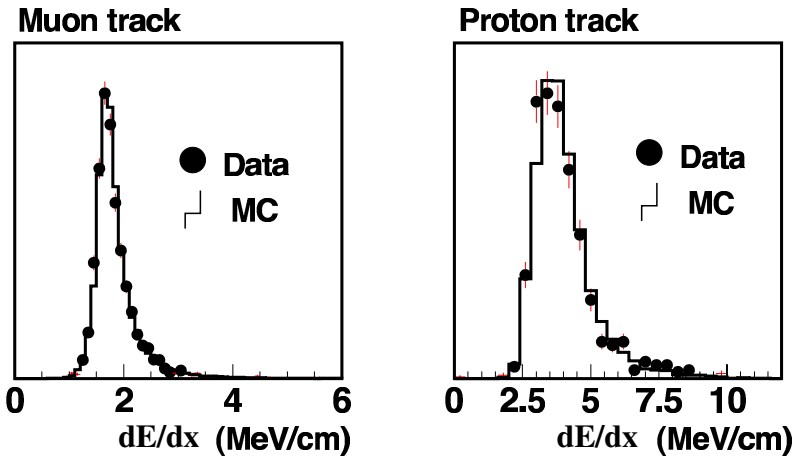

Figure 6.15: Comparison between the dE/dx distribution of the muon (left) and proton (right) track in MC and in data.

0 indicates a proton. The track with MuCL greater than 0.04 is categorized as pion-like, and it should be the pion track, while the track with MuCL less than 0.04 is categorized as proton-like. The cut corresponds to the maximal purity square times efficiency of selecting single $p\pi^+$ events. The purity square times efficiency distribution is showed in Figure 6.17. Hence, we ask for a pion-like and a proton-like track in the three track sample. The purity of having a proton in the proton-like sample is 87%, and the purity of having a pion in the pion-like sample 49%.

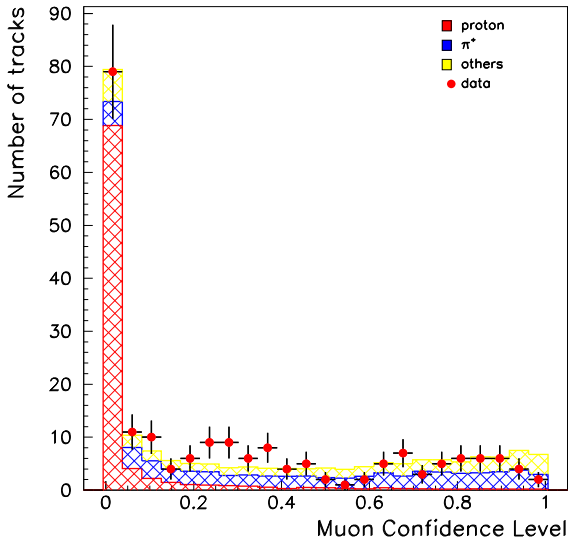

Figure 6.16: Muon confidence level (MuCL) in the three track sample. Red color are true protons, blue color are true pions, yellow colors are others particles. Red points are data. χ^2 = 39.9, ndof = 23.

The single pπ^+ purity in the selected sample is 58%, and the efficiency 1%. The purity increases 9% from the initial purity in the three track sample (see Table 6.3). Table 6.6 shows the purity and the efficiency for the signal and the background in this selection. The number of selected events in data is 53.

CCpπ^+ selection	purity (%)	efficiency (%)
CCpπ^+	58	1.0
CCQE	2	< 0.1
CCnπ^+	4	0.2
CCpπ^0	6	0.3
CCNπ	29	0.8
Others	1	< 0.1

Table 6.6: Purity and efficiency in the three track CCpπ^+ selection based on the nominal MC. The purity is refered to the selected sample and the efficiency to the initial sample.

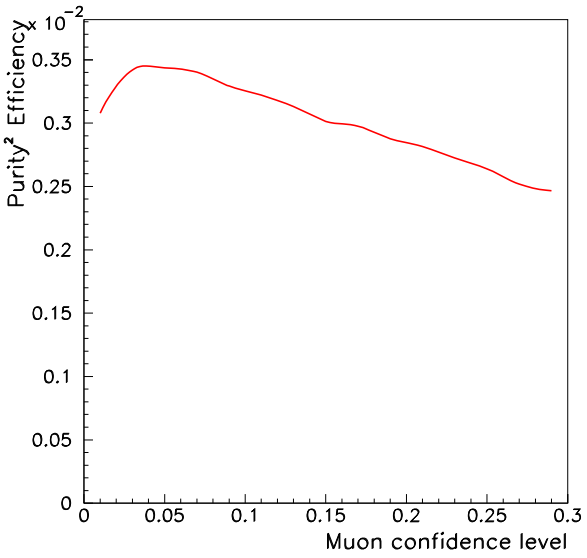

Figure 6.17: Purity square times efficiency of selecting CC$p\pi^+$ events in the three track sample as a function of muon confidence level value

We consider both the single $p\pi^+$ selection in the two track sample and in the three track sample to construct the exclusive single pion selection. The statistics from the three track sample is about 3% of the total number of events in the selection.

Table 6.7 shows the purity and the efficiency for the signal and the background in the $p\pi^+$ selection. The number of selected events in data is 1619.

CC$p\pi^+$ selection	purity (%)	efficiency (%)
CC$p\pi^+$	41.0	13.0
CCQE	18.6	3.2
CC$n\pi^+$	8.4	8.3
CC$p\pi^0$	9.6	10.0
CC$N\pi^+$	21.0	11.0
Others	1.7	0.3

Table 6.7: Purity and efficiency in the two and three track CC$p\pi^+$ selection based on the nominal MC. The purity is refered to the selected sample and the efficiency to the initial sample.

6.3.1.3 Proton-like and pion-like in the two track non-QE sample

The separation into proton-like and pion-like in the two track non-QE sample can be also performed, even though this separation was not used to select single pion events in the analysis. Figure 6.18 shows the MuCL for the second track in the two non-QE track sample. The purity square times efficiency of classifying true pions in the non-QE pion sample has the maximun at 0.04. The purity of having a proton below this cut is 93% and the purity of having a pion above this cut is 52%. The proton-like sample represents the 52% of the total two track non-QE sample and the pion-like represents the 48%.

This separation was not used in the analysis because we searched for (p,n)π^+ events, not only for pions. Moreover, 1) this selection does not improve the purity in any of the selections: in the proton-like sample the CCQE background is higher, as the multi-pion background in the pion-like sample; 2) selecting exclusive or inclusive single pion in one or other sample (proton-like or pion-like) reduces the statistics approximately a factor 2 of the total statistics considering both samples[2].

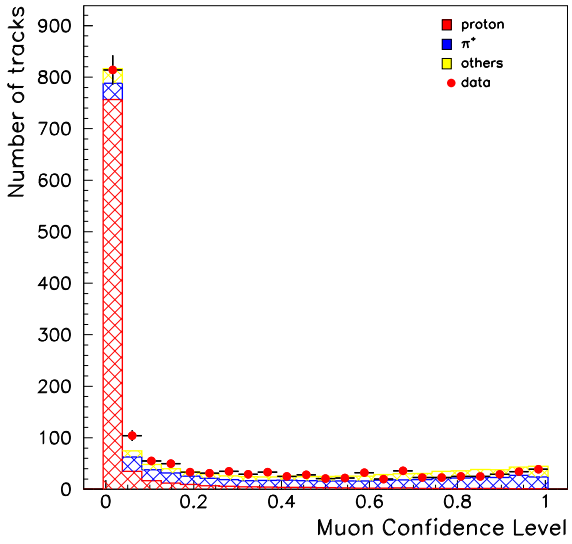

Figure 6.18: Muon confidence level (MuCL) in the two non-QE track sample. χ^2 = 49.7, ndof = 23.

[2]As a check the complete analysis was done considering the proton-like, and, separately, the pion-like subselections in the exclusive and inclusive single pion selections; the results obtained were very close to the ones presented in this work but with larger statistical error.

6.3.2 CCQE selection

In order to select CCQE interactions we consider the one track sample and the two track QE-like sample. The one track sample is composed by all the events with only one track. The CCQE interaction purity is 56% (as shown in Table 6.3) and the efficiency is 48%. The number of selected events in data is 7638.

For the two track sample, we used the anti-single pion selection, which is the QE-like selection, based on the opening angle $\Delta\theta_p$ (see Figure 6.12). The events with $\Delta\theta_p$ less than 20 degrees are considered QE-like. This cut is also the optimal cut to maximize purity times efficiency for selecting CCQE interactions. The CCQE purity in the selected sample is 78%, and the efficiency 12%. The purity increases 32% from the initial purity in the two track sample (see Table 6.3). The number of selected events in data is 1256. Table 6.8 shows the purity and the efficiency for the signal and the background in the CCQE one and two track selection.

CCQE selection	purity (%)	efficiency (%)
CCQE	60	60
CC$p\pi^+$	20	34
CC$n\pi^+$	5.5	33
CC$p\pi^0$	5.5	33
CCNπ	8	24
Others	2	4

Table 6.8: Purity and efficiency in the one and two track CCQE selection based on the nominal MC. The purity is refered to the selected sample and the efficiency to the initial sample.

6.4 Basic distributions

Following we show some basic variables for the three selections that have been performed. In Figures 6.19, 6.20, and 6.21 we show the distribution of the number of hits of the muon track and the number of hits of those vertex tracks in the event.

In Figures 6.22, 6.23, and 6.24 we show the muon momentum and angle distribution for each of the three considered samples. These variables are used to reconstructed the neutrino energy in the following Chapter.

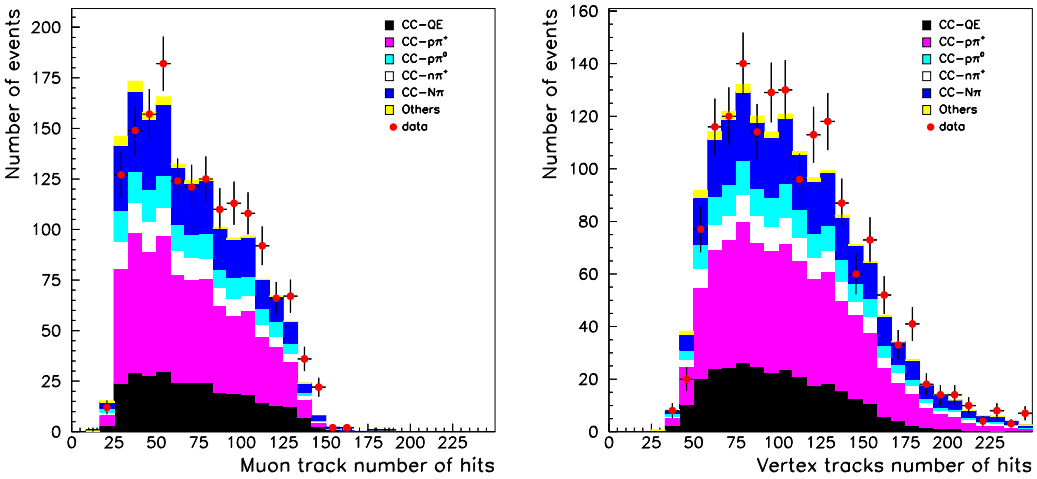

Figure 6.19: Distribution of the number of hits of the muon track (left) and vertex tracks (right) in the single $p\pi^+$ selection. $\chi^2 = 35.94$, ndof = 21 (left); $\chi^2 = 43.53$, ndof = 26 (right).

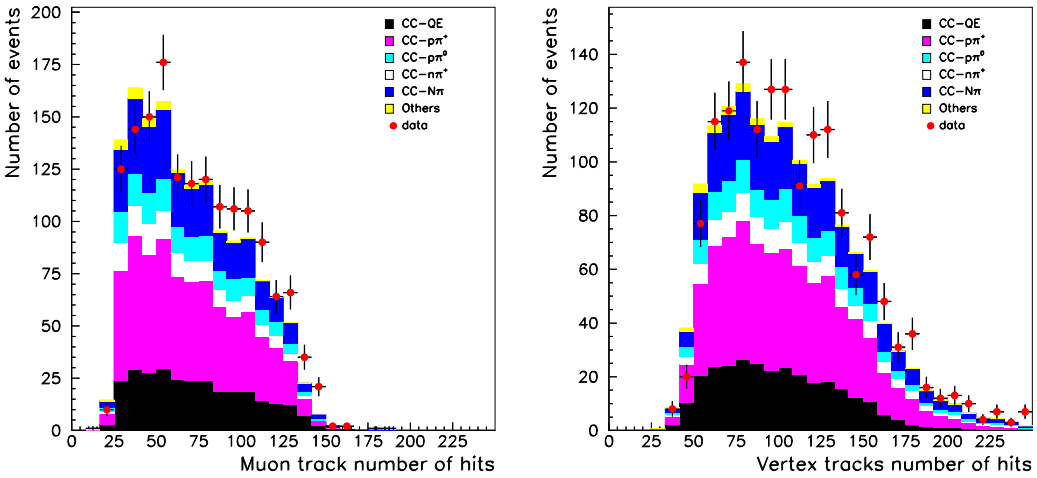

Figure 6.20: Distribution of the number of hits of the muon track (left) and vertex tracks (right) in the single $1\pi^+$ selection. $\chi^2 = 36.84$, ndof = 21 (left); $\chi^2 = 47.57$, ndof = 26 (right).

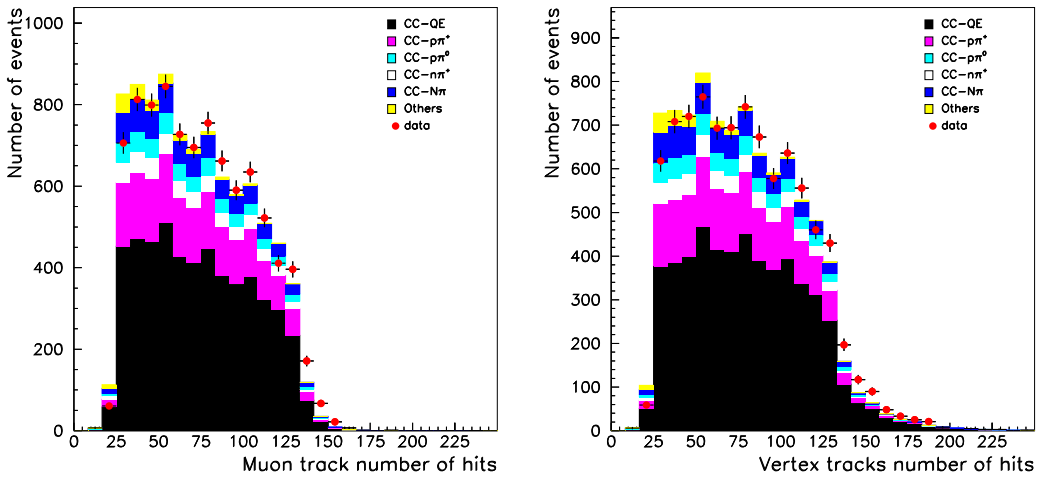

Figure 6.21: Distribution of the number of hits of the muon track (left) and vertex tracks (right) in the CCQE selection. χ^2 = 124.33, ndof = 21 (left); χ^2 = 109.04, ndof = 28 (right).

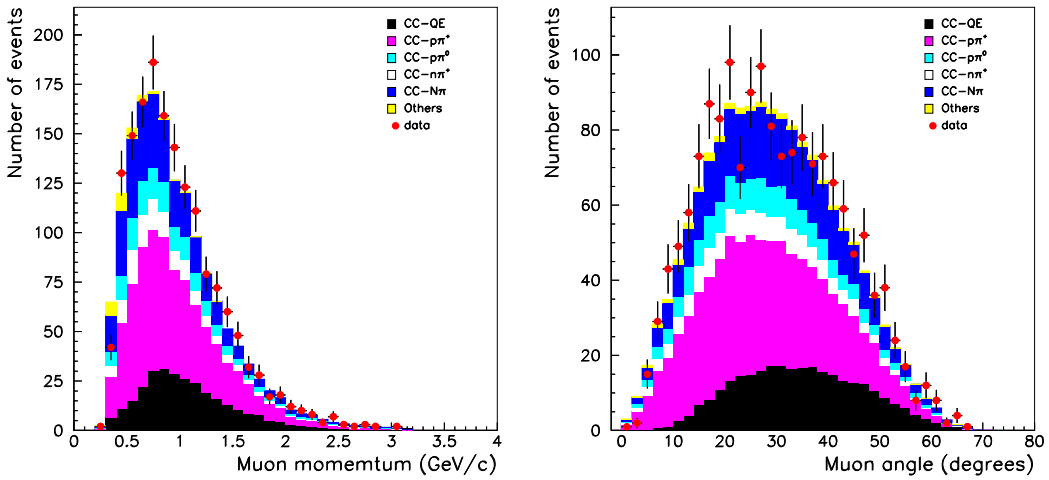

Figure 6.22: Muon momentum and angle distribution for single $p\pi^+$. χ^2 = 25.00, ndof = 29 (left); χ^2 = 56.18, ndof = 34 (right).

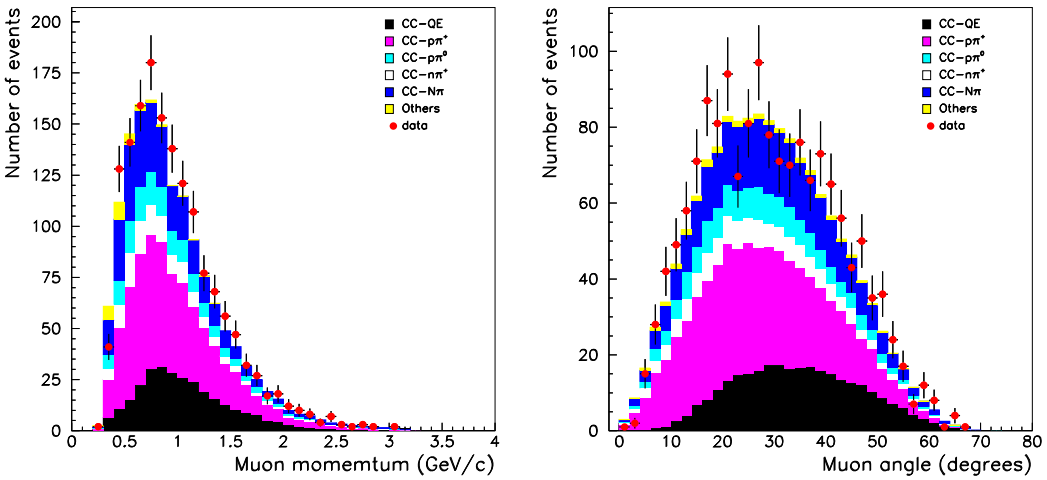

Figure 6.23: Muon momentum and angle distribution for single $1\pi^+$. χ^2 = 25.02, ndof = 29 (left); χ^2 = 57.07, ndof = 34 (right).

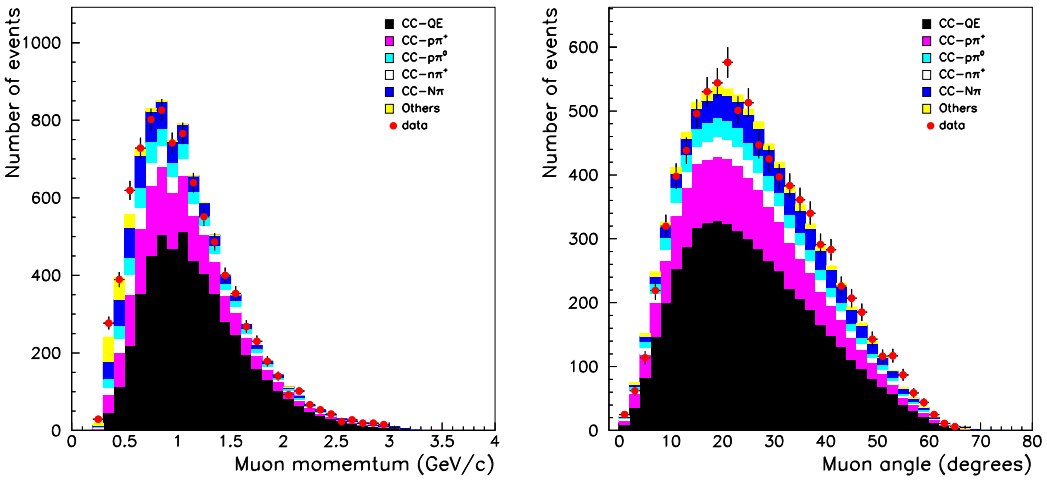

Figure 6.24: Muon momentum and angle distribution for CCQE. χ^2 = 34.60, ndof = 31 (left); χ^2 = 64.69, ndof = 34 (right).

6.5 Selection summary

Table 6.9 summarizes the purities, efficiencies and number of events for these selections.

selection	purity (%)	efficiency (%)	number of events
CCpπ^+	41	13	1619
CC1π^+	49	11	1566
CCQE	60	60	8894

Table 6.9: Purity, efficiency and number of selected events in the CCpπ^+ selection, CC1π^+ selection, and CCQE selection. The purity and the efficiency are based on the nominal MC. The purity is refered to the selected sample and the efficiency to the initial sample. The number of events is taken from data.

Figure 6.25 shows a two track event display for an event selected as single pion. Figure 6.26 shows a three track event display for an event selected as single pπ^+.

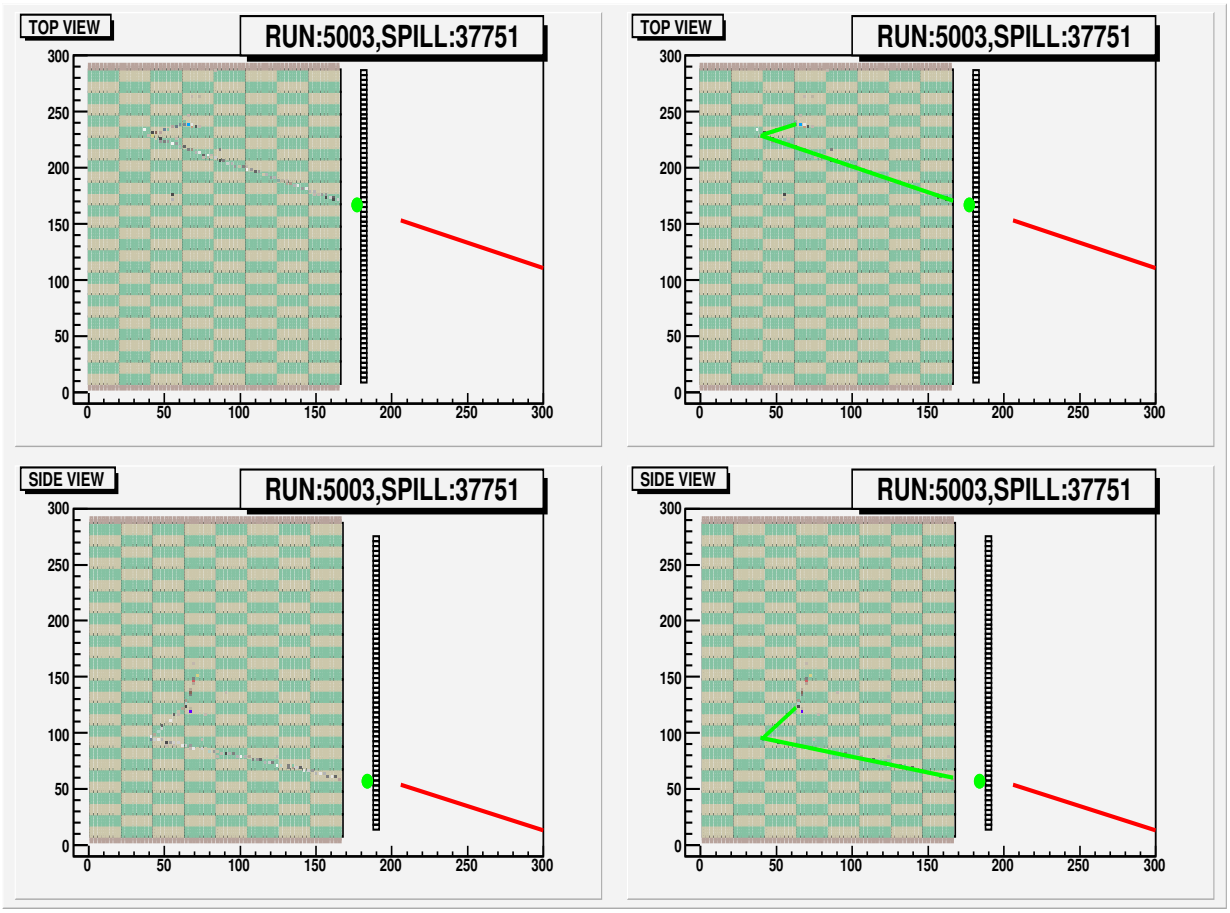

Figure 6.25: Event display of a two track selected single $p\pi^+$ and $1\pi^+$ event. The left part of the display shows the hits (color points) left in the detector after the neutrino interaction. The right part of it shows the 3D reconstructed tracks (green lines). The top part shows the top view; and the bottom part the side view of the SciBar detector. The green point indicates that some energy in deposited in the Electronic Calorimeter. The red line is the extrapolation of the track going to MRD. The track leaving the detector is the muon track. The other track is a pion-like track.

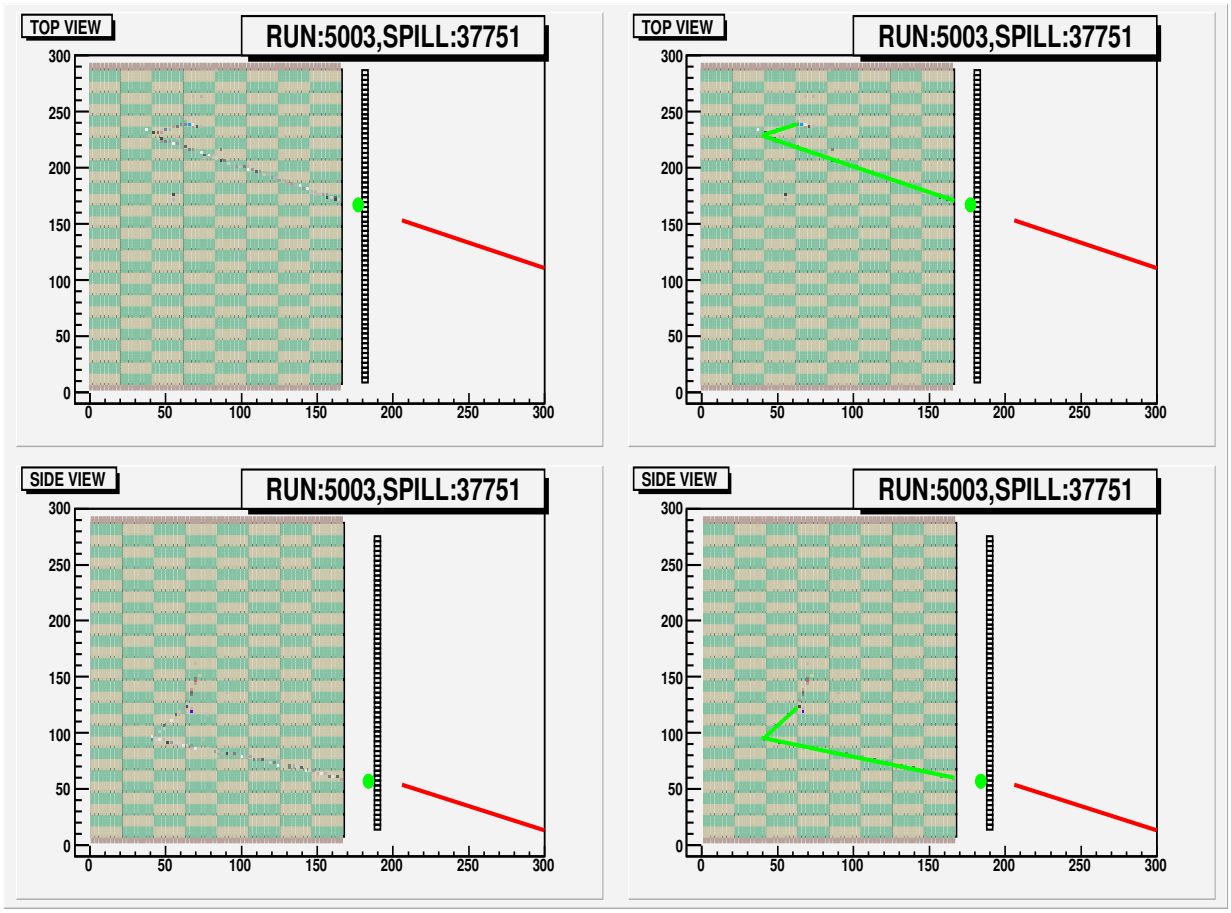

Figure 6.26: Event display of a three track selected single $p\pi^+$ event. The left part of the display shows the hits (color points) left in the detector after the neutrino interaction. The right part of it shows the 3D reconstructed tracks (green lines). The top part shows the top view; and the bottom part the side view of the SciBar detector. The green point indicates that some energy in deposited in the Electronic Calorimeter. The red line is the extrapolation of the track going to MRD. The track leaving the detector is the muon track. The shortest track is a proton-like track and the remaining track is a pion-like track.

Chapter 7

Measurement of the Single Pion Cross Section

In this Chapter we describe how the measurement of the exclusive and inclusive single pion cross section is done. The same method is used to measure both cross sections, so we will not distinguish between the two cross section along this Chapter: we name them by single pion interactions (CCπ^+).

7.1 Method to determine the Single Pion Cross Section Ratio

The method used in the analysis to measure the single pion cross section is a cut-based analysis, where a single pion enriched data sample is selected, and then corrected for the purity and the efficiency values that depend on the MC.

Clearly, this method relies heavily on the MC; therefore if the true cross section is vastly different from the one predicted in the MC, this method will fail. However, there is no indication that this is the case.

We measure the total cross section of the single pion interaction (σ_{π^+}) and the cross section as a function of the neutrino energy ($\sigma_{\pi^+}(E_\nu)$). In this analysis, we normalize the observed rate of CCπ^+ events after correcting for the purity and the efficiency to that of CCQE events, and equate that to the ratio of CCπ^+ to CCQE cross sections. In doing the analysis this way, we use the

fact that the same neutrino flux generates the different event samples. Using the ratio allow us to neglect the uncertainties in the neutrino flux prediction.

We make use the CCQE, CCpπ^+, and CC1π^+ data samples described in Chapter 6 to infer the total CCπ^+ to CCQE cross section ratio:

$$R = \frac{\sigma_{\mathrm{CC}\pi^+}}{\sigma_{\mathrm{CCQE}}} = \frac{N_{\mathrm{CC}\pi^+}}{N_{\mathrm{CCQE}}} \tag{7.1}$$

where $N_{\mathrm{CC}\pi^+}$ is the true and initial number of CCπ^+ events in data, and N_{CCQE} is the true and initial number of CCQE events in data.

Correction factors to the data samples are applied in order to account for sample contamination from non-CCπ^+ and non-CCQE neutrino-induced backgrounds, for CCπ^+ and CCQE selection efficiency and migrations from one data sample to another. These correction factors are based on the Monte Carlo predictions. We first define the background-subtracted yields of CCπ^+ or CCQE events in the S_{π^+} and S_{QE} data samples as follows:

$$\begin{aligned} N(\text{CCQE+CC}\pi^+; S_{\pi^+}) &= N(\text{all}; S_{\pi^+}) - N(\text{bgr}; S_{\pi^+}) \\ N(\text{CCQE+CC}\pi^+; S_{QE}) &= N(\text{all}; S_{QE}) - N(\text{bgr}; S_{QE}) \end{aligned} \tag{7.2}$$

$N(\text{CCQE+CC}\pi^+; S_{\pi^+})$ is the signal and $N(\text{bck}; S_{\pi^+})$ the background in the S_{π^+} sample. $N(\text{CCQE+CC}\pi^+; S_{QE})$ the signal and $N(\text{bck}; S_{QE})$ the background in the CCQE. The signal is obtained by applying the purity of both CCπ^+ and CCQE interactions in the corresponding data sample.

We then use the following signal selection efficiency and migration matrix to obtain the separate CCQE and CCπ^+ signal yields integrated over the full K2K neutrino energy spectrum, N_{CCQE} and $N_{CC\pi^+}$ in Equation 7.1:

$$\begin{pmatrix} N(\text{CCQE+CC}\pi^+; S_{\pi^+}) \\ N(\text{CCQE+CC}\pi^+; S_{QE}) \end{pmatrix} = \begin{pmatrix} \frac{\varepsilon(\text{CC}\pi^+; S_{\pi^+})}{\varepsilon(\text{CC}\pi^+)} & \frac{\varepsilon(\text{CCQE}; S_{\pi^+})}{\varepsilon(\text{CCQE})} \\ \frac{\varepsilon(\text{CC}\pi^+; S_{QE})}{\varepsilon(\text{CC}\pi^+)} & \frac{\varepsilon(\text{CCQE}; S_{QE})}{\varepsilon(\text{CCQE})} \end{pmatrix} \begin{pmatrix} \varepsilon(\text{CC}\pi^+) N_{\mathrm{CC}\pi^+} \\ \varepsilon(\text{CCQE}) N_{\mathrm{CCQE}} \end{pmatrix} \tag{7.3}$$

where $\varepsilon(\text{CC}\pi^+; S_{\pi^+})$ ($\varepsilon(\text{CCQE}; S_{\pi^+})$) is the efficiency of selecting CCπ^+ (CCQE) events in the S_{π^+} single pion sample, $\varepsilon(\text{CC}\pi^+; S_{QE})$ ($\varepsilon(\text{CCQE}; S_{QE})$) is the efficiency of selecting CCπ^+ (CCQE) events in the S_{QE} quasi-elastic sample, $\varepsilon(\text{CC}\pi^+) \equiv \varepsilon(\text{CC}\pi^+; S_{\pi^+}) + \varepsilon(\text{CC}\pi^+; S_{QE})$, and $\varepsilon(\text{CCQE}) \equiv \varepsilon(\text{CCQE}; S_{\pi^+}) + \varepsilon(\text{CCQE}; S_{QE})$. Hence, the measurement given by Equation 7.1 is obtained by solving the system of Equations 7.3, fully accounting for the relatively low CCQE and CCπ^+ purities expected in the S_{QE} and S_{π^+} data samples, respectively. The statistical error is propagated assuming that the number of data entries in the two samples are independent.

The purity is defined as the fraction of events selected as signal which is really the single pion and CCQE signal searched for respect to the total number of events selected as single pion or as CCQE.

$$\text{purity} = \frac{\text{number of true selected events}}{\text{total number of events in the selection}} \tag{7.4}$$

The efficiency is defined as the fraction of events selected as signal which is really the single pion or CCQE signal looked for in the different samples respect to the total number of single pion events or CCQE in the initial sample. For initial sample, we mean the events with the true event vertex interaction inside the fiducial volume.

$$\text{efficiency} = \frac{\text{number of true selected events}}{\text{number of true events in the initial sample}} \tag{7.5}$$

The analysis is done based on the different proportions of the true CCπ^+ and CCQE in the S^+_π and S_QE samples. Since our physical value at the end is the ratio $\frac{N_{\text{CC}\pi^+}}{N_{\text{CCQE}}}$, the correlation is very strong between the two samples. This would have not been the case if the two samples S were more successfully enriched. We have purities of finding the signal of the 40% in the CCpπ^+ enriched sample, 49% in the CC1π^+ one and 60% in the CCQE sample.

In addition to performing the cross section ratio measurement integrated over the full K2K neutrino energy range, we also measure its dependence as a function of neutrino energy. The differential measurement is given for four energy bins, whose boundaries are chosen to yield comparable statistical uncertainties in the cross section ratio. To this end, we generalize the 2×2 matrix formalism of Equation 7.3 to a 5×5 formalism, where rows and columns now index both data samples and neutrino energy ranges, as defined in Table 7.1.

Index	Sample	Neutrino Energy (GeV)
1	$S_1 \equiv S_{\pi^+,E_1}$	E_1 <1.35
2	$S_2 \equiv S_{\pi^+,E_2}$	1.35< E_2 <1.72
3	$S_3 \equiv S_{\pi^+,E_3}$	1.72< E_3 <2.22
4	$S_4 \equiv S_{\pi^+,E_4}$	E_4 >2.22
5	$S_5 \equiv S_{QE}$	E_5 unconstrained

Table 7.1: Index notation for energy-dependent cross section ratio measurement.

The 5×5 correction matrix applied to background-subtracted samples now corrects not only for data samples signal efficiencies and migrations from one data sample to another, but also for neutrino energy reconstruction biases and smearing effects. The neutrino energy is reconstructed according to Equation 3.2 for the different samples. The considerations taken in the reconstruction and the obtained distributions are presented in Section 7.2.

More specifically, the CCπ^+-enriched data samples $S_i \equiv S_{\pi^+,E_i}$ with $i = 1,\ldots,4$ in Equation 7.6 are classified in terms of reconstructed neutrino energy, while CCπ^+ corrected yields $N_{\mathrm{CC}\pi^+,E_j}$ are given in terms of true neutrino energy E_j, $j = 1,\ldots,4$:

$$N(\mathrm{CCQE{+}CC}\pi^+;S_i) = \sum_{j=1}^{4} M_{ij}\,\varepsilon(\mathrm{CC}\pi^+,E_j)N_{\mathrm{CC}\pi^+,E_j} + M_{i5}\,\varepsilon(\mathrm{CCQE})N_{\mathrm{CCQE}} \tag{7.6}$$

As for the measurement integrated over all neutrino energies, the following conditions on the rows and columns of the migration matrix M must be true for the energy-dependent measurement:

$$\sum_{j=1}^{4} M_{ij}\,\varepsilon(\mathrm{CC}\pi^+,E_j)N_{\mathrm{CC}\pi^+,E_j} + M_{i5}\,\varepsilon(\mathrm{CCQE})N_{\mathrm{CCQE}} + N(\mathrm{bgr};S_i) = N(\mathrm{all};S_i);$$

$$\sum_i M_{ij} = 1 \tag{7.7}$$

where $N(\mathrm{all};S_i)$ is the total number of observed events in the five selection samples.

The matrix elements $(M_{ij}, i,j = 1,\ldots,4)$ give the fraction of selected single pion events with true energy in bin j that are reconstructed in energy bin i of the single pion data sample. The matrix element M_{55} is the fraction of selected CCQE events that are reconstructed in the quasi-elastic data sample. The matrix elements $(M_{5j}, j = 1,\ldots,4)$ give the fraction of selected single pion events with true energy in bin j which are reconstructed in the quasi-elastic data sample. Finally, the matrix elements $(M_{i5}, i = 1,\ldots,4)$ are the fraction of selected CCQE events which are reconstructed in energy bin i of the single pion data sample. Figure 7.1 shows a sketch of the 5×5 dimensional system that we used in the case of the energy dependent measurement.

Solving for Equations 7.6 gives the following values: $N_{CC\pi,E_1}$, $N_{CC\pi,E_2}$, $N_{CC\pi,E_3}$, $N_{CC\pi,E_4}$ and N_{CCQE}. The CCπ^+-to-CCQE cross-section ratios for each neutrino energy bin is then obtained as:

$$R_j = \frac{N_{CC\pi,E_j}}{f_j N_{CCQE}} \tag{7.8}$$

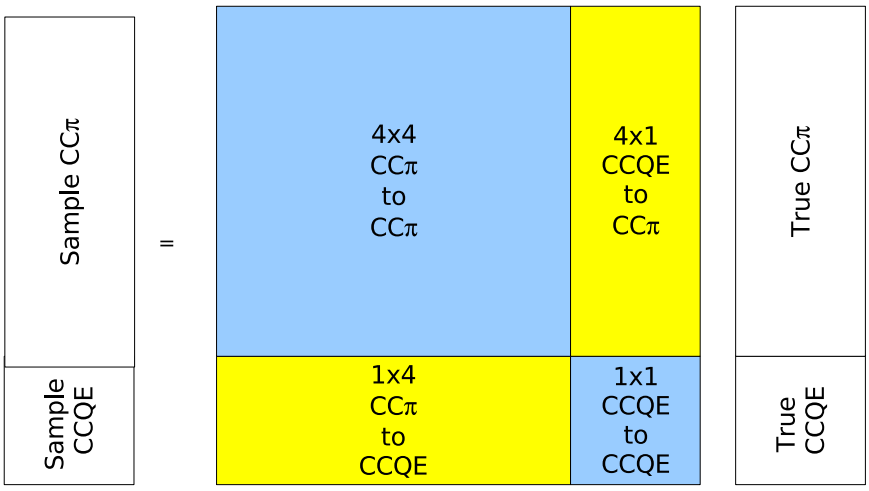

Figure 7.1: Scheme of the migration matrix application.

f_j is the predicted fraction of true CCQE events in the E_j true neutrino energy bin. The statistical error propagation is achieved by a toy Monte Carlo simulation, where we fluctuate each of the $N(\text{CCQE+CC}\pi^+; S_i)$ yields that are independent according to Poisson statistics, and sum quadratically the errors induced in the corresponding cross section ratios.

7.2 Reconstruction of the neutrino energy

We measure the energy dependent cross section using the method explained above, for that we need to reconstruct the neutrino energy. We use the kinematic variables of the muon track to reconstruct the neutrino energy for each of the selection entering in the analysis, assuming a two body collision:

$$\nu_\mu p \rightarrow \mu^- \Delta^{++}$$
$$\nu_\mu n \rightarrow \mu^- \Delta^{+}$$
$$\nu_\mu n \rightarrow \mu^- p$$

Then, we write the neutrino energy as in Equation 3.2:

$$E_{\nu}^{rec} = \frac{(m_N - V)E_\mu + \frac{m_X^2 - (m_N - V)^2 - m_\mu^2}{2}}{(m_N - V) - E_\mu + p_\mu \cos\theta_\mu}$$

where m_N, m_X, m_μ, E_μ, V are the nucleon target mass, the incoming hadron mass, the muon mass, and muon energy, and nuclear potential set at 27 MeV, respectively. For the single pion interaction, we set the proton mass, m_p, as the nucleon target mass, and the Breit-Wigner mass of the delta resonance Δ^{++}, $m_{\Delta^{++}} = 1.232$ GeV as the mass of the incoming hadron. Figure 7.2 shows the incoming hadron mass distribution for the exclusive single pion channel and for the inclusive single pion channel as predicted for the nominal MC. For the CCQE, the nucleon mass is the the neutron mass, m_n, and the proton mass, m_p, is the mass of the hadron in the final state.

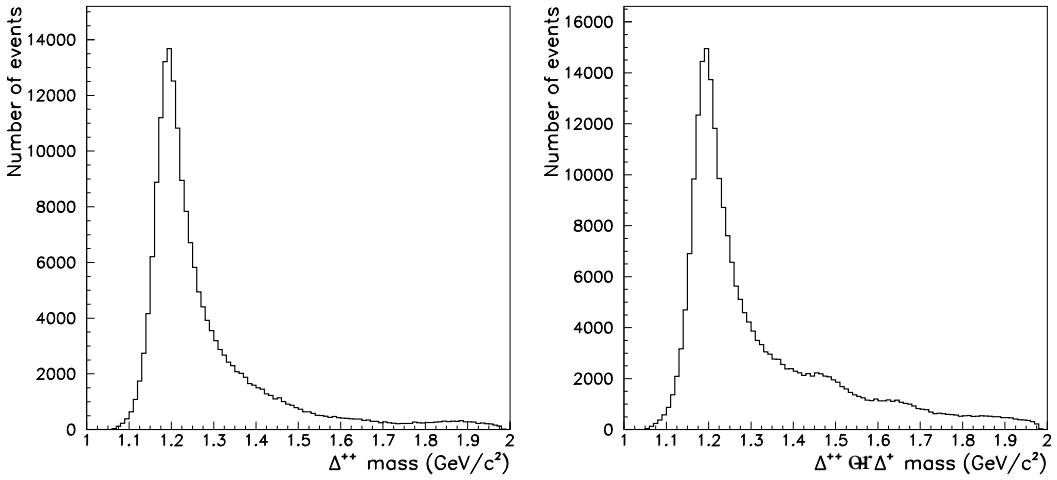

Figure 7.2: Hadron mass distribution for the exclusive (left) and inclusive (right) single pion channel.

Figure 7.3 shows the neutrino energy reconstructed for those single $p\pi^+$ events. Figure 7.4 shows the neutrino energy reconstructed for those single $1\pi^+$ events. Figure 7.5 shows the neutrino energy reconstructed for those CCQE events. The distributions are normalized to the number of events in the CC sample. In the right side of these figures we show the energy resolution by comparing the prediction from the Monte Carlo with the reconstructed MC (true minus reconstructed).

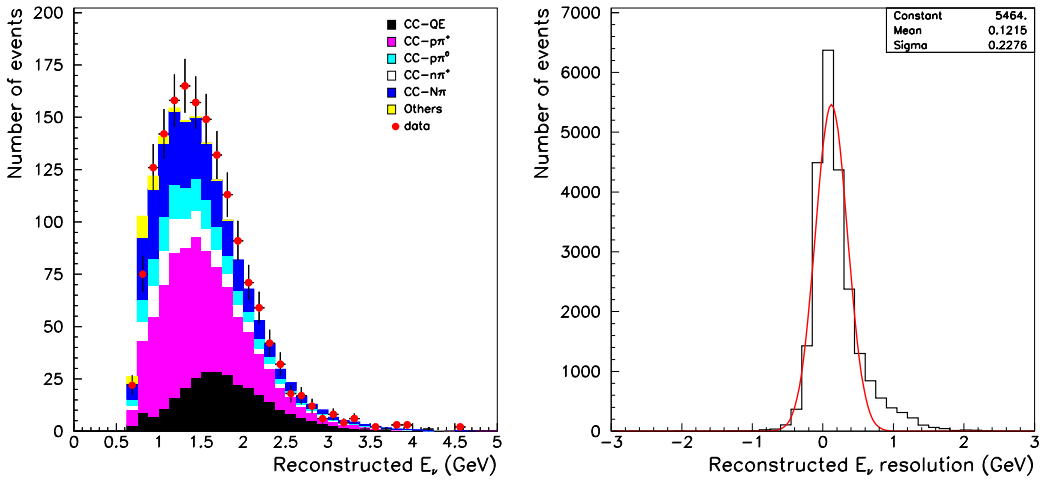

Figure 7.3: Reconstructed neutrino energy for single $p\pi^+$ (left): $\chi^2 = 33.60$, ndof = 29. Energy resolution (right).

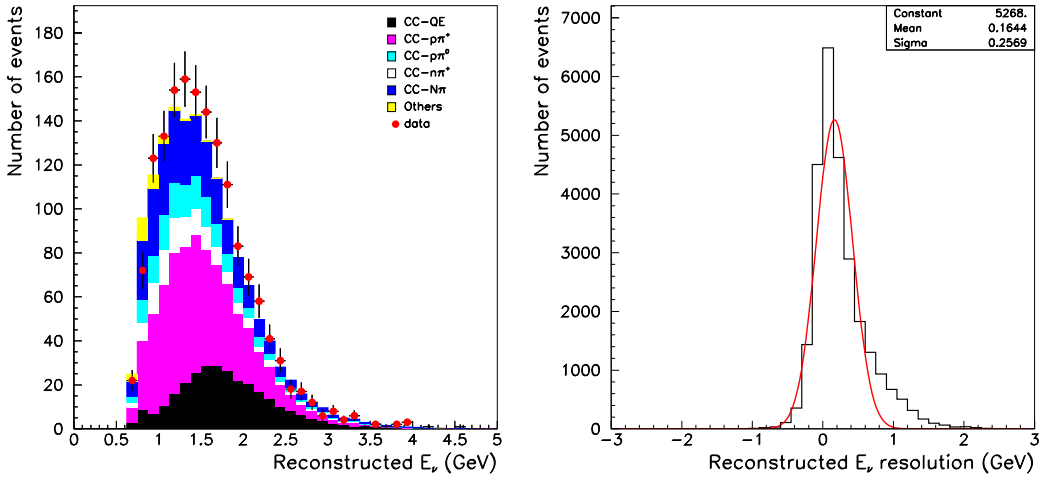

Figure 7.4: Reconstructed neutrino energy for single $1\pi^+$ (left): $\chi^2 = 31.01$, ndof = 29. Energy resolution (right).

Figure 7.6 shows the three reconstructed neutrino energy in the four energy bins that are used in the analysis for the single pion selection, and in one energy bin for the CCQE selection.

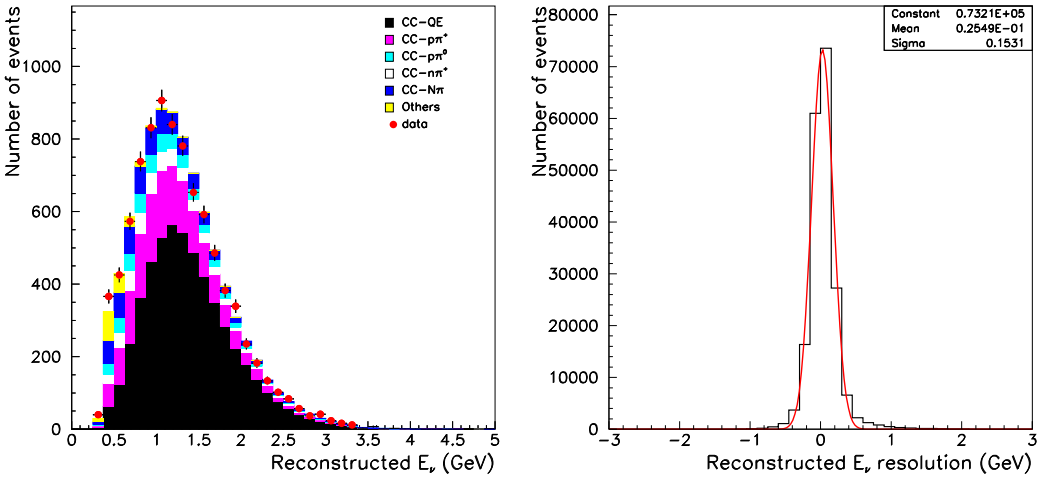

Figure 7.5: Reconstructed neutrino energy for CCQE: χ^2 = 31.03, ndof = 33. Energy resolution (right).

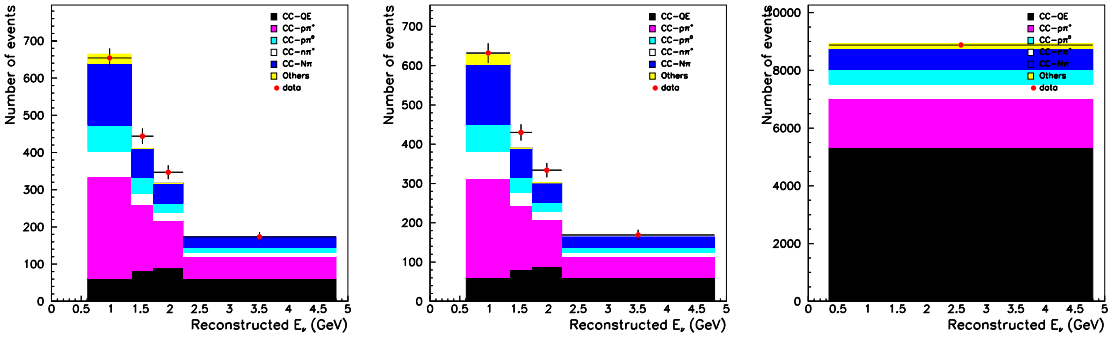

Figure 7.6: Reconstructed neutrino energy for single pπ^+ (left), single 1π^+ (center), and CCQE (right) in the 4 energy bins. χ^2 = 5.12, ndof = 4 (right); χ^2 = 14.01, ndof = 4 (center); χ^2 = 0.23, ndof = 1 (left).

In Figure 7.7 we show the lepton momentum transfer (Q^2) for each of the three considered samples. The Q^2 is defined as follows

$$Q^2 = -q^2 = 2E_\nu(E_\mu - p_\mu cos\theta) - m_\mu^2 \tag{7.9}$$

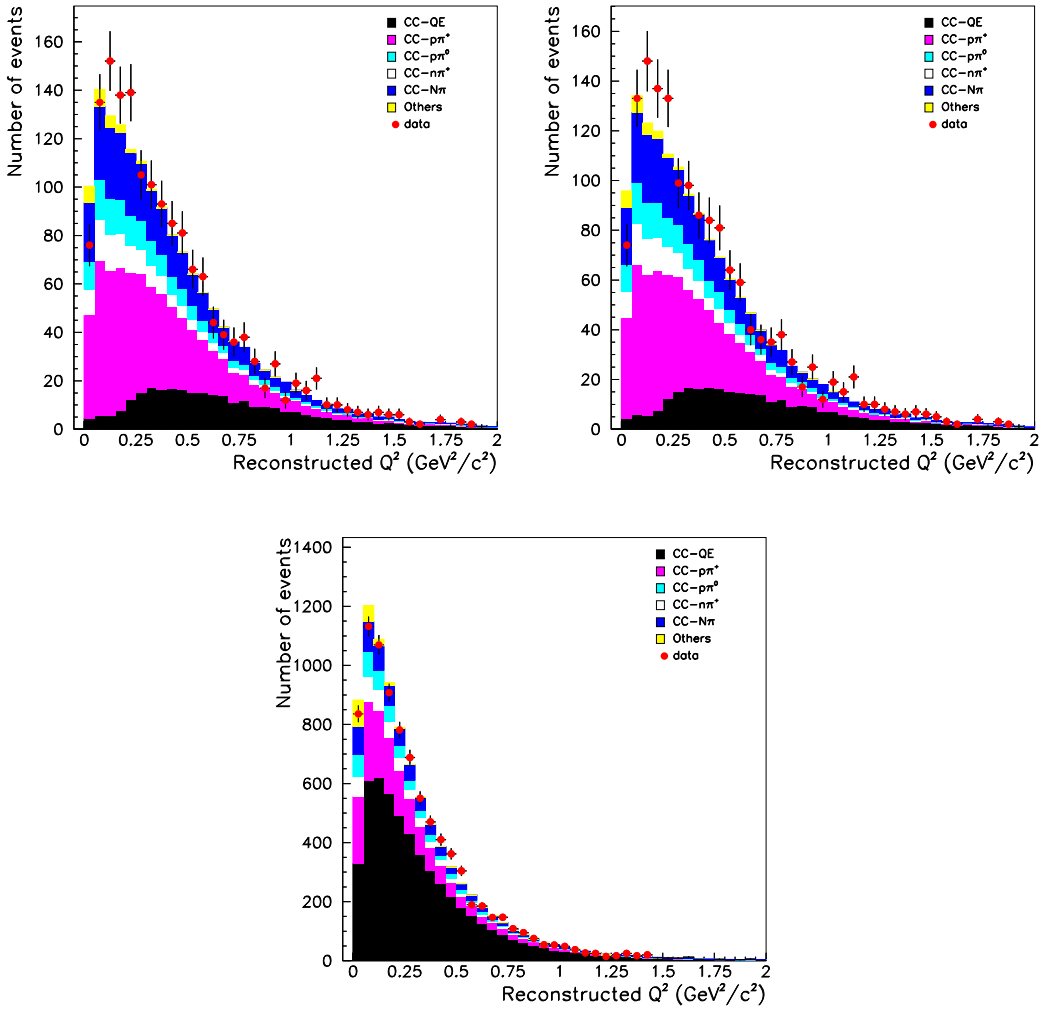

Figure 7.7: Left: Q^2 distribution in the single pπ^+ selection. χ^2 = 39.16, ndof = 38. Right: Q^2 distribution in the single $1\pi^+$ selection. χ^2 = 40.23, ndof = 38. Center bottom: Q^2 distribution in the single CCQE selection. χ^2 = 65.43, ndof = 40.

7.3 Corrections factors from MC for the energy dependet measurement

The purities and efficiencies used to get the overall measurement were presented in Chapter 6. Before presenting the result and for completeness we provide the purity, efficiency and number

of selected events in data for the different energy samples in which the single pion selection is divided. Table 7.2 shows the purity for the 4 energy bins for the single $p\pi^+$ selected events and background. Table 7.3 shows the purity for the 4 energy bins for the single $1\pi^+$ selected events and background. In these tables the samples are defined in the reconstructed neutrino energy.

CC$p\pi^+$ selection	E_1	E_2	E_3	E_4
CC$p\pi^+$	41	42.3	40.3	34.3
CCQE	9.2	19.7	28.1	34.7
CC$n\pi^+$	10.4	7.8	6.3	6.4
CC$p\pi^0$	10.7	10.	8.2	8.0
CCNπ	24.9	19.4	17.0	16.6
Others	3.9	0.1	0.1	0.

Table 7.2: Energy dependent purity in the two and three track CC$p\pi^+$ selection based on the nominal MC.

CC$1\pi^+$ selection	E_1	E_2	E_3	E_4
CC$1\pi^+$	51.0	49.9	45.7	39.6
CCQE	9.7	20.8	29.41	36.3
CC$p\pi^0$	10.9	10.2	8.3	8.1
CCNπ	24.5	19.	16.5	16.0
Others	4.0	0.1	0.1	0.

Table 7.3: Energy dependent purity in the two track CC$1\pi^+$ selection based on the nominal MC.

The efficiency in the true neutrino energy bins is quoted in Table 7.4 for $p\pi^+$ interaction, and in Table 7.5 for $1\pi^+$, and in Table 7.6 for CCQE. The efficiency for the signal in the CCQE for the 4 energy bins is needed to get the efficiency of selecting single pion in each energy bin in that selection. The number of selected events in each one of the three selections for the different energy bins is shown in Table 7.7.

CC$p\pi^+$ selection	E_1	E_2	E_3	E_4
CC$p\pi^+$	6.6	15.4	18.6	20.0
CCQE	2.2	4.4	5.0	4.8
CC$n\pi^+$	3.2	7.3	11.5	15.2
CC$p\pi^0$	4.2	10.5	14.7	18.2
CC$N\pi$	2.3	7.0	12.3	16.5
Others	0.1	0.3	0.6	1.3

Table 7.4: Energy dependent efficiency in the two and three track CC$p\pi^+$ selection based on the nominal MC.

CC$1\pi^+$ selection	E_1	E_2	E_3	E_4
CC$1\pi^+$	5.7	12.4	15.4	17.0
CCQE	2.2	4.4	5.0	4.7
CC$p\pi^0$	4.1	10.3	14.1	18.5
CC$N\pi$	2.2	6.6	11.3	15.2
Others	0.1	0.3	0.6	1.3

Table 7.5: Energy dependent efficiency in the two track CC$1\pi^+$ selection based on the nominal MC.

CCQE selection	E_1	E_2	E_3	E_4
CCQE	47.1	71.3	75.9	73.3
CC$p\pi^+$	21.1	38.7	43.9	46.7
CC$n\pi^+$	17.0	30.3	39.9	48.9
CC$p\pi^0$	19.5	33.5	41.6	47.8
CC$N\pi$	7.4	17.8	26.2	32.3
Others	1.0	2.6	3.7	5.77

Table 7.6: Energy dependent efficiency in the one and two track CCQE selection based on the nominal MC.

7.4 Behaviour of the migration matrix

We quote in this Section the migration matrix elements before and after the inversion. The matrix (M_{ij}) elements before inversion in black color are the fraction of signal single pion events with

Selection	E_1	E_2	E_3	E_4
CCpπ^+	654	444	347	174
CC1π^+	632	430	334	170
CCQE	5340	1793	1196	565

Table 7.7: Number of events in the three selections for the different energy bins.

true energy in bin j (from 1 to 4) in the single pion selection which are reconstructed in bin i (from 1 to 4). The matrix element before selection in green color is the fraction of signal CCQE events with true energy in that bin. The matrix elements in blue color placed in the horizontal are the fraction of signal single pion events which are reconstructed in the CCQE selection and with true energy in bin j (from 1 to 4). The matrix elements in blue color placed in the vertical are the fraction of signal CCQE events which are reconstructed in the different bins of the single pion selection.The marix elements of the diagonal represent the fraction of those signal events with true and reconstructed neutrino energy in the same bin. The matrix constructed from the pπ^+ selection and the CCQE selection is:

$$\begin{pmatrix} 0.212 \pm 0.003 & 0.120 \pm 0.002 & 0.055 \pm 0.002 & 0.033 \pm 0.002 & 0.011 \pm 0.000 \\ 0.025 \pm 0.001 & 0.142 \pm 0.002 & 0.083 \pm 0.002 & 0.024 \pm 0.001 & 0.015 \pm 0.000 \\ 0.001 \pm 0.000 & 0.022 \pm 0.001 & 0.144 \pm 0.003 & 0.082 \pm 0.003 & 0.016 \pm 0.000 \\ 0.000 \pm 0.000 & 0.001 \pm 0.000 & 0.016 \pm 0.001 & 0.160 \pm 0.004 & 0.011 \pm 0.000 \\ 0.763 \pm 0.007 & 0.715 \pm 0.007 & 0.702 \pm 0.007 & 0.701 \pm 0.010 & 0.948 \pm 0.003 \end{pmatrix}$$

As an explicit example:

- The matrix element M_{22} indicates that about 14% of the signal single pion events with true neutrino energy between 1.35 and 1.72 GeV are reconstructed in the same bin in the single pion selection.
- The matrix element M_{53} indicates that about 70% of the signal single pion events with true neutrino energy between 1.72 and 2.22 GeV are reconstructed in the CCQE selection.

The matrix constructed from the $1\pi^+$ selection and the CCQE interaction is:

$$\begin{pmatrix} 0.203 \pm 0.003 & 0.124 \pm 0.002 & 0.069 \pm 0.002 & 0.038 \pm 0.002 & 0.011 \pm 0.000 \\ 0.023 \pm 0.001 & 0.124 \pm 0.002 & 0.081 \pm 0.002 & 0.032 \pm 0.001 & 0.015 \pm 0.000 \\ 0.001 \pm 0.000 & 0.019 \pm 0.001 & 0.117 \pm 0.002 & 0.079 \pm 0.002 & 0.016 \pm 0.000 \\ 0.000 \pm 0.000 & 0.001 \pm 0.000 & 0.012 \pm 0.001 & 0.130 \pm 0.003 & 0.011 \pm 0.000 \\ 0.773 \pm 0.007 & 0.732 \pm 0.006 & 0.721 \pm 0.006 & 0.721 \pm 0.009 & 0.948 \pm 0.003 \end{pmatrix}$$

The inverted matrix constructed from the pπ^+ selection and the CCQE interaction is:

$$\begin{pmatrix} 5.230 & -4.550 & 0.644 & -0.764 & 0.008 \\ -0.776 & 8.739 & -4.557 & 1.488 & -0.065 \\ 0.411 & -1.217 & 8.301 & -3.818 & -0.083 \\ 0.240 & 0.235 & -0.613 & 6.820 & -0.074 \\ -4.105 & -2.206 & -2.776 & -2.726 & 1.214 \end{pmatrix}$$

The inverted matrix constructed from the 1π^+ selection and the CCQE interaction is:

$$\begin{pmatrix} 5.491 & -5.714 & 0.645 & -0.707 & 0.022 \\ -0.917 & 10.330 & -6.412 & 1.932 & -0.062 \\ 0.507 & -1.544 & 10.522 & -5.607 & -0.096 \\ 0.321 & 0.305 & -0.733 & 8.505 & -0.093 \\ -4.403 & -2.377 & -3.022 & -3.123 & 1.229 \end{pmatrix}$$

7.5 Measurement of the Cross Section Ratio

Table 7.8 and 7.9 show the overall and the energy dependent measurement of the cross section ratio CCpπ^+ to CCQE. Table 7.10 and 7.11 show the overall and the energy dependent measurement of the cross section ratio CC1π^+ to CCQE.

Measurement
0.614 ± 0.061 (stat.)

Table 7.8: Measurment of the CCpπ^+ to CCQE cross section ratio.

E_ν (GeV)	Measurement
≤ 1.35	0.429 ± 0.071 (stat.)
1.35-1.72	0.689 ± 0.112 (stat.)
1.72-2.22	0.788 ± 0.126 (stat.)
$2.22 \leq$	0.674 ± 0.146 (stat.)

Table 7.9: Measurment of the energy dependent CCpπ^+ to CCQE cross section ratio.

Measurement
0.850 ± 0.080 (stat.)

Table 7.10: Measurment of the CC1π^+ to CCQE cross section ratio.

E_ν (GeV)	Measurement
≤ 1.35	0.522 ± 0.103 (stat.)
1.35-1.72	0.960 ± 0.179 (stat.)
1.72-2.22	1.170 ± 0.206 (stat.)
$2.22 \leq$	1.135 ± 0.225 (stat.)

Table 7.11: Measurment of the energy dependent CC1π^+ to CCQE cross section ratio.

Chapter 8

Systematic effects

In this Chapter we describe the sources of uncertainties affecting the measurements. The systematic sources are separated in five different categories: systematic due to the MC statistics, neutrino interaction model, nuclear effects, detector effects, and systematics coming from the reconstruction of the events.

The systematic uncertainty due to the MC statistics is evaluated in the nominal analysis. To compute the other systematic errors we redo all the analysis modifying the parameters related to the interaction model, σ_{model}, nuclear effects, $\sigma_{nuclear}$, detector effects, $\sigma_{detector}$, and reconstruction effects, σ_{reco}, affecting MC, data or both. Once the analysis is completely redone, we compute the deviation of the value obtained with respect to the nominal one, which is the obtained with the nominal MC-data set; this value is quoted as the error. Hence, the systematic uncertainty is the quadratic combination of the different systematic errors.

8.1 MC statistics

The error due to the MC statistics is included as a systematic error. We get the error in the measurement of the total cross section ratio using MC as data and then quoting the statistical error on the measurement as the statistical error due to the MC.

8.2 Interaction model

The axial-vector mass for the CCQE interaction is set in the neutrino interaction model to 1.1 GeV/c^2. The error in this value is estimated to be about $\pm$0.1 GeV/c^2 from the fit to the shape of the square of the momentum transfer from the nucleon to the nucleus in an analysis of data from the SciFi detector [109]. We quote a systematic error on M_A^{CCQE} varying it by $\pm$ 0.1 GeV/c^2. In this analysis, we measure the overall normalization of the CCQE cross section. So when varying the M_A^{CCQE} value, the total cross section is re-weighted back to the nominal value.

As described in Section 3.4.4, we apply the Bodek and Yang correction to multi-pion and DIS events. We change the correction factor by $\pm 30\%$ of the difference between applying or not applying the Bodek correction. Other studies related to neutrino interactions that have been developed in SciBar show that the multi-pion and DIS cross section decreases a factor of 40% when the Bodek correction is applied [112]. The Bodek correction modify the lepton momentum transfer of the multi-pion and DIS interactions, but at the time this correction decreases the total cross section to a value which is not in agreement with data. In counting this effect we apply a reweighting in the multi-pion and DIS cross section of 1.40; redo the analysis and quote the deviation from the nominal value as a systematic error. The error due to applying this reweight is set in both directions.

Also as described in Section 3.4.4, we reweight the neutrino flux according to the spectrum fit. To determine the systematic error due to the flux reweighting, we vary the weighting factors, taking into account their error and the correlation among them. The square root of the error matrix (where the diagonal elements are σ_i and the off-diagonal elements are $\sqrt{Cov(f_i, fj)}$) is shown below (see [56]). The weighting factor are given in Table 3.2.

$$\sqrt{M} = \begin{pmatrix} 0.4386 & -0.0316 & 0.0728 & 0.0000 & -0.0221 & -0.0076 & -0.0348 & 0.0081 \\ -0.0316 & 0.0751 & 0.0197 & 0.0000 & 0.0190 & 0.0062 & 0.0129 & 0.0243 \\ 0.0728 & 0.0197 & 0.0600 & 0.0000 & 0.0338 & 0.0163 & 0.0344 & 0.0171 \\ 0.0000 & 0.0000 & 0.0000 & 0.0000 & 0.0000 & 0.0000 & 0.0000 & 0.0000 \\ -0.0221 & 0.0190 & 0.0338 & 0.0000 & 0.0404 & -0.0186 & 0.0453 & 0.0220 \\ -0.0076 & 0.0620 & 0.0163 & 0.0000 & -0.0186 & 0.0528 & -0.0585 & 0.0511 \\ -0.0348 & 0.0129 & 0.0344 & 0.0000 & 0.0453 & -0.0585 & 0.1367 & -0.1014 \\ 0.0081 & 0.0243 & 0.0171 & 0.0000 & 0.0220 & 0.0511 & -0.1014 & 0.1835 \end{pmatrix}$$

8.3 Nuclear effects

Hadrons produced in neutrino interactions often rescatter inside the target nucleus. This process, called nuclear effect changes kinematics of the hadrons. The NEUT MC simulation ([68]) includes the interaction of mesons and nucleons within the nucleus.

For pions, absorption, scattering and charge exchange are considered; proton rescattering inside the target nucleus is also simulated. Pion absorption interactions are those ones in which no pion is left in the final state; pion scattering, meaning the nucleus is left in an excited/ground state and/or one or more nucleons are knocked out of the nucleus; charge exchange, meaning the final state pion charge differs from the initial pion charge. Proton rescattering means that the proton change its direction and energy inside the nucleus by interacting with nucleons.

The effect of changing the cross section of pion absorption, pion scattering, and proton rescattering in the nucleus is considered as a systematic error. In the momentum range of pions from Δ^{++} decay, the cross section measurement uncertainty for both pion absorption and pion scattering (including charge exchange) is approximately 30%; therefore the cross section for pion absorption and pion scattering are each changed by $\pm$ 30% to evaluate the systematic error. The uncertainty in the cross section of proton rescattering inside the nucleus is about 10%, and so the cross section of proton rescattering is varied by $\pm$ 10% to evaluate the systematic error.

The nuclear effects can alter the momentum and angular distribution of particles in the event, thus affecting the number of observed tracks, the angle between tracks, and the energy deposition.

In NEUT, the maximun Fermi momentum of nucleons is set to 225 MeV/c for carbon and oxygen [56]. For carbon, the value should be approximately 221 $\pm$ 5 MeV/c according to [106]. We calculate the systematic error due to this effect by eliminating events in which the Fermi momentum of the nucleon is greater than 220 MeV/c. The error in quoted in both sides. The effect of the Fermi motion in the $\Delta\theta_p$ distribution was already discussed in Section 5.7.

8.4 Detector effects

Crosstalk between channel is modeled as shown in Figure 8.1. In this model, the amount of crosstalk in the neighboring channels (n) is set and then the amount of crosstalk in the diagonal channels and in the second crown is determined by the ratios given in the figure. For the nominal MC, the amount of crosstalk is set to 3.25%. To evaluate the systematic effect of changing the

crosstalk model, the crosstalk parameter (n) is changed by its systematic error of 0.25%, i.e to 3.0% and to 3.5%. The crosstalk parameter is modified in both MC and data. For details, see [84]. The crosstalk is simulated in MC and then corrected; and it is corrected in data.

$\frac{n}{8}$	$\frac{n}{5}$	$\frac{n}{4}$	$\frac{n}{5}$	$\frac{n}{8}$
$\frac{n}{5}$	$\frac{n}{2}$	n	$\frac{n}{2}$	$\frac{n}{5}$
$\frac{n}{4}$	n		n	$\frac{n}{4}$
$\frac{n}{5}$	$\frac{n}{2}$	n	$\frac{n}{2}$	$\frac{n}{5}$
$\frac{n}{8}$	$\frac{n}{5}$	$\frac{n}{4}$	$\frac{n}{5}$	$\frac{n}{8}$

Figure 8.1: Crosstalk model.

Crosstalk can affect the tracking in three ways: 1) crosstalk hits can extend the length of a track or make fake tracks; 2) crosstalk hits near the track can alter the reconstructed angle of the track; and 3) crosstalk hits can alter the dE/dx of a track.

PMT resolution is nominally set at 40%. This value was chosen by tuning the dE/dx per plane for muons in the MC to match the data. The dE/dx distribution is shown in Figure 8.2. The estimated error in the PMT value is 10%, so the resolution is changed by $\pm$ 10% to evaluate the systematic effect. The PMT resolution can change the dE/dx of the track.

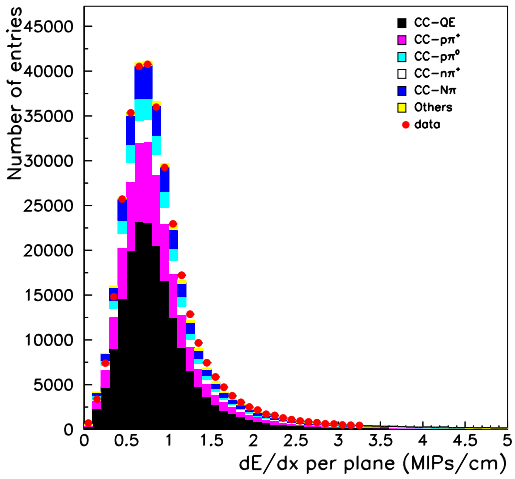

Figure 8.2: Distribution of the dE/dx per plane of the muon track. The unit MIP equals to 2.2 MeV.

The model for scintillator quenching as described in Section 4.3.3 relies on Birk's constant, which was measured in SciBar to be 0.0208 ± 0.0023. The constant is changed within its error (± 0.0023) to evaluate the systematic error due to the model. The scintillator quenching affects the dE/dx in the MC.

8.5 Reconstruction effects

Figure 8.3 shows the photo-electron distribution considered to set the hit threshold. A big discrepancy is found in the low photo-electron region: a (software) hit threshold is nominally set at 2.0 photo-electrons.

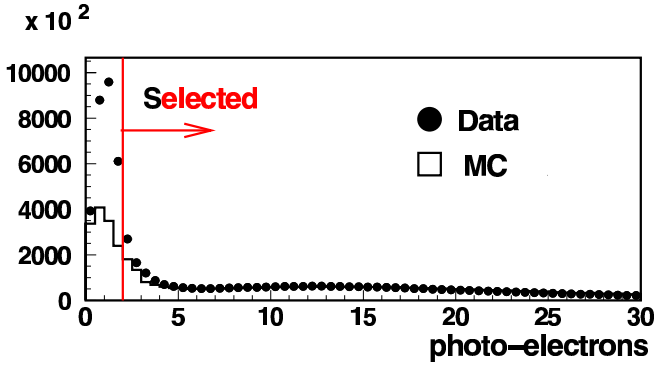

Figure 8.3: Number of photo-electron distribution for all hits survived after the crosstalk correction.

The photo-electron distribution after the simulation and the reconstruction is shown in Figure 8.4. A (software) hit threshold is nominally set at 2.0 photoelectrons (pe) in both data and MC to eliminate hits from noise in data that is not simulated. To evaluate the systematic error due to the threshold, we look for the variation in MC that makes the hit photo-electron efficiency equal in data and MC. This variation is a 15% of the hit threshold value. We increase the threshold in MC by 15% and assume that the change due to decreasing the threshold is the same magnitude. We avoid decreasing the threshold, as a lower threshold would be in the region of data-MC discrepancy.

The systematic uncertainty in the muon momentum scale factor in data (as described in Subsection 6.1.2) is $\pm 2.7\%$. This factor does not affect directly the number of events or tracks; but it can have an effect in the reconstructed variables that use the muon momentum information.

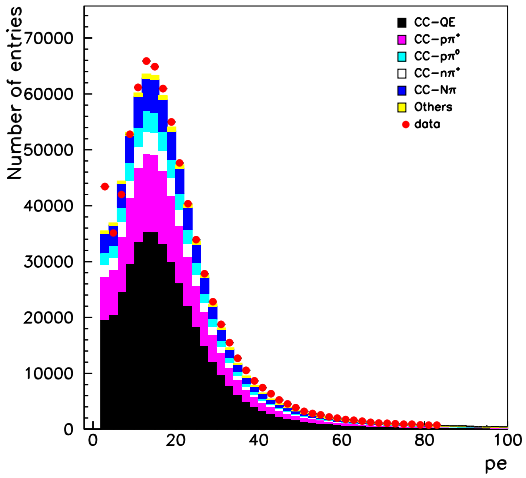

Figure 8.4: Photo-electron distribution for the muon tracks.

A difference in angular resolution between data and MC could also be a systematic source to be taking into account. We want to know the resolution associated to the tangent distribution in MC and data. In order to do that, we select good muon tracks in SciBar. These muon tracks are coming from 1 track events and have a two view matching mode smaller than 4: the difference between the track endpoints is at most 3 planes from one view to the other (See Appendix A for detail). The muon track is break into two; the two halves are fitted independently to get 'new' tracks. From the slope of these new tracks we get the tangent resolution, σ_{tan}, as the difference between the two slopes.

We follow this procedure from data and from MC. Figure 8.5 shows the σ_{tan} (including σ_{tan_x} and σ_{tan_y}). The left plot corresponds to data; and the right to MC. The fit was done to two Gaussian distributions. The square difference between the two narrow Gaussians is $\sqrt{0.03091^2 - 0.02965^2} = 0.009$; this difference in the tangent resolution implies a difference of 0.5 degrees. The tangent resolution in data is larger than in MC. So, we smear muon tangents in MC data by 0.009. The error due to smear MC by this quantity is set in both directions.

Figure 8.6 shows the dependency of the tangent resolution in data and in MC with the muon energy. For both, data and MC, the tangent resolution decreases increasing the muon energy. For high muon energy the effect of the multiple scattering is smaller, so the tangent resolution is narrower. In addition, we can see that the tangent resolution for data is larger than for MC.

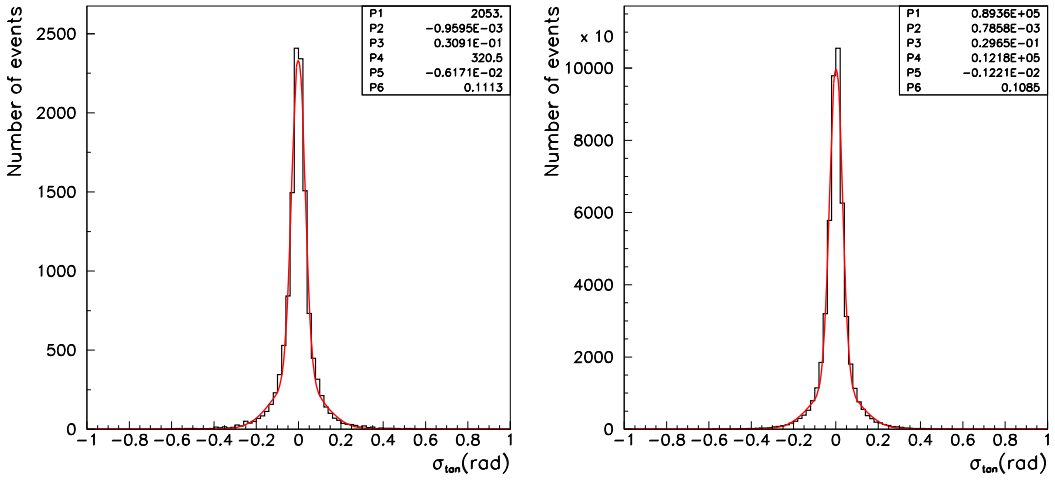

Figure 8.5: Tangent resolution σ_{tan} in data (left); and in MC (right).

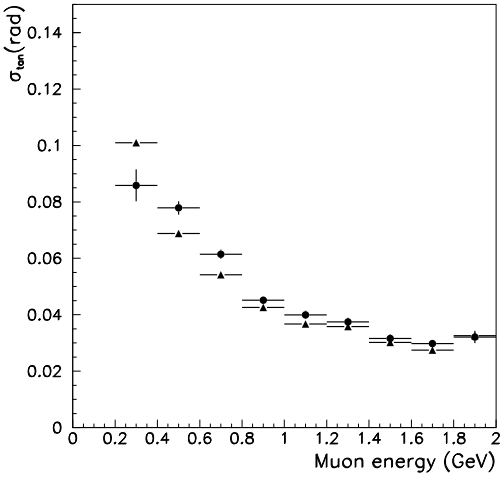

Figure 8.6: Dependency of the tangent resolution in data and in MC with the muon energy. Black points are data; triangles are MC.

Figure 8.7 shows the dependency of the tangent resolution in data and in MC with the muon tangent. Muons with high angles are those ones with smaller momentum; so the fact that

increasing the tangent, the tangent resolution increases, could be also an effect of the multiple scattering. In this case the tangent resolution for data is also larger than for MC.

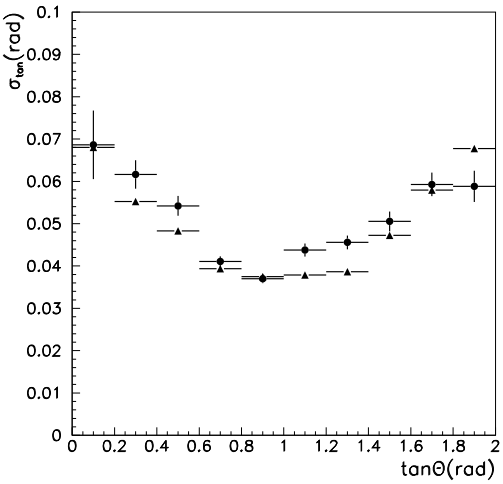

Figure 8.7: Dependency of tangent resolution in data and in MC with the muon tangent. Black points are data; triangles are MC.

8.6 Systematic effect in the cut distributions

The effect of the difference between data and MC in the reconstructed variables where we cut in the analysis: distance to the vertex interaction point, number of tracks at vertex, $\Delta\theta_p$, and MuCL are discussed in the following. Figure 8.8 shows the distribution of the distance to the reconstructed vertex interaction point, showing data and the data variation in black bars (including statistical error) and MC variation in yellow bands due to the previous systematics effects; the variation band is set from the nominal value. Figure 8.9 shows the number of tracks at vertex; Figure 8.10 shows the $\Delta\theta_p$ distribution under the same considerations; and Figure 8.11 shows the MuCL distribution.

The disagreement between data and MC in this distributions is covered by the data/MC variations due to the other systematic effects; so we do not quote any error on these variables.

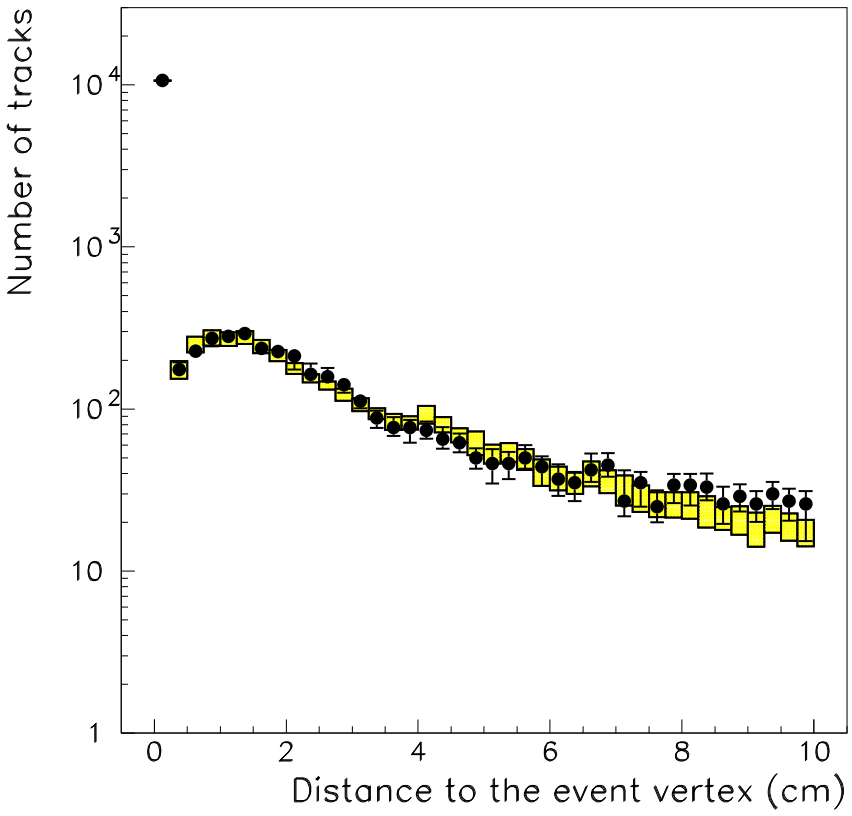

Figure 8.8: Distance to the reconstructed vertex interaction point. Black points are data, and bars the data variation due to the systematic effects considered in data (crosstalk) and statistical error; and yellow box, the MC variation band. χ^2 = 29.46, ndof = 40.

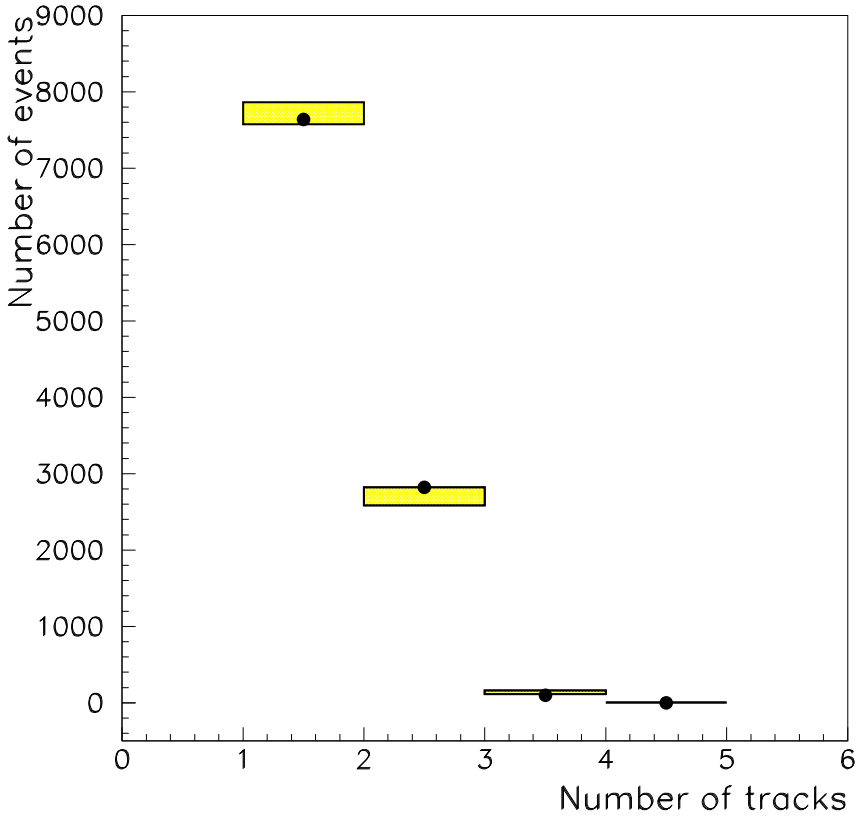

Figure 8.9: Number of tracks distribution. Black points are data, and bars the data variation due to the systematic effects considered in data (crosstalk) and statistical error; and yellow box, the MC variation band. χ^2 = 3.46, ndof = 4.

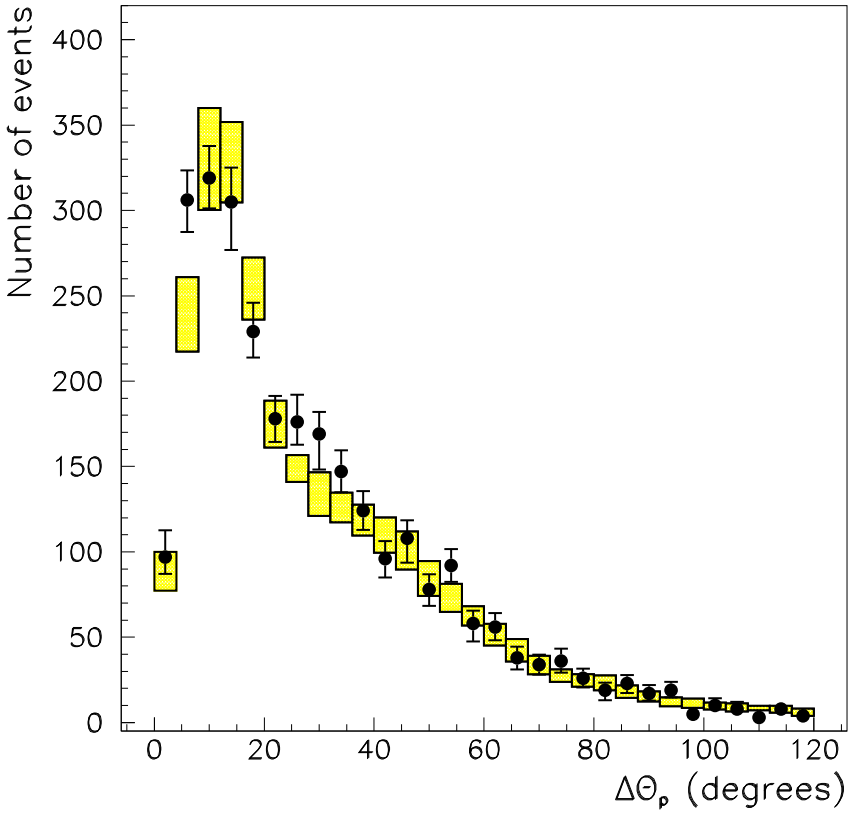

Figure 8.10: $\Delta\theta_p$ distribution. Black points are data, and bars the data variation due to the systematic effects considered in data (muon momentum scale, and crosstalk) and statistical error; and yellow box, the MC variation band. χ^2 = 32.58, ndof = 30.

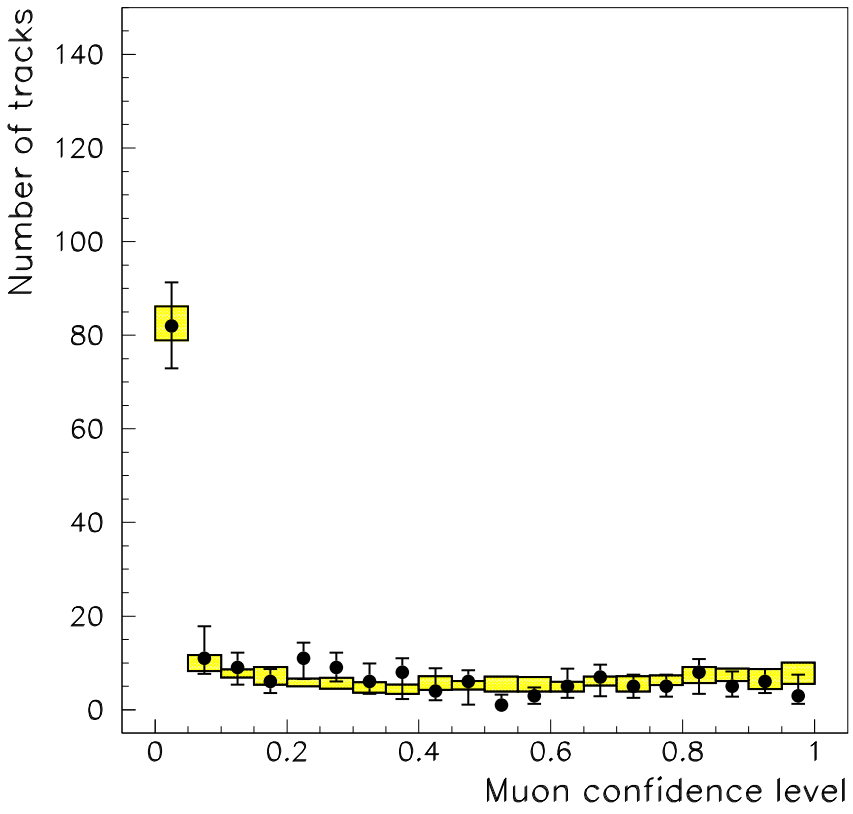

Figure 8.11: MuCL distribution. Black points are data, and bars the data variation due to the systematic effects considered in data (crosstalk) and statistical error; and yellow box, the MC variation band. χ^2 = 6.36, ndof = 20.

8.7 Systematic uncertainties on the measurement of the cross section of the single pπ^+ interaction normalized to CCQE

In order to get the total systematic error, if for a particular effect the two variations are in the same direction, the largest one is considered to contribute in that direction, and we do not quote any variation in the other direction.

The detailed contribution to the systematic uncertainty on the measurement of the cross section of the single pπ^+ interaction normalized to CCQE appears in Table 8.1. The systematic errors for the measurement done in the 4 energy bins are quoted in Tables 8.2, 8.3, 8.4, and 8.5. Tables show the contribution to the final systematic error from each one of the considered systematic sources. The dominant contribution to the final error comes from the nuclear effects.

8.8 Systematic uncertainties on the measurement of the cross section of the single 1π^+ interaction normalized to CCQE

The detailed contribution to the systematic uncertainty on the measurement of the cross section of the single 1π^+ interaction normalized to CCQE appears in Table 8.6. The systematic errors for the measurement done in the 4 energy bins are quoted in Tables 8.7, 8.8, 8.9, and 8.10.

8.9 Statistical MC uncertainties on the measurement of the cross section ratio

We quoted now the statistical error for the nominal MC, as for those where some parameter have been changed in the simulation or reconstruction (detector effects), and for those statistically independent (nuclear effects) in order to check if the statistics of the different samples are comparable. The statistical error for the nuclear effect MCs is around twice of the nominal MC one. The statistical error of the exclusive measurement using the appropriate MC-data set is given in Table 8.11. The statistical error of the inclusive measurement using the appropriate MC-data set is given in Table 8.12.

source of systematic	error
MC statistics	+0.009 -0.009
Model effects	
M_A (CCQE) $\pm$0.1	+0.021 -0.021
Bodek/Yang Corr $\pm$30%	-0.021 +0.023
Nπ weighting	$\pm$ 0.056
Neutrino Flux	+0.010 -0.008
Sub-total	+0.065 -0.064
Nuclear effects	
π absorption $\pm$30%	+0.053 -0.015
π inelastic scattering $\pm$30%	+0.062 -0.022
proton rescattering $\pm$10%	+0.021 -0.007
Fermi motion ($\pm$ 5MeV/c)	$\pm$ 0.004
Sub-total	+0.084 -0.028
Detector effects	
Cross talk $\pm$0.25%	+0.035 -0.021
PMT resolution $\pm$10%	+0.025 -0.010
Quenching constant $\pm$0.0023	+0.005 +0.012
Sub-total	+0.045 -0.023
Reconstruction effects	
Hit threshold $\pm$15%	$\pm$ 0.035
Muon momemtum scale $\pm$2.7%	-0.004 +0.003
Angular resolution (smeared by 0.009)	$\pm$ 0.007
Sub-total	+0.036 -0.036
Total	+0.121 -0.082

Table 8.1: Systematic errors for the overall CCpπ^+ to CCQE cross section ratio.

source of systematic	error
MC statistics	+0.011 -0.011
Model effects	
M_A (CCQE) $\pm$0.1	+0.016 -0.017
Bodek/Yang Corr $\pm$30%	-0.027 +0.029
Nπ weighting	$\pm$ 0.051
Neutrino Flux	+0.007 -0.008
Sub-total	+0.061 -0.061
Nuclear effects	
π absorption $\pm$30%	+0.051 -0.052
π inelastic scattering $\pm$30%	+0.024 +0.028
proton rescattering $\pm$10%	+0.027 +0.039
Fermi motion ($\pm$ 5MeV/c)	$\pm$ 0.004
Sub-total	+0.070 -0.052
Detector effects	
Cross talk $\pm$0.25%	+0.031 +0.033
PMT resolution $\pm$10%	+0.012 -0.006
Quenching constant $\pm$0.0023	+0.020 +0.001
Sub-total	+0.040 -0.006
Reconstruction effects	
Hit threshold $\pm$15%	$\pm$ 0.015
Muon momemtum scale $\pm$2.7%	-0.035 +0.092
Angular resolution (smeared by 0.009)	$\pm$ 0.006
Sub-total	+0.093 -0.039
Total	+0.138 -0.090

Table 8.2: Systematic errors for the CCpπ^+ to CCQE cross section ratio in the first energy bin.

source of systematic	error
MC statistics	+0.020 -0.020
Model effects	
M_A (CCQE) $\pm$0.1	+0.023 -0.022
Bodek/Yang Corr $\pm$30%	-0.020 +0.021
Nπ weighting	$\pm$ 0.051
Neutrino Flux	+0.014 -0.015
Sub-total	+0.061 -0.061
Nuclear effects	
π absorption $\pm$30%	+0.006 -0.006
π inelastic scattering $\pm$30%	+0.112 -0.115
proton rescattering $\pm$10%	+0.030 -0.092
Fermi motion ($\pm$ 5MeV/c)	$\pm$ 0.001
Sub-total	+0.116 -0.147
Detector effects	
Cross talk $\pm$0.25%	+0.028 -0.058
PMT resolution $\pm$10%	+0.021 -0.004
Quenching constant $\pm$0.0023	-0.022 +0.021
Sub-total	+0.041 -0.062
Reconstruction effects	
Hit threshold $\pm$15%	$\pm$ 0.036
Muon momemtum scale $\pm$2.7%	-0.116 +0.008
Angular resolution (smeared by 0.009)	$\pm$ 0.008
Sub-total	+0.038 -0.122
Total	+0.144 -0.211

Table 8.3: Systematic errors for the CCpπ^+ to CCQE cross section ratio in the second energy bin.

source of systematic	error
MC statistics	+0.028 -0.028
Model effects	
M_A (CCQE) $\pm$0.1	+0.015 -0.016
Bodek/Yang Corr $\pm$30%	-0.017 +0.019
Nπ weighting	$\pm$ 0.057
Neutrino Flux	+0.024 -0.021
Sub-total	+0.066 -0.065
Nuclear effects	
π absorption $\pm$30%	+0.107 +0.011
π inelastic scattering $\pm$30%	+0.060 +0.092
proton rescattering $\pm$10%	+0.067 -0.067
Fermi motion ($\pm$ 5MeV/c)	$\pm$ 0.005
Sub-total	+0.156 -0.005
Detector effects	
Cross talk $\pm$0.25%	+0.043 -0.039
PMT resolution $\pm$10%	+0.042 -0.019
Quenching constant $\pm$0.0023	+0.039 +0.022
Sub-total	+0.072 -0.043
Reconstruction effects	
Hit threshold $\pm$15%	$\pm$ 0.036
Muon momemtum scale $\pm$2.7%	+0.088 -0.004
Angular resolution (smeared by 0.009)	$\pm$ 0.019
Sub-total	+0.097 -0.041
Total	+0.210 -0.093

Table 8.4: Systematic errors for the CC$p\pi^+$ to CCQE cross section ratio in the third energy bin.

source of systematic	error
MC statistics	+0.042 -0.042
Model effects	
M_A (CCQE) $\pm$0.1	+0.004 -0.013
Bodek/Yang Corr $\pm$30%	-0.013 +0.016
Nπ weighting	$\pm$ 0.067
Neutrino Flux	+0.057 -0.050
Sub-total	+0.089 -0.085
Nuclear effects	
π absorption $\pm$30%	+0.076 +0.004
π inelastic scattering $\pm$30%	+0.032 -0.129
proton rescattering $\pm$10%	+0.048 -0.045
Fermi motion ($\pm$ 5MeV/c)	$\pm$ 0.018
Sub-total	+0.097 -0.138
Detector effects	
Cross talk $\pm$0.25%	+0.049 -0.032
PMT resolution $\pm$10%	+0.024 -0.018
Quenching constant $\pm$0.0023	-0.027 +0.002
Sub-total	+0.055 -0.046
Reconstruction effects	
Hit threshold $\pm$15%	$\pm$ 0.067
Muon momemtum scale $\pm$2.7%	+0.225 -0.258
Angular resolution (smeared by 0.009)	$\pm$ 0.119
Sub-total	+0.263 -0.292
Total	+0.302 -0.340

Table 8.5: Systematic errors for the CCpπ^+ to CCQE cross section ratio in the fourth energy bin.

source of systematic	error
MC statistics	+0.012 -0.012
Model effects	
M_A (CCQE) $\pm$0.1	+0.024 -0.024
Bodek/Yang Corr $\pm$30%	-0.031 +0.033
Nπ weighting	$\pm$ 0.079
Neutrino Flux	+0.013 -0.011
Sub-total	+0.090 -0.089
Nuclear effects	
π absorption $\pm$30%	+0.089 -0.023
π inelastic scattering $\pm$30%	+0.084 -0.029
proton rescattering $\pm$10%	+0.034 -0.007
Fermi motion ($\pm$ 5MeV/c)	$\pm$ 0.008
Sub-total	+0.127 -0.039
Detector effects	
Cross talk $\pm$0.25%	+0.044 -0.034
PMT resolution $\pm$10%	+0.034 -0.015
Quenching constant $\pm$0.0023	+0.011 +0.016
Sub-total	+0.058 -0.037
Reconstruction effects	
Hit threshold $\pm$15%	$\pm$ 0.049
Muon momemtum scale $\pm$2.7%	-0.005 +0.005
Angular resolution (smeared by 0.009)	$\pm$ 0.011
Sub-total	+0.050 -0.050
Total	+0.174 -0.116

Table 8.6: Systematic errors for the overall CC1π^+ to CCQE cross section ratio.

source of systematic	error
MC statistics	+0.015 -0.015
Model effects	
M_A (CCQE) $\pm$0.1	+0.017 -0.018
Bodek/Yang Corr $\pm$30%	-0.036 +0.038
Nπ weighting	$\pm$ 0.066
Neutrino Flux	+0.010 -0.011
Sub-total	+0.079 -0.078
Nuclear effects	
π absorption $\pm$30%	+0.059 -0.088
π inelastic scattering $\pm$30%	+0.023 +0.021
proton rescattering $\pm$10%	+0.018 +0.062
Fermi motion ($\pm$ 5MeV/c)	$\pm$ 0.005
Sub-total	+0.089 -0.088
Detector effects	
Cross talk $\pm$0.25%	+0.020 +0.033
PMT resolution $\pm$10%	+0.009 -0.010
Quenching constant $\pm$0.0023	+0.025 -0.007
Sub-total	+0.042 -0.012
Reconstruction effects	
Hit threshold $\pm$15%	$\pm$ 0.020
Muon momemtum scale $\pm$2.7%	-0.048 +0.111
Angular resolution (smeared by 0.009)	$\pm$ 0.021
Sub-total	+0.115 -0.056
Total	+0.171 -0.132

Table 8.7: Systematic errors for the CC1π^+ to CCQE cross section ratio in the first energy bin.

source of systematic	error
MC statistics	+0.031 -0.031
Model effects	
M_A (CCQE) $\pm$0.1	+0.026 -0.026
Bodek/Yang Corr $\pm$30%	-0.029 +0.032
Nπ weighting	$\pm$ 0.075
Neutrino Flux	+0.022 -0.021
Sub-total	+0.088 -0.087
Nuclear effects	
π absorption $\pm$30%	+0.022 +0.014
π inelastic scattering $\pm$30%	+0.186 -0.151
proton rescattering $\pm$10%	+0.084 -0.143
Fermi motion ($\pm$ 5MeV/c)	$\pm$ 0.005
Sub-total	+0.205 -0.208
Detector effects	
Cross talk $\pm$0.25%	+0.032 -0.080
PMT resolution $\pm$10%	+0.035 -0.002
Quenching constant $\pm$0.0023	-0.024 +0.031
Sub-total	+0.057 -0.084
Reconstruction effects	
Hit threshold $\pm$15%	$\pm$ 0.046
Muon momemtum scale $\pm$2.7%	-0.183 +0.042
Angular resolution (smeared by 0.009)	$\pm$ 0.025
Sub-total	+0.067 -0.190
Total	+0.242 -0.308

Table 8.8: Systematic errors for the CC1π^+ to CCQE cross section ratio in the second energy bin.

source of systematic	error
MC statistics	+0.044 -0.044
Model effects	
M_A (CCQE) $\pm$0.1	+0.019 -0.018
Bodek/Yang Corr $\pm$30%	-0.030 +0.032
Nπ weighting	$\pm$ 0.088
Neutrino Flux	+0.034 -0.033
Sub-total	+0.102 -0.100
Nuclear effects	
π absorption $\pm$30%	+0.189 -0.003
π inelastic scattering $\pm$30%	+0.050 +0.138
proton rescattering $\pm$10%	-0.028 +0.114
Fermi motion ($\pm$ 5MeV/c)	$\pm$ 0.007
Sub-total	+0.260 -0.029
Detector effects	
Cross talk $\pm$0.25%	+0.082 -0.051
PMT resolution $\pm$10%	+0.054 -0.032
Quenching constant $\pm$0.0023	+0.058 +0.045
Sub-total	+0.114 -0.060
Reconstruction effects	
Hit threshold $\pm$15%	$\pm$ 0.054
Muon momemtum scale $\pm$2.7%	+0.107 +0.013
Angular resolution (smeared by 0.009)	$\pm$ 0.042
Sub-total	+0.127 -0.068
Total	+0.330 -0.145

Table 8.9: Systematic errors for the CC1π^+ to CCQE cross section ratio in tht third energy bin.

source of systematic	error
MC statistics	+0.066 -0.066
Model effects	
M_A (CCQE) $\pm$0.1	-0.001 -0.013
Bodek/Yang Corr $\pm$30%	-0.026 +0.029
Nπ weighting	$\pm$ 0.111
Neutrino Flux	+0.085 -0.077
Sub-total	+0.143 -0.138
Nuclear effects	
π absorption $\pm$30%	+0.148 +0.015
π inelastic scattering $\pm$30%	+0.043 -0.197
proton rescattering $\pm$10%	+0.112 -0.087
Fermi motion ($\pm$ 5MeV/c)	$\pm$ 0.032
Sub-total	+0.193 -0.218
Detector effects	
Cross talk $\pm$0.25%	+0.074 -0.058
PMT resolution $\pm$10%	+0.037 -0.029
Quenching constant $\pm$0.0023	-0.025 -0.011
Sub-total	+0.083 -0.069
Reconstruction effects	
Hit threshold $\pm$15%	$\pm$ 0.109
Muon momemtum scale $\pm$2.7%	+0.344 -0.396
Angular resolution (smeared by 0.009)	$\pm$ 0.216
Sub-total	+0.421 -0.464
Total	+0.496 -0.540

Table 8.10: Systematic errors for the CC1π^+ to CCQE cross section ratio in the fourth energy bin.

source of systematic	error
MC statistics	$\pm$ 0.009
Reconstruction effects	
Hit threshold $\pm$15%	$\pm$ 0.010
Nuclear effects	
π absorption $\pm$30%	$\pm$ 0.016
π inelastic scattering $\pm$30%	$\pm$ 0.018
proton rescattering $\pm$10%	$\pm$ 0.016
Detector effects	
Cross talk $\pm$0.25%	$\pm$ 0.009
PMT resolution $\pm$10%	$\pm$ 0.009
Quenching constant $\pm$0.0023%	$\pm$ 0.009

Table 8.11: Statistical errors for the overall CCpπ^+ to CCQE cross section ratio for the different MC samples.

source of systematic	error
MC statistics	$\pm$ 0.011
Reconstruction effects	
Hit threshold $\pm$15%	$\pm$ 0.011
Nuclear effects	
π absorption $\pm$30%	$\pm$ 0.019
π inelastic scattering $\pm$30%	$\pm$ 0.021
proton rescattering $\pm$10%	$\pm$ 0.019
Detector effects	
Cross talk $\pm$0.25%	$\pm$ 0.011
PMT resolution $\pm$10%	$\pm$ 0.011
Quenching constant $\pm$0.0023%	$\pm$ 0.011

Table 8.12: Statistical errors for the overall CC1π^+ to CCQE cross section ratio for the different MC samples.

Chapter 9

Results and Discussion

We discuss the results on the measurement of the cross section of the single pion interaction normalized to charged current quasi-elastic interactions in this Chapter. We present the measurement through different tables, given the measurement integrated in energy and for the different energy bins. We present first the measurement of the exclusive (CCpπ^+) cross section normalized to CCQE, and after, the measurement of the inclusive (CC1π^+) cross section normalized to CCQE. The statistical and systematic errors are also quoted.

The results are compared with those ones from the MC prediction and from previous experimental results. The agreement between them is discussed.

9.1 Measurement of the cross section of the single pπ^+ interaction normalized to CCQE interaction

The **measurement of the cross section of the single pπ^+ interaction normalized to the CCQE interaction integrated in the whole neutrino energy range** is quoted in Table 9.1. Furthermore, the MC prediction is also quoted with the corresponding statistical error. The expected measurement is obtained considering the number of events in the initial sample with the interaction vertex inside the fiducial volume for the different selections. The result is presented in Figure 9.1, where the measurement and the MC prediction are shown.

Measurement	MC prediction
0.614 ± 0.061 (stat.) $^{+0.121}_{-0.082}$ (syst.)	0.565 ± 0.002 (stat.)

Table 9.1: Measurment of the CC$p\pi^+$ to CCQE cross section ratio.

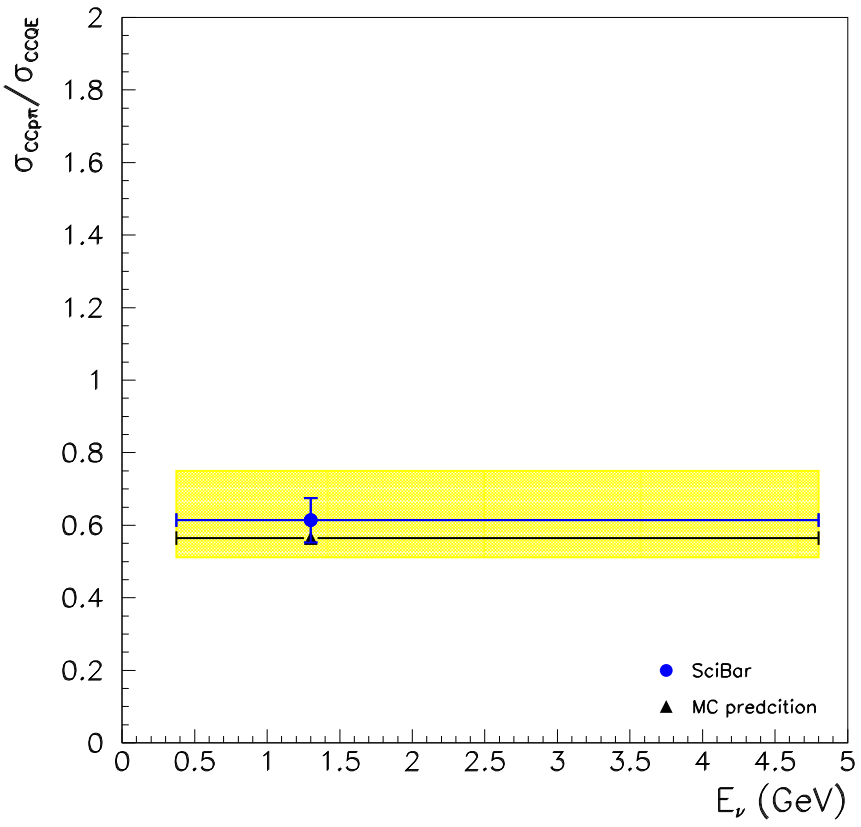

Figure 9.1: Comparison between the total exclusive measurement normalized to CCQE and MC prediction. Blue point corresponds to data result, and blue error bar to the corresponding statistical error; yellow box represents the total error. Black point respresents the MC prediction.

The **measurement of the cross section of the single pπ^+ interaction normalized to the CCQE interaction for the different neutrino energy bins** is quoted in Table 9.2 where the MC prediction is also shown. The result is presented in Figure 9.2, where the measurement and the MC prediction are shown. The measurement is in good agreement with MC prediction.

Eν (GeV)	Measurement	MC prediction
$\leq$ 1.35	0.429 ± 0.071 (stat.) $^{+0.138}_{-0.090}$ (syst.)	0.441 ± 0.002 (stat.)
1.35-1.72	0.689 ± 0.112 (stat.) $^{+0.144}_{-0.211}$ (syst.)	0.695 ± 0.004 (stat.)
1.72-2.22	0.788 ± 0.126 (stat.) $^{+0.210}_{-0.093}$ (syst.)	0.782 ± 0.006 (stat.)
2.22 $\leq$	0.674 ± 0.146 (stat.) $^{+0.302}_{-0.340}$ (syst.)	0.860 ± 0.009 (stat.)

Table 9.2: Measurment of the energy dependent CCpπ^+ to CCQE cross section ratio.

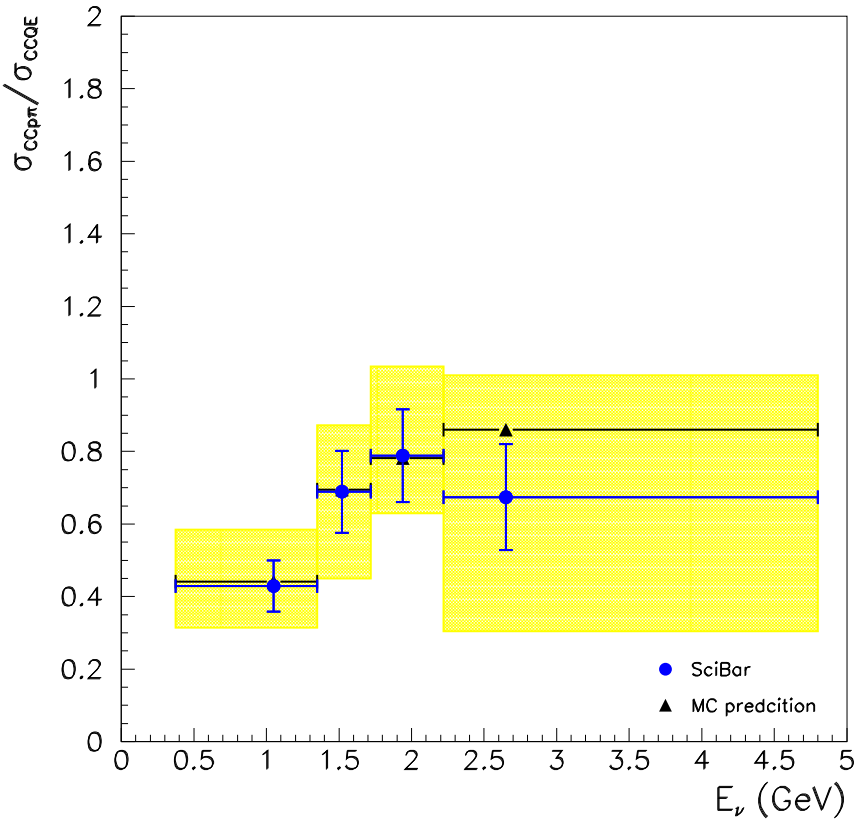

Figure 9.2: Comparison between the energy dependent exclusive measurement normalized to CCQE and MC prediction as a function of the neutrino energy. Blue points correspond to data result, and blue error bars to the corresponding statistical errors; yellow boxes represent the total error. The width of the box represents the size of the neutrino energy bin. Black points respresent the MC prediction.

9.2 Measurement of the cross section of the single $1\pi^+$ interaction normalized to CCQE interaction

The **measurement of the cross section of the single $1\pi^+$ interaction normalized to the CCQE interaction integrated in the whole neutrino energy range** is quoted in Table 9.3. The result is presented in Figure 9.3, where the measurement and the MC prediction are shown.

Measurement	MC prediction
0.850 ± 0.080 (stat.) $^{+0.174}_{-0.116}$ (syst.)	0.740 ± 0.002 (stat.)

Table 9.3: Measurment of the CC$1\pi^+$ to CCQE cross section ratio.

The **measurement of the cross section of the single $1\pi^+$ interaction normalized to the CCQE interaction for the different neutrino energy bins** is quoted in Table 9.4 where the MC prediction is also shown. The result is also presented in Figure 9.4, where the measurement and the MC prediction are shown.

Eν (GeV)	Measurement	MC prediction
≤ 1.35	0.522 ± 0.103 (stat.) $^{+0.171}_{-0.132}$ (syst.)	0.535 ± 0.002 (stat.)
1.35-1.72	0.960 ± 0.179 (stat.) $^{+0.242}_{-0.308}$ (syst.)	0.924 ± 0.005 (stat.)
1.72-2.22	1.170 ± 0.206 (stat.) $^{+0.330}_{-0.145}$ (syst.)	1.117 ± 0.007 (stat.)
$2.22 \leq$	1.135 ± 0.225 (stat.) $^{+0.496}_{-0.540}$ (syst.)	1.300 ± 0.012 (stat.)

Table 9.4: Measurment of the energy dependent CC$1\pi^+$ to CCQE cross section ratio.

The presented measurement is in good agreement with MC prediction.

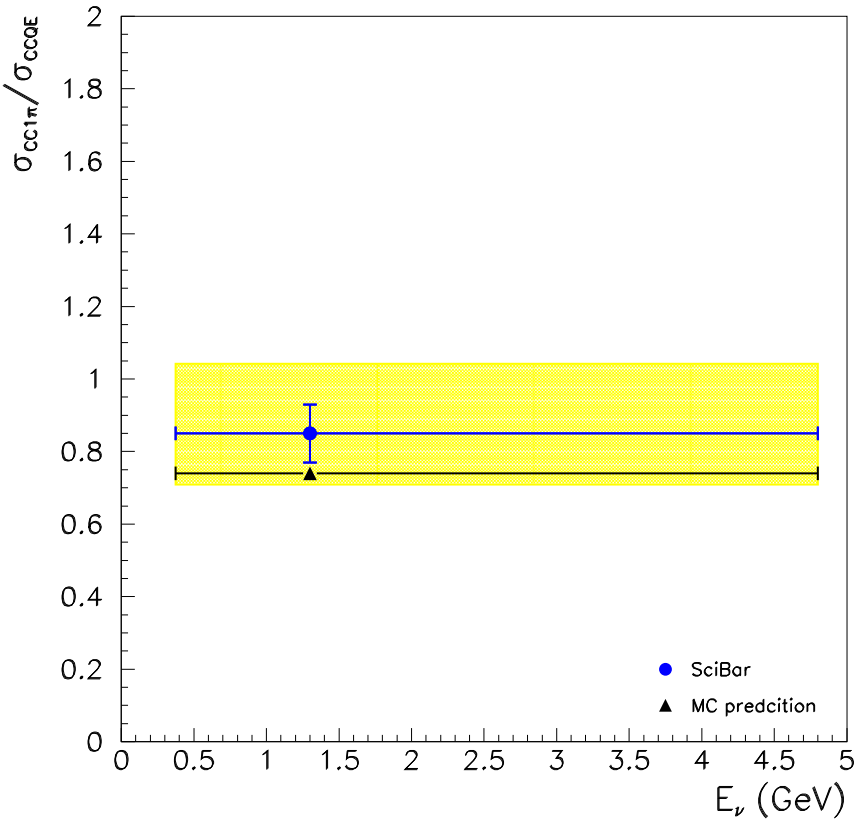

Figure 9.3: Comparison between the total inclusive measurement normalized to CCQE and MC prediction. Blue point corresponds to data result, and blue error bar to the corresponding statistical error; yellow box represents the total error. Black point respresents the MC prediction.

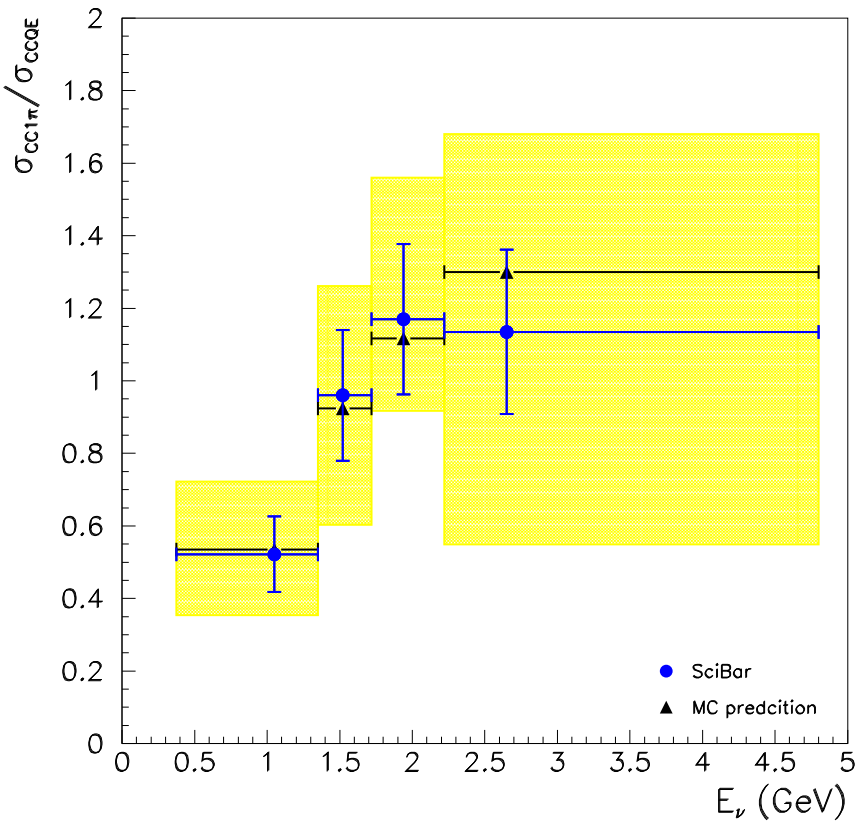

Figure 9.4: Comparison between the energy dependent inclusive measurement normalized to CCQE and MC prediction. Blue points correspond to data result, and blue error bars the to corresponding statistical errors; yellow boxes represent the total error. The width of the box represents the size of the neutrino energy bin. Black points respresent the MC prediction.

9.3 Previous experiments and their results

We present in this section the measurement normalized to CCQE for the previous experimental results. There are only a few experiments that have made measurements of the CC1π^+ interaction for muon neutrinos in the neutrino energy region of K2K experiment.

The Argonne (ANL) bubble chamber experiment provided cross section measurements of all 3 CC1π interaction modes [113], [94] and the CCQE interaction [101]. Of the two results published for CCpπ^+ production by the ANL experiment, the later paper incorporates the data for both experiments, so only the later result is included in the plots.

The Brookhaven (BNL) bubble chamber experiment also made measurements of all the 3 CC1π modes [114], but they did not publish a measurement of the CCQE cross section explicitly (though they did publish a measurement of the CCQE axial-vector mass M_A [102]). However, they provide the cross section ratio of the CCpπ^+ to CCQE interaction in [115].

The Gargamelle (GGM) bubble chamber experiment done at CERN made a measurement of the cross section of the pπ^+ mode [95] and the CCQE cross section [116], [103]. The most recent result on the CCQE cross section is used here to make the comparison; which is the measurement from [116].

The MiniBooNe neutrino oscillation experiment has published a preliminary result for the CC1π^+ cross section [117], and the paper also explicitly shows the CC1π^+ to CCQE cross section as a function of neutrino energy.

To compute the ratio of the cross sections for the ANL experiment we use the information of single pion pπ^+ and 1π^+ cross section from Table 9.5, and the information of CCQE from 9.6. For the GGM experiment the measurement of the single pion pπ^+ cross section is taken from Table 9.7, and for CCQE from 9.8. Table 9.9 shows the single pion pπ^+ cross section ratio for both ANL and GGM set of previous experimental results, and for the BNL results; and Table 9.10 shows the single pion 1π^+ cross section ratio for the ANL previous experimental results and MiniBooNe preliminary results.

$E_\nu(GeV)$	$\sigma(\nu_\mu p \to \mu^- p\pi^+)$ (10^{-38} cm^2)	$\sigma(\nu_\mu N \to \mu^- 1\pi^+)$ (10^{-38} cm^2)
0.30 - 0.50	0.019 ± 0.006	0.028 ± 0.008
0.50 - 0.75	0.155 ± 0.017	0.216 ± 0.021
0.75 - 1.00	0.335 ± 0.030	0.444 ± 0.036
1.00 - 1.25	0.435 ± 0.042	0.567 ± 0.049
1.25 - 1.50	0.488 ± 0.055	0.654 ± 0.066
1.50 - 2.50	0.707 ± 0.087	-
2.50 - 3.50	0.722 ± 0.174	-
3.50 - 6.00	0.552 ± 0.150	-

Table 9.5: ANL experiment: Radecky et al 1982 single pπ^+ measurement [94].

$E_\nu(GeV)$	$\sigma(\nu_\mu n \to \mu^- p)$ (10^{-38} cm^2)
0.15 - 0.30	0.29 ± 0.08
0.30 - 0.50	0.57 ± 0.10
0.50 - 0.70	0.77 ± 0.10
0.70 - 0.90	0.72 ± 0.14
0.90 - 1.25	1.12 ± 0.12
1.25 - 1.50	1.15 ± 0.28
1.50 - 2.00	1.02 ± 0.21
2.00 - 6.00	1.18 ± 0.33

Table 9.6: ANL experiment: Barish et al 1977 CCQE measurement [101].

$E_\nu(GeV)$	$\sigma(\nu_\mu p \to \mu^- p\pi^+)$ (10^{-38} cm^2)
1.00 - 1.5	0.47 ± 0.12
1.50 - 2.00	0.60 ± 0.09
2.00 - 3.00	0.50 ± 0.07
3.00 - 4.00	0.45 ± 0.08
4.00 - 10.0	0.47 ± 0.09

Table 9.7: GGM experiment: Lerche et al 1978 single pπ^+ measurement [95]

.

$E_\nu(GeV)$	$\sigma(\nu_\mu n \to \mu^- p)$ (10^{-38} cm^2)
1.00 - 1.25	0.96 ± 0.16
1.25 - 1.50	0.85 ± 0.14
1.50 - 2.00	0.67 ± 0.12
2.00 - 2.50	0.92 ± 0.11
2.50 - 3.00	0.94 ± 0.13
3.00 - 4.00	0.90 ± 0.12
4.00 - 8.50	0.70 ± 0.12

Table 9.8: GGM experiment: Pohl et al 1979 CCQE measurement [116].

Since the measurements were not done in exactly the same energy bins, they were linearly combined as:

- The $\sigma(\nu_\mu n \to \mu^- p)$ value in 9.6 for energy bin from 0.70 to 0.90 GeV is taken as $\sigma(\nu_\mu n \to \mu^- p)$ for energy bin from 0.75 to 0.95 GeV.
- The $\sigma(\nu_\mu n \to \mu^- p)$ value in 9.6 for energy bin from 0.90 to 1.25 GeV is taken as $\sigma(\nu_\mu n \to \mu^- p)$ for energy bin from 1.00 to 1.25 GeV.
- The $\sigma(\nu_\mu n \to \mu^- p)$ value in 9.6 for energy bin from 1.50 to 2.00 GeV plus a fraction of the $\sigma(\nu_\mu n \to \mu^- p)$ value for energy bin from 2.00 to 6.00 GeV is taken as $\sigma(\nu_\mu n \to \mu^- p)$ for energy bin from 1.50 to 2.50 GeV. The fraction taken is 1/8 of the total value.
- The $\sigma(\nu_\mu n \to \mu^- p)$ value in 9.8 for energy bin from 1.00 to 1.50 GeV is computed as the mean value of the measurement from 1.00 to 1.25 and 1.25 to 1.50 GeV.
- The $\sigma(\nu_\mu n \to \mu^- p)$ value in 9.8 for energy bin from 2.00 to 3.00 GeV is computed as the mean value of the measurement from 2.00 to 2.50 and 2.50 to 3.00 GeV.

E_ν(GeV)	ANL		E_ν(GeV)	BNL		E_ν(GeV)	GGM
0.30 - 0.50	0.033 ± 0.012		0.5 - 0.70	0.05 ± 0.03		1.00 - 1.50	0.520 ± 0.180
0.50 - 0.75	0.201 ± 0.034		0.70 - 0.90	0.31 ± 0.04		1.50 - 2.00	0.896 ± 0.210
0.75 - 1.00	0.465 ± 0.100		0.90 - 1.10	0.45 ± 0.04		2.00 - 3.00	0.538 ± 0.124
1.00 - 1.25	0.388 ± 0.056		1.10 - 1.30	0.52 ± 0.05		3.00 - 4.00	0.500 ± 0.111
1.25 - 1.50	0.424 ± 0.114		1.30 - 1.50	0.56 ± 0.05			
1.50 - 2.50	0.604 ± 0.136		1.50 - 1.70	0.58 ± 0.06			
			1.70 - 2.10	0.64 ± 0.05			
			2.10 - 2.70	0.66 ± 0.07			
			2.70 - 4.10	0.78 ± 0.08			

Table 9.9: $R = \frac{\sigma(\nu_\mu p \to \mu^- p \pi^+)}{\sigma(\nu_\mu n \to \mu^- p)}$.

E_ν(GeV)	ANL		E_ν(GeV)	MiniBooNe
0.30 - 0.50	0.049 ± 0.016		0.5 - 0.7	0.20 ± 0.10
0.50 - 0.75	0.280 ± 0.046		0.7 - 0.8	0.32 ± 0.10
0.75 - 1.00	0.617 ± 0.130		0.8 - 0.9	0.44 ± 0.11
1.00 - 1.25	0.506 ± 0.070		0.9 - 1.0	0.54 ± 0.10
1.25 - 1.50	0.569 ± 0.150		1.0 - 1.1	0.67 ± 0.17
-	-		1.1 - 1.2	0.77 ± 0.17
-	-		1.2 - 1.3	0.79 ± 0.21
-	-		1.3 - 1.4	0.93 ± 0.30

Table 9.10: $R = \frac{\sigma(\nu_\mu N \to \mu^- n' \pi^+)}{\sigma(\nu_\mu n \to \mu^- p)}$.

9.4 Comparison with the previous experiments

9.4.1 Scaling the result

In order to make feasible the comparison we need to scale the results to take into account the difference among the targets that were used in the different experiments and in SciBar. SciBar is made of polystyrene (C_8H_8) which has 56 protons and 48 neutrons. Therefore, what we are really measuring is the cross section ratio over C_8H_8; not over the single nucleon. For the exclusive

cross section ratio, that is:

$$\sigma(\nu(C_8H_8) \to \mu^- p\pi^+) = 56\sigma(\nu p \to \mu^- p\pi^+)$$
$$\sigma(\nu(C_8H_8) \to \mu^- p) = 48\sigma(\nu n \to \mu^- p)$$

being the measurement

$$\begin{aligned} R_{measured} &= \frac{\sigma(\nu(C_8H_8) \to \mu^- p\pi^+)}{\sigma(\nu(C_8H_8) \to \mu^- p)} \\ &= \frac{7\sigma(\nu p \to \mu^- p\pi^+)}{6\sigma(\nu n \to \mu^- p)} \end{aligned} \tag{9.1}$$

Hence, we scale the cross section measurement of the single $p\pi^+$ normalized to CCQE by a factor being 6/7 in order to get the single nucleon cross section ratio. This scaling is not needed in the cases of the ANL, BNL and GGM results because they provide the cross section over a single nucleon.

In the inclusive cross section ratio, scaling the results is not so straight forward. We are considering for this measurement the following cross sections:

$$\sigma(\nu(C_8H_8) \to \mu^- p\pi^+) = 56\sigma(\nu p \to \mu^- p\pi^+)$$
$$\sigma(\nu(C_8H_8) \to \mu^- n\pi^+) = 48\sigma(\nu n \to \mu^- n\pi^+)$$
$$\sigma(\nu(C_8H_8) \to \mu^- p) = 48\sigma(\nu n \to \mu^- p)$$

being the measurement

$$\begin{aligned} R_{measured} &= \frac{\sigma(\nu(C_8H_8) \to \mu^- p\pi^+) + \sigma(\nu(C_8H_8) \to \mu^- n\pi^+)}{\sigma(\nu(C_8H_8) \to \mu^- p)} \\ &= \frac{7\sigma(\nu p \to \mu^- p\pi^+) + 6\sigma(\nu n \to \mu^- n\pi^+)}{6\sigma(\nu n \to \mu^- p)} \end{aligned} \tag{9.2}$$

The scaling factor can be extracted from

$$R = f \times R_{measured}$$

where the ratio R is the single nucleon cross section ratio.

We define the ratios:

$$S_p \equiv \frac{\sigma(\nu(C_8H_8) \to \mu^- p\pi^+)}{\sigma(\nu(C_8H_8) \to \mu^- p\pi^+) + \sigma(\nu(C_8H_8) \to \mu^- n\pi^+)}$$
$$S_n \equiv \frac{\sigma(\nu(C_8H_8) \to \mu^- n\pi^+)}{\sigma(\nu(C_8H_8) \to \mu^- p\pi^+) + \sigma(\nu(C_8H_8) \to \mu^- n\pi^+)}$$

By assuming that the ratios S_p and S_n are approximately the same in data as in the MC. Then,

$$R = [(6/7)S_p + S_n]R_{measured}$$

Thus the scaling factor is $f = (6/7)S_p + S_n$ where S_p and S_n are calculated from the MC. The obtained value of f is 0.89; it was also obtained for the energy dependent cross section ratio turning out to be approximately the same[1].

9.4.2 Comparison

Figure 9.5 shows the comparison of the total exclusive measurement with previous experimental results. Figure 9.6 shows the comparison of the energy dependent exclusive measurement with previous experimental results.

Figure 9.7 shows the comparison of the total inclusive measurement with previous experimental results. Figure 9.8 shows the comparison of the energy dependent inclusive measurement with previous experimental results. The presented measurement are in good agreement with previous experimental results.

[1]The f value of 0.89 can be also obtained from the presented cross section ratio measurements: assuming a double ratio in S_p and S_n, that is, normalizing the cross section to the CCQE cross section.

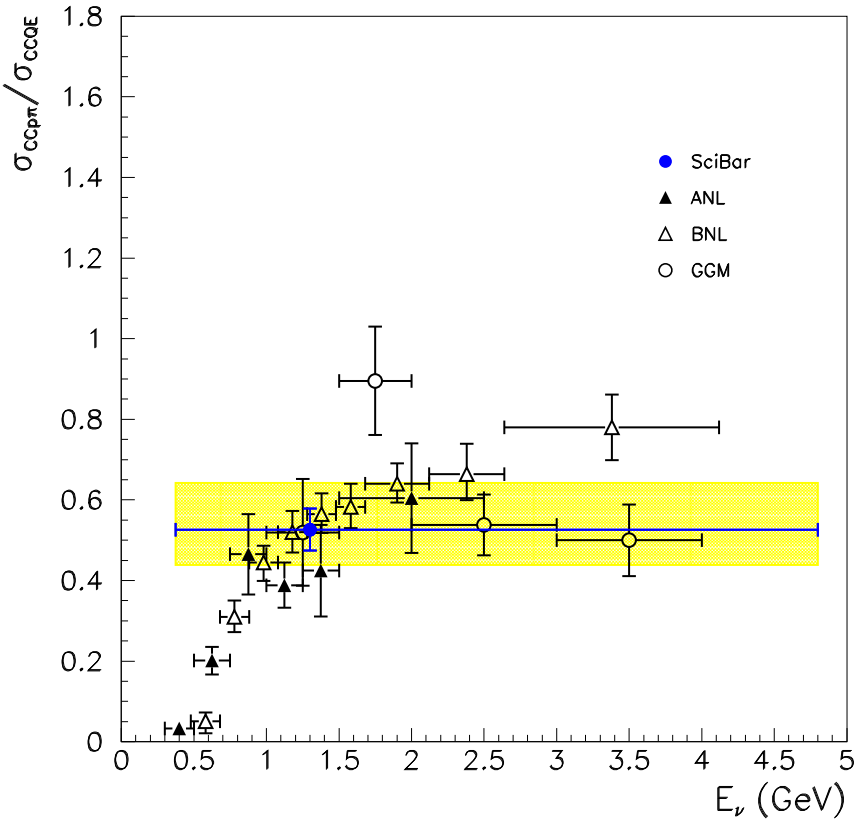

Figure 9.5: Comparison between the total exclusive measurement normalized to CCQE, and ANL [94, 113], BNL [115], and GGM [95, 116] previous experimental results. Blue point corresponds to SciBar data result, and blue error bar to the corresponding statistical errors; yellow box represents the total error.

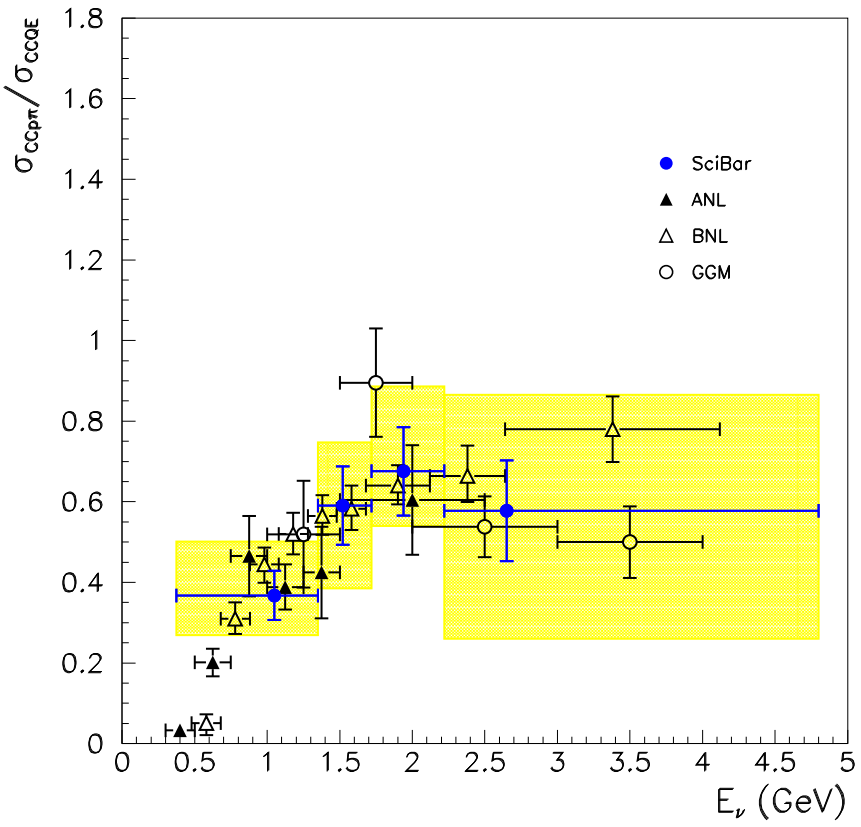

Figure 9.6: Comparison between the energy dependent exclusive measurement normalized to CCQE, and ANL [94, 113], BNL [115], and GGM [95, 116] previous experimental results. Blue points correspond to SciBar data result, and blue error bars to the corresponding statistical errors; yellow boxes represent the total error. The width of the box represents the size of the neutrino energy bin.

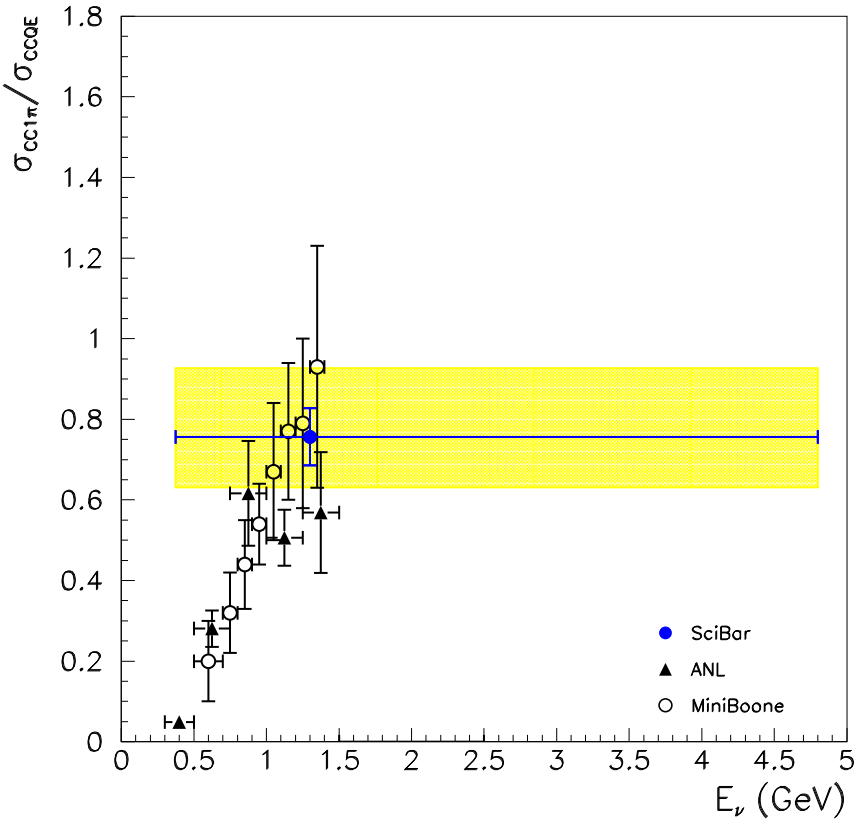

Figure 9.7: Comparison between the overall inclusive measurement normalized to CCQE, and ANL [94, 113], and MiniBooNE [117] previous experimental results. Blue point corresponds to SciBar data result, and blue error bar to the corresponding statistical errors; yellow box represents the total error.

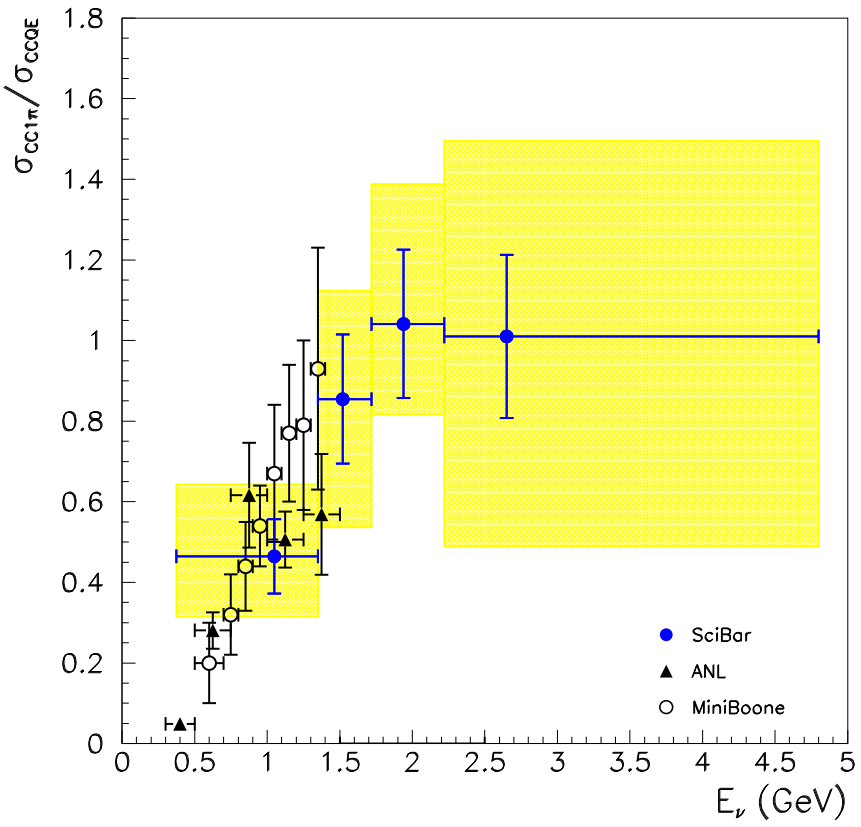

Figure 9.8: Comparison between the energy dependent inclusive measurement normalized to CCQE, and ANL [94, 113], and MiniBooNE [117] previous experimental results. Blue points correspond to SciBar data result, and blue error bars to the corresponding statistical errors; yellow boxes represent the total error. The width of the box represents the size of the neutrino energy bin.

9.5 Measurement of the cross section of the single nπ^+ interaction normalized to CCQE

Once the ratio of both inclusive and exclusive single pion cross section were measured, we can extract the ratio of the cross section of the interaction channel nπ^+. This is presented in Figure 9.9 and in Figure 9.10, only showing statistical errors.

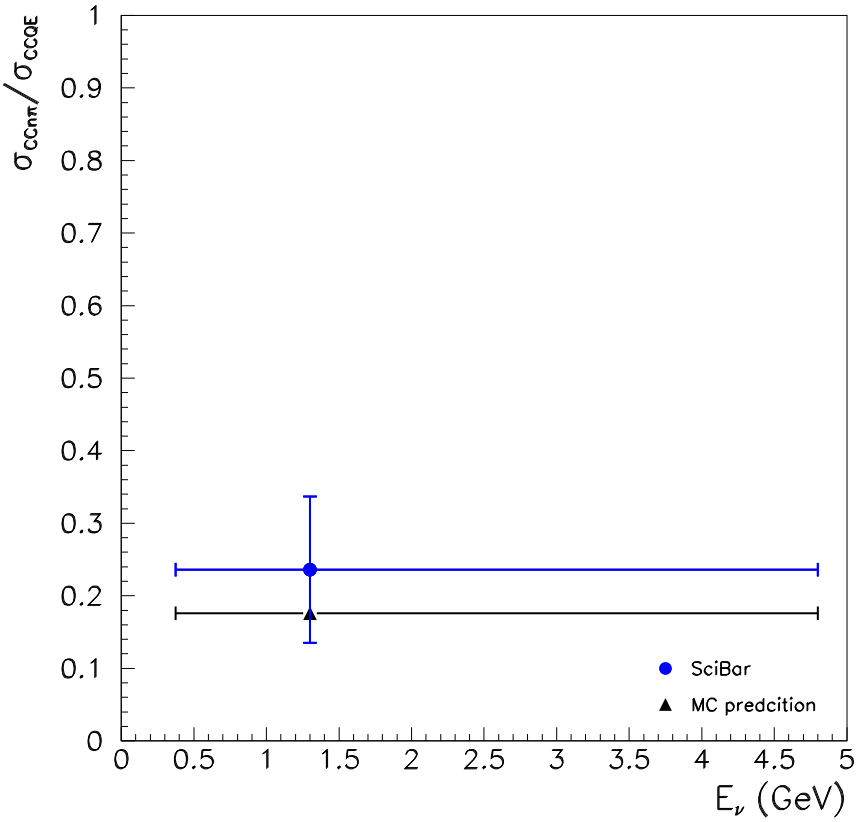

Figure 9.9: Comparison between the CCnπ^+ measurement normalized to CCQE and MC prediction. Blue point corresponds to data result, and blue error bar to the corresponding statistical error. Black point respresents the MC prediction.

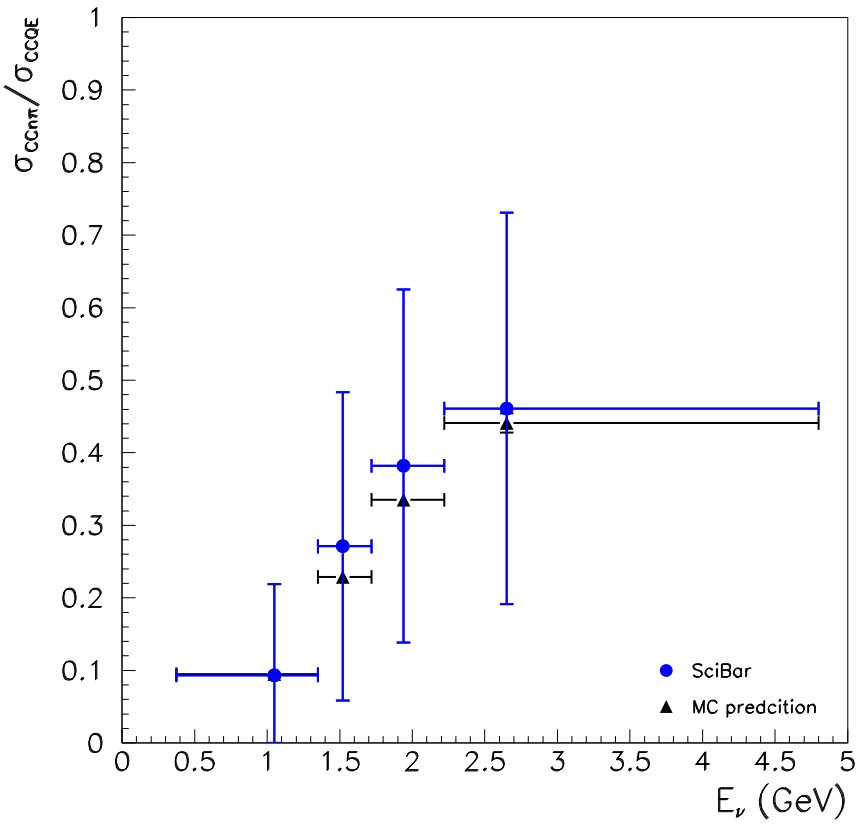

Figure 9.10: Comparison between the energy dependent CC$n\pi^+$ measurement normalized to CCQE and MC prediction. Blue points correspond to data result, and blue error bars to the corresponding statistical error. Black points respresents the MC prediction.

9.6 Cross checks

In this final section of the Results and Discussion Chapter we want to present two cross checks of the measurements that have been presented. First, we show the measurement of the exclusive cross section ratio using the single pion selection performed in the the two and three track sample, only in the two track sample, and only in the three track sample. We already know that the two track sample is the dominant, so we expect obtain similar results using only this sample in the selection. But we want to study how these two measurements compare with the one done only using the three track sample; since the statistics of this samples is very small we also expect larger

error bars, for both statistical and systematic errors. Figure 9.11 shows the comparison among the three total measurements. Figure 9.12 shows the comparison among the three measurements as a function of the neutrino energy. Appendix C.1 and C.2 show explicitly the measurement and the systematic errors.

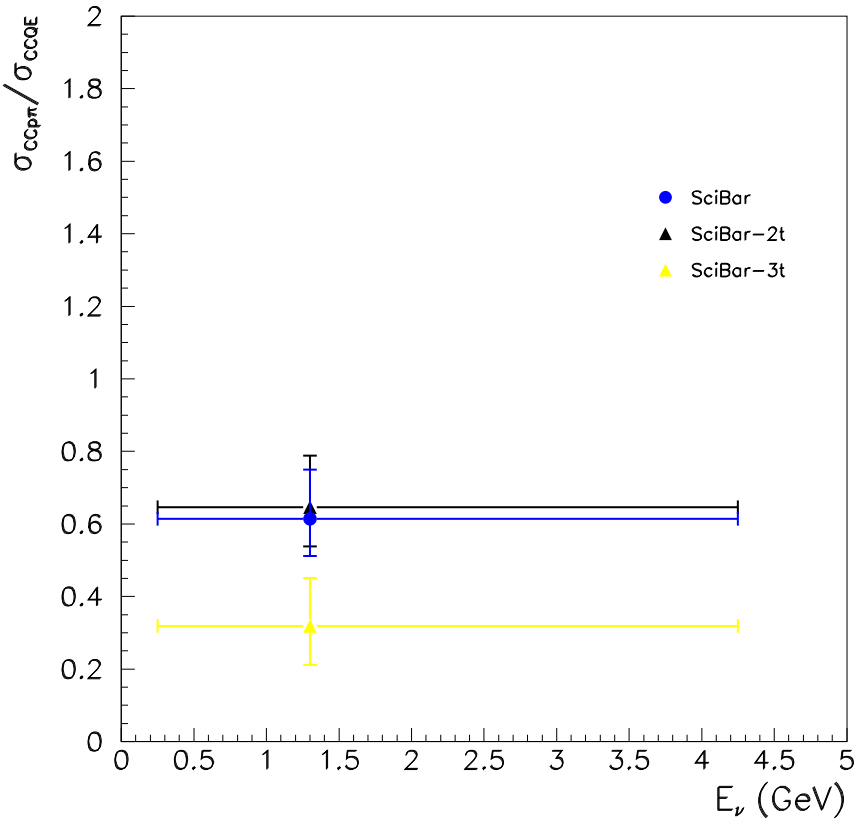

Figure 9.11: Comparison between the total measurement normalized to CCQE for the three ways of selecting CCpπ^+ : two and the track sample (blue), two track sample (black), three track sample (yellow).

The second cross check consist on evaluating how sensible is the measurement to the final hadron mass in the single pion selection. We set this mass to be the Breit-Wigner mass given us a value of 1.232 GeV. We measured the cross section using different mass, from 1.2 GeV to 1.3GeV in steps of 0.1 GeV. Figure 9.13 shows the measurement of the single pπ^+ cross section ratio as a function of the neutrino energy. Figure 9.14 shows the measurement of the single 1π^+ cross

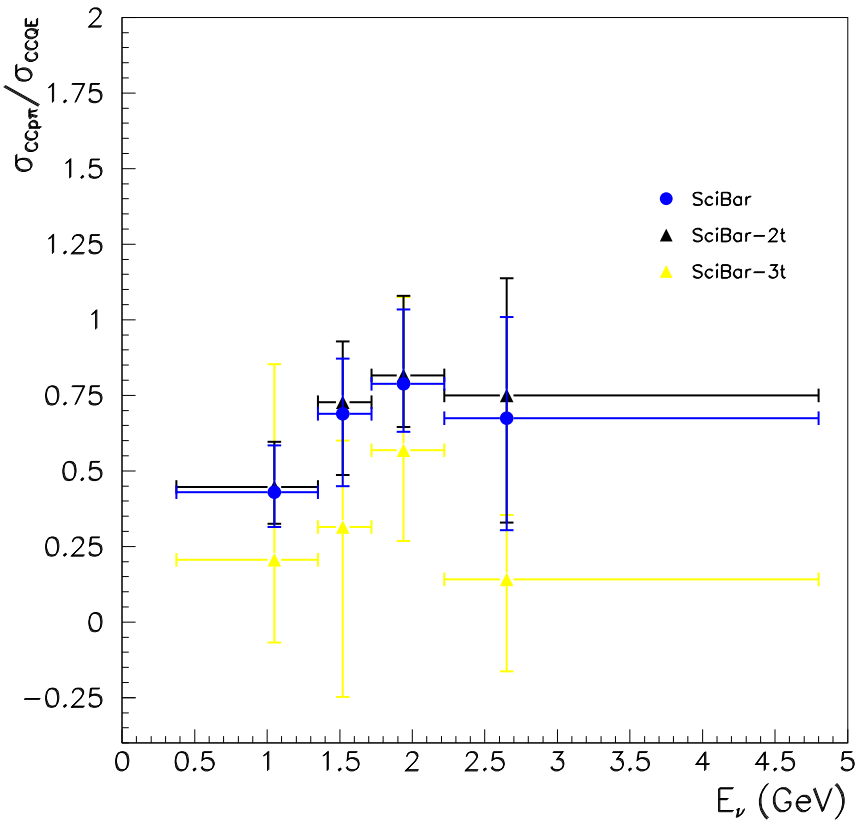

Figure 9.12: Comparison between the energy dependent measurement normalized to CCQE for the three ways of selecting CC$p\pi^+$: two and the track sample (blue), two track sample, three track sample (yellow).

section ratio as a function of the neutrino energy. The possible variations in the measurement are covered only with the statisitcal errors of the nominal measurement.

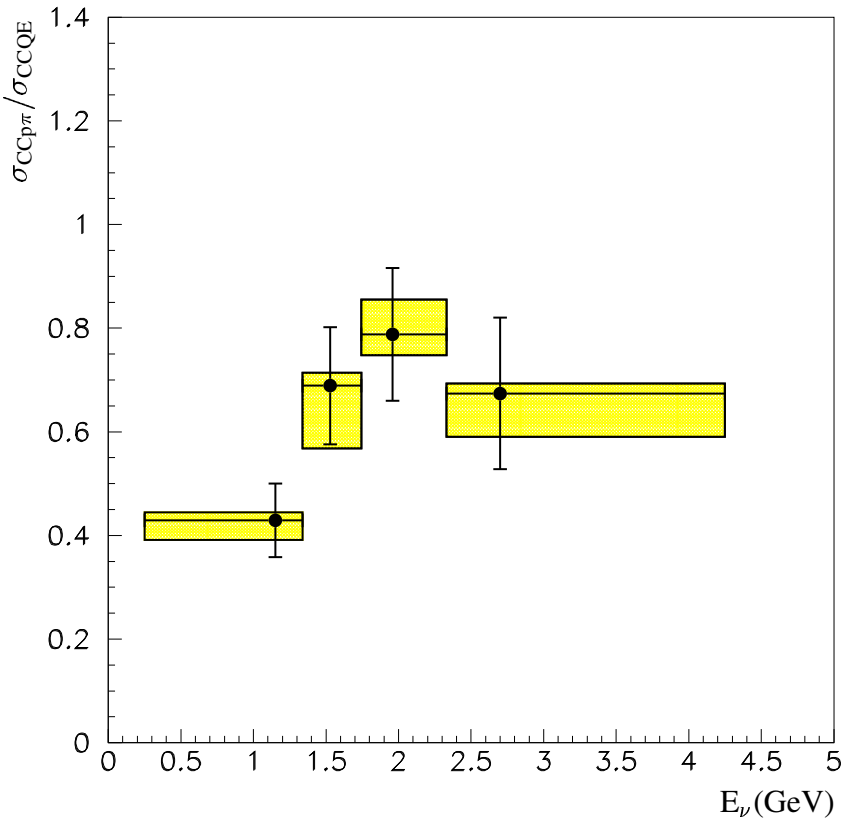

Figure 9.13: Comparison among nominal single $p\pi^+$ measurement and those ones obtained with different final hadron mass values: from 1.2 to 1.3 GeV in steps of 0.1. Black points are data and bars are only statistical errors. The yellow band is the square root of the difference between each one of the measurement for the different values of the final hadron mass and the nominal added quadratically. The positive and negative variations are considered independently.

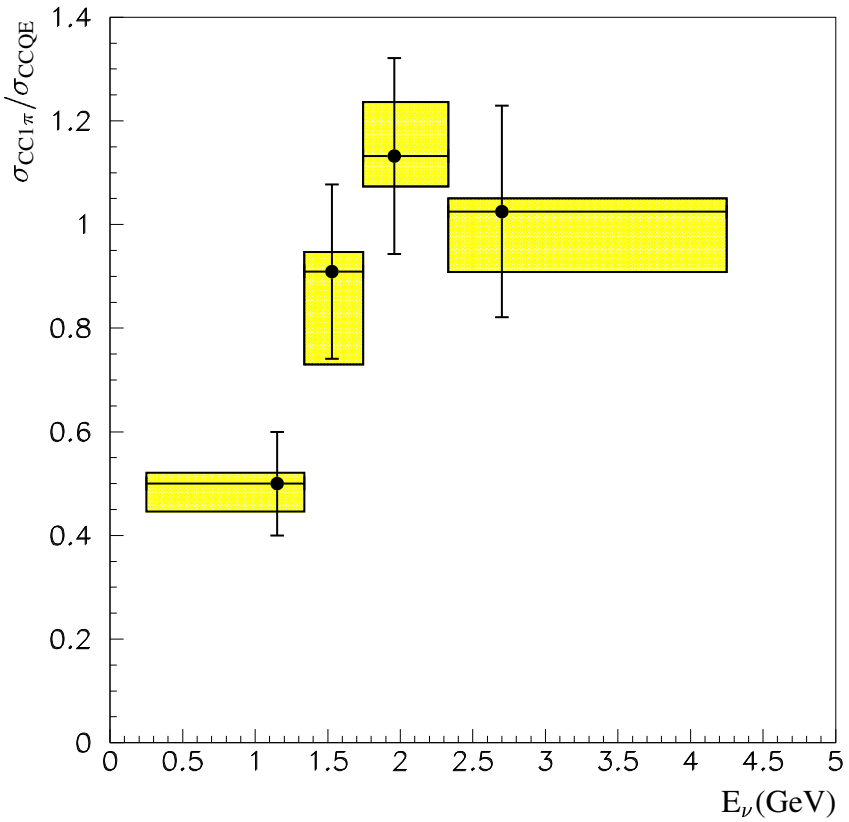

Figure 9.14: Comparison among nominal single $1\pi^+$ measurement and those ones obtained with different final hadron mass values: from 1.2 to 1.3 GeV in steps of 0.1. Black points are data and bars are only statistical errors. The yellow band is the square root of the difference between each one of the measurement for the different values of the final hadron mass and the nominal added quadratically. The positive and negative variations are considered independently.

Chapter 10

Conclusions

Low energy neutrino interactions are studied in support of neutrino oscillation experiments. At the K2K experiment all neutrino interactions are used to compare the number of neutrino events in the Near Detector (ND) and in the Far Detector (SK), among them, the CCQE neutrino interactions are used to compare the energy spectrum in ND and SK. Single Pion interaction is the main background to the CCQE interaction. This interaction is also the second dominant channel at energies around 1 GeV. The aim of this work was to study the single pion interaction and to measure the cross section of this interaction. The measured CCQE cross section is used as a reference.

The measurement was done for the exclusive (CCpπ^+), and the inclusive (CCNπ^+) single pion channel. We provide an overall cross section measurement and an energy dependent measurement.

Table 10.1 shows the measurement of the overall cross section ratio CCpπ^+ to CCQE, and 10.2 the measurement as a function of the neutrino energy.

Measurement
0.614 ± 0.061 (stat.) $^{+0.121}_{-0.082}$ (syst.)

Table 10.1: Measurment of the CCpπ^+ to CCQE cross section ratio.

Table 10.3 shows the measurement of the overall cross section ratio CC1π^+ to CCQE, and 10.4 the measurement as a function of the neutrino energy.

Eν (GeV)	Measurement
≤ 1.35	0.429 ± 0.071 (stat.) $^{+0.138}_{-0.090}$ (syst.)
1.35-1.72	0.689 ± 0.112 (stat.) $^{+0.144}_{-0.211}$ (syst.)
1.72-2.22	0.788 ± 0.128 (stat.) $^{+0.210}_{-0.093}$ (syst.)
$2.22 \leq$	0.674 ± 0.146 (stat.) $^{+0.302}_{-0.340}$ (syst.)

Table 10.2: Measurment of the energy dependent CCpπ^+ to CCQE cross section ratio.

Measurement
0.850 ± 0.080 (stat.) $^{+0.174}_{-0.116}$ (syst.)

Table 10.3: Measurment of the CC1π^+ to CCQE cross section ratio.

Eν (GeV)	Measurement
≤ 1.35	0.522 ± 0.103 (stat.) $^{+0.171}_{-0.132}$ (syst.)
1.35-1.72	0.960 ± 0.179 (stat.) $^{+0.242}_{-0.308}$ (syst.)
1.72-2.22	1.170 ± 0.206 (stat.) $^{+0.330}_{-0.145}$ (syst.)
$2.22 \leq$	1.135 ± 0.225 (stat.) $^{+0.496}_{-0.540}$ (syst.)

Table 10.4: Measurment of the energy dependent CC1π^+ to CCQE cross section ratio.

The presented results are in agreement with results from previous experiments.

Among the prospects on neutrino experiments at low energies the SciBoone experiment [118], the T2K experiment [119, 120, 121] and the MINERvA experiment [122] will be studied the neutrino nucleus interactions both in support of neutrino oscillation experiments and also to study the strong dynamics of the nucleon and nucleus that affect these interactions.

Bibliography

[1] W. Pauli. Pauli's letter of the 4^{th} of December 1930. *CERN-ARCH-PLC Pauli letter collection : letter to Lise Meitner*, 1930.

[2] C. L. Cowan F. Reines. Detection of the free neutrino. *Phys. Rev.*, 92:830–831, 1956.

[3] F. Reines and C. Cowan. The Reines-Cowan experiments: Detecting the Poltergeist. *Los Alamos Sci. (1997) No. 25 4-27*, 1997.

[4] L. D. Landau. On the conservation laws for weak interactions. *Nucl. Phys.*, 3:127–131, 1957.

[5] Salam A. On parity conservation and neutrino mass. *Nuovo Cim.*, 5:299–301, 1957.

[6] Lee T. D. and Yang C. N. Parity Nonconservation And A Two Component Theory Of The Neutrino. *Phys. Rev.*, 105:1671–1675, 1957.

[7] G. Danby et all. Observation of high-energy neutrino reactions and the existence of two kinds of neutrinos. *Phys. Rev. Lett.*, 9:36–44, 1962.

[8] B. T. Cleveland et al. Measurement of the solar electron neutrino flux with the Homestake Chlorine detector. *Astrophys. J.*, 496:505–526, 1998.

[9] K. Kodama et al. Observation of tau-neutrino interactions. *Phys. Lett.*, B504:218–224, 2001.

[10] Precision electroweak measurements on the Z resonance. *Phys. Rept.*, 427:257, 2006.

[11] Ch. Kraus et al. Final results from phase II of the Mainz neutrino mass search in tritium beta decay. *Eur. Phys. J.*, C40:447–468, 2005.

[12] Beat Jegerlehner, Frank Neubig, and Georg Raffelt. Neutrino oscillations and the Supernova 1987A signal. *Phys. Rev.*, D54:1194–1203, 1996.

[13] K. et all Assamagan. Upper limit of the muon-neutrino mass and charged-pion mass from momentum analysis of a surface muon beam. *Phys. Rev. D*, 53(11):6065–6077, Jun 1996.

[14] R. Barate et al. An upper limit on the tau neutrino mass from three- and five-prong tau decays. *Eur. Phys. J.*, C2:395–406, 1998.

[15] Ettore Majorana. Theory of the symmetry of electrons and positrons. *Nuovo Cim.*, 14:171–184, 1937.

[16] H. V. Klapdor-Kleingrothaus, A. Dietz, H. L. Harney, and I. V. Krivosheina. Evidence for neutrinoless double beta decay. *Mod. Phys. Lett.*, A16:2409–2420, 2001.

[17] L. Baudis et al. Limits on the neutrino mass in the 0.1-eV range. *Phys. Rev. Lett.*, 83:41–44, 1999.

[18] D. N. Spergel et al. First year Wilkinson Microwave Anisotropy Probe (WMAP) observations: Determination of cosmological parameters. *Astrophys. J. Suppl.*, 148:175, 2003.

[19] Uros Seljak et al. Cosmological parameter analysis including SDSS Ly-alpha forest and galaxy bias: Constraints on the primordial spectrum of fluctuations, neutrino mass, and dark energy. *Phys. Rev.*, D71:103515, 2005.

[20] A. Pich. The Standard model of electroweak interactions. 1994.

[21] H. Tsujimoto. Relation between CKM and MNS matrices induced by bi-maximal rotations in the seesaw mechanism. *J. Phys. Soc. Jap.*, 75:054101, 2006.

[22] Samoil M. Bilenky, C. Giunti, and W. Grimus. Phenomenology of neutrino oscillations. *Prog. Part. Nucl. Phys.*, 43:1–86, 1999.

[23] Samoil M. Bilenky, C. Giunti, and W. Grimus. Phenomenology of neutrino oscillations. *Prog. Part. Nucl. Phys.*, 43:1–86, 1999.

[24] T. K. Kuo and James Pantaleone. Neutrino oscillations in matter. *Rev. Mod. Phys.*, 61:937, 1989.

[25] M. Freund, M. Lindner, S. T. Petcov, and A. Romanino. Testing matter effects in very long baseline neutrino oscillation experiments. *Nucl. Phys.*, B578:27–57, 2000.

[26] Y. Fukuda et al. Evidence for oscillation of atmospheric neutrinos. *Phys. Rev. Lett.*, 81:1562–1567, 1998.

[27] Y. Fukuda et al. Measurement of the flux and zenith-angle distribution of upward through-going muons by Super-Kamiokande. *Phys. Rev. Lett.*, 82:2644–2648, 1999.

[28] W. W. M. Allison et al. The atmospheric neutrino flavor ratio from a 3.9 fiducial kiloton-year exposure of Soudan 2. *Phys. Lett.*, B449:137–144, 1999.

[29] M. Ambrosio et al. Measurement of the atmospheric neutrino-induced upgoing muon flux using MACRO. *Phys. Lett.*, B434:451–457, 1998.

[30] M. Ambrosio et al. Matter effects in upward-going muons and sterile neutrino oscillations. *Phys. Lett.*, B517:59–66, 2001.

[31] M. Ishitsuka. Atmospheric neutrinos: Latest results from Super- Kamiokande. *Nucl. Phys.*, A721:509–512, 2003.

[32] Y. Fukuda et al. Atmospheric muon-neutrino / electron-neutrino ratio in the multigev energy range. *Phys. Lett.*, B335:237–245, 1994.

[33] J. N. Bahcall. Neutrino Astrophysics. *Cambridge, UK. University Press*, 1989.

[34] Y. Fukuda et al. Solar neutrino data covering solar cycle 22. *Phys. Rev. Lett.*, 77:1683–1686, 1996.

[35] W. Hampel et al. GALLEX solar neutrino observations: Results for GALLEX IV. *Phys. Lett.*, B447:127–133, 1999.

[36] M. Altmann et al. GNO solar neutrino observations: Results for GNO I. *Phys. Lett.*, B490:16–26, 2000.

[37] J. N. Abdurashitov et al. Measurement of the solar neutrino capture rate with gallium metal. *Phys. Rev.*, C60:055801, 1999.

[38] S. Fukuda et al. Solar B-8 and he p neutrino measurements from 1258 days of Super-Kamiokande data. *Phys. Rev. Lett.*, 86:5651–5655, 2001.

[39] M. B. Smy. Solar neutrino precision measurements using all 1496 days of Super-Kamiokande-I data. *Nucl. Phys. Proc. Suppl.*, 118:25–32, 2003.

[40] Q. R. Ahmad et al. Measurement of the charged current interactions produced by B-8 solar neutrinos at the Sudbury Neutrino Observatory. *Phys. Rev. Lett.*, 87:071301, 2001.

[41] Q. R. Ahmad et al. Direct evidence for neutrino flavor transformation from neutral-current interactions in the Sudbury Neutrino Observatory. *Phys. Rev. Lett.*, 89:011301, 2002.

[42] Q. R. Ahmad et al. Measurement of day and night neutrino energy spectra at SNO and constraints on neutrino mixing parameters. *Phys. Rev. Lett.*, 89:011302, 2002.

[43] John N. Bahcall, M. C. Gonzalez-Garcia, and Carlos Pena-Garay. Robust signatures of solar neutrino oscillation solutions. *JHEP*, 04:007, 2002.

[44] K. Eguchi et al. First results from KamLAND: Evidence for reactor anti- neutrino disappearance. *Phys. Rev. Lett.*, 90:021802, 2003.

[45] T. Araki et al. Measurement of neutrino oscillation with KamLAND: Evidence of spectral distortion. *Phys. Rev. Lett.*, 94:081801, 2005.

[46] M. Apollonio et al. Limits on neutrino oscillations from the CHOOZ experiment. *Phys. Lett.*, B466:415–430, 1999.

[47] F. Boehm et al. Search for neutrino oscillations at the Palo Verde nuclear reactors. *Phys. Rev. Lett.*, 84:3764–3767, 2000.

[48] F. Boehm et al. Results from the Palo Verde neutrino oscillation experiment. *Phys. Rev.*, D62:072002, 2000.

[49] D. G. Michael et al. Observation of muon neutrino disappearance with the MINOS detectors and the NuMI neutrino beam. *Phys. Rev. Lett.*, 97:191801, 2006.

[50] A. Aguilar et al. Evidence for neutrino oscillations from the observation of anti-nu/e appearance in a anti-nu/mu beam. *Phys. Rev.*, D64:112007, 2001.

[51] D. Meloni. Telling three from four neutrino scenarios. 2002.

[52] E. D. Zimmerman. BooNE has begun. *eConf*, C0209101:TH05, 2002.

[53] S. H. Ahn et al. Detection of accelerator produced neutrinos at a distance of 250-km. *Phys. Lett.*, B511:178–184, 2001.

[54] M. H. Ahn et al. Indications of neutrino oscillation in a 250-km long- baseline experiment. *Phys. Rev. Lett.*, 90:041801, 2003.

[55] E. Aliu et al. Evidence for muon neutrino oscillation in an accelerator- based experiment. *Phys. Rev. Lett.*, 94:081802, 2005.

[56] M. H. Ahn et al. Measurement of neutrino oscillation by the K2K experiment. *Phys. Rev. D.*, 74:072003, 2006.

[57] F. Bergsma et al. A search for neutrino oscillations. *Z. Phys.*, C40:171, 1988.

[58] M. Gruwe et al. Search for muon-neutrino $\rightarrow$ tau-neutrino oscillation. *Phys. Lett.*, B309:463–468, 1993.

[59] F. Dydak et al. A search for muon-neutrino oscillations in the delta M**2 range 0.3-eV**2 to 90-eV**2. *Phys. Lett.*, B134:281, 1984.

[60] S. Nakayama et al. Measurement of single pi0 production in neutral current neutrino interactions with water by a 1.3-GeV wide band muon neutrino beam. *Phys. Lett.*, B619:255–262, 2005.

[61] A. Suzuki et al. Design, construction, and operation of SciFi tracking detector for K2K experiment. *Nucl. Instrum. Meth.*, A453:165–176, 2000.

[62] S. Kawabata et al. Topaz barrel electromagnetic calorimeter. *Nucl. Instrum. Meth.*, A270:11, 1988.

[63] T. Ishii et al. Near muon range detector for the K2K experiment: Construction and performance. *Nucl. Instrum. Meth.*, A482:244–253, 2002.

[64] H. Maesaka. Evidence for muon neutrino oscillation in an accelarator-based experiment. *http://www-he.scphys.kyoto-u.ac.jp/theses/doctor/maesaka_dt.pdf, Kyoto University*, 2005.

[65] H. Noumi et al. Precision positioning of SuperKamiokande with GPS for a long-baseline neutrino oscillation experiment. *Nucl. Instrum. Meth.*, A398:399–408, 1997.

[66] Y. Cho et al. Pion production in proton-beryllium collisions at 12.4 Gev/c. *Phys. Rev.*, D4:1967–1974, 1971.

[67] M. G. Catanesi et al. Measurement of the production cross-section of positive pions in p Al collisions at 12.9-GeV/c. *Nucl. Phys.*, B732:1–45, 2006.

[68] Y. Hayato. NEUT. *Nucl. Phys. Proc. Suppl.*, 112:171–176, 2002.

[69] C. H. Llewellyn Smith. Neutrino reactions at accelerator energies. *Phys. Rept.*, 3:261, 1972.

[70] D. Rein and L. M. Sehgal. Neutrino excitation of baryon resonances and single pion production. *Ann. Phys.*, 133:79, 1981.

[71] D. Rein. Angular distribution in neutrino induced single pion production processes. *Z. Phys.*, C35:43–64, 1987.

[72] M. Hasegawa et al. Search for coherent charged pion production in neutrino carbon interactions. *Phys. Rev. Lett.*, 95:252301, 2005.

[73] M. Gluck, E. Reya, and A. Vogt. Dynamical parton distributions of the proton and small x physics. *Z. Phys.*, C67:433–448, 1995.

[74] A. Bodek and U. K. Yang. Modeling deep inelastic cross sections in the few GeV region. *Nucl. Phys. Proc. Suppl.*, 112:70–76, 2002.

[75] Torbjorn Sjostrand. PYTHIA 5.7 and JETSET 7.4: Physics and manual. 1995.

[76] Masayuki Nakahata et al. Atmospheric neutrino background and pion nuclear effect for kamioka nucleon decay experiment. *J. Phys. Soc. Jap.*, 55:3786, 1986.

[77] Computing GEANT, Application Software Group and Networks Division. Detector Description and Simulation Tool. *Application Software Group, Computing and Networks Division*, CERN Program Libray Long Writeup W5013, 1993.

[78] J. Delorme J. Marteau and M. Ericson. Nuclear effects in neutrino nucleus interactions. *Nucl. Instrum. Meth*, A451:76–80, 2000.

[79] S. Yamamoto et al. Design, construction, and initial performance of SciBar detector in K2K experiment. *IEEE Trans. Nucl. Sci.*, 52:2992–2997, 2005.

[80] K. Nitta et al. The K2K SciBar detector. *Nucl. Instrum. Meth.*, A535:147–151, 2004.

[81] A. Glazov, I. Kisel, E. Konotopskaya, and G. Ososkov. Filtering tracks in discrete detectors using a cellular automaton. *Nucl. Instrum. Meth.*, A329:262–268, 1993.

[82] Technical design report. *NuMI-L-337*, 1998.

[83] Anna Pla-Dalmau. Extruded plastic scintillator for the MINOS calorimeters. *Frascati Phys. Ser.*, 21:513–522, 2001.

[84] L. Whitehead. SciBar analysis internal note: Study of SciBar crosstalk simulation. *http://neutrino.kek.jp/internal/scibar/notes/lisa_xtalknote_v1.pdf*, 2006.

[85] S. Buontempo et al. Construction and test of calorimeter modules for the CHORUS experiment. *Nucl. Instrum. Meth.*, A349:70–80, 1994.

[86] J.B. Birk. *Proc. Phys. Soc.*, A64:874, 1951.

[87] A.Y. Rodriguez. Master Thesis. Alignment of SciBar detector at K2K experiment. *Universitat Autonoma de Barcelona*, 2004.

[88] Status of the N and Delta resonances. *Phys. Lett. B*, 592:66, 866, 2004.

[89] R. P. Feynman, M. Kislinger, and F. Ravndal. Current matrix elements from a relativistic quark model. *Phys. Rev.*, D3:2706–2732, 1971.

[90] F. Ravndal. Weak production of nuclear resonances in a relativistic quark model. *Nuovo Cim.*, A18:385–415, 1973.

[91] A. Salam. Elementary Particle Theory. *edited by N. Svartholm (Almqvist and Wiksell, Stockholm)*, page 367, 1968.

[92] Steven Weinberg. A model of leptons. *Phys. Rev. Lett.*, 19:1264–1266, 1967.

[93] F. Ravndal. Neutrino excitation of nucleon resonances in a quark model. *Lett. Nuovo Cim.*, 3:631–636, 1972.

[94] G. M. Radecky et al. Study of single pion production by weak charged currents in low-energy neutrino d interactions. *Phys. Rev.*, D25:1161–1173, 1982.

[95] W. Lerche et al. Experimental study of the reaction neutrino P $\rightarrow$ MU- P PI+. (Gargamelle neutrino propane experiment). *Phys. Lett.*, B78:510–514, 1978.

[96] X. Espinal. Ph.D. Thesis. Measurement of the axial-vector mass in neutrino carbon interactions. *Universitat Autonoma de Barcelona*, 2006.

[97] C. H. Llewellyn Smith. Neutrino reactions at accelerator energies. *Phys. Rept.*, 3:261, 1972.

[98] F. J. Ernst, R. G. Sachs, and K. C. Wali. Electromagnetic Form Factors of the Nucleon. *Phys. Rev.*, 119(3):1105–1114, Aug 1960.

[99] R. Gran et al. Measurement of the quasi-elastic axial vector mass in neutrino oxygen interactions. *Phys. Rev.*, D74:052002, 2006.

[100] L. A. Ahrens et al. Precise determination of sin**2-theta-w from measurements of the differential cross-sections for muon-neutrino p $\rightarrow$ muon-neutrino p and anti-muon-neutrino p $\rightarrow$ anti- muon-neutrino p. *Phys. Rev. Lett.*, 56:1107, 1986.

[101] S. J. Barish et al. study of neutrino interactions in hydrogen and deuterium: Description of the experiment and study of the reaction neutrino d $\rightarrow$ mu- P P(s). *Phys. Rev.*, D16:3103, 1977.

[102] N. J. Baker et al. Quasielastic neutrino scattering: a measurement of the weak nucleon axial vector form-factor. *Phys. Rev.*, D23:2499–2505, 1981.

[103] S. Bonetti et al. Study of quasielastic reactions of neutrino and anti-neutrino in Gargamelle. *Nuovo Cim.*, A38:260–270, 1977.

[104] S. V. Belikov et al. Quasielastic neutrino and anti-neutrinos scattering: Total cross-sections, axial vector form-factor. *Z. Phys.*, A320:625, 1985.

[105] R. Johnson and N. Suwonjaydee. Note on LLewellyn-Smith's Pauli supression model. *http://www.physics.uc.edu/ johnson/Boone/cross_sections/fermi_motion/ LlewellynSmithModel/LSfermi.pdf*, 2004.

[106] E. J. Moniz et al. Nuclear fermi momenta from quasielastic electron scattering. *Phys. Rev. Lett.*, 26:445–448, 1971.

[107] D. Ashery et al. True absorption and scattering of pions on nuclei. *Phys. Rev.*, C23:2173–2185, 1981.

[108] H. W. Bertini. Nonelastic interactions of nucleons and pi mesons with complex nuclei at energies below 3 gev. *Phys. Rev.*, C6:631–659, 1972.

[109] R. Gran. SciFi analysis internal note: Note on proton rescattering. *http://neutrino.kek.jp/scifi/scifima/note-ProtonRescattering.pdf*, 2005.

[110] Passage of particles through matter. *Phys. Lett. B*, 592:243, 2004.

[111] M. Hasegawa. Measurements of neutrino oscillation parameters with neutrino-nucleus interaction studies in the K2K experiment. *http://www-he.scphys.kyoto-u.ac.jp/theses/doctor/masaya_dt.pdf, Kyoto University*, 2006.

[112] G. Jover Manas. Thesis in preparation. Measurement of the cross section of the multipion interaction in a carbon target using the SciBar detector at K2K experiment. *Universitat Autonoma de Barcelona*, estimated 2007.

[113] S. J. Barish et al. Study of neutrino interactions in hydrogen and deuterium: Inelastic charged current reactions. *Phys. Rev.*, D19:2521, 1979.

[114] T. Kitagaki et al. Charged current exclusive pion production in neutrino deuterium interactions. *Phys. Rev.*, D34:2554–2565, 1986.

[115] Kitagaki, T. and others. Study of neutrino d $\rightarrow$ mu- p p(s) and neutrino d $\rightarrow$ mu- Delta++ (1232) n(s) using the BNL 7-foot deuterium filled bubble chamber. *Phys. Rev.*, D42:1331–1338, 1990.

[116] M. Pohl et al. Experimental study of the reaction neutrino n $\rightarrow$ mu- p. *Lett. Nuovo Cim.*, 26:332–336, 1979.

[117] M. O. Wascko. Charged current single pion cross section measurement at MiniBooNE. *Nucl. Phys. Proc. Suppl.*, 159:50–55, 2006.

[118] K. Hiraide. The SciBar detector at FNAL booster neutrino experiment. *Nucl. Phys. Proc. Suppl.*, 159:85–90, 2006.

[119] Letter of Intent. neutrino oscillation experiment at JHF. *http://neutrino.kek.jp/jhfnu/loi/loi.v2.030528.pd*.

[120] Y. Yamada. The T2K program. *Nucl. Phys. Proc. Suppl.*, 155:28–32, 2006.

[121] D. Karlen. Near detectors for the T2K experiment. *Nucl. Phys. Proc. Suppl.*, 159:91–96, 2006.

[122] D. Naples et al. MINERvA: High statistics neutrino scattering using a fine-grained detector. *Int. J. Mod. Phys.*, A20:3078–3081, 2005.

Appendix A

Tracking and Matching definition in SciBar

The problem of pattern recognition appears frequently in high energy physics; the application of Cellular Automata algorithms for track finding and data filtering have been already used to solve it. In this Appendix we present some aspects of the developing of a cellular automaton for track pattern recognition for the SciBar detector of the K2K experiment, and also how the 2-dimensional tracks matching is performed in SciBar.

A.1 Tracking

Cellular Automata are dynamical systems that evolve in discrete steps. Each cell has a value associated. In the simplest model, one has a single bit cell: false or true. The laws of the evolution are local. The dynamics of the system is controlled by a fixed set of rules in accordance with which the new state of a cell is calculated on the basis of the states of the neighbors. It is important that the change of states is made simultaneously and in parallel, with time proceeding discretely. Using a Cellular Automata for pattern recognition simplifies and speeds up the process. The preliminary search for tracks involves only a collection of experimental points sorting them into tracks groups; it is not needed to make a precise analysis of the data at the preliminary searching stages. Details in Cellular Automanta can be found in [81].

The separation between layers at the SciBar detector favor the segment model of a Cellular Automaton, where the elementary unit is a segment connecting two hits in neighboring layers. The low energy neutrino interactions in the SciBar detector produce very spherical events, with

inclined tracks with respect to the cell topology of the detector. These tracks produce groups of hits per detector per plane. Tracks with a common vertex and small opening angle also produce clustering of segments close to the production point. The Cellular Automata algorithm tries to maximize the efficiency of hit collection producing several equivalent paths for each of the tracks. The clustering of consecutive detector hits contained inside a plane reduces the number of combinatorial paths followed by the Cellular Automaton algorithm, and the final recombination of equivalent tracks candidates. The algorithm simply groups hits in a cluster and associates the geometrical center to the new detector hit. Then, only segments with a common end may be considered as neighbors. Taking into account the detector segmentation and the maximum multiple scattering an upper limit on the χ^2 can be imposed. The χ^2 is computed from the linear least square fit to the three point belonging to two neighbor cells. To take into account detector inefficiencies and geometrical acceptance of the fiber piling, one may include segments that connect points that skip over one layer. The collection of track candidates is done by starting from the segment with the lowest position value and adding the neighbor with the consecutive position value. At these levels tracks with splitting branches are considered. After the possible combinations the longest track is kept; and the other possibles branches, if they are, are considered as the splits of the previous track. Finally, some quality cuts are applied to get the secondary tracks among the branch tracks.

A.2 Matching

Once the tracks are constructed in the 2-dimensional (2D) views a matching is performed to get the 3-dimensional (3D) tracks. The 2D tracks are associated to tracks in the other view based in a set of criteria with decreasing level of importance. The 2D tracks associated to other views are removed from the track pool and not used in consecutive trials. This way the 2D tracks are used only once and always with the highest quality possible. There are five types of matching, although the algorithms are only three with different numerical conditions. Within each of these categories, the segments are also given priorities from the profile of energy deposition along the track. The energy deposition profile contains information on the position and angle of the other segment view via the dependency of the charge attenuation along the WLS fiber.

The first type of matching is the so called MRD based matching. This method looks for two segments with a high quality matching to a MRD segment. The SciBar segments are requested to leave the detector block to be considered in this category.

The second method ask that both edges of track in both views have to be near in z. If one track is leaving the detector from one side, the track is extrapolated to take in account the veto bars (Figure A.1). Depending on the distance between the edge z position for both views, three matching classes are defined. *ClassI*, if the difference is just less than the distance between one plane and the next in the same view. *ClassII*, if the difference is less than the distance between one plane and the three next ones. *ClassIII*, if the difference is less than the distance between one plane and the five next ones. *ClassII* and *ClassIII* are needed to recover matching tracks that have cross talk in the edge on one view, or tracks that seems to be leaving the detector from the side but are not really leaving and are extrapolated (Figure A.2).

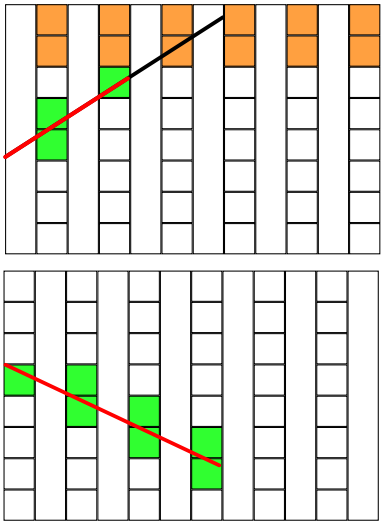

Figure A.1: Extrapolation of a track leaving the detector from the side in one view. The green blocks are the cells with signal. The orange blocks are the veto channels. The red line is the reconstructed track in 2D.

The third method, called *ClassIV*, only ask that one track edge in both views have to be very close in z. For *ClassIV* we take the edge matching equal to that of *ClassII* but applied to either edge of the segment. This class gives tracks with lower quality than the others. One of the 2D projections is extrapolated in order to match with the other edge of the track in the other view; in this case the 3D track is reconstructed having several planes without signal. Track parameters as the length or the dE/dx would be wrongly reconstructed. The *ClassIV* tracks were not used in the analysis.

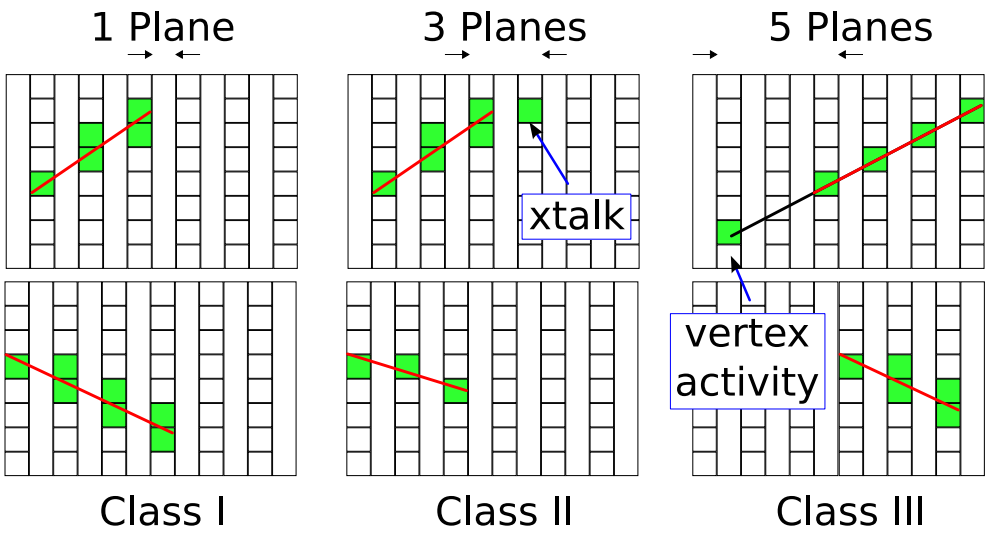

Figure A.2: Example of matching tracks accepted by each class. *ClassI*, if the difference is just less than the distance between one plane and the next in the same view. *ClassII*, if the difference is less than the distance between one plane and the three next ones. *ClassIII*, if the difference is less than the distance between one plane and the five next ones. The green blocks are the cells with signal. The red line is the reconstructed track in 2D.

Appendix B

SciBar Calculations

B.1 Coordinate Systems

The neutrino beam is oriented 1.075° downward from horizontal:

$$\phi_{beam} = -1.075^{\circ} \tag{B.1}$$

So the transformation from the xyz coordinate system to the beam coordinate system (x'y'z', where z' is the beam direction) is a rotation around the x axis of -1.075°. The rotation matrix is:

$$R = \begin{pmatrix} 1 & 0 & 0 \\ 0 & \cos\phi_{beam} & -\sin\phi_{beam} \\ 0 & \sin\phi_{beam} & \cos\phi_{beam} \end{pmatrix}$$

A vector $\vec{v}$ in the xyz coordinate system can be expressed in the beam coordinate system (x'y'z') as

$$\vec{v'} = R\vec{v}. \tag{B.2}$$

The reverse transformation is

$$\vec{v} = R^{-1}\vec{v'}. \tag{B.3}$$

where

$$R^{-1} = \begin{pmatrix} 1 & 0 & 0 \\ 0 & \cos\phi_{beam} & \sin\phi_{beam} \\ 0 & -\sin\phi_{beam} & \cos\phi_{beam} \end{pmatrix}$$

See Figure B.1. In the beam coordinate system (x'y'z'), the neutrino's momentum vector is (assuming the mass of the neutrino is negligible):

$$\vec{p'_\nu} = \langle 0, 0, E_\nu \rangle \tag{B.4}$$

The neutrino's momentum vector in the xyz system is given by:

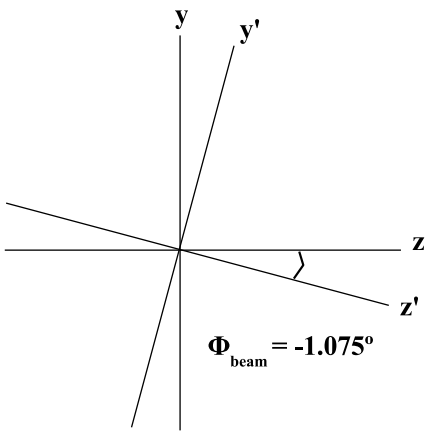

Figure B.1: xyz coordinate system vs. beam (x'y'z') coordinate system.

$$\vec{p_\nu} = \langle 0, E_\nu \sin\phi_{beam}, E_\nu \cos\phi_{beam} \rangle \tag{B.5}$$

Note that the SciBar track reconstruction is done in the xyz system and so the angular variables Sbtx (tangent in the X view) and Sbty (tangent in the Y view) that are used for all kinematic calculations are given in the xyz system.

B.2 Calculation of Angles

Given Sbtx and Sbty (in the xyz system), how do we calculate angles θ and ϕ in the xyz system and angles θ' and ϕ' in the beam system? How do we calculate Sbtx' and Sbty' in the beam system?

Let $\vec{v}$ be a vector in the xyz system.

$$\begin{aligned} v_x &= |\vec{v}| \cos\phi \sin\theta \\ v_y &= |\vec{v}| \sin\phi \sin\theta \\ v_z &= |\vec{v}| \cos\theta \end{aligned} \tag{B.6}$$

with

$$\begin{aligned} \text{Sbtx} &= \frac{v_x}{v_z} \\ \text{Sbty} &= \frac{v_y}{v_z} \end{aligned} \tag{B.7}$$

Calculating θ and ϕ (in the xyz system):

$$\begin{aligned} \sqrt{\text{Sbtx}^2 + \text{Sbty}^2} &= \sqrt{(\frac{v_x}{v_z})^2 + (\frac{v_y}{v_z})^2} \\ &= \sqrt{(\frac{|\vec{v}| \cos\phi \sin\theta}{|\vec{v}| \cos\theta})^2 + (\frac{|\vec{v}| \sin\phi \sin\theta}{|\vec{v}| \cos\theta})^2} \\ &= \sqrt{(\cos^2\phi + \sin^2\phi)(\frac{\sin\theta}{\cos\theta})^2} \\ &= \sqrt{\tan^2\theta} \\ \sqrt{\text{Sbtx}^2 + \text{Sbty}^2} &= \tan\theta \end{aligned} \tag{B.8}$$

$$\begin{aligned} \frac{\text{Sbty}}{\text{Sbtx}} &= \frac{v_y/v_z}{v_x/v_z} \\ &= \frac{v_y}{v_x} \\ &= \frac{|\vec{v}| \sin\phi \sin\theta}{|\vec{v}| \cos\phi \sin\theta} \\ &= \frac{\sin\phi}{\cos\phi} \\ \frac{\text{Sbty}}{\text{Sbtx}} &= \tan\phi \end{aligned} \tag{B.9}$$

Calculating θ' and ϕ' (the beam system):

The representation of the vector $\vec{v}$ in the beam system, $\vec{v'}$, can be found using the rotation matrix, R, given in B.1, with $\phi_{beam} = -1.075°$.

$$\vec{v'} = R\vec{v}$$

$$\begin{pmatrix} v'_x \\ v'_y \\ v'_z \end{pmatrix} = \begin{pmatrix} 1 & 0 & 0 \\ 0 & \cos\phi_{beam} & -\sin\phi_{beam} \\ 0 & \sin\phi_{beam} & \cos\phi_{beam} \end{pmatrix} \begin{pmatrix} v_x \\ v_y \\ v_z \end{pmatrix}$$

$$\begin{pmatrix} v'_x \\ v'_y \\ v'_z \end{pmatrix} = \begin{pmatrix} v_x \\ \cos\phi_{beam} v_y - \sin\phi_{beam} v_z \\ \sin\phi_{beam} v_y + \cos\phi_{beam} v_z \end{pmatrix}$$

$$\begin{pmatrix} v'_x \\ v'_y \\ v'_z \end{pmatrix} = \begin{pmatrix} |\vec{v}| \cos\phi \sin\theta \\ \cos\phi_{beam} |\vec{v}| \sin\phi \sin\theta - \sin\phi_{beam} |\vec{v}| \cos\theta \\ \sin\phi_{beam} |\vec{v}| \sin\phi \sin\theta + \cos\phi_{beam} |\vec{v}| \cos\theta \end{pmatrix}$$

Therefore,

$$\left|\vec{v'}\right| \cos\theta' = v'_z = \sin\phi_{beam} |\vec{v}| \sin\phi \sin\theta + \cos\phi_{beam} |\vec{v}| \cos\theta$$

$$\left|\vec{v'}\right| = |\vec{v}|$$

$$\cos\theta' = \sin\phi_{beam} \sin\phi \sin\theta + \cos\phi_{beam} \cos\theta \tag{B.10}$$

and

$$\tan\phi' = \frac{v'_y}{v'_x} = \frac{\cos\phi_{beam} \sin\phi \sin\theta - \sin\phi_{beam} \cos\theta}{\cos\phi \sin\theta} \tag{B.11}$$

Calculating Sbtx' and Sbty' (the beam system):

$$\begin{aligned} \text{Sbtx}' &= \frac{v'_x}{v'_z} \\ &= \frac{v_x}{\sin\phi_{beam} v_y + \cos\phi_{beam} v_z} \\ &= \frac{\frac{v_x}{v_z}}{\sin\phi_{beam} \frac{v_y}{v_z} + \cos\phi_{beam} \frac{v_z}{v_z}} \\ \text{Sbtx}' &= \frac{\text{Sbtx}}{\sin\phi_{beam} \text{Sbty} + \cos\phi_{beam}} \end{aligned} \tag{B.12}$$

$$
\begin{aligned}
\mathrm{Sbty}' &= \frac{v_y'}{v_z'} \\
&= \frac{\cos\phi_{beam} v_y - \sin\phi_{beam} v_z}{\sin\phi_{beam} v_y + \cos\phi_{beam} v_z} \\
&= \frac{\cos\phi_{beam} \frac{v_y}{v_z} - \sin\phi_{beam} \frac{v_z}{v_z}}{\sin\phi_{beam} \frac{v_y}{v_z} + \cos\phi_{beam} \frac{v_z}{v_z}} \\
\mathrm{Sbty}' &= \frac{\cos\phi_{beam}\mathrm{Sbty} - \sin\phi_{beam}}{\sin\phi_{beam}\mathrm{Sbty} + \cos\phi_{beam}}
\end{aligned}
\tag{B.13}
$$

B.3 Calculation of Momentum Elements

P_μ is the muon momentum in the xyz coordinate system.

$$
\begin{aligned}
\mathrm{Sbtx} &= \frac{p_{\mu x}}{p_{\mu z}} \\
\mathrm{Sbty} &= \frac{p_{\mu y}}{p_{\mu z}}
\end{aligned}
\tag{B.14}
$$

Therefore,

$$
\begin{aligned}
p_{\mu x} &= p_{\mu z}\mathrm{Sbtx} \\
p_{\mu x} &= p_\mu cos\theta \mathrm{Sbtx} \\
p_{\mu x} &= \frac{p_\mu \mathrm{Sbtx}}{\sqrt{\mathrm{Sbtx}^2 + \mathrm{Sbty}^2 + 1}}
\end{aligned}
\tag{B.15}
$$

$$
\begin{aligned}
p_{\mu y} &= p_{\mu z}\mathrm{Sbty} \\
p_{\mu y} &= p_\mu cos\theta \mathrm{Sbty} \\
p_{\mu y} &= \frac{p_\mu \mathrm{Sbty}}{\sqrt{\mathrm{Sbtx}^2 + \mathrm{Sbty}^2 + 1}}
\end{aligned}
\tag{B.16}
$$

B.4 Calculation of Neutrino Energy

Assuming the interaction is charged-current quasi-elastic (CCQE), i.e. $\nu n \rightarrow \mu p$, conservation of momentum gives us these relations:

$$\begin{aligned} p_{\mu x} + p_{px} &= 0 \\ p_{\mu y} + p_{py} &= E_\nu \sin\phi_{beam} \\ p_{\mu z} + p_{pz} &= E_\nu \cos\phi_{beam} \end{aligned} \tag{B.17}$$

Using conservation of energy, we can solve for the neutrino's energy, E_ν, as follows:

$$E_\nu + m_n - V = E_\mu + E_p$$

$$(E_\nu - E_\mu) + (m_n - V) = E_p = \sqrt{m_p^2 + p_p^2}$$

$$[(E_\nu - E_\mu) + (m_n - V)]^2 = m_p^2 + p_{px}^2 + p_{py}^2 + p_{pz}^2$$

$$\begin{gathered}(E_\nu - E_\mu)^2 + (m_n - V)^2 + 2(E_\nu - E_\mu)(m_n - V) \\ = m_p^2 + p_{\mu x}^2 + (E_\nu \sin\phi_{beam} - p_{\mu y})^2 + (E_\nu \cos\phi_{beam} - p_{\mu z})^2\end{gathered}$$

$$\begin{gathered}E_\nu^2 - 2E_\nu E_\mu + E_\mu^2 + (m_n - V)^2 + 2E_\nu(m_n - V) - 2E_\mu(m_n - V) = \\ m_p^2 + p_{\mu x}^2 + E_\nu^2 \sin^2\phi_{beam} + p_{\mu y}^2 - 2E_\nu \sin\phi_{beam} p_{\mu y} + E_\nu^2 \cos^2\phi_{beam} + p_{\mu z}^2 - 2E_\nu \cos\phi_{beam} p_{\mu z}\end{gathered}$$

$$\begin{gathered}E_\nu^2 - 2E_\nu E_\mu + E_\mu^2 + (m_n - V)^2 + 2E_\nu(m_n - V) - 2E_\mu(m_n - V) \\ = m_p^2 + (p_{\mu x}^2 + p_{\mu y}^2 + p_{\mu z}^2) + E_\nu^2(\sin^2\phi_{beam} + \cos^2\phi_{beam}) - 2E_\nu(\sin\phi_{beam} p_{\mu y} + \cos\phi_{beam} p_{\mu z})\end{gathered}$$

$$\begin{gathered}-2E_\nu E_\mu + E_\mu^2 + (m_n - V)^2 + 2E_\nu(m_n - V) - 2E_\mu(m_n - V) \\ = m_p^2 + p_\mu^2 - 2E_\nu(\sin\phi_{beam} p_{\mu y} + \cos\phi_{beam} p_{\mu z})\end{gathered}$$

$$\begin{gathered}-2E_\nu E_\mu + 2E_\nu(m_n - V) + 2E_\nu(\sin\phi_{beam} p_{\mu y} + \cos\phi_{beam} p_{\mu z}) \\ = -E_\mu^2 - (m_n - V)^2 + 2E_\mu(m_n - V) + m_p^2 + p_\mu^2\end{gathered}$$

$$\begin{gathered}2E_\nu[-E_\mu + (m_n - V) + \sin\phi_{beam} p_{\mu y} + \cos\phi_{beam} p_{\mu z}] \\ = m_p^2 + (p_\mu^2 - E_\mu^2) - (m_n - V)^2 + 2E_\mu(m_n - V)\end{gathered}$$

$$2E_\nu[-E_\mu + (m_n - V) + \sin\phi_{beam} p_{\mu y} + \cos\phi_{beam} p_{\mu z}] = m_p^2 - m_\mu^2 - (m_n - V)^2 + 2E_\mu(m_n - V)$$

$$E_\nu = \frac{1}{2}\frac{m_p^2 - m_\mu^2 - (m_n - V)^2 + 2E_\mu(m_n - V)}{-E_\mu + (m_n - V) + \sin\phi_{beam}p_{\mu y} + \cos\phi_{beam}p_{\mu z}} \tag{B.18}$$

where E = energy, m = mass, p = momentum, V = nuclear potential = 27 MeV, and the subscripts p, n, μ, ν represent the proton, neutron, muon, and neutrino, respectively.

B.5 Calculation of $\Delta\theta_p$

$\Delta\theta_p$ is defined as the angle between expected proton direction (calculated assuming a CCQE interaction) and the observed direction of the second track.

$$\Delta\theta_p = \theta_p(\text{expected}) - \theta_2(\text{observed}) \tag{B.19}$$

The angle between the two vectors is calculated as follows:

$$\cos\Delta\theta_p = \frac{\vec{p_p}}{|\vec{p_p}|} \cdot \frac{\vec{p_2}}{|\vec{p_2}|} \tag{B.20}$$

From equation B.17,

$$\vec{p_p} = \langle -p_{\mu x}, E_\nu \sin\phi_{beam} - p_{\mu y}, E_\nu \cos\phi_{beam} - p_{\mu z}\rangle \tag{B.21}$$

So,

$$\frac{\vec{p_p}}{|\vec{p_p}|} = \frac{\langle -p_{\mu x}, E_\nu \sin\phi_{beam} - p_{\mu y}, E_\nu \cos\phi_{beam} - p_{\mu z}\rangle}{\sqrt{p_{\mu x}^2 + (E_\nu \sin\phi_{beam} - p_{\mu y})^2 + (E_\nu \cos\phi_{beam} - p_{\mu z})^2}} \tag{B.22}$$

$\frac{\vec{p_2}}{|\vec{p_2}|}$ is just a unit vector in the direction of the observed second track.

$$\vec{p_2} = \langle p_{2x}, p_{2y}, p_{2z}\rangle \parallel \langle p_{2x}/p_{2z}, p_{2y}/p_{2z}, 1\rangle = \langle \text{Sbtx}_2, \text{Sbty}_2, 1\rangle$$

$$\frac{\vec{p_2}}{|\vec{p_2}|} = \frac{\langle \text{Sbtx}_2, \text{Sbty}_2, 1\rangle}{\sqrt{\text{Sbtx}_2^2 + \text{Sbty}_2^2 + 1}} \tag{B.23}$$

Therefore,

$$\cos\Delta\theta_p = \frac{-p_{\mu x}\text{Sbtx}_2 + (E_\nu \sin\phi_{beam} - p_{\mu y})\text{Sbty}_2 + (E_\nu \cos\phi_{beam} - p_{\mu z})}{\sqrt{p_{\mu x}^2 + (E_\nu \sin\phi_{beam} - p_{\mu y})^2 + (E_\nu \cos\phi_{beam} - p_{\mu z})^2}\sqrt{\text{Sbtx}_2^2 + \text{Sbty}_2^2 + 1}}$$

and

$$\Delta\theta_p = \arccos(\cos\Delta\theta_p) \tag{B.24}$$

We need to make an adjustment in this calculation if the second track is backward, that is, the downstream end of the track is closer than the upstream end to the muon vertex. In Figure B.2, the muon track is labeled μ, the expected proton track is labeled **p**, and tracks **1** and **2** are examples of candidate proton tracks. Track **1** is forward and track **2** is backward. We want to calculate $\Delta\theta_p(1)$, the angle between the expected proton track and track **1**, and $\Delta\theta_p(2)$, the angle between the expected proton track and track **2**. The variable Sbtx is just the slope of the line created when

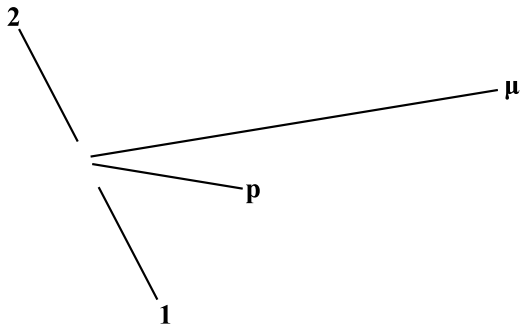

Figure B.2: The muon track is labeled μ, the expected proton track is labeled **p**, and tracks **1** and **2** are examples of candidate proton tracks. Track **1** is forward and track **2** is backward.

the track is projected on the xz plane (etc. for Sbty). So in Figure B.2, Sbtx(1) = Sbtx(2) because the lines have the same slope. Defining $\vec{p} = \langle \text{Sbtx}, \text{Sbty}, 1\rangle$, means that $\vec{p}(1) = \vec{p}(2)$, shown in Figure B.3. And so we get $\Delta\theta_p(1) = \Delta\theta_p(2) = \alpha$.

Clearly, this is not correct; the vectors for track **1** and track **2** should be in opposite directions, and $\Delta\theta_p(2) = 180^\circ - \alpha$, as can be seen in Figure B.4. However, our definition, $\vec{p} = \langle \text{Sbtx}, \text{Sbty}, 1\rangle$, forces the z component of $\vec{p}$ to be positive. To correct this, we take $\vec{p} \rightarrow -\vec{p}$ for backward tracks. In this example, this means $\vec{p}(2) = -\vec{p}(1)$. So then $\cos\Delta\theta_p(2) = -\cos\Delta\theta_p(1) = -\cos\alpha$. This gives us the correct result for $\Delta\theta_p(2)$ because:
$\arccos(\cos\Delta\theta_p(2)) = \arccos(-\cos\Delta\theta_p(1)) = \arccos(-\cos\alpha) = 180^\circ - \alpha$.

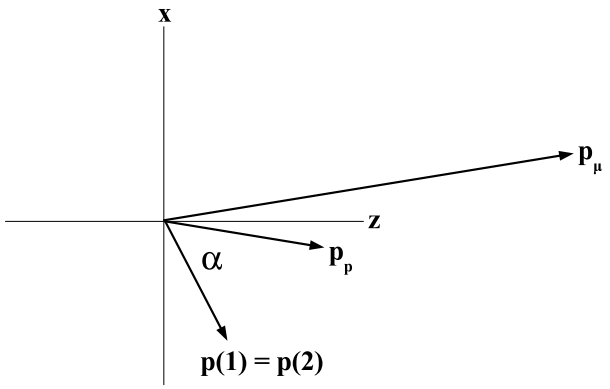

Figure B.3: Momentum vectors of the tracks shown in Figure B.2. Defining $\vec{p} = \langle \mathrm{Sbtx}, \mathrm{Sbty}, 1 \rangle$ gives tracks **1** and **2** the same momentum vector, which is incorrect.

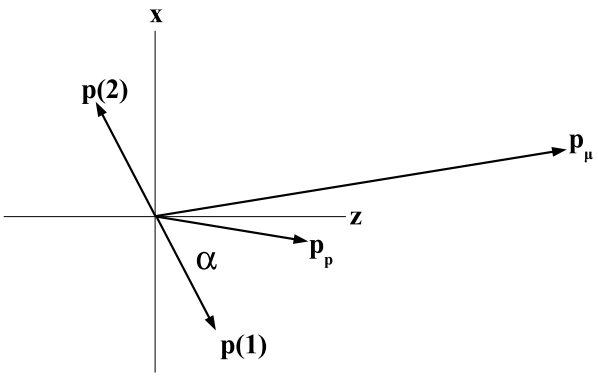

Figure B.4: Correct momentum vectors of the tracks shown in Figure B.2. (Track **2** correctly points backwards).

B.6 Calculation of momentum transfer, q^2

Calculation of q^2 (square of 4-momentum transfer) in the xyz coordinate system:

$$
\begin{aligned}
q^2 &= (p_\nu - p_\mu)^2 \\
&= (E_\nu - E_\mu)^2 - (\vec{p_\nu} - \vec{p_\mu})^2 \\
&= E_\nu^2 + E_\mu^2 - 2E_\nu E_\mu - (p_{\nu x} - p_{\mu x})^2 - (p_{\nu y} - p_{\mu y})^2 - (p_{\nu z} - p_{\mu z})^2 \\
&= E_\nu^2 + E_\mu^2 - 2E_\nu E_\mu - p_{\mu x} - (E_\nu sin\phi_{beam} - p_{\mu y})^2 - (E_\nu sin\phi_{beam} - p_{\mu z})^2 \\
&= E_\nu^2 + E_\mu^2 - 2E_\nu E_\mu - p_{\mu x} - p_{\mu y} - p_{\mu z} - E_\nu^2(\sin^2\phi_{beam} + \cos^2\phi_{beam}) \\
&+ 2E_\nu(p_{\mu y} sin\phi_{beam} + p_{\mu z} cos\phi_{beam}) \\
&= E_\nu^2 + E_\mu^2 - 2E_\nu E_\mu - p_\mu - E_\nu^2 + 2E_\nu(p_{\mu y} sin\phi_{beam} + p_{\mu z} cos\phi_{beam}) \\
q^2 &= -2E_\nu(E_\mu - p_{\mu y} sin\phi_{beam} - p_{\mu z} cos\phi_{beam}) + m_\mu^2
\end{aligned}
\tag{B.25}
$$

$$
Q^2 = -q^2 = 2E_\nu(E_\mu - p_{\mu y} sin\phi_{beam} - p_{\mu z} cos\phi_{beam}) - m_\mu^2 \tag{B.26}
$$

Appendix C

Systematic error on the measurement of the cross section of the single pπ^+ interaction

C.1 Using only the 2 track sample

Total measurement:

Measurement	MC prediction
0.646 ± 0.067 (stat.) $^{+0.125}_{-0.084}$ (syst.)	0.565 ± 0.002 (stat.)

Table C.1: Measurment of the CCpπ^+ to CCQE cross section ratio.

Energy dependent measurement:

Eν (GeV)	Measurement	MC prediction
≤ 1.35	0.447 ± 0.074 (stat.) $^{+0.130}_{-0.097}$ (syst.)	0.441 ± 0.002 (stat.)
1.35-1.72	0.727 ± 0.121 (stat.) $^{+0.161}_{-0.208}$ (syst.)	0.695 ± 0.004 (stat.)
1.72-2.22	0.816 ± 0.138 (stat.) $^{+0.225}_{-0.101}$ (syst.)	0.782 ± 0.006 (stat.)
$2.22 \leq$	0.750 ± 0.164 (stat.) $^{+0.350}_{-0.387}$ (syst.)	0.860 ± 0.009 (stat.)

Table C.2: Measurment of the energy dependent CCpπ^+ to CCQE cross section ratio.

The detailed contribution to the systematic uncertainty on the measurement of the cross section of the single pπ^+ interaction normalized to CCQE appears in Table C.3.

The systematic errors for the measurement done in the 4 energy bins are quoted in Tables C.4, C.5, C.6, and C.7.

source of systematic	error
MC statistics	+0.010 -0.010
Model effects	
M_A (CCQE) $\pm$0.1	-0.016 +0.018
Bodek/Yang Corr $\pm$30%	-0.023 +0.025
Nπ weighting	$\pm$ 0.058
Neutrino Flux	+0.010 -0.008
Sub-total	+0.066 -0.065
Nuclear effects	
π absorption $\pm$30%	+0.061 -0.017
π inelastic scattering $\pm$30%	+0.059 -0.020
proton rescattering $\pm$10%	+0.024 -0.004
Fermi motion ($\pm$ 5MeV/c)	$\pm$ 0.006
Sub-total	+0.088 -0.027
Detector effects	
Cross talk $\pm$0.25%	+0.032 -0.024
PMT resolution $\pm$10%	+0.025 -0.011
Quenching constant $\pm$0.0023	+0.008 +0.012
Sub-total	+0.042 -0.026
Reconstruction effects	
Hit threshold $\pm$15%	$\pm$ 0.036
Muon momemtum scale $\pm$2.7%	-0.004 +0.004
Angular resolution (smeared by 0.009)	$\pm$ 0.008
Sub-total	+0.037 -0.037
Total	+0.125 -0.084

Table C.3: Systematic errors for the overall CCpπ^+ to CCQE cross section ratio.

source of systematic	error
MC statistics	+0.011 -0.011
Model effects	
M_A (CCQE) $\pm$0.1	-0.008 +0.010
Bodek/Yang Corr $\pm$30%	-0.027 +0.030
Nπ weighting	$\pm$ 0.052
Neutrino Flux	+0.009 -0.007
Sub-total	+0.062 -0.060
Nuclear effects	
π absorption $\pm$30%	+0.042 -0.060
π inelastic scattering $\pm$30%	+0.019 +0.021
proton rescattering $\pm$10%	+0.020 +0.045
Fermi motion ($\pm$ 5MeV/c)	$\pm$ 0.005
Sub-total	+0.065 -0.060
Detector effects	
Cross talk $\pm$0.25%	+0.016 +0.021
PMT resolution $\pm$10%	+0.011 -0.007
Quenching constant $\pm$0.0023	+0.018 -0.001
Sub-total	+0.030 -0.007
Reconstruction effects	
Hit threshold $\pm$15%	$\pm$ 0.016
Muon momemtum scale $\pm$2.7%	-0.040 +0.086
Angular resolution (smeared by 0.009)	$\pm$ 0.012
Sub-total	+0.088 -0.045
Total	+0.130 -0.097

Table C.4: Systematic errors for the CCpπ^+ to CCQE cross section ratio in the first energy bin.

source of systematic	error
MC statistics	+0.021 -0.021
Model effects	
M_A (CCQE) $\pm$0.1	-0.022 +0.023
Bodek/Yang Corr $\pm$30%	-0.021 +0.022
Nπ weighting	$\pm$ 0.054
Neutrino Flux	+0.015 -0.016
Sub-total	+0.064 -0.064
Nuclear effects	
π absorption $\pm$30%	+0.020 +0.012
π inelastic scattering $\pm$30%	+0.122 -0.099
proton rescattering $\pm$10%	+0.048 -0.101
Fermi motion ($\pm$ 5MeV/c)	$\pm$ 0.003
Sub-total	+0.133 -0.141
Detector effects	
Cross talk $\pm$0.25%	+0.025 -0.058
PMT resolution $\pm$10%	+0.025 -0.002
Quenching constant $\pm$0.0023	-0.014 +0.021
Sub-total	+0.041 -0.060
Reconstruction effects	
Hit threshold $\pm$15%	$\pm$ 0.033
Muon momemtum scale $\pm$2.7%	-0.118 +0.024
Angular resolution (smeared by 0.009)	$\pm$ 0.018
Sub-total	+0.045 -0.124
Total	+0.161 -0.208

Table C.5: Systematic errors for the CCpπ^+ to CCQE cross section ratio in the second energy bin.

source of systematic	error	
MC statistics	+0.030	-0.030
Model effects		
M_A (CCQE) $\pm$0.1	-0.025	+0.021
Bodek/Yang Corr $\pm$30%	-0.019	+0.019
Nπ weighting	$\pm$ 0.058	
Neutrino Flux	+0.023	-0.023
Sub-total	+0.069	-0.070
Nuclear effects		
π absorption $\pm$30%	+0.116	+0.010
π inelastic scattering $\pm$30%	+0.044	+0.089
proton rescattering $\pm$10%	-0.022	+0.090
Fermi motion ($\pm$ 5MeV/c)	$\pm$ 0.004	
Sub-total	+0.172	-0.022
Detector effects		
Cross talk $\pm$0.25%	+0.057	-0.035
PMT resolution $\pm$10%	+0.037	-0.023
Quenching constant $\pm$0.0023	+0.035	+0.032
Sub-total	+0.076	-0.042
Reconstruction effects		
Hit threshold $\pm$15%	$\pm$ 0.038	
Muon momemtum scale $\pm$2.7%	+0.088	-0.008
Angular resolution (smeared by 0.009)	$\pm$ 0.024	
Sub-total	+0.099	-0.046
Total	+0.225	-0.101

Table C.6: Systematic errors for the CCpπ^+ to CCQE cross section ratio in the third energy bin.

source of systematic	error
MC statistics	+0.046 -0.046
Model effects	
M_A (CCQE) $\pm$0.1	-0.031 +0.022
Bodek/Yang Corr $\pm$30%	-0.015 +0.017
Nπ weighting	$\pm$ 0.072
Neutrino Flux	+0.063 -0.055
Sub-total	+0.099 -0.097
Nuclear effects	
π absorption $\pm$30%	+0.093 +0.002
π inelastic scattering $\pm$30%	+0.020 -0.136
proton rescattering $\pm$10%	+0.075 -0.061
Fermi motion ($\pm$ 5MeV/c)	$\pm$ 0.022
Sub-total	+0.123 -0.151
Detector effects	
Cross talk $\pm$0.25%	+0.047 -0.039
PMT resolution $\pm$10%	+0.023 -0.019
Quenching constant $\pm$0.0023	-0.022 -0.008
Sub-total	+0.052 -0.049
Reconstruction effects	
Hit threshold $\pm$15%	$\pm$ 0.074
Muon momemtum scale $\pm$2.7%	+0.254 -0.291
Angular resolution (smeared by 0.009)	$\pm$ 0.151
Sub-total	+0.305 -0.336
Total	+0.350 -0.387

Table C.7: Systematic errors for the CCpπ^+ to CCQE cross section ratio in the fourth energy bin.

C.2 Using only the 3 track sample

Total measurement:

Measurement	MC prediction
0.319 ± 0.092 (stat.) $^{+0.095}_{-0.054}$ (syst.)	0.565 ± 0.002 (stat.)

Table C.8: Measurment of the CCpπ^+ to CCQE cross section ratio.

Energy dependent measurement:

Eν (GeV)	Measurement	MC prediction
≤ 1.35	0.206 ± 0.264 (stat.) $^{+0.590}_{-0.071}$ (syst.)	0.441 ± 0.002 (stat.)
1.35-1.72	0.314 ± 0.268 (stat.) $^{+0.101}_{-0.494}$ (syst.)	0.695 ± 0.004 (stat.)
1.72-2.22	0.568 ± 0.256 (stat.) $^{+0.437}_{-0.155}$ (syst.)	0.782 ± 0.006 (stat.)
$2.22 \leq$	0.141 ± 0.182 (stat.) $^{+0.113}_{-0.245}$ (syst.)	0.860 ± 0.009 (stat.)

Table C.9: Measurment of the energy dependent CCpπ^+ to CCQE cross section ratio.

The detailed contribution to the systematic uncertainty on the measurement of the cross section of the single pπ^+ interaction normalized to CCQE appears in Table C.10.

The systematic errors for the measurement done in the 4 energy bins are quoted in Tables C.11, C.12, C.13, and C.14.

source of systematic	error
MC statistics	+0.024 -0.024
Model effects	
M_A (CCQE) $\pm$0.1	-0.008 +0.008
Bodek/Yang Corr $\pm$30%	-0.009 +0.009
Nπ weighting	$\pm$ 0.028
Neutrino Flux	+0.004 -0.005
Sub-total	+0.031 -0.031
Nuclear effects	
π absorption $\pm$30%	+0.003 -0.003
π inelastic scattering $\pm$30%	+0.061 -0.024
proton rescattering $\pm$10%	+0.005 -0.019
Fermi motion ($\pm$ 5MeV/c)	$\pm$ 0.007
Sub-total	+0.062 -0.031
Detector effects	
Cross talk $\pm$0.25%	+0.055 +0.011
PMT resolution $\pm$10%	+0.019 -0.003
Quenching constant $\pm$0.0023	-0.009 +0.008
Sub-total	+0.059 -0.009
Reconstruction effects	
Hit threshold $\pm$15%	$\pm$ 0.018
Muon momemtum scale $\pm$2.7%	$\pm$ 0.000
Angular resolution (smeared by 0.009)	$\pm$ 0.001
Sub-total	+0.018 -0.018
Total	+0.095 -0.054

Table C.10: Systematic errors for the overall CCpπ^+ to CCQE cross section ratio.

source of systematic	error	
MC statistics	+0.057	-0.057
Model effects		
M_A (CCQE) $\pm$0.1	-0.004	+0.006
Bodek/Yang Corr $\pm$30%	-0.018	+0.020
Nπ weighting	$\pm$ 0.033	
Neutrino Flux	+0.004	-0.003
Sub-total	+0.039	-0.038
Nuclear effects		
π absorption $\pm$30%	+0.142	+0.079
π inelastic scattering $\pm$30%	+0.379	+0.226
proton rescattering $\pm$10%	+0.113	+0.004
Fermi motion ($\pm$ 5MeV/c)	$\pm$ 0.002	
Sub-total	+0.420	-0.002
Detector effects		
Cross talk $\pm$0.25%	+0.292	+0.196
PMT resolution $\pm$10%	+0.032	+0.021
Quenching constant $\pm$0.0023	+0.080	+0.048
Sub-total	+0.304	-0.00
Reconstruction effects		
Hit threshold $\pm$15%	$\pm$ 0.018	
Muon momemtum scale $\pm$2.7%	+0.060	+0.272
Angular resolution (smeared by 0.009)	$\pm$ 0.009	
Sub-total	+0.273	-0.020
Total	+0.590	-0.071

Table C.11: Systematic errors for the CCpπ^+ to CCQE cross section ratio in the first energy bin.

source of systematic	error
MC statistics	+0.068 -0.068
Model effects	
M_A (CCQE) $\pm$0.1	-0.008 +0.007
Bodek/Yang Corr $\pm$30%	-0.005 +0.006
Nπ weighting	$\pm$ 0.016
Neutrino Flux	+0.009 -0.009
Sub-total	+0.021 -0.020
Nuclear effects	
π absorption $\pm$30%	-0.127 -0.084
π inelastic scattering $\pm$30%	-0.260 -0.381
proton rescattering $\pm$10%	-0.128 -0.017
Fermi motion ($\pm$ 5MeV/c)	$\pm$ 0.016
Sub-total	+0.016 -0.422
Detector effects	
Cross talk $\pm$0.25%	+0.040 -0.020
PMT resolution $\pm$10%	-0.029 -0.027
Quenching constant $\pm$0.0023	-0.117 -0.021
Sub-total	+0.040 -0.122
Reconstruction effects	
Hit threshold $\pm$15%	$\pm$ 0.049
Muon momemtum scale $\pm$2.7%	-0.097 -0.207
Angular resolution (smeared by 0.009)	$\pm$ 0.031
Sub-total	+0.058 -0.215
Total	+0.101 -0.494

Table C.12: Systematic errors for the CCpπ^+ to CCQE cross section ratio in the second energy bin.

source of systematic	error	
MC statistics	+0.067	-0.067
Model effects		
M_A (CCQE) $\pm$0.1	-0.014	+0.013
Bodek/Yang Corr $\pm$30%	-0.011	+0.012
Nπ weighting	$\pm$ 0.045	
Neutrino Flux	+0.012	-0.011
Sub-total	+0.050	-0.050
Nuclear effects		
π absorption $\pm$30%	+0.027	+0.046
π inelastic scattering $\pm$30%	+0.340	+0.230
proton rescattering $\pm$10%	+0.217	-0.072
Fermi motion ($\pm$ 5MeV/c)	$\pm$ 0.001	
Sub-total	+0.406	-0.072
Detector effects		
Cross talk $\pm$0.25%	-0.064	-0.085
PMT resolution $\pm$10%	+0.077	+0.015
Quenching constant $\pm$0.0023	+0.049	-0.006
Sub-total	+0.091	-0.085
Reconstruction effects		
Hit threshold $\pm$15%	$\pm$ 0.013	
Muon momemtum scale $\pm$2.7%	+0.081	+0.052
Angular resolution (smeared by 0.009)	$\pm$ 0.067	
Sub-total	+0.106	-0.068
Total	+0.437	-0.155

Table C.13: Systematic errors for the CCpπ^+ to CCQE cross section ratio in the third energy bin.

source of systematic	error
MC statistics	+0.078 -0.078
Model effects	
M_A (CCQE) $\pm$0.1	-0.011 +0.006
Bodek/Yang Corr $\pm$30%	-0.002 +0.003
Nπ weighting	$\pm$ 0.019
Neutrino Flux	+0.011 -0.009
Sub-total	+0.023 -0.024
Nuclear effects	
π absorption $\pm$30%	-0.060 -0.034
π inelastic scattering $\pm$30%	+0.006 -0.156
proton rescattering $\pm$10%	-0.139 +0.019
Fermi motion ($\pm$ 5MeV/c)	$\pm$ 0.010
Sub-total	+0.022 -0.218
Detector effects	
Cross talk $\pm$0.25%	+0.022 -0.009
PMT resolution $\pm$10%	+0.015 +0.002
Quenching constant $\pm$0.0023	-0.048 +0.038
Sub-total	+0.046 -0.049
Reconstruction effects	
Hit threshold $\pm$15%	$\pm$ 0.001
Muon momemtum scale $\pm$2.7%	-0.007 +0.005
Angular resolution (smeared by 0.009)	$\pm$ 0.058
Sub-total	+0.058 -0.058
Total	+0.113 -0.245

Table C.14: Systematic errors for the CCpπ^+ to CCQE cross section ratio in the fourth energy bin.